Biomimetic Oxygenation Reactions in Metal Cryptates

Laura Chaloner

A Thesis

In the Department

Of

Chemistry and Biochemistry

Presented in Partial Fulfillment of the Requirements

For the Degree of

Doctor of Philosophy (Chemistry) at

Concordia University

Montreal, Quebec, Canada

July 2015

CONCORDIA UNIVERSITY
SCHOOL OF GRADUATE STUDIES

This is to certify that the thesis prepared

By: Laura Chaloner

Entitled: Biomimetic Oxygenation Reactions in Metal Cryptates

and submitted in partial fulfillment of the requirements for the degree of

complies with the regulations of the University and meets the accepted standards with respect to originality and quality.

Signed by the final examining committee:

Dr. D. Fraser — Chair

Dr. G. Hanan — External Examiner

Dr. P. Bianucci — External to Program

Dr. L. Cuccia — Examiner

Dr. P. Forgione — Examiner

Dr. X. Ottenwaelder — Thesis Supervisor

Approved by

Chair of Department or Graduate Program Director

Dean of Faculty

Abstract

Biomimetic Oxygenation Reactions in Metal Cryptates

Laura Chaloner, Ph. D.
Concordia University, 2015

Oxygenase metallo-enzymes are an inspiration for the development of one-step C-H bond hydroxylations reactions. Presented here are two synthetic models (cryptands **LTEA** and **LTTA**), that are inspired by the second-coordination sphere features of such enzymes. The reactivity of copper(II)- and iron(III)-hydroperoxo species with these cryptands were studied, as they are key intermediates proposed in the catalytic cycles of C-H bond hydroxylation performed by oxygenases. Ultimately, this work was developed to further our understanding of oxygenation reactions by guiding the reactivity of copper(II)- and iron(III)-hydroperoxo intermediates with second coordination sphere features.

The structure and the reactivity of copper(II) complexes of **LTEA** was influenced by the second coordination sphere. Reaction of the complexes with basic hydrogen peroxide in methanol led to the formation of copper(II)-hydroperoxo intermediates. The mechanism of the reaction was studied by low-temperature mass spectrometry, electron paramagnetic resonance and stopped-flow ultraviolet/visible spectroscopy. Both the starting complexes and intermediates were constrained by the cryptand to square-based geometries. The decomposition of the intermediates via self-oxidation was probed by deuterating select positions on the cryptand. A small kinetic isotope effect of 1.5, in conjunction with the analysis of the demetallated organic products, reveals that the cryptand steers the reactivity towards a direct oxygen-atom transfer to a tertiary amine on the cryptand, forming an N-oxide.

A novel cryptand, **LTTA**, was designed and synthesized in high-yields and was shown to be ditopic through X-ray crystallography and NMR spectroscopy. The reaction of iron(II)-triflate complexes of **LTTA** with hydrogen peroxide or iodosylbenzene led to an intramolecular aromatic C-H bond hydroxylation, to afford an iron(III)-phenolate species, which was characterized by mass spectrometry, electron paramagnetic resonance and stopped-flow ultraviolet/visible spectroscopy. The kinetic analysis from the reaction of the iron(II) complex with hydrogen peroxide led to the identification of an iron(III)-hydroperoxo intermediate, formed prior to the iron(III)-phenolate. The iron(III)-hydroperoxo is proposed to first undergo heterolytic cleavage to form a high-valent Fe(V)-oxo-hydroxo, a mechanism comparable to C-H bond activation in Rieske dioxygenases.

Acknowledgements

First and foremost, I thank my research supervisor, Dr. Xavier Ottenwaelder, whose wealth of knowledge and subtle but effective motivation has guided me through the Ph.D. program. It is his guidance and support that has allowed me to mature as a chemist.

I thank my committee members, Dr. Louis Cuccia and Dr. Pat Forgione for providing a valuable outsiders perspective to my research. Their advice and direction was greatly appreciated.

I thank all the XoRG members, past and present, who have contributed to both scientific and non-scientific discussions with a special thanks to those who have become life-long friends.

Significant portions of this research were only possible because of collaborations. For this reason I thank Dr. Fabrice Thomas, Dr. Michael Neidig and Dr. Siegfried Schindler. I thank the inorganic research groups of Dr. Garry Hanan and Dr. Hein Schaper at University of Montreal for their help.

I would like to thank the Department of Chemistry and Biochemistry at Concordia University. It has been a joy to work within the department and that is in large part because of the friendly work environment. I would like to single out a select few who have guided my academics, provided training for various instruments or who have provided general helped; Dr. Heidi Muchall (GPD), Alain Tessier (MS Specialist), Vincent Lau (Technician), and Dr. Alexey Denisov (NMR specialist).

I thank NSERC, CFI and FRQNT for funding this research. I am also thankful for awards from, FRQNT-Centre in Green Chemistry and Catalysis (Stage International) and Concordia University (Mobility, Accelerator and Conference travel grants).

Finally, I thank my family and friends who have always support me. There have been laughs and tears along the way and I am very thankful to have shared those moments.

Contribution from Authors

Formation and Reactivity of a Biomimetic Hydroperoxocopper(II) Cryptate

Laura Chaloner	Experimental work for the synthesis and reactivity of complexes and intermediates, data analysis, writing, editing and proofing
Mohammad S. Askari	Low temperature-stopped flow, data analysis, editing, proofing and bibliography
Adrian Kutteh	Ligand synthesis
Siegfried Schindler	Editing, proofing and funding for stopped-flow experiments
Xavier Ottenwaelder	Research supervisor, funding, data analysis, writing, editing and proofing

Supramolecular Control of Monooxygenase Reactivity in a Copper(II) Cryptate

Laura Chaloner	Experimental work for the synthesis and reactivity of complexes, data analysis, writing, editing and proofing
Alyona Khomutovskaya	Optimized the synthesis of deuterated cryptand
Fabrice Thomas	EPR analysis, writing, editing, proofing, funding for stopped-flow and EPR experiments
Xavier Ottenwaelder	Research supervisor, funding, data analysis, writing, editing and proofing

Bio-Inspired Oxidation Chemistry of a Cu(II)-Fluoride Cryptate with C_3-Symmetry

Laura Chaloner	Experimental work, data analysis, writing, editing and proofing
Xavier Ottenwaelder	Research supervisor, funding, editing and proofing

High-yield Synthesis of Potentially Ditopic Coordinating Cryptands and their Metal Complexes

Laura Chaloner	Experimental work, data analysis, writing, editing and proofing
Xavier Ottenwaelder	Research supervisor, funding, data analysis, writing, editing and proofing

Formation and Reactivity of a Fe(III)-Hydroperoxo Supported by a Coordinating Cryptand

Laura Chaloner	Experimental work, data analysis, writing, editing and proofing
Xavier Ottenwaelder	Research supervisor, funding, editing and proofing

Table of Contents

List of Figures

List of Schemes

List of Charts

List of Tables

List of Abbreviations

α-KG	α-ketoglutarate
ANOVA	Analysis of variance
B	Magnetic field
BA	N-benzyl-6-((bis(pyridin-2-ylmethyl)amino)methyl)pyridin-2-amine
ABLM	Activated Bleomycin
BDE	Bond Dissociation Energy
BLM	Bleomycin
bpba	Bis(2-pyridylmethyl)tert-butylamine
BPPA	Bis(6-pivalamide-2-pyridylmethyl)-(2-pyridylmethyl)amine
CDO	Carbazole 1,9a-dioxygenase
CHN	Carbon Hydrogen Nitrogen (elemental analysis)
COSY	Correlation Spectroscopy
CSI	Cold Spray Ionization
DβM	Dopamine-β-monooxygenase
Δ_o	Octahedral field splitting parameter
$\Delta H^{\ddagger}$	Enthalpy of activation
$\Delta S^{\ddagger}$	Entropy of activation
DFT	Density Functional Theory
$^{DMA}N_3S$	2-((((4-(dimethylamino)pyridin-2-yl)methyl)(2-((2-ethylbenzyl)thio)ethyl)amino)methyl)-N,N-dimethylpyridin-4-amine
DNA	Deoxyribonucleic Acid
ε	Molar Absorptivity
EDTA	Ethylenediaminetetraacetic acid
EPR	Electron Paramagnetic Resonance
ESI	Electrospray Ionization
ET	Electron Transfer
η	Hapticity
Et_3N	Triethylamine
Equiv.	Equivalents
g	g-factor
HAT	Hydrogen-atom transfer
His-Gly-His	Histidine- Glycine- Histidine
hν	Photon energy
HS	High Spin
HSAB	Hard and Soft Acids and Bases
IR/NIR	Infrared/Near Infrared
k_{obs}	Pseudo-ordered rate constant

k	Rate constant
K	Equilibrium constant
KIE	Kinetic Isotope Effect
L	Ligand
LMCT	Ligand to metal charge transfer
LS	Low Spin
M	Metal or metal ion
m/z	Mass-to-charge ratio
MCD	Magnetic circular dichroism
MeCN	Acetonitrile
MeOH	Methanol
MLCT	Metal-to-ligand charge-transfer
MPPH	2-Methyl-1-Phenyl-2-Propyl-Hydroperoxide
MS	Mass spectrometry
μ_B	Bohr magneton
N_2O_2	See chart 5, C
$N3Py^{amide}SR$	See chart 10, B
N_3S	2-bis(6-methyl-2-pyridylmethyl)amino-1-(phenylthio)ethane
N4Py	N,N-bis(2-pyridylmethyl)bis(2-pyridyl)methylamine
NDO	Naphthalene 1,2-dioxygenase
NMR	Nuclear Magnetic Resonance
NOESY	Nuclear Overhauser effect spectroscopy
OAT	Oxygen-Atom Transfer
ORTEP	Oak Ridge Thermal Ellipsoid Plot
PhIO	Iodosylbenzene
PHM	Peptidylglycine-α-hydroxylating monooxygenase
PyTacn	1-(2-pyridylmethyl)-4,7-dimethyl-1,4,7-triazacyclononane
r_{vdW}	Van der Waals radius
SC-XRD	Single-Crystal X-Ray Diffraction
TAML	Tetraamido macrocyclic ligand
TβM	Tyramine β-monooxygenase
TBP	Trigonal Bipyramidal
TEA	Triethanolamine
TLC	Thin-layer chromatography
TMC	N-tetramethylated cyclam
TMG_3 -Tren	Tris(tetramethylguanidino)
TMIMA	Tris((1-methyl-imidazol-2-yl)methyl)amine
TPA	Tris-(2-pyridylmethyl)amine
$TPyA^{Ar}$	Tris-(5-arylpyrrol-2- methyl)amine

TPA^{Ph}	6-Phenyl(tris(2-pyridylmethyl)amine)
Tren	Tris-(2-aminoethyl)amine
TTA	Tris-(4-methanol-1-ethyltriazole)amine
UV/Vis	Ultraviolet/Visible

Chapter 1: Introduction

1.1 Purpose

A coveted synthetic oxidation method is the selective one-step hydroxylation of C-H bonds.[1] This reaction provides access to functionalized molecules that have great utility in synthetic chemistry. Aliphatic C-H bond hydroxylation is challenging, however, because the strength of C-H bonds makes the reaction kinetically inert, necessitating the need for strong oxidants, high temperatures or acid/base additives to complete the reaction. These conditions are not favourable for chemo- and regioselective reactions nor do they fall in line with green chemistry objectives. This has created a research space to develop mild C-H bond oxidation reactions.[2-3] Significant progress has been made in this field by using a variety of transition metal catalysts, organometallic catalysts, or Fenton chemistry.[4] For example, White and coworkers have developed iron catalysts capable of selective, and more notably, predictable aliphatic C-H bond oxidations.[5] Pérez and coworkers have developed a trispyrazolylborate copper catalyst that can activate hydrogen peroxide and catalyze the conversion of cycloalkanes and hexanes to alcohols, ketones and alkenes.[6] Despite this remarkable progress, much remains to be improved in terms of efficiency, and selectivity.

Nature has created several enzymes that can selectively hydroxylate a C-H bond at ambient temperature, using dioxygen as the oxidant and forming water as a by-product.[7-8] For this reason, these biological systems serve as inspiration to develop synthetic oxidative transformations.[9] Dioxygen is an ideal oxidant because it is abundant, accessible and environmentally friendly. The pitfall lies in the fact that it has a triplet ground state and is therefore an inert molecule. To overcome this, transition metals are used to reduce dioxygen by 1 or 2 electrons, transforming it into a radical species or a singlet species with greater electrophilic reactivity. This process is easily performed by metallo-proteins where the metal active sites are located within a protective pocket surrounded by the backbone of the enzymes.[10] In many cases, however, the exact nature of the activation of O_2 and the resultant M/O_2 chemistry is still unclear.

The long term goal of designing environmentally friendly oxidation methods first requires an understanding of the mechanisms that enzymes facilitate. This is the primary focus of biomimetic inorganic chemistry.[1] Synthetic metal complexes are designed to activate small molecules in a similar manner to biological systems.[11] The coordination environment of the metal ions and the protective

pocket in enzymes are key features that are used as inspiration for ligand design in synthetic systems. The benefit of biomimetic chemistry is that it allows for simplified data analysis and the use of spectroscopic techniques that may not be applicable to enzymes.

1.2 Background

1.2.1 Biological Systems

The most prevalent d-block ions found in the human body are iron, copper and zinc. Oxidative biological systems have incorporated iron and copper into their structures, in part, because of their redox properties.[12] Iron and copper each have two common oxidation states, Cu(I)/Cu(II) and Fe(II)/Fe(III). Oxidative enzymes reduce dioxygen to an active intermediate that can abstract a hydrogen atom and/or transfers an oxygen atom(s) (Scheme 1),[12-13] and have been categorized as monooxygenase, dioxygenase or oxidase. Oxygenase reactions are distinguished by the transfer of one or two oxygen atoms to a substrate.[12] Examples are methane monooxygenase that catalyze the conversion of methane into methanol and naphthalene 1,2 dioxygenase (NDO) that transforms naphthalene into 1R, 2S-1,2-dihydronaphthalene-1,2-diol. Oxidases, on the other hand, catalyze dehydrogenation reactions using dioxygen as an oxidant and forming water or hydrogen peroxide as the by-product. An example is galactose oxidase that transforms a primary alcohol into an aldehyde with dioxygen as the electron acceptor.[12] Enzymes can be further classified as mono, di, tri or multi-nuclear depending on the number of metal ions involved directly at the active site. Finally, the enzymes with an iron-containing active site are classified based on the coordination environment of the metal centre, namely heme or non-heme depending on the presence of a porphyrin ring.

We are interested in the coordination chemistry aspects of C-H bond hydroxylation reactions and our research is inspired by non-heme mononuclear mono- or dioxygenases. Although copper- and iron-containing enzymes both preform C-H bond hydroxylation reactions, each class of enzymes has developed individual mechanisms to activate dioxygen.

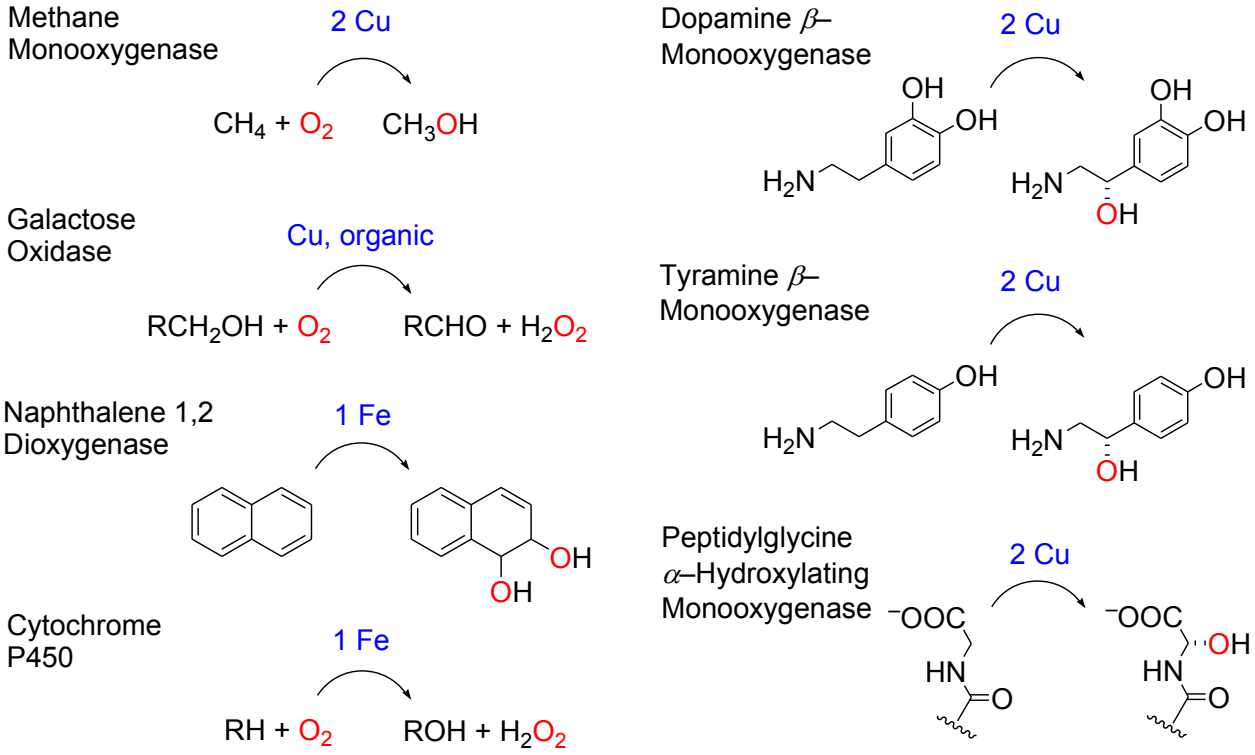

Scheme 1. Oxygenase and oxidase reactions of a selection of copper and iron enzymes.

Several intermediates and binding modes are possible from the interaction of dioxygen with Cu and Fe (Scheme 2). The hapticity denoted by η corresponds to the number of oxygen atoms coordinated to the metal. The coordination mode can be either end-on (η^1) with one oxygen atom coordinated to the metal or side-on (η^2) with two oxygen atoms coordinated. Bridging oxygen atoms are indicated by the symbol μ. The initial coordination of dioxygen to a metal is normally coupled to an electron transfer (ET) to form a superoxo intermediate. Addition of an electron from the metal or an external source to the superoxo leads to peroxo intermediates. If the provided electron is coupled to a proton transfer then a hydroperoxo intermediate is formed. Further reduction of the dioxygen intermediates leads to O-O bond cleavage and formation of oxo, oxo-hydroxo or oxyl intermediates. These intermediates are proposed in hydrogen-atom transfer (HAT) and oxygen atom transfer (OAT) reactions. Mechanistically, OATs are characterized by the direct transfer of an oxygen atom from a donor to an acceptor group while HAT is the transfer of a hydrogen atom from one functional group to the other.[14-15]

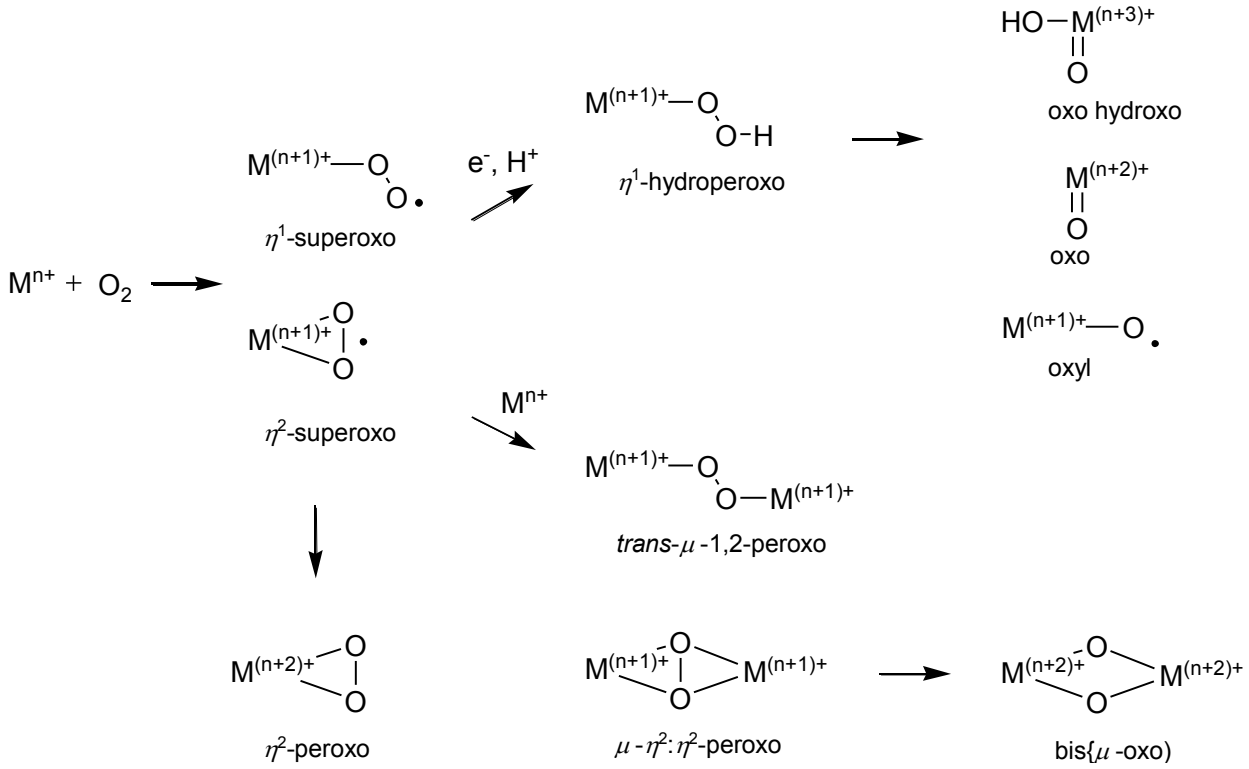

Scheme 2. M/O_2 pathways and typical intermediates

1.2.1.1 Mononuclear copper monooxygenases

The enzymes peptidylglycine-α-hydroxylating monooxygenase (PHM), dopamine-β-monooxygenase (DβM) and tyramine-β-monooxygenase (TβM) activate molecular dioxygen to achieve C-H bond hydroxylation, and their structures and mechanisms of action have been well studied.[7,16] PHM catalyzes the hydroxylation of a glycine-extended peptide to form peptidyl-α-hydroxyglycine, DβM catalyzes the hydroxylation of dopamine to form norepinephrine and TβM hydroxylates tyramine, forming octopamine (Scheme 1).[17] By activating dioxygen at a mononuclear Cu(I) active site (Cu_B), a hydrogen-atom transfer (HAT) from the substrate occurs. As the HAT is often the rate-limiting step it, coupled with the transfer of the oxygen atom, are the most important steps. The suggested mononuclear reaction intermediates responsible for C-H bond functionalization in these enzymes are:[17]

- Cu(II)-superoxo,
- Cu(II)-hydroperoxo,
- Cu(II)-oxyl/Cu(III)-oxo

Initially, a Cu(II)-hydroperoxo intermediate was proposed for the HAT,[18] but with the accumulation of several studies described below, a Cu(II)-superoxo species is now viewed as the intermediate responsible for the HAT.[1,19-21]

The crystal structure of PHM has been solved and based on spectroscopic, sequencing and kinetic data, the active site structures of DβM and TβM are similar.[22-23] The enzymes consist of two domains; each domain has a copper binding site. The active site (Cu_B), where dioxygen binds, has a tetrahedral geometry coordinated to two histidines, a methionine and a water molecule. The metal centre in the second domain (Cu_A) is coordinated to three histidines in a T-shape (Figure 1).[20] Both copper sites are directed towards the inter-domain space and are solvent accessible.[22] The two metal centres are separated by a distance of 11 Å and are maintained at this distance throughout the reaction, eliminating the possibility of a dinuclear species during the catalytic cycle.[22] In PHM, the substrate cleft is designed to specifically bind peptides with a terminal glycine residue. When the substrate is docked, it acts as a bridge between the two domains.[22] With PHM, the major interaction tethering the substrate to the enzyme is hydrogen bonding between the peptide and amino acid residues in both domains.

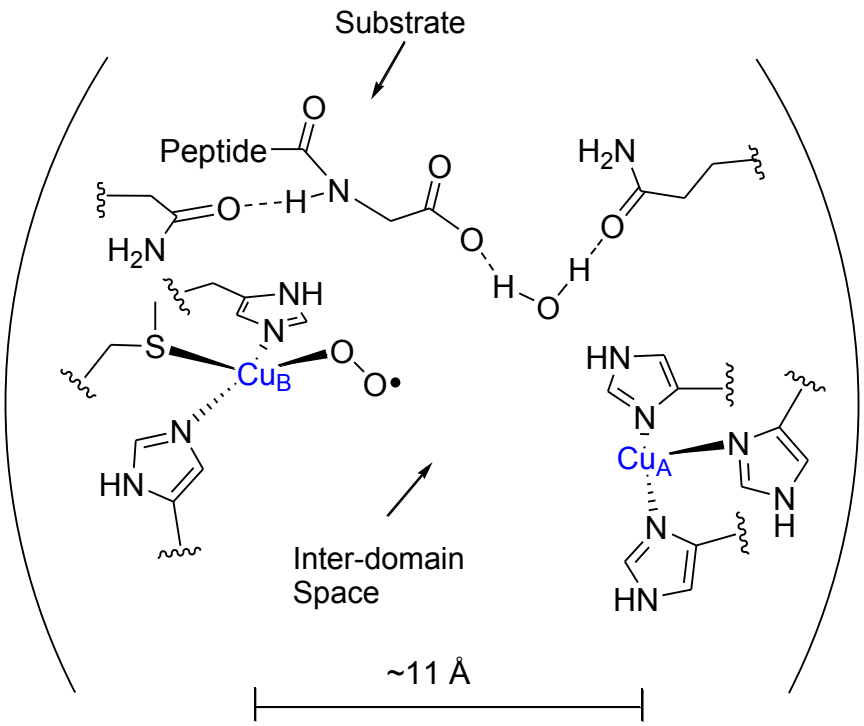

Figure 1. The active site structure of PHM and with a docked substrate and Cu(II)-superoxo intermediate

The resting state of the PHM is the oxidized form with both copper in the Cu(II) oxidation state. The metal centres are reduced to Cu(I) by two ascorbates to give the active form for of the enzyme. In the active form, the enzyme can bind and reduce dioxygen. In 2004, Prigge and coworkers obtained a crystal structure of the initial binding, providing valuable information on the mechanism of action. The key feature of the crystal structure is that dioxygen is bound end-on to Cu_B as either a Cu(I)-dioxygen or a Cu(II)-superoxo species. The tetrahedral geometry of the copper centre is maintained by coordinating O_2 to the previously solvent-occupied position. Furthermore, the Cu/O_2 complex is positioned such that a simple rotation around the Cu-O_2 bond would place the distal oxygen atom in a prime location for abstracting a hydrogen atom from the substrate. Finally, the structure shows that both the substrate and a water molecule create a hydrogen bonding network across the inter-domain space.[24]

Although the crystal structures provide valuable information such as the coordination mode of dioxygen, it only provides snapshots of the reaction. The majority of the research that has been used to explain the reaction pathway has been achieved by Klinman and coworkers. The mechanism proposed by Klinman (Scheme 3, A) starts with reversible binding of the substrate and coordination of dioxygen in a random order, step a.[25] An electron is transferred from the copper centre to the dioxygen to form the end-on Cu(II)-superoxo intermediate. In step b, the intermediate abstracts a hydrogen atom from the substrate forming a Cu(II)-hydroperoxo and a substrate radical. In step c, an electron is transferred from $Cu_{A,}$ and the hydroperoxo moiety is cleaved heterolytically to form Cu(II)-oxyl and water. The Cu(II)-oxyl combines with the radical on the substrate in step d, completing the oxygen atom transfer.[17] A second mechanism, proposed by Solomon and coworkers based on a computational approach, involves rebound of a hydroxyl group from the hydroperoxo intermediate onto the substrate (Scheme 3, B). Instead of a heterolytic cleavage in step c, the hydroperoxo undergoes homolytic cleavage. The formed Cu(II)-oxyl intermediate undergoes a proton/electron transfer from Cu_A forming a Cu(II)-hydroxyl group in step d.[7]

A Cu(II)-hydroperoxo intermediate could abstract a hydrogen from the substrate but DFT (Density Functional Theory) calculations showed that the HAT by a Cu(II)-superoxo intermediate is kinetically and thermodynamically more favorable.[21,26] Further support for the Cu(II)-superoxo HAT was provided by the ^{18}O Kinetic isotope effect (KIE) of PHM and DβM that was compared to the well-known mechanism of galactose oxidase.[27-28] As previously mentioned, galactose oxidase catalyzes the oxidation of an alcohol to an aldehyde and O_2 is then used as an oxidant to regenerate the catalyst. A HAT by a superoxo

intermediate is proposed in the regeneration of the catalyst.[28] The three ^{18}O KIE's for the HAT (DβM, PHM and galactose oxidase) were found to be the same (≥ 1.019) suggesting that the three enzymes undergo similar HAT steps.

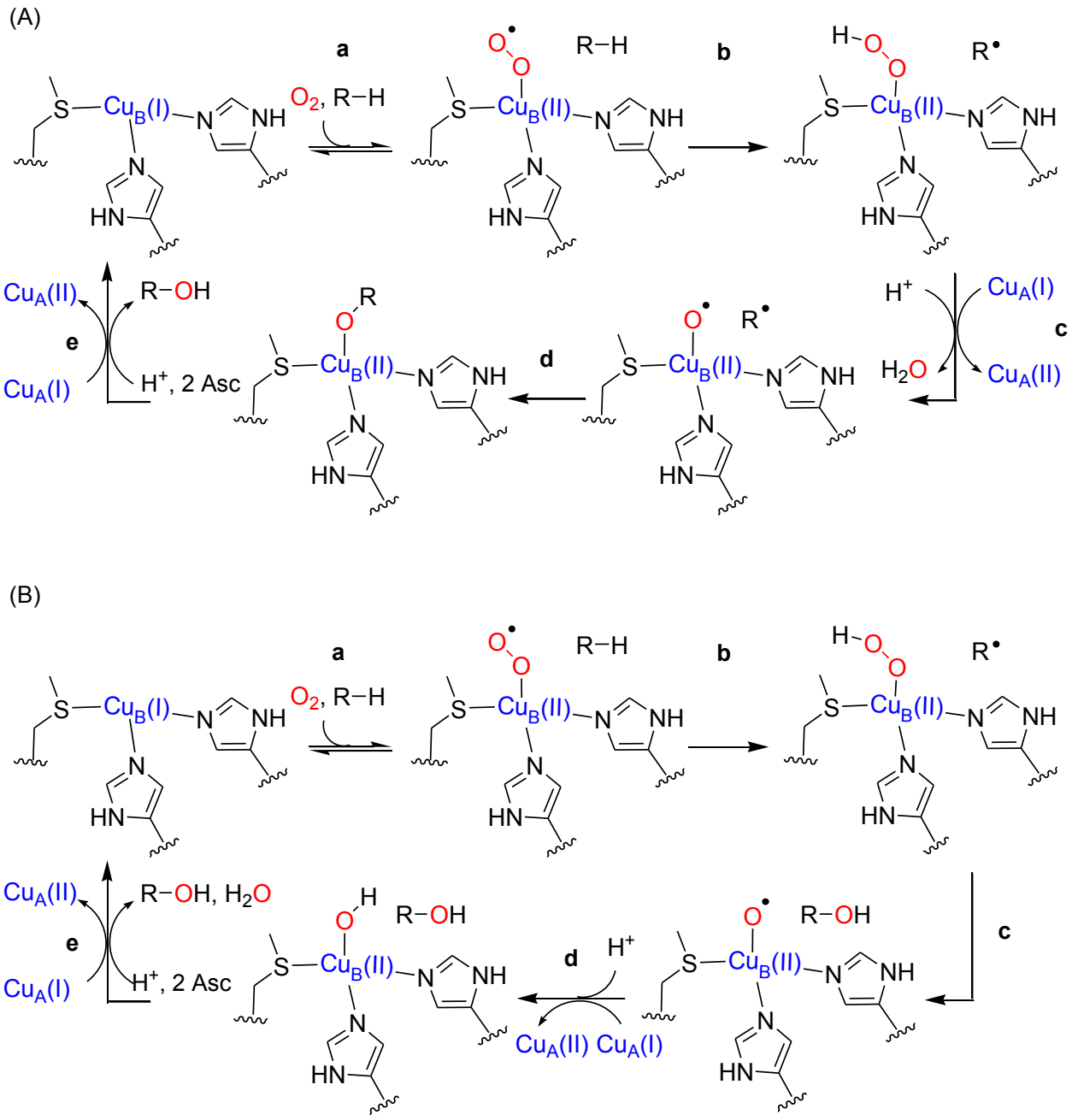

Scheme 3. Proposed mechanisms of C-H bond hydroxylation by mononuclear copper monooxygenase. (A) Heterolytic cleavage mechanism; (B) Rebound mechanism.

Over the course of the reaction, an electron is transferred from Cu_A to Cu_B. The transfer of the electron across the 11 Å solvent void has been puzzling and demonstrates how a protein can elegantly use the second coordination sphere of the active site to achieve its means. Based on the crystal structure of the substrate-docked enzymes, Prigge and coworkers suggested that the electron is transferred through a hydrogen-bond network composed of a water molecule and the substrate.[24] This ET pathway was invested by Klinman by substituting the PHM substrate with peptides of varying length. It was found that the different substrates had very little effect on the electron transfer pathway leading to the conclusion that the ET was either through the protein backbone, the inter-domain solvent cleft or a combination thereof.[29]

The mechanism of DβM, PHM and more recently TβM has been fleshed out in the last couple of decades yet aspects of the mechanism are unclear. Certain questions still need to be answered such as how is the oxygen atom transferred from the hydroperoxo intermediate to the substrate (is it a rebound or heterolytic cleavage mechanism) and how does the coordination sphere mediate the ET from Cu_A to Cu_B (protein backbone or inter-domain spaces)?

1.2.1.2 Heme and Non-heme iron enzymes

Part of our research is focused on biomimetic reactions of non-heme iron enzymes that perform C-H bond hydroxylations. This section will focus on what is currently known about these enzymes. Despite structural differences, the mechanisms of non-heme and heme enzymes have commonalities and the activation of O_2 by both types of enzymes will be discussed.

One of the many roles of cytochromes P450 is to metabolize drugs by hydroxylating aliphatic C-H bonds, increasing their water solubility and susceptibility to further degradation and excretion.[30] To achieve this, the enzyme employs different oxidation states of iron to transform O_2 into a potent electrophilic intermediate. The iron centre of P450's has an octahedral geometry consisting of a porphyrin ring in the equatorial position and water and methionine in the axial positions (step a). In the resting state, the Fe(III) centre is low spin (LS). Binding of the substrate, releases the water molecule and changes the spin state of the iron from LS to high spin (HS) (step b).[30] The change in spin state increases the reduction potential of the iron favoring the reduction to Fe(II) (step c).[31] It is the Fe(II) complex that reduces O_2 forming an Fe(III)-superoxo (step d). Contrary to copper monooxygenases, the superoxo intermediate does not abstract a hydrogen atom. An electron and proton are instead transferred to the

superoxo to form an Fe(III)-hydroperoxo intermediate (step e). The hydroperoxo intermediate is protonated, followed by heterolytic cleavage of the O-O bond. The result is the formation of "compound I", a LS Fe(IV)-oxo with a porphyrin-π-cation radical (step f). In 2010, Rittle and Green were able to provide convincing kinetic data that confirmed compound I as the intermediate responsible for abstracting the hydrogen atom from the substrate.[32] Upon hydrogen-atom abstraction, an Fe(IV)-hydroxide is formed and a subsequent rebound mechanism is proposed to complete the C-H bond hydroxylation step.

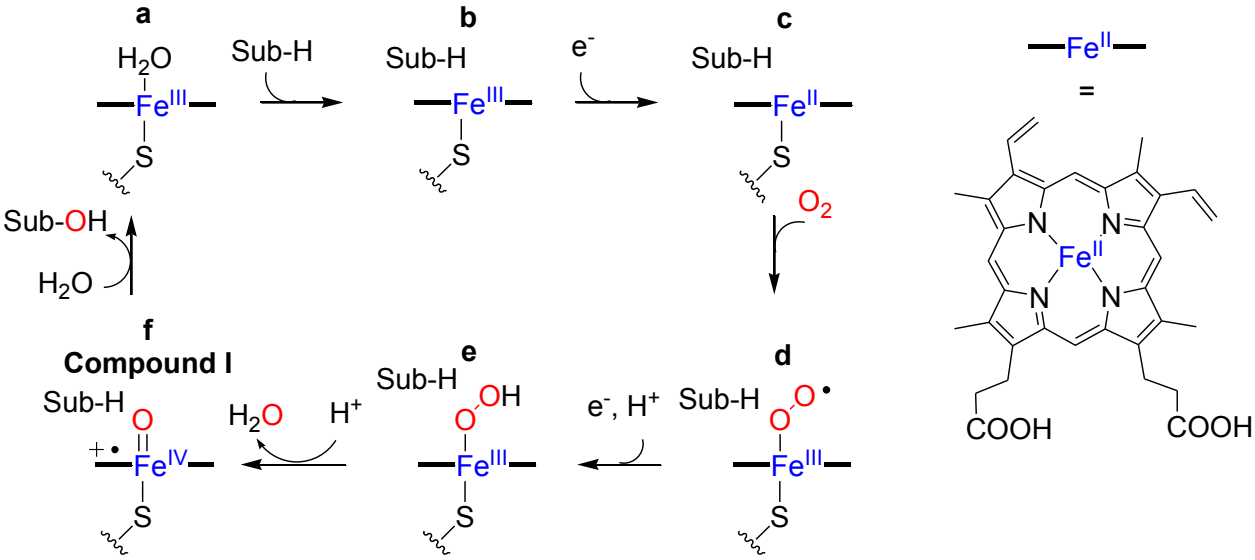

Scheme 4. Left: Proposed mechanisms of C-H bond hydroxylation by cytochrome P450 Right: Protoporphyrin-IX with coordinated Fe.

The oxidation potency of cytochromes P450 relies on the porphyrin ring to delocalize the radical cation of compound I, but what happens in enzymes where the coordination environment only contains a redox-innocent ligand? The reactivity of non-heme monooxygenase iron systems is much less understood compared with that of cytochromes P450. Three examples will be discussed.

Bleomycin (BLM) is a glycopeptide with a non-heme bound Fe(II) active site that initiates DNA strand scission.[33] Although BLM is not classified as an enzyme, it shows similar reactivity to mononuclear metallo-enzyme and is therefore worth mentioning. The active form (ABLM) that instigates a HAT leading to DNA strand scission is a LS Fe(III)-hydroperoxo species. Three pathways have been proposed for the HAT (Scheme 5).[10] The first pathway is direct abstraction of a hydrogen atom by the hydroperoxo

intermediate. The second option is heterolytic cleavage of the O-O bond to form a high valent 'Fe(V)-oxo' followed by HAT. Akin to the heme system, in this scenario the metal centre has a Fe(IV) oxidation state and the ligand is oxidized. The third scenario is homolytic cleavage of the O-O to form an Fe(IV)-oxo intermediate to abstracts the hydrogen atom. Through computational and experimental studies, Solomon et al. have shown that the most probable pathway is by direct attack of the hydroperoxo intermediate to abstract a hydrogen atom from DNA.[34-35] Despite extensive work to elucidate the mechanism of bleomycin, conclusive experimental evidence of the intermediate responsible for the HAT step does not exist.

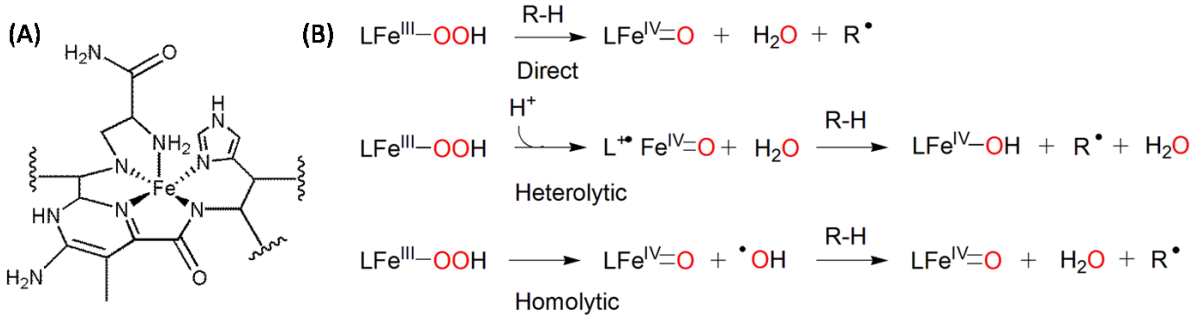

Scheme 5. (A) Coordination sphere of bleomycin (B) Three proposed reaction pathways for HAT by Bleomycin.

Rieske dioxygenases are a class of enzymes that are responsible for the *cis*-dihydroxylation of aromatic rings. Two specific examples are naphthalene 1,2-dioxygenase (NDO) and carbazole 1,9a-dioxygenase (CDO), both of which coordinate iron with 2 histidines and 1 carboxylate group. This coordination motif is common among many mononuclear non-heme enzymes and is called the facial triad.[36-37] Crystal structures of oxygenated NDO and CDO reveal different binding modes of O_2 (Chart 1). The crystal structure of NDO has O_2 coordinated side-on to the mononuclear iron centre.[38] The proposed mechanism by Ramaswamy and coworkers is: the side-on O_2 is activated by a 2-electron reduction to form an Fe(III)-peroxo intermediate that can attack the substrate in concerted mechanism.[38-39] The crystal structure of oxygenated CDO shows an end-on Fe(III)-peroxo intermediate that is likely protonated in the low pH environment. Through crystallographic evidence, Nojiri and coworkers attribute the different binding modes between the two enzymes to the presence or absence of substrate during the crystallization process.[40] In the absence of substrate, O_2 coordinates end-on and in the presence of substrate, the enzymes undergo a conformational change allowing O_2 to coordinate side-on. It is proposed that the side-on peroxo intermediate is the active species that reacts with the

substrate.[40] In a study using benzoate-1,2-dioxygenase, it was determined via EPR (electron paramagnetic resonance) and Mössbauer that the Fe(III)-peroxo intermediate is high spin (HS) (S= 5/2),[41] in contrast with the LS Fe(III)-hydroperoxo found in bleomycin. There are several questions surrounding the mechanism of *cis*-dihydroxylation by Rieske dioxygenases. Despite having the crystal structures of oxygenated NDO and CDO, it is still unclear if the peroxo intermediate is protonated. Furthermore, does the peroxo intermediate attack the substrate directly or does it first undergo a heterolytic cleavage to form high valent Fe(V)-oxo-hydroxo intermediate?

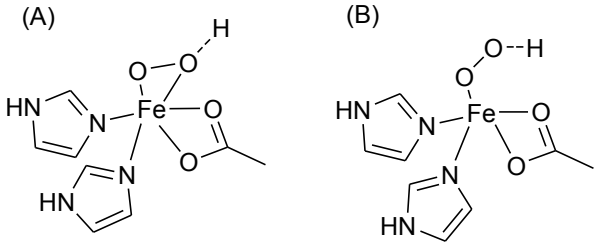

Chart 1. Facial triad coordination motif (A) Side-on peroxo and (B) End-on peroxo. The peroxo may be protonated.

A second family of enzymes responsible for arene hydroxylation reactions, among other transformations, is the α-ketoglutarate (α-KG)-dependent enzymes.[42] The hydroxylation reaction involves an α-KG cofactor and upon binding of O_2 forms a Fe(III)-superoxo intermediate (Scheme 6). The superoxo intermediate attacks the cofactor forming an Fe(III)- alkylperoxo intermediate that leads to an Fe(IV)-oxo and release of CO_2 from the cofactor.[42] The Fe(IV)-oxo intermediate has been proven spectroscopically to be HS and is proposed to attack the aromatic ring.[37]

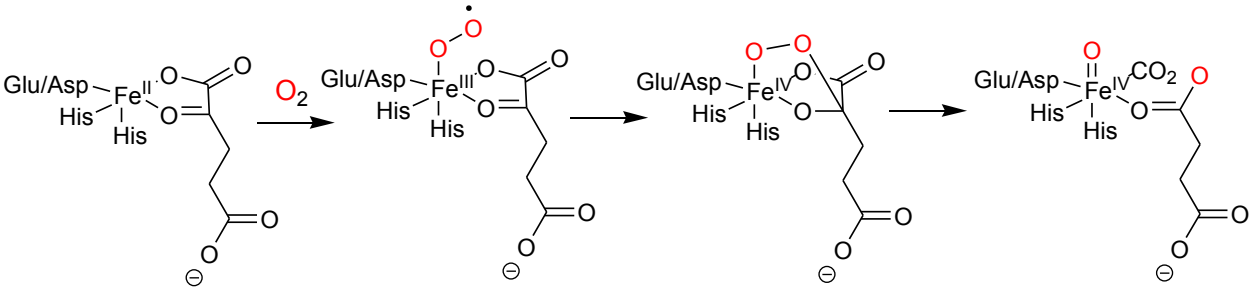

Scheme 6. Formation of the Fe(IV)-oxo in α-ketoglutarate (α-KG)-dependent enzymes.

Four biological systems have been described in this section with different intermediates proposed for the key mechanistic step of C-H bond hydroxylation. The commonality in all cases is the formation of a

Fe(III)-OOR (R = H or alkyl). While the fate of the Fe(III)-hydroperoxo intermediate in biological systems has been controversial, synthetic models have helped provide insight into the possible mechanisms.

1.2.2 Synthetic models

Synthetic models have been use to evaluate possible mechanisms of C-H bond activation and determine whether they could occur in biological systems. The goals of the synthetic mimics are to stabilize and characterize the proposed intermediates and to study their reactivity to gain insight into the oxidative transformations. The numerous possible redox and protic states of the metals and O_2, combined with several possible nuclearities, make M/O_2 chemistry very difficult to control in a beaker, in contrast to the controlled environment provided by a protein pocket.[12] In addition, most of the M/O_2 species are too oxidative to be stable at room temperature and must to be studied at low temperatures (typically -80°C).[12,43] It is possible to overcome these experimental constraints by using well-designed ligands to enhance the stability of the intermediates.

The research presented in this thesis is centered on the characterization and reactivity of copper and iron hydroperoxo intermediates. The Cu(II)-superoxo intermediate has been established as the intermediate responsible for HAT in mononuclear copper monooxygenases.[21] At the same time, bio-inspired Cu(II)-hydroperoxo complexes are able to initiate oxidative transformations.[44-52] Fe(III)-hydroperoxo intermediate is a common intermediate found in iron enzymes and is therefore a useful starting point for synthetic models. The reactions that take place with both copper and iron intermediates are often intramolecular leading to oxidation of the coordinating ligand. Although these intramolecular reactions have no prospects of being catalytic, they do provide valuable insight into the mechanism of their reactivity. The following section will focus on the advancements of synthetic models for characterizing the intermediates and studying their reactivity.

1.2.2.1 Synthetic models of Cu(II)-superoxo

The end-on Cu(II)-superoxo, in model systems, is formed from the reaction of Cu(II) with O_2. It is difficult to study/isolate due its high reactivity and propensity to dimerize.[53] Despite the difficulties, an end-on Cu(II)-superoxo species has been crystallized using a sterically demanding and electron-rich ligand, TMG_3Tren (TMG_3 = Tris(tetramethylguanidino), Tren = tris(2-aminoethyl)amine) (Chart 2, A).[19] In terms of reactivity, most Cu(II)-superoxo species typically undergo intramolecular C-H hydroxylations. The

exception is the example by Karlin and coworkers showed that exhibited a HAT from an exogenous substrate. The Cu(II)-superoxo supported by NMe_2-TPA (TPA = Tris[(2-pyridyl)methyl]amine) (Chart 2, B) abstracted a hydrogen from phenols to form phenoxyl radicals among other products.[54] Recently, Karlin and coworkers showed that the HAT reaction by the Cu(II)-superoxo could be improved by replacing a N donor with a S donor group (Chart 2, C).[55] One of the major drawbacks with the $^{DMA}N_3S$ system was that the Cu(II)-superoxo could only be formed at low temperatures (-135 °C), otherwise the formation of dimers prevent the reactivity.

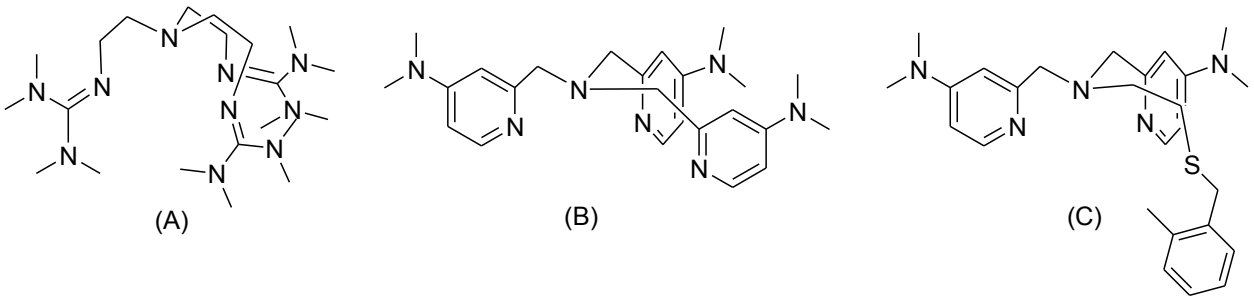

Chart 2. (A) TMG_3Tren (B) NMe_2-TPA (C) $^{DMA}N_3S$

1.2.2.2 Synthetic models of Cu(II)-hydroperoxo

In biological systems, the Cu(II)-hydroperoxo is formed from a Cu(II)-superoxo that abstracts a hydrogen atom from the substrate. In model systems a Cu(II)-hydroperoxo can be formed in a similar fashion or via the shunt pathway.[56] The shunt pathway for copper systems involves the reaction of hydrogen peroxide with a base, typically triethylamine (Et_3N), to form a hydroperoxo anion that coordinates to a Cu(II) centre. This pathway was investigated by Itoh and coworkers and an equilibrium between H_2O_2/Et_3N and $HOO^- \cdot Et_3NH^+$ was invoked.[57] The benefit of the shunt pathway is that the starting complex is an air-stable Cu(II)-species and the oxidant (H_2O_2) is a liquid making it easy to measure exact quantities/equivalents. These two parameters reduce the experimental constraints in forming the unstable hydroperoxo intermediate making the shunt pathway the most commonly used method to form hydroperoxo intermediates.[56]

The stability of Cu(II)-hydroperoxo intermediates is dramatically impacted by second coordination sphere interactions such as steric bulk and hydrogen bonding. Masuda and coworkers have examined the hydrogen bonding effects and found that the stability of the intermediate is increased with hydrogen bonding to the proximal oxygen. Two hydrogen-bond donors are incorporated into the BPPA

(bis(6-pivalamide-2-pyridylmethyl)-(2-pyridylmethyl)amine) ligand (Chart 3, A) resulting in the first fully characterized crystal structure of a mononuclear Cu(II)-hydroperoxo intermediate.[58] Karlin and coworkers went a step further and used the proximal hydrogen bonding to produce a complex capable of reversibly binding of the hydroperoxo moiety (Chart 3, B).[59] Masuda and coworkers also looked at hydrogen bonding to the distal oxygen of Cu(II)-hydroperoxo (Chart 3, C) and found that this modification accelerates the decomposition.[49] Other factors that influence the stability of the intermediate included the geometry of the metal centre and coordination of different functional groups.[60] A Cu(II)-hydroperoxo with trigonal-bipyramidal geometry is more stable than a Cu(II)-hydroperoxo with square-planar geometry.[45] When carboxylate groups are designed into the ligand to coordinate copper, the O-O bond strength is weakened and the Cu-O bond is strengthened, this decreases the stability of the hydroperoxo intermediates dramatically.[61]

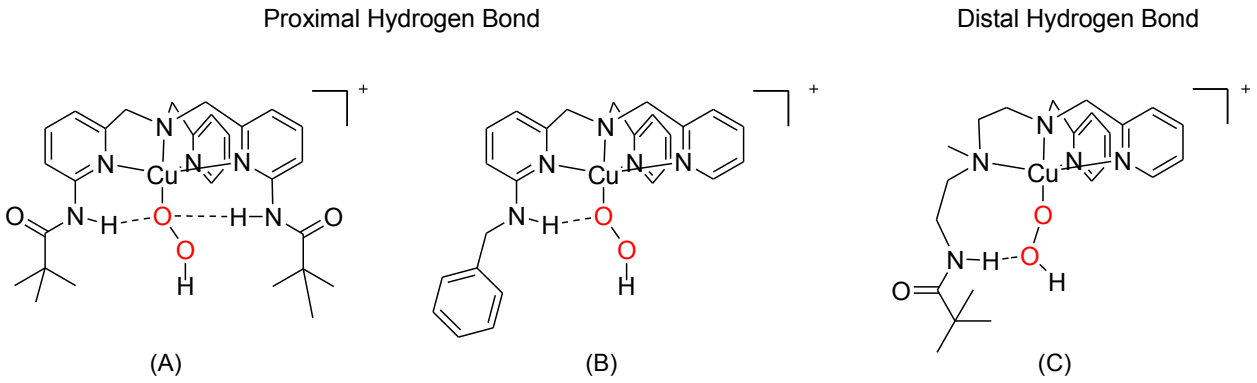

Chart 3. Hydrogen bonding in copper(II)-hydroperoxo intermediates: (A) BPPA-Cu(II)-hydroperoxo,[58] (B) BA-Cu(II)-hydroperoxo[59] and (C) L-Cu(II)-hydroperoxo.[49]

The typical reactions with Cu(II)-hydroperoxo intermediates are N-dealkylations originating from C-H bond hydroxylations, aryl C-H bond hydroxylations and oxygen-atom transfer reactions. Karlin and coworkers investigated Cu(II)-hydroperoxo-initiated N-dealkylation and N-debenzylation reactions.[47,52] Both intramolecular reactions proceed via abstraction of a hydrogen atom by the hydroperoxo intermediate followed by the loss of water and a rebound mechanism to form an alkoxide (Cu(II)-O-R) (Scheme 7). The alkoxide is then protonated leading to the final products, an aldehyde and amine. Support for the formation of an alkoxide is from the reactivity of a $TMG_3TrenCu(II)OOH$ intermediate that decomposes into a crystallographically characterized alkoxide $[TMG_3TrenO\text{-}Cu^{II}]^+$.[44] Karlin and coworkers also reported the first example of an aryl hydroxylation by a mononuclear Cu(II)-hydroperoxo

by using a TPA-derived ligand with a well-positioned aromatic ring.[51] The proposed mechanism is similar to that of the dealkylation mechanism where a Cu(II)-phenolate intermediate is formed and protonation leads to the final product (Scheme 7). An interesting mechanism that has been proposed by Karlin and coworkers is the cleavage of the O-O bond of the hydroperoxo intermediate leading to a Cu(III)-oxo or Cu(II)-oxyl species that causes the HAT. However, evidence for the high-valent copper intermediate lies mainly in mass spectrometry (MS) data, leaving the need for more convincing data.[47]

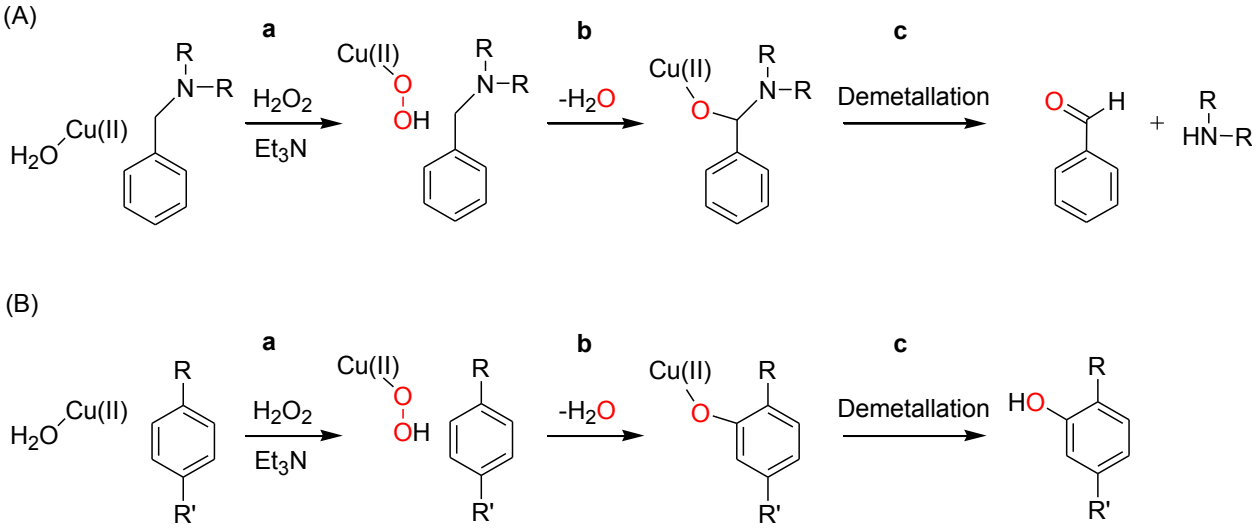

Scheme 7. Proposed mechanism for (A) N-debenzylation[47] and (B) arene-hydroxylation[51] initiated by a Cu(II)-hydroperoxo intermediate.

There are few examples of intermolecular reactions of Cu(II)-hydroperoxo intermediates and most involve OATs and not HATs. Masuda and coworkers were able to catalytically oxidize dimethylsulfide and thioanisole to dimethylsulfoxide and phenyl methyl sulfoxide, respectively, using the bpba (bis(2-pyridylmethyl)tert-butylamine) copper complex shown in Chart 4, A.[45] Nam and coworkers were able to oxidize triphenylphosphine (PPh_3) using a pentadentate ligand, N4Py (N,N-bis(2-pyridylmethyl)bis(2-pyridyl)methylamine), but no other reactivity was observed (Chart 4, B).[50] Recently, a thermally stable Cu(II)-hydroperoxo intermediate has been formed using a well-tailored N_2O_2 ligand system (Chart 4, C).[46] DFT shows that the intermediate is stabilized through hydrogen bonding of the peroxide hydrogen to the phenolate group of the ligand. With the introduction of a substrate, toluene or *o*-xylene, catalytic C-H bond oxidation is observed. The authors propose Fenton-like chemistry for the intermolecular HAT rather than an inner-sphere oxidation mechanism. It is, however, an interesting example because it

demonstrates that the hydroperoxo intermediate can be stabilized without deactivating its reactivity and will help guide future ligand designs. Overall, Cu(II)-hydroperoxo intermediates have been successful in intermolecular OATs to easily oxidized substrates but more difficult reactions such as inner-sphere C-H bond hydroxylations present a greater challenge.

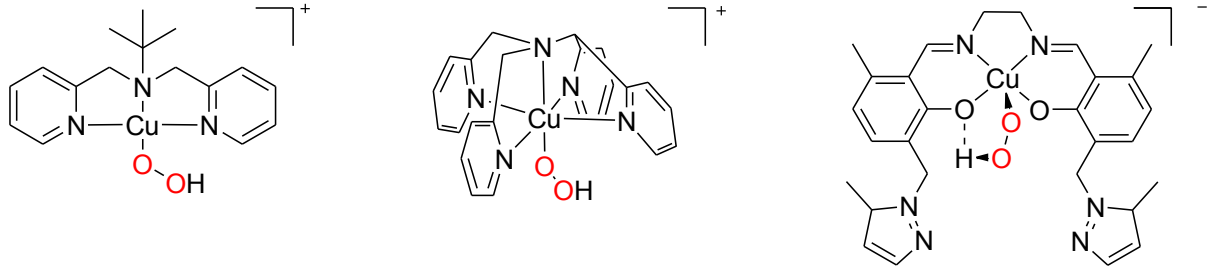

Chart 4. Cu(II)-hydroperoxo species capable of intermolecular reactions.

In studying the stability and reactivity of the Cu(II)-hydroperoxo intermediate, very few groups have incorporated donor groups that resemble the amino acids (histidine and methionine). Two examples of ligands are TMIMA (tris((1-methyl-imidazol-2-yl)methyl)amine) and N_3S (2-bis(6-methyl-2-pyridylmethyl)amino-1-(phenylthio)ethane), both containing donor groups that are similar to amino acid residues (Chart 5, A and B).[62-63] In both cases, incorporating the residues has a stabilizing effect on the hydroperoxo intermediate. The ligand with the most biological resemblance was a tripeptide (His-Gly-His) studied by Karlin and coworkers (Chart 5, C).[64] A Cu(II)-hydroperoxo intermediate of the tripeptide was formed and characterized. With all three ligands (TMIMA, N_3S, and His-Gly-His), HAT reactions have not been investigated.

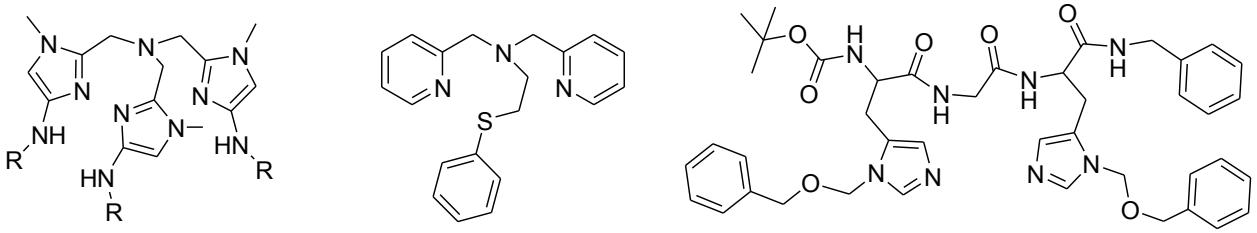

Chart 5. Ligands with donor groups that resemble amino-acids.

The chemistry of the Cu(II)-hydroperoxo intermediates is becoming more understood but there are still unanswered questions, such as whether or not the hydroperoxo intermediate is capable of HAT.

Karlin and coworkers has proposed a high-valent copper species that initiates the HAT for the examples involving intramolecular oxidation reactions[51] while Ali and coworkers have proposed an outer-sphere oxidation for the catalytic intermolecular oxidation reactions with the N_2O_2 ligand system.[46] Although there is enough convincing evidence that a Cu(II)-hydroperoxo intermediate can lead to C-H bond oxidation or OAT, the mechanism of action is still unclear.

1.2.2.3 Synthetic models of Fe(III)-hydroperoxo

Non-heme iron chemistry has been extensively studied with several reviews covering the topic.[37,43,65-70] This section focuses on Fe(III)-hydroperoxo intermediates with an emphasis on arene hydroxylations. Starting from an Fe(II) complex, the Fe(III)-hydroperoxo intermediate can be formed from the reaction of O_2 or via the shunt pathway; where 1.5 equivalents of H_2O_2 is necessary to oxide the iron centre and coordinate the hydroperoxo intermediate.[71]

Model Fe(III)-hydroperoxo species are unstable and difficult to isolate. The first spectroscopically characterized model Fe(III)-hydroperoxo compound has been reported by Mascharak and coworkers.[72] It is formed by reacting an Fe(II) complex of a synthetic model of BLM with O_2 or hydrogen peroxide and characterized by EPR as a LS spin Fe(III)-hydroperoxo. Both HS and LS Fe(III)-hydroperoxo have been successfully isolated at low temperatures and spectroscopically characterized.[73-74] To date, there are no crystal structures of model Fe(III)-hydroperoxo intermediates.

The reactivity of HS and LS Fe(III)-hydroperoxo intermediates have been studied and compared. Both intermediates are generally classified as sluggish oxidants, only being able to abstract weak C-H bonds (bond dissociation energies (BDE) < 88 kcal mol^{-1}).[75] Nam and coworkers compared the OAT reaction of HS $[(TMC)Fe(III)(OOH)]^{+}$ (TMC = tetramethylcyclam) to a LS $[(N4Py)Fe(III)(OOH)]^{+2}$ (Chart 6). HS Fe(III)-hydroperoxo intermediates are capable of sulfoxidations while LS intermediates showed little to no OAT.[76] In hydrogen-abstraction reaction from xanthene by $[(TMC)Fe(III)(OOH)]^{+}$ and $[(N4Py)Fe(III)(OOH)]^{+2}$, the HS Fe(III)-hydroperoxo was found to be marginally better than the LS species.[77-78] Despite both HS and LS hydroperoxo complexes being able to abstract hydrogen atoms with weak BDEs, there has been no evidence that a Fe(III)-hydroperoxo directly abstracts a hydrogen from strong C-H bond such as those in DNA (BDE ≥ 92 kcal mol^{-1}).[68] This leaves questions as to whether the hydroperoxo intermediate is really the hydrogen bond abstractor in the DNA strand cleavage by BLM or is another intermediate with higher valency responsible.

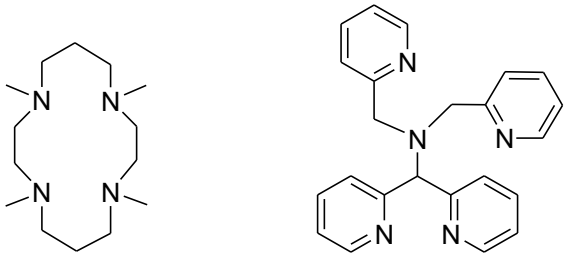

(A) TMC (B) N4Py

Chart 6. The two ligand used to compare HS versus LS Fe(III)-hydroperoxo.

The debate for direct attack of the hydroperoxo intermediate versus O-O bond cleavage can be extended to arene hydroxylation reactions. With model systems, the majority of authors propose O-O bond cleavage before electrophilic attack on the aromatic ring.[79-84] Homolytic cleavage leads to a Fe(IV)-oxo intermediate and a hydroxyl radical while heterolytic cleavage leads to an Fe(V)-oxo and a hydroxide anion. The two pathways can be roughly distinguished by probing the mechanism with radical trapping agents or isotope labelling studies and analyzing the products. Generally, site-specific hydroxylations and regioselective products indicates heterolytic cleavage while multiple side products and isomers indicates homolytic cleavage. More specifically, water-assisted cleavage is observed with heterolytic cleavage and identified by $^{18/16}O$ studies (Scheme 8) and homolytic cleavage can be identified by the product analysis of the reaction with MPPH (2-methyl-1-phenyl-2-propyl-hydroperoxide).[37,85] A 1,2-hydride shift is observed in α-KG dependent enzymes that are known to react through an Fe(IV)-oxo intermediate.[37] The observation of a 1,2-hydride shift in synthetic models has therefore been used to support the formation of an Fe(IV)-oxo intermediate. This shift is, however, possible with both heterolytic and homolytic cleavage pathways (Scheme 8). Fontecave and coworkers used a series of complexes to help determine when heterolytic versus homolytic cleavage would occur. Their findings show that heterolytic cleavage is favored in complexes with two adjacent labile ligands such as acetonitrile (MeCN) and homolytic cleavage is favored with two non-labile ligands (Cl^-).[84] Both intramolecular and intermolecular arene hydroxylations have been explored with evidence supporting both heterolytic or homolytic O-O cleavage.[68]

Heterolytic Cleavage

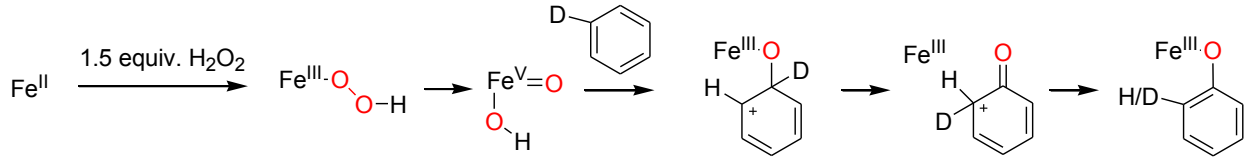

Water-Assisted Heterolytic Cleavage

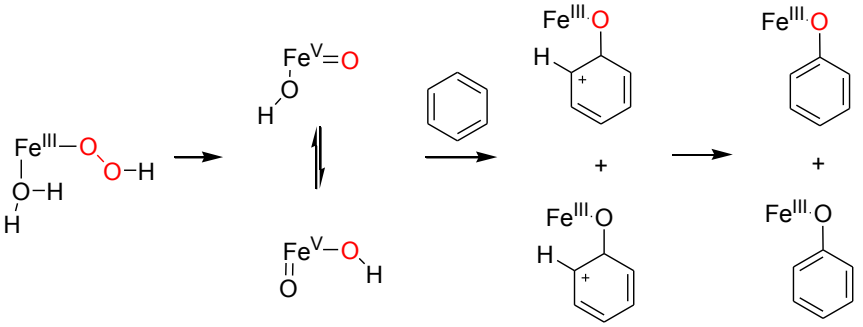

Homolytic Cleavage

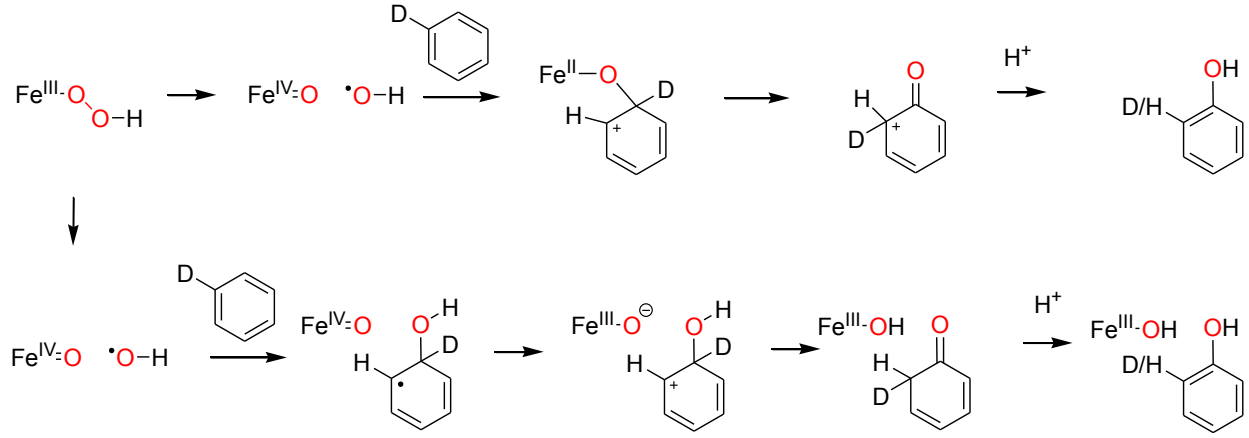

Scheme 8. Suggested mechanisms for arene hydroxylation through heterolytic, water-assisted heterolytic, and homolytic cleavage.

Homolytic cleavage of the Fe(III)-hydroperoxo or related Fe(III)-alkylperoxo into a Fe(IV)-oxo has only been proven indirectly in intramolecular arene hydroxylation reactions.[79-80,86] In a specific example, an Fe(IV)-oxo is indirectly identified by probing the mechanism of *t*BuOOH with TPA^{Ph}Fe (TPA= tris(2-pyridylmethyl)amine) (Chart 7, A).[79] Radical trapping agents prove that a radical intermediate is formed, consistent with homolytic cleavage. Furthermore, isotope labelling studies show a 1,2-hydride shift, a rearrangement also observed in α-KG enzymes. Fe(IV)-oxo intermediates have also been implicated in

intermolecular arene hydroxylations, again through indirect observations. In this case the ligands have an ethylene diamine backbone with pendant methyl pyridyl groups (Chart 7, B). The iron complex is reacted with hydrogen peroxide to form a Fe(III)-hydroperoxo species at -60 °C.[74] This species is then used to oxidize benzene to phenol with UV/Vis monitoring. Although no Fe(IV)-oxo intermediate is observed, mechanistic studies support the formation of this Fe(IV)-oxo intermediate.[82] Chang and coworkers directly linked a HS Fe(IV)-oxo with intramolecular arene hydroxylation using a $TPyA^{Ar}$ (tris(5-arylpyrrol-2-methyl)amine) (Chart 7, C).[87] The HS Fe(IV)-oxo is formed directly from the reaction of an Fe(II) complex with trimethylamine oxide and observed by UV/Vis and MS. The reaction supports the notion that an Fe(IV)-oxo can affect arene hydroxylation but does not prove O-O bond homolysis from a Fe(III)-hydroperoxo intermediate. These studies provide indirect evidence that Fe(III)-hydroperoxo species can undergo O-O bond homolysis to form Fe(IV)-oxo intermediates capable of arene hydroxylation.

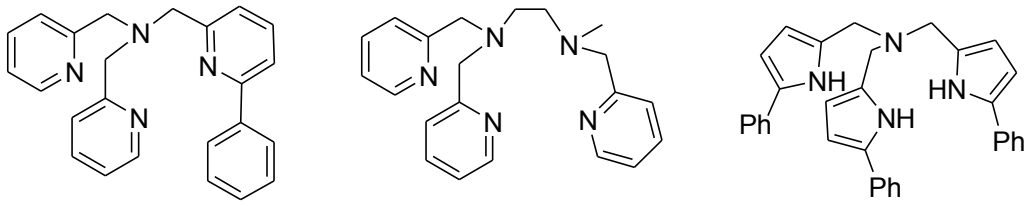

(A) TPA^{Ph} (B) Ethylene diamine backbone (C) tpa^{Ar}

Chart 7. Ligands used to study arene hydroxylation through Fe(IV)-oxo intermediates

The Fe(V)-oxo-hydroxo intermediate has been proposed as the key intermediate in the *cis*-dihydroxylation by enzymes of the Rieske dioxygenase family and model complexes are helping to support this claim. Fe(V)-oxo intermediates have been indirectly observed in intramolecular[81] and intermolecular arene hydroxylations.[85,88] In a specific case of intermolecular arene hydroxylation an Fe(III)-hydroperoxo is formed and decayed into a Fe(III)-phenolate.[85] The C-H activation is proposed to be initiated by Fe(V) intermediate. Interestingly, when an Fe(IV)-oxo is generated from PhIO, no phenolate is observed upon decomposition of the Fe(IV)-oxo, eliminating the possibility of a homolytic cleavage pathway. In 2007, the first Fe(V)-oxo was isolated at -60°C and has been characterized by several spectroscopic techniques.[89] The ligand system is a tetraamido macrocyclic ligand (TAML) with the four deprotonated amide functions stabilizing the high-valent iron centre (Chart 8, A). Supported by the TAML ligand, the reactivity of Fe(V)-oxo was compared to an Fe(IV)-oxo and the Fe(V)-oxo was found

to be 4 times more reactive in the sulfoxidation of thioanisole.[90] In 2011, with the development of cold-spray ionization MS (CSI-MS) and through careful isotope labelling strategies, Costas and coworkers were able to identify a Fe(V)-oxo-hydroxo intermediate using the Pytacn (1-(2-pyridylmethyl)-4,7-dimethyl-1,4,7-triazacyclononane) (Chart 8, B).[91] This is the first instance of an Fe(V)-oxo-hydroxo intermediate being directly observed in an arene hydroxylation and *cis*-dihydroxylation reaction. With support from model complexes, the Fe(V)-oxo-hydroxo intermediate is emerging as a likely candidate in the mechanism of Rieske dioxygenases.

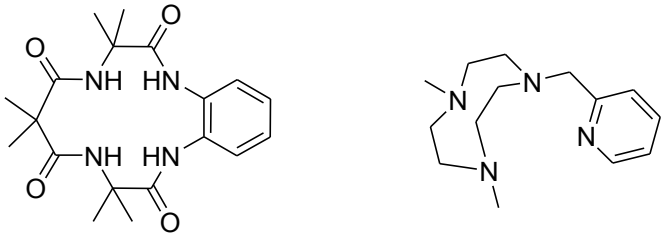

(A) TAML (B) Pytacn

Chart 8. Ligands used to form Fe(V)-oxo intermediates.

The Fe/O_2 chemistry has previously centered on the identification of homolytic cleavage versus heterolytic cleavage. This section has presented evidence that both pathways can lead to arene hydroxylation. Heterolytic cleavage leads to a radical-free pathway with the benefit of greater selectivity. This has opened new research directions that are now focused on characterizing and controlling the reactivity of Fe(V)-oxo species.

1.3 Approach

Insight into the mechanism of enzymatic M/O_2 oxidations can be gained from fundamental studies with simple complexes. Two important aspects required for studying M/O_2 systems are (1) identifying and characterizing the intermediates and (2) studying the reaction pathway. It is difficult to achieve both aspects within the same system because increasing stability of the intermediate decreases or extinguishes its reactivity. Conversely, if the system is highly reactive the intermediates are too short-lived to be observed. Further difficulties in studying M/O_2 intermediates arise from dimerization. The increased stability in dimer complexes dramatically reduces the C-H activations or OAT reactions.[92] To circumvent the difficulties inherent in studying reactive intermediates, a combination of low temperatures and well-designed ligands need to be used. The following section will first introduce

important concepts in ligand design such as the coordination sphere and pre-organization, both of which are used influence M/O_2 chemistry. The second part focuses on the methods and techniques used to form and characterize the coordination complexes and their intermediates. It provides a basic introduction to concepts that are not necessarily detailed in each chapter.

1.3.1 The Coordination Sphere

The coordination sphere of a metal ion is broken down into first and second coordination spheres. In relation to M/O_2 complexes, both coordination spheres are needed to control the nuclearity of the complexes, protect the active site and stabilize specific intermediates without stopping the reactivity. Each coordination sphere is described separately in the following section to highlight the impact on M/O_2 complexes.

The first coordination sphere is composed of the metal and the coordinated ligands. The nature of the donor atoms influences the electronic properties of the metal as well as the coordination number and the geometry. The properties of the M/O_2 centres have been influenced by incorporating donor groups similar to those found in amino acids (N, S or O) with examples described in section 1.2.2.1 or by tailoring the donor strength of specific functional groups. Schindler and coworkers used this second concept to modify the nitrogen groups in Tren-based ligands. In changing the tertiary amines in Me_6Tren to strongly basic guanidine functions in TMG_3Tren, they were able to stabilize and crystallize an end-on Cu(II)-superoxo intermediate for the first time (Chart 2, A).[19] Alternatively, Que and coworkers used TMG_3Tren to constrain the geometry of an iron complex to TPB forcing a HS Fe(IV) centre as well as crystallize an Fe(IV)-oxo intermediate.[93-94]

The second coordination sphere is the atoms/groups/residues that are not directly coordinated to the metal centre but are in close proximity. This includes neutral, ionic molecules and the ligand or protein backbone. The second coordination sphere influences the first coordination sphere through weak interactions such as hydrogen bonding, π-interactions or steric effects.[95] With TMG_3Tren complexes, the intermediates are protected from intermolecular reactions by steric bulk. Hydrogen bonding has also been used to influence Cu(II)-hydroperoxo intermediates as mentioned in section 1.2.2.1 or to stabilize Fe(III)/(IV)-oxo intermediates. Borovik and coworkers obtained a crystal structure of a unique Fe(III)-O^- intermediate using the tripodal ligand tris[(*N*-9-*tert*-butylureaylato)-*N*-ethyl)]aminato that provides three hydrogen bond donors to stabilize the oxo moiety (Chart 9, A).[96-97] They were also able to isolate

and characterize a Fe(IV)-oxo intermediate with the same hydrogen bonding ligand.[96] Goldberg and coworkers used a ligand (N3Py^{amide}SR) with a single hydrogen bond donor in conjunction with a thioether in the first coordination sphere to generate a Fe(IV)-oxo intermediate capable of intermolecular sulfoxidation (Chart 9, B).[98] In this case the hydrogen bonding was found to increase the rate of sulfoxidation in comparison to a complex with no hydrogen bonding group.

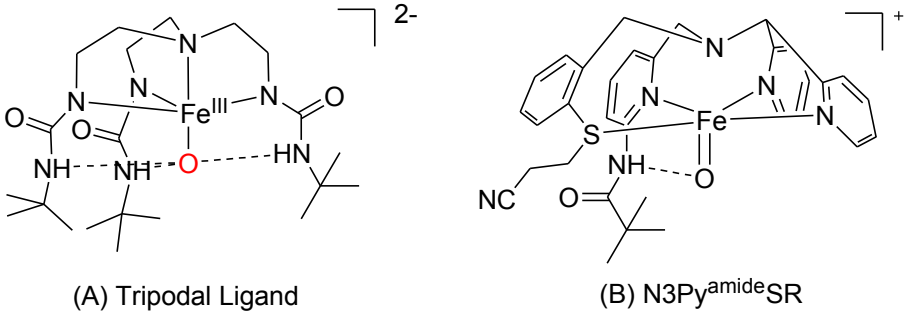

(A) Tripodal Ligand (B) N3Py^{amide}SR

Chart 9. Second coordination sphere interaction

1.3.2 Macrocycles and Cryptands

Macrocycles have been used to drive forward the understanding of Fe/O_2 chemistry and have played an important role in Cu/O_2 chemistry. Their success is, in large part, attributed to the macrocyclic effect; described as the greater ion specificity and stability of coordination complexes in comparison to opened-chain ligands. The specificity of a macrocycle can be tailored by considering complementary pairing of ligands to metals based on size, geometric preference (ligand field stabilization energies) and electronic effects (the hard and soft acids and bases (HSAB) concepts).[99] The increased stability of macrocyclic complexes compared to opened-chain ligands is an inherent effect of the pre-organized system (macrocycle is constrained by enforcing the topology and rigidity of the structure prior to coordination of an ion). Upon coordination of an ion, a macrocycle undergoes very little rearrangement, favouring the formation of the complex. The complex is further stabilized because a macrocycle is less solvated compared to an opened-chain ligand requiring less energy upon complexation.[99] Also, a greater stability is observed because a dissociated donor atom is still near the metal and will reassociate faster than a donor atom in an opened-chain ligand.[100]

The enhanced stability of macrocyclic complexes enables preparation of resilient species and facilitates their characterization. It has been shown that macrocycles such as TAML and Pytacn are effective in studying the elusive Fe(V)-oxo intermediate as mentioned in section 1.2.2.2. The macrocycle

TMC (Chart 6) has been used extensively to characterize and study the reactivity of a side-on Fe(III)-peroxo, an Fe(III)-hydroperoxo and an Fe(IV)-oxo.[78,101-105] Crystal structures of both the Fe(III)-peroxo and Fe(IV)-oxo have been obtained while the Fe(III)-hydroperoxo was characterized spectroscopically. The Fe(III)-peroxo was found to have a limited reaction scope, only capable of aldehyde deformylation,[106] while the Fe(IV)-oxo was able to perform a variety of electrophilic oxidation reactions (OATs and HATs).[107] The Fe(III)-hydroperoxo intermediate was able to act as both a nucleophile, for an aldehyde deformylation reaction, and electrophile, for HATs and OATs.[107] With these intermediates, the important feature is the macrocycle that stabilizes the intermediates, allowing for the reactions to be observed.

Cryptands are macrobicycles that can exhibit an even greater stabilizing effect compared to macrocycles, called the cryptate effect. The three-dimensional scaffold reduces the flexibility and increases the ion specificity.[108] This translates to a decreased rate of dissociation of coordinated ions or substrates.[109] There are several factors that influence the binding and stability of transition metal complexes in cryptands. These include the donor atoms (N, P and S), arrangement of binding sites (5-6 chelates), flexibility of the linking or shaping groups (aliphatic chains vs rings) and the size of the macrobicycle.[100] These factors will dictate the chemistry of the coordination complex.

In M/O_2 chemistry, the three-dimensional scaffold of cryptands can also provide a protective pocket to help control nuclearity and prevent side reactions. These supramolecular structures can influence the M/O_2 chemistry through second coordination sphere interactions. Supramolecular cavitands such as calixarenes, cyclodextrins and cyclotriveratrylenes have been used to study biomimetic Fe and Cu reactions, but they only provide a protective pocket and do not benefit from the cryptate effect.[110] The use of cryptands for mimicking mononuclear Fe and Cu monooxygenase reactions is largely unexplored. The sole examples are calix[6]arenes capped by Tren or TPA (tris(2-pyridylmethyl)amine) (Chart 10).[111-112] The cryptands with Cu(I)-centres react with O_2 (TPA-based ligand reacts only in the solid state), but the intermediates are too reactive to be observed. The postulated Cu(II)-superoxo intermediates undergo intramolecular C-H bond hydroxylations with the cryptands. The supramolecular structures proved valuable in protecting the Cu(I) centre from dimerization as well as disproportionation. The potential benefits from the cryptate effect and protection of the active site has created a space for further studies into Cu/O_2 and Fe/O_2 intermediates supported by cryptands.

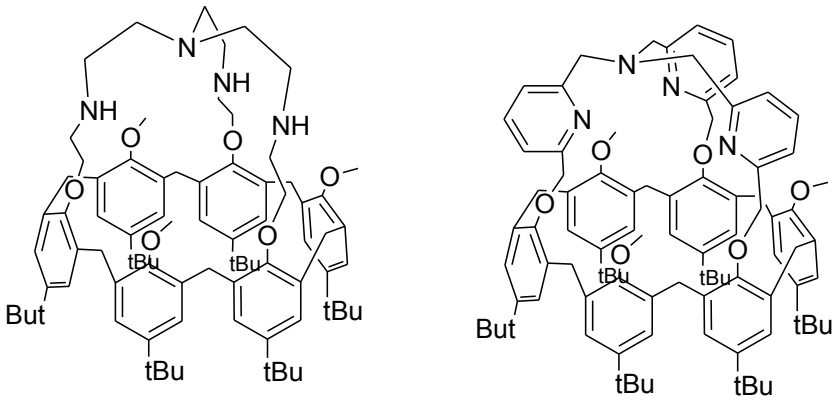

Chart 10. Calix[6]arenes capped with Tren and TPA

Ditopic cryptands have two separate binding sites and can act as dual-host systems.[113] They are of particular interest to this research because they have the potential to coordinate the metal centres and concurrently interact with anions or substrates (metal-assisted anion or substrate coordination). Oxygenase and oxidase enzymes use first and second coordination sphere interactions to place the metal centre, oxidant and substrate in close proximity to each other. In model systems, the approach of the oxidant or substrate to the complex has an entropic cost that could be partially reduced by the use of ditopic cryptands, similar to enzymes. Rather than forming metal-assisted anion coordination complexes, cryptands typically form cascade complexes where two metals ions are coordinated with an anion between them.[114] Alternatively, cryptands or protonated cryptands simply encapsulate anions without metals.[115] With bio-inspired goals, metal-assisted anion coordinating cryptands are a research target.

What distinguishes the present research from previous biomimetic studies is the use of cryptands to influence the second coordination sphere of the metal centre to decipher the mechanism of C-H bond hydroxylation and oxygen-atom transfers.

1.3.3 Ligand Design

The cryptands used in this thesis were chosen or designed based on several characteristics with the end goal of synthesizing stable mononuclear Cu(II) and Fe(II) complexes capable of forming hydroperoxo intermediates. The structure of cryptands can be divided into three moieties: coordinating moiety, protective pocket and spacer. To form a macrobicycle the coordinating moiety requires three pendant arms. For stability, the donor groups should form 5 or 6 chelates upon complexation. Lewis-base

nitrogen donor atoms can accommodate the borderline Lewis acids Fe(II) and Cu(II) and their higher oxidation states. Tren, a tripodal pentadentate ligand with amine donor groups with ethyl linkers, fits this need. Two different protective pockets were used for the ligands. One protective pocket is a potential anion receptor[116-117] (TTA = Tris-(4-methanol-1-ethyltriazole)amine) moiety) while the other pocket is non-coordinating (TEA = Triethanolamine). Finally, the spacer, m-phenylene, was used for both cryptands based on the ability of the precursor benzaldehydes to reversibly condense with Tren as discussed in the next section. Combining the different components produces the structures in Chart 11. Non-methylated **LTEA** was previously synthesized by Bharadwaj and Chand and methyl groups were added to reduce the number of intramolecular side reactions.[118] The synthesis of **LTTA** will be presented in Chapter 5.

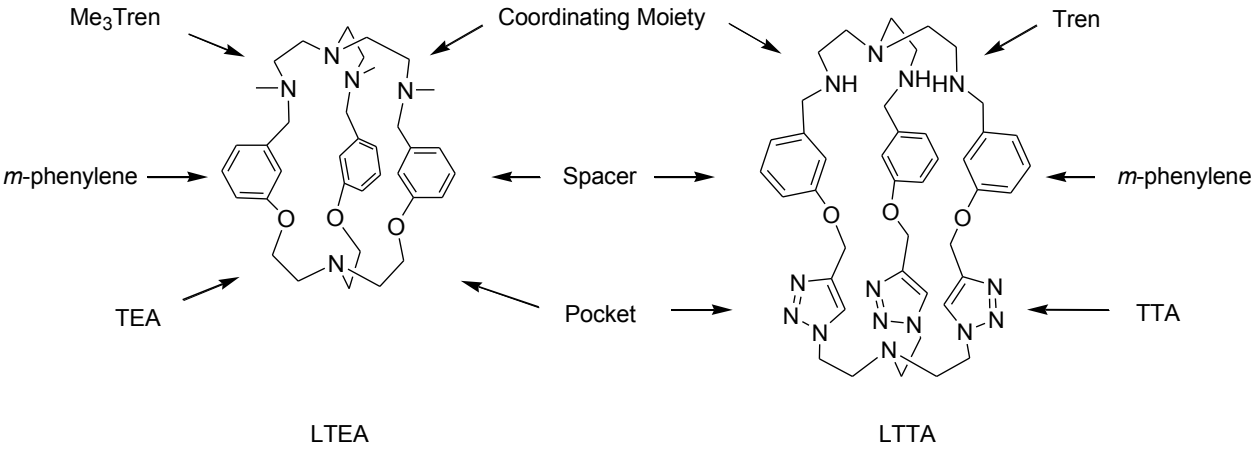

Chart 11. Cryptand design (A) **LTEA** (B) **LTTA**

1.3.4 Synthesis of Cryptands

Assembly of the coordinating moiety, spacer and protective cavity can be a synthetic challenge, with the most difficult step being completion of the macrobicycle. **LTTA** and **LTEA** are formed by reacting two tripods together (tripod coupling).[119] The tripod coupling can occur as either a reversible or irreversible reaction. The irreversible reaction connects 3 arms of one molecule to 3 arms of a second molecule. After the pairing of the first two arms, the following 2 pairs of arms react in an intramolecular fashion. Low yields (<15 %) for this reaction are attributed to irreversible intermolecular reactions creating long-chained molecules. With the reversible reactions, the formation of an intermolecular reaction is possible, but it can be reversed and with time the thermodynamically favorable structure will prevail.

One of the most common reversible reactions in the synthesis of cryptands is the Schiff base condensation between an aldehyde and primary amine. The reaction produces an imine that can then be easily reduced to a secondary amine. The yield of reversible tripod coupling can be further improved by changing experimental conditions such as high dilution, cold temperatures and templating ions.[119] High dilution and cold temperatures reduce the number of intermolecular collisions to improve yields (< 30 %) but a templating ion has the greatest impact on improving yields (> 70 %). A templating ion can affect the kinetics of the reaction by fixing a reactant in a conformation that is conducive to tripod coupling. Alternatively, the equilibrium of the reaction can be shifted by forming a stable complex with one of the products, directing the reaction towards that product.[120]

1.3.5 Characterization of Complexes and Intermediates

1.3.5.1 Ligand Field

The d orbitals of transition metal complexes split into different energy levels, resulting in a net electronic stabilization.[121] In an octahedral field the orbitals are split into e_g and t_{2g} as shown in (Scheme 9, A. The octahedral field splitting parameter, Δ_O, is affected by both the ligand and metal, and the effect on splitting can be estimated using the spectrochemical series. Weak-field ligands lead to smaller Δ_O and strong-field ligands lead to larger Δ_O. With iron complexes, high-spin and low-spin configurations are possible. Low-spin complexes are favored by a larger Δ_O, where Δ_O must compensate for the electron-pairing energy. High-spin complexes are favored by smaller Δ_O. Nitrogen donor atoms are moderate-to-strong field ligands that would typically favour low-spin complexes. Steric constraint and alkylation, however, weakens the ligand field and in the case of a Tren-based cryptands, high-spin complexes are common.[122-123] Although iron complexes prefer octahedral geometry, geometries with lower coordination numbers are observed; an example is the Fe(II)-triflate complex of TMG_3Tren that adopts TBP geometry (Chart 2).[93-94] Cu(II) has a d^9 electronic configuration and, in an octahedral field, has an orbitally degenerate ground state. The complexes undergo a Jahn-Teller distortion, generally with the z axis elongating and the xy plane compressing to remove the degeneracy and attain a more stable ground state (Scheme 9). Cu(II) complexes are known to adopt several different geometries with the common geometries shown in Scheme 9.

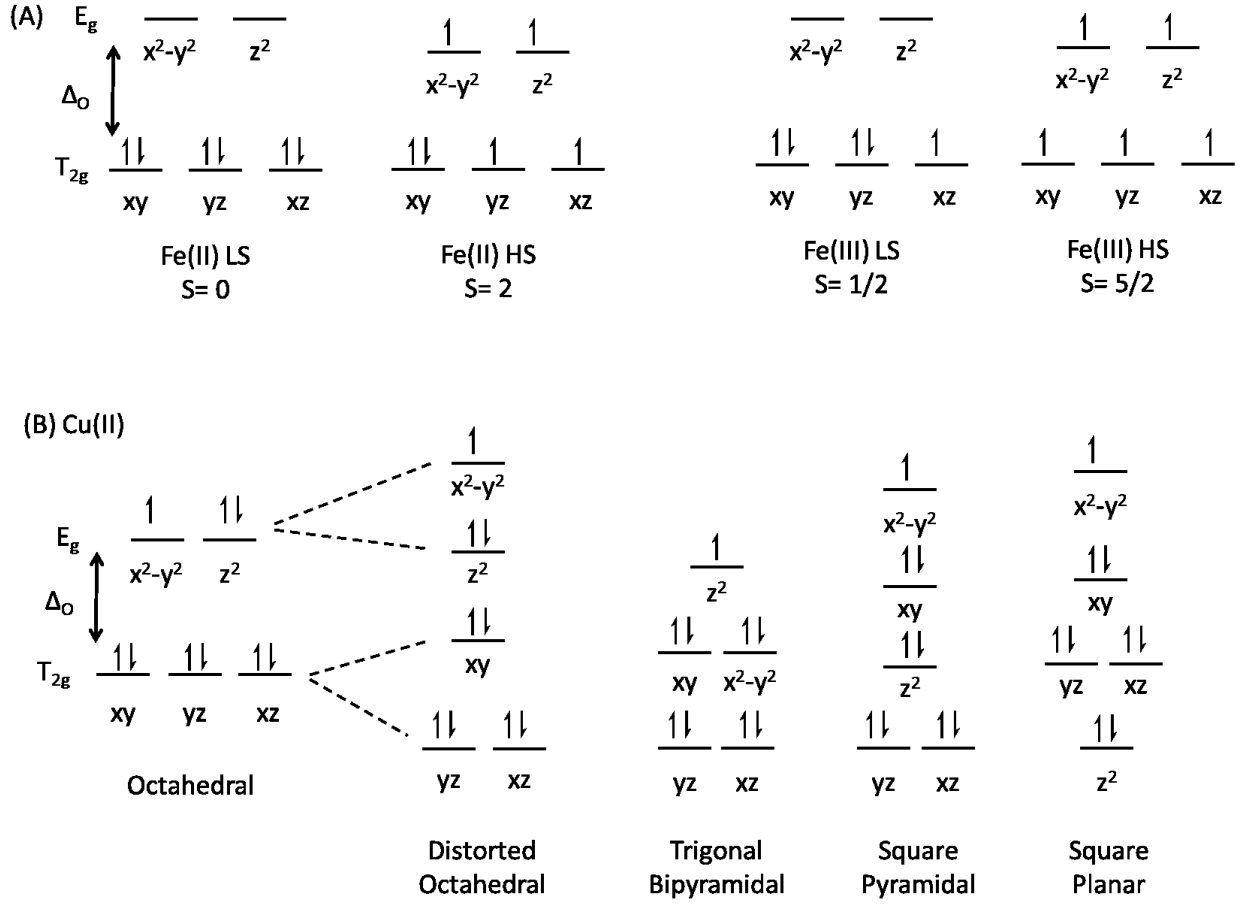

Scheme 9. d-Orbital splitting diagrams (A) Orbital splitting in octahedral geometry of Fe(II) and Fe(III) complexes (B) Jahn-Teller distortion in octahedral complexes and other common Cu(II) geometries (splitting of the energy levels is not drawn to scale).

1.3.5.2 Ultra-Violet/Visible Absorption Spectroscopy

Excitation of an electron in the d orbitals gives rise to ligand-field transitions. These transitions are parity-forbidden and therefore have molar absorptivities (ε) of around 100 M^{-1} cm^{-1}. In Cu(II) complexes, the d→d transitions are in the visible (390–700 nm) and near IR (750–2500 nm) region of the electromagnetic spectrum and can provide information on the geometry of the complex with a simple UV/Vis spectrometer. Tren-based complexes with TBP geometries are characterized by two transitions at approximately 900-1000 nm and 660-840 nm[124-126] whereas the square-pyramidal geometry is characterized by a λ_{max} between 520-670 nm and a shoulder between 620-870 nm.[124,127] The UV/Vis bands of copper(II) complexes are broad and often overlapping, complicating the assignment of the

geometry. The d→d transitions in iron complexes are in the near infrared region and are best observed using low-temperature magnetic circular dichroism,[70] a technique not covered or used here.

Coordination complexes can also exhibit charge-transfer transitions which involve a transfer of electron density between orbitals with a large change in dipole moment. The transfer of electron density can be a metal-to-ligand charge transfer (MLCT) or a ligand-to-metal charge transfer (LMCT). Because the charge transfer band is directly linked to the metal ligand interaction, it can be used to identify different intermediates. Cu(II)-hydroperoxo intermediates have LMCT ranging from 350 to 400 nm with ε of around 1000 M^{-1} cm^{-1}.[56] Fe(III)-hydroperoxo intermediates are found within a wider range of wavelengths (452 to 600 nm)[37,73,128] and exhibit varied molar absorptivity (900 to 2780 M^{-1} cm^{-1}).[129-130] Other relevant complexes such as Fe(III)-phenolate show charge transfers between 330-340 nm and 530-650 nm (ε > 1000 M^{-1} cm^{-1}) [131-132] and Fe(IV)-oxo species have ligand field transitions between 750-900 nm (ε = 100 to 400 M^{-1} cm^{-1}).[107] The reactivity of the intermediates can be followed by observing the formation and decomposition of the charge transfers and ligand field transitions.

A kinetic analysis is possible by following the formation and decay of the charge transfer of the intermediates over time. Due to the high reactivity of the intermediates a low temperature stopped-flow UV/Vis is necessary. This involves two syringes that inject through a rapid mixer, into a UV/Vis cell. The flow into the cell is stopped mechanically by a block. Once the flow is stopped, data acquisition begins. The mechanical mixing and stopped-flow allow for acquisition of data to begin on a millisecond timescale. Submerging the tubing and cell in an organic solvent allows cooling to low temperatures.

1.3.5.3 Electron Paramagnetic Resonance

Electron paramagnetic resonance (EPR) spectroscopy is a method that provides local insight into the electronic structure of paramagnetic samples.[133] Application of a static magnetic field, B, to a sample will cause electrons to align in a parallel or anti-parallel orientation to B. This causes the Zeeman splitting of energy levels of the electron into two. If radiation, *hν*, is applied to the sample that is equal to the energy difference, ΔE, between the "Zeeman levels", absorption will occur, causing the resonance condition; as described by $\Delta E = h\nu = g\mu_B B$. The g-factor, g, is at the centre of the spectral lines and reflects the environment of an electron (comparable to the chemical shift in NMR), μ_B is the Bohr magneton, B is the magnetic field. Absorption intensity is affected by the difference in population between splitting levels as governed by the Boltzmann distribution. Typically *hν* frequency is held

constant (in the microwave region, GHz), with the strength of B varied, and the spectrum is obtained as the first derivative of the absorption. The spectral lines created by the Zeeman effect are further split by hyperfine coupling with the nucleus by $2nI+1$, where n is the number of equivalent nuclei and I is the nuclear spin. The degree of splitting is given by the hyperfine coupling constant, A. The equation $h\nu = g\mu_B B$ has an isotropic g-factor where the principal g-factors are $g_x = g_y = g_z$ giving one resonant line in the spectrum. The principal g factors can be anisotropic where $g_x = g_y \neq g_z$ is axial and $g_x \neq g_y \neq g$ is rhombic.

With S = 1/2 spin state, Cu(II) complexes are ideal for electronic structure determination by EPR. The nuclear spin of copper is I = 3/2, where the absorption bands are split into 4 transitions. The electrons in different orbitals will have different g values providing a means to determine the highest occupied molecular orbital. A $d(x^2-y^2)^1$ ground state is characterized by g∥ > g⊥ and a $d(z^2)^1$ ground state has g⊥ > g∥ (Figure 2). Returning to (Scheme 9), EPR can then be used to distinguish TBP from square-planar/pyramidal. In Fe(III) complexes, EPR can distinguish between HS (S = 5/2) and LS (S = 1/2) states. LS complexes have typical g values close to 2 but have been observed between 4 and 0 and HS complexes with a high degree of rhombicity have g values close to 4.3.[134]

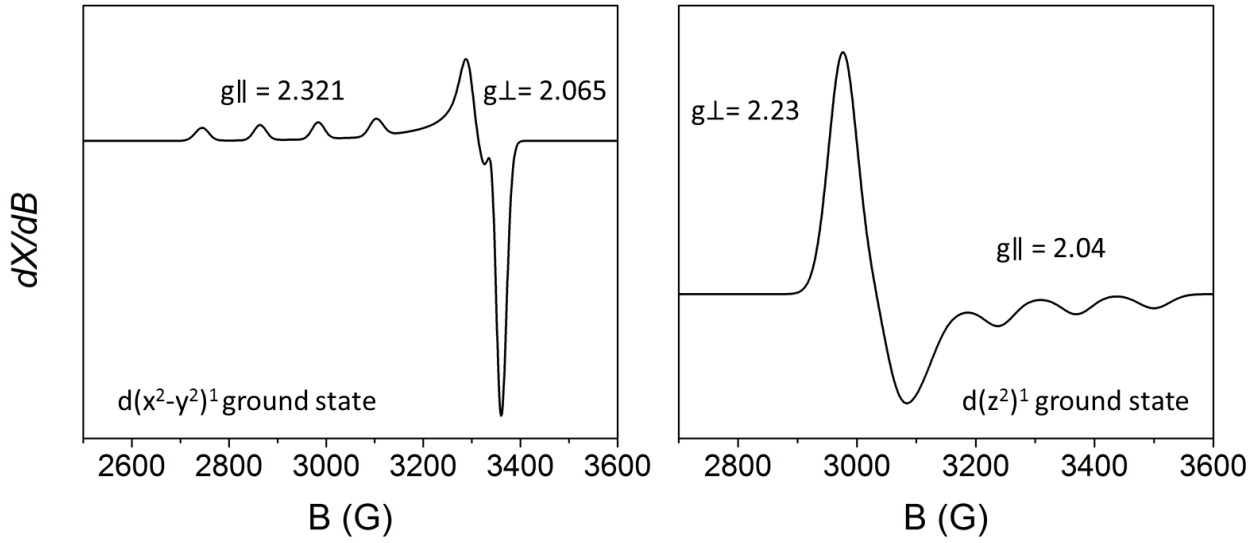

Figure 2. Simulated EPR spectra Left: g∥ > g⊥ Right: g⊥ > g∥. The EPR were simulated with Easyspin.[135]

1.3.5.4 Other Characterization methods

Crystal structures acquired using single-crystal X-ray diffraction (SC-XRD) can provide valuable information regarding the structure and geometry of ligands and complexes in the solid state. Analysis

of the X-ray diffraction pattern provides information regarding electron density in a single crystal. In an iterative process, a model is fit to the electron density, identifying atoms and their positions within a unit cell. In combination with CHN analysis to confirm composition of the bulk material X-ray crystallography is a powerful characterization technique, but informs only on the solid-state sample.

Mass spectrometry analyzes the mass-to-charge ratio of ions. For inorganic complexes, it can be used to determine the types of ionic species in solution. Electrospray ionization (ESI) is the typical method used because it is a soft ionization method and easily allows for direct injection of the sample. Upon injection of the sample, a warm desolvation gas removes the solvent and creates highly charged droplets that undergo coulombic explosions, resulting in free ions of the analyte. A more recent advancement in the field of inorganic mass spectrometry is cold-spray ionization (CSI), which is a modification of ESI that allows samples to become ionized at low temperatures.[136] The low temperatures increase the polarizability of the analyte leading to dissociation of the counterion. This ionization method is a much softer method and the cold temperatures are beneficial in studying temperature-sensitive intermediates.

1.4 Organization of the Thesis

The goal of this research was to study reactive intermediates with coordinating cryptands to evaluate how the coordination sphere impacts their structure and reactivity. The thesis is broken down into 5 manuscripts to address the overall goal. Chapters 2 and 3 look at the reactivity of Cu(II)-acetate complexes supported by **LTEA**. Chapter 2 focuses on the formation of a Cu(II)-hydroperoxo intermediate by using low-temperature stopped-flow UV/Vis and mass spectrometry. Chapter 3 provides a more detailed analysis of the formation and reactivity/decomposition of the Cu(II)-hydroperoxo intermediate. In that work, focus was placed on characterization of the Cu(II)-acetate complex and the hydroperoxo intermediate in solution using EPR, CSI-MS, and stopped-flow UV/Vis. Chapter 4 explores the reactivity of Cu(II)-halide complexes of **LTEA**. The halide complexes were characterized in both the solid and solution state and their propensity to form a Cu(II)-hydroperoxo intermediate was investigated. The impact of the cryptand on the structure and reactivity of the copper complexes is discussed throughout chapters 2-4.

A novel cryptand, **LTTA** is introduced in Chapter 5. The high-yielding synthesis is presented along with coordination complexes. The ditopic nature of the cryptand is also a topic in chapter 5. Finally, Chapter

6, describes how Fe(II) complexes of **LTTA** were formed and reacted with oxidants. An Fe(III)-hydroperoxo intermediate was identified in an intramolecular C-H bond hydroxylation reaction. This reaction was investigated and a mechanism proposed.

Supporting information for the manuscripts in chapters 3-6 are found in Appendices 1-4.

Chapter 2: Formation and Reactivity of a Biomimetic Hydroperoxocopper(II) Cryptate

Laura Chaloner,[a] Mohammad S. Askari,[a] Adrian Kutteh,[a] Siegfried Schindler,[b] and Xavier Ottenwaelder*[a]

[a] Department of Chemistry and Biochemistry, Concordia University, 7141 Sherbrooke W, Montreal, QC, H4B 1R6, Canada

[b] Institut für Anorganische und Analytische Chemie, Justus Liebig Universität, Heinrich-Buff-Ring 58, D-35392 Gießen, Germany

DOI: 10.1002/ejic.201100080

2.1 Abstract

Copper(II)-hydroperoxo species are proposed as key intermediates in the catalytic cycles of copper-monooxygenase enzymes that perform C–H bond hydroxylation. Herein we report on the oxidation chemistry of a copper(II) complex with a coordinating cryptand based on a peralkylated tetradentate tris(2-aminoethyl)amine (Tren) moiety. X-ray crystallography of the copper(II) acetate complex of this cryptand revealed that the copper(II) ion is in a square-pyramidal environment, with the cryptand acting only as a tridentate ligand. This geometry is conserved in solution and likely results from restraints imposed by the semi-rigid cryptand. Reaction of this complex with basic hydrogen peroxide in methanol led to the decomposition of the complex with an oxygen-atom transfer to the ligand, as evidenced by mass spectrometry analysis after reaction and demetallation. Low-temperature stopped-flow experiments (down to –90 °C) support the formation of a copper(II)-hydroperoxo intermediate, CuOOH, before ligand oxygenation occurs. It is proposed that this intermediate performs the oxygen-atom transfer to a weak benzylic C–H bond of the cryptand, thereby mimicking the behavior of dopamine-β-hydroxylase.

2.2 Introduction

The ease with which enzymes perform oxidation reactions has long been coveted by synthetic chemists.[9,137] In this respect, copper monooxygenases are enzymes of particular interest because they can hydroxylate C-H bonds using low-toxicity copper as the key element.[138] Specifically, the enzyme peptidylglycine-α-hydroxylating monooxygenase (PHM) can hydroxylate a C-H bond in a glycine-extended peptide.[20,24,139] This enzyme activates dioxygen (O_2) at a mononuclear Cu(I) ion (Cu_B) and

performs insertion of one oxygen atom into the substrate with the assistance of a second mononuclear Cu(I) ion (Cu_A) located at a distance of 11Å from Cu_B. The enzyme dopamine-β-hydroxylase (DβH), which hydroxylates the benzylic position of dopamine, has a very similar active site to that of PHM.[140] The suggested mononuclear reaction intermediates involved in the C-H bond functionalization in these enzymes are the: Cu(II)-superoxo [Cu^{II}-($O_2^{\bullet-}$)], Cu(II)-hydroperoxo [Cu^{II}-(OOH^-)], Cu(III)-peroxo [Cu^{III}-(O_2^{2-})] and Cu(II)-oxyl/Cu(III)-oxo [Cu^{II}-($O^{\bullet-}$)/Cu^{III}-(O^{2-})] complexes.[1,21,53,141] A Cu(II)-hydroperoxo species was first proposed as the active intermediate, but a Cu(II)-superoxo species is now seen as a more likely culprit.[1,10,21,26,53,140-144] In particular, experimental evidence for the Cu(II)-superoxo intermediate lies in the solid-state molecular structure of oxygenated crystals of PHM, in which the best structural fit at the active site is an end-on Cu(II)-superoxo species.[24]

Many synthetic efforts have been made to prepare and study reactive mononuclear Cu complexes that would be similar to the intermediates proposed in the enzymatic catalytic cycles.[1,9,12,16,19,44,54,111-112,145-149] Of interest to the present study are Cu(II)-hydroperoxo species prepared using multidentate ligands. One such complex has been crystallographically characterized; it is supported by a tetradentate ligand that stabilizes the hydroperoxo group through hydrogen bonds.[58] This species shows little reactivity due to its stability. Because most Cu(II)-hydroperoxo species are reactive, however, they are studied only in solution at low temperatures to prevent their decomposition. These species are thus characterized by spectroscopic means (UV/Vis features, resonance Raman, EPR).[45,47-49,51-52,60,63,150-152]

Herein we report oxidation studies on a Cu(II) complex of a coordinating cryptand based on the tris(2-aminoethyl)amine (Tren) ligand (Scheme 10); the peralkylated Tren moiety is well-known to support Cu/O_2 chemistry.[153-155] We were curious to study the effects of the semi-rigidity and the cavity of a cryptand on the reactivity of a Cu(II)-hydroperoxo species given that second-sphere interactions are possible between the Cu(II)-hydroperoxo species and the inside of the cryptand cavity. Such second-sphere interactions have been shown to be key factors in stabilizing reactive intermediates in metal-dioxygen chemistry.[58,92] In addition, the cryptand arms are based on benzyl linkers, which mimic the benzylic position that undergoes hydroxylation in the substrate of DβH.

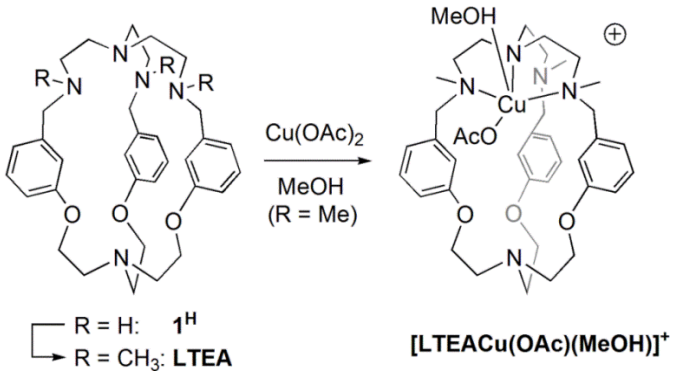

Scheme 10. Ligand **LTEA** and preparation of its Cu(II) acetate complex.

2.3 Results and Discussion

The synthesis of the macrobicyclic ligand **LTEA** involves *N*-Methylation of the known cryptand $\mathbf{1}^{\mathbf{H}}$. [118,156] Methylation was found to simplify the products deriving from the oxidation reactions carried out below; complexes of the non-methylated ligand $\mathbf{1}^{\mathbf{H}}$ readily oxidized to imine compounds, thereby hampering the study of the oxygen-atom transfer reaction.[157] Slow diffusion of acetonitrile into a dichloromethane solution of **LTEA** at –30 °C yielded single crystals of **LTEA** that were amenable to X-ray diffraction analysis (Table 1). The molecular structure (Figure 3) indicates that the cryptand adopts an endo-endo conformation, as does its parent, $\mathbf{1}^{\mathbf{H}}$.[118] The molecule displays an overall C_1 symmetry, notably due to the twist of the N4 arm of the Tren moiety with one CH_2 (C19) inside the cavity. The bottom of the molecule displays three weak C–H···O contacts between the OCH_2 and the O atoms in the range 2.727–2.879 Å (Van der Waals radii: $r_{vdW}(H)$ = 1.20 Å, $r_{vdW}(O)$ = 1.52 Å). The molecule also wraps itself around weak C_{arom}–H···C_{arom} contacts between the aromatic groups (3.053–3.225 Å; r_{vdW} (C) = 1.70 Å). Lastly a triangular set of H···H contacts is observed between two benzylic CH_2 groups on N2 and N5 and the Tren $N4CH_2$ group from the twisted arm (2.405–2.470 Å). Although very weak, these multiple interactions certainly exist to counteract the void that would be created by an open cavity and testify to a certain flexibility of the semi-rigid cryptand.

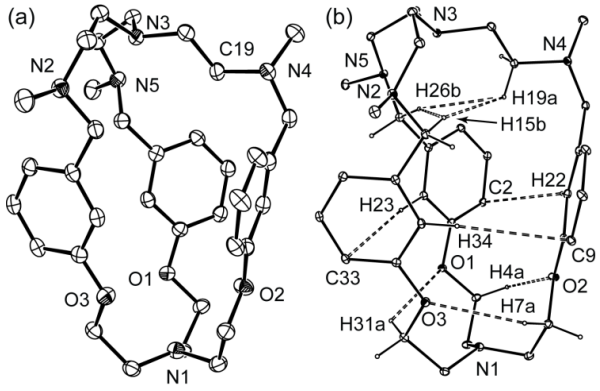

Figure 3. (a) ORTEP representation of **LTEA** at 50% ellipsoid probability. Hydrogen atoms have been omitted for clarity. (b) ORTEP representation of **LTEA** at 20% ellipsoid probability emphasizing the weak interatomic contacts (only selected hydrogens shown).

Table 1. Crystal data and details of structure determination for **LTEA** and **[LTEACu(OAc)(MeOH)](SbF$_6$)**.

	LTEA	[**LTEA**Cu(OAc)(MeOH)](SbF$_6$)
Empirical formula	$C_{36}H_{51}N_5O_3$	$C_{39}H_{58}CuF_6N_5O_6Sb$
Formula mass (g mol^{-1})	601.82	992.19
Colour, habit	colorless, rod	blue, plate
Crystal dimensions (mm)	0.40 x 0.10 x 0.10	0.10 x 0.08 x 0.04
Crystal system	orthorhombic	triclinic
Space group	P $2_12_12_1$	P −1
Z	4	2
a (Å)	13.2018(8)	11.4632(7)
b (Å)	13.5649(8)	13.0625(8)
c (Å)	18.4945(10)	14.8682(9)
α (°)	90	94.176(3)
β (°)	90	98.893(3)
γ (°)	90	104.495(2)
V (Å^3)	3312.0(3)	2115.0(2)
D_{calc} (Mg m^{-3})	1.207	1.558
Radiation	Mo Kα	Cu Kα
Temperature	110 K	150 K
θ range for collection (º)	5.43−27.53	3.52−67.91
μ (mm^{-1})	0.08	6.354
F(000)	1304	1018
Observed reflections	7109	33408
Independent reflections	4139 (R_{int} = 0.024)	7533 (R_{int} = 0.070)
Data/restraints/parameters	4139 / 0 / 400	7533 / 0 / 542
Goodness of fit on F^2	1.119	1.045
R indices (all data)	R_1 = 0.0423	R_1 = 0.0462
wR_2 indices (I > 2σ(I))	wR_2 = 0.0854	wR_2 = 0.1219
Largest diff. peak/hole (e Å^{-3})	0.23 / –0.18	1.634 / –1.049

The binding of Cu(II) to **LTEA** was found to be highly dependent upon the choice of counterion. With BF_4^- or NO_3^- counterions, the Cu(II) complex did not form fully (incomplete coordination) in water, methanol or ethanol, as indicated by a large residual ligand peak in the ESI-MS analysis. By contrast, the reaction of **LTEA** with Cu(II) acetate or formate in methanol or ethanol yielded a blue solution with only one ESI-MS peak corresponding to the complexes **[LTEACu(OAc)]$^+$** or **[LTEACu(O_2CH)]$^+$**, respectively (Figure 4). With the $CF_3SO_3^-$ counterion, complexation only went to completion in an aprotic solvent such as THF; in protic solvents or in the presence of water or H_2O_2, the complex dissociated readily and the oxidation studies could not be conducted. Details on the oxidation studies that were performed on the acetate complex are given below.

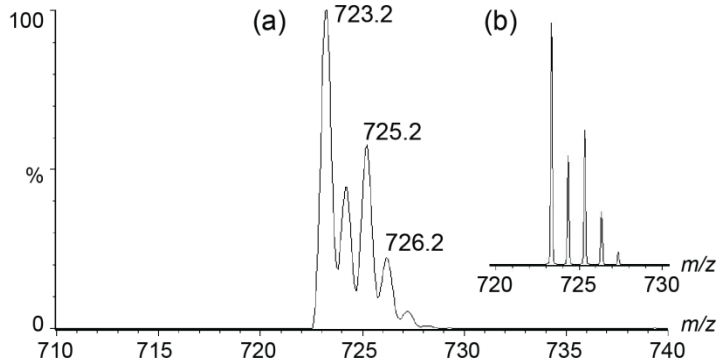

Figure 4. (a) ESI-MS spectrum of **[LTEACu(OAc)]$^+$**. (b) Predicted isotopic pattern of **[LTEACu(OAc)]$^+$**.

The acetate complex **[LTEACu(OAc)]$^+$** was isolated and characterized in the solid state. By adding $NaSbF_6$ to a methanol solution of the acetate complex and allowing the solvent to evaporate, well-defined blue crystals of **[LTEACu(OAc)(MeOH)](SbF$_6$)** formed within one hour. These crystals were studied by X-ray crystallography (Figure 5, Table 1). The structure of this complex displays several striking features. The Cu(II) ion is coordinated by only three of the four nitrogen atoms of the Tren moiety; the arm that is not coordinated (N4 arm) extends away from the metal ion. The square-pyramidal geometry of the Cu(II) ion is completed by an acetate ion in the equatorial position *trans* to the central Tren nitrogen atom (N1) and a methanol molecule at the apical position. Though slightly disordered at the methyl position, the methanol molecule is further involved in hydrogen bonding with the non-coordinated oxygen atom of the acetate ion (O2···O6 = 2.583 Å). The square-pyramidal geometry of the metal ion could be the consequence of the semi-rigidity of the cryptand, but Cu(II) complexes of ligand **1^H** with CN^-, SCN^- and N_3^- ions adopt a distorted trigonal-bipyramidal geometry with

all four nitrogen atoms of the Tren moiety coordinated.[118] In **[LTEACu(OAc)(MeOH)](SbF$_6$)**, the *N*-Methyl groups, especially on N4 atom, may sterically hamper the cryptand to adopt a pseudo-C_3 conformation when the acetate anion is coordinated.

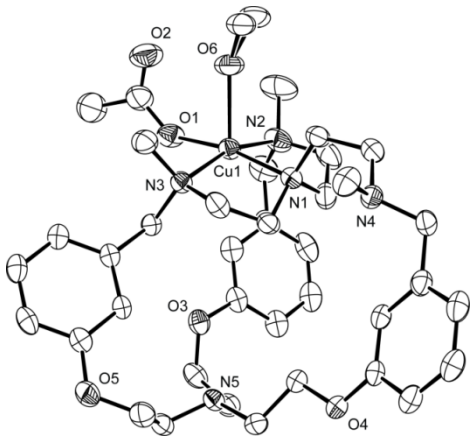

Figure 5. ORTEP drawing of **[LTEACu(OAc)(MeOH)](SbF$_6$)** at 50% ellipsoid probability. The SbF_6^- counterion and hydrogen atoms have been omitted for clarity. Selected bond lengths [Å]: Cu1-O1: 1.961(3), Cu1-O6: 2.271(3), Cu1-N1: 2.050(3), Cu1-N2: 2.073(3), Cu1-N3: 2.096(3).

The solution structure of the acetate complex was investigated by Electron Paramagnetic Resonance (EPR spectroscopy). The EPR spectra at 77 K of a methanol solution formed by adding Cu(II) acetate to **LTEA** and that of dissolved **[LTEACu(OAc)(MeOH)](SbF$_6$)** crystals in methanol both display an axial signal with $g_{//}$ = 2.21 ($A_{//}$ = 180 G) greater than $g_{\perp}$ = 2.03, consistent with a $d(x^2\text{-}y^2)^1$ electronic configuration. These spectra confirm the square-pyramidal geometry of the Cu(II) ion in solution (for comparison, the aforementioned **1^H** complexes remain trigonal bipyramidal in solution).[118] Coupled with the ESI-MS indicating a **[LTEACu(OAc)]$^+$** formulation, this suggests that the acetate ion is still occupying an equatorial position of the Cu(II) complex in methanol solution.

The **[LTEACu(OAc)]$^+$** complex was reacted under the oxidative conditions commonly used to generate Cu(II)-hydroperoxo species. The reaction of **[LTEACu(OAc)]$^+$** with one equivalent of H_2O_2 and Et_3N in methanol was followed by UV/Vis spectroscopy between +20 and –60 °C. The reaction mixture gradually changed from blue to green but no band could be unambiguously assigned to the Cu(II)-hydroperoxo species, **[LTEACuOOH]$^+$**, which is expected to display a hydroperoxo-to-Cu charge-transfer around 380 nm ($\varepsilon \approx$ 900-1700 M^{-1} cm^{-1}).[45,49,51,58,60,152] To study the oxidation process under more controlled conditions, the reaction was also carried out with 100 equivalents of H_2O_2 and Et_3N between –40 and –

90 °C in a low-temperature stopped-flow spectrophotometer (Figure 6).[158-160] This increase in H_2O_2/Et_3N concentration led to a faster formation of an intermediate along a bimolecular pathway, which permitted its observation. The time-resolved spectral traces indicated a growth from the spectrum of **[LTEACu(OAc)]$^+$** to that of a species with a distinct band shouldering around 380 nm and features in the visible range (Figure 6). This species then decayed in a slower process. Multivariate kinetic fitting of the growth using the Specfit software indicated a single exponential growth consistent with pseudo-first-order conditions. The fitting procedure revealed that the intermediate has absorptions at approximately 380 nm ($\varepsilon \approx 2000\ M^{-1}\ cm^{-1}$) and at 560 nm ($\varepsilon \approx 250\ M^{-1}\ cm^{-1}$), which are typical of the Cu(II)-hydroperoxo species, **[LTEACuOOH]$^+$**.[45,49,51,58,60,152] Fitting at several temperatures and Eyring analysis of the pseudo-first-order rate constants indicated that the growth process is associative with $\Delta H^{\ddagger} = 25.2\ kJ\ mol^{-1}$ and $\Delta S^{\ddagger} = -146\ J\ K^{-1}\ mol^{-1}$ (Figure 6). No dimeric species (end-on or side-on peroxodicopper(II) and bis(μ-oxo)dicopper(III))[12] were observed in any of the conditions used (concentration of H_2O_2/Et_3N, time of reaction). After being formed, the Cu(II)-hydroperoxo complex decayed to a mixture of species with a relatively silent UV/Vis spectrum (Figure 7). Fitting the decay process between –40 °C and +20 °C, however, did not lead to a single consistent kinetic model, suggesting the involvement of more than a single step.

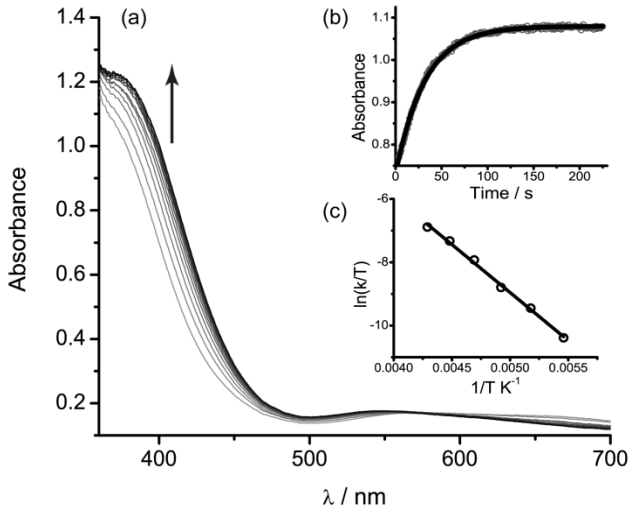

Figure 6. Stopped-flow UV/Vis spectroscopic studies of the reaction of **[LTEACu(OAc)]$^+$** with 100 equiv. of a 1:1 H_2O_2/NEt_3 mixture in MeOH at -70˚C; $[Cu]_{total}$ = 0.5 mM after mixing. (a) Time-resolved absorption spectra for the first 450 s of the reaction; a spectrum is measured every 9 s; first spectrum at 4.5 s. (b) Growth profile at 395 nm with first-order fit. (c) Eyring plot from the pseudo-first order rate constants measured at -90, -80, -70, -60, -50 and

-40˚C: 5.66×10^{-3}, 1.55×10^{-2}, 3.07×10^{-2}, 7.72×10^{-2}, 0.147 and 0.238 s^{-1}, respectively (standard deviations from fitting within 1.4-3.7%).

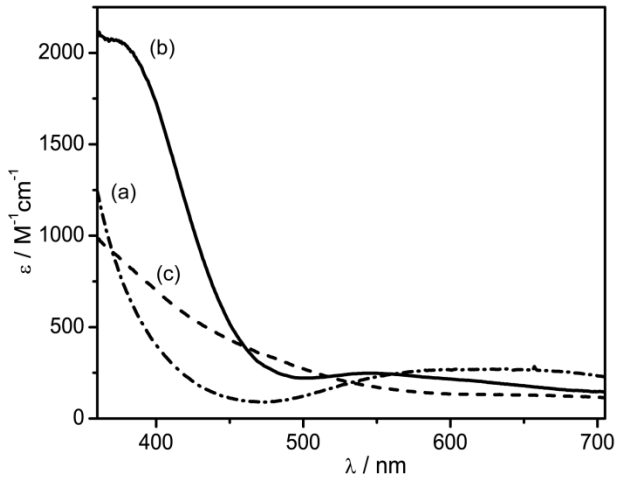

Figure 7. (a) UV/Vis spectra of **[LTEACu(OAc)]**$^{+}$ at 20 °C. (b, c) UV/Vis spectra of the Cu(II)-hydroperoxo intermediate (b, full) at –70 °C and the decay solution (c, dashed) at –40 °C deduced from stopped-flow measurements; in both cases the molar absorptivities were corrected from ca. ~15% and ~10% solvent contraction, respectively.

A comparison can be made between the present complex and the one studied by Itoh and coworkers in terms of the kinetics of formation and decay of the Cu-hydroperoxo intermediate.[57,160] As is the case with **[LTEACu(OAc)]**$^{+}$, Itoh's complex has an initial square-pyramidal geometry around the Cu centre and it is believed that this geometry is conserved in their Cu-hydroperoxo intermediate. The second-order rate-constants in Itoh's case fall in the range 4-5.1 × 10^{4} M^{-1} s^{-1} at –90 °C. By comparison, [**LTEACu(OAc)**]$^{+}$ is formed at a much slower rate, approximately 0.11 M^{-1} s^{-1} at –90 °C. This dramatic reduction in the rate of formation of the intermediate likely results from the steric demands and rigidity of the cryptand, which hamper substitution reactions in the Cu coordination sphere. Conversely, the cryptand-based intermediate decays qualitatively faster than Itoh's or other Cu(II)-hydroperoxo intermediates. The rigidity of the cryptand is likely restricting movements of the arms that contain the sensitive CH bonds and this pre-arrangement is entropically beneficial for the oxygen-atom transfer step.

To decipher the nature of the reaction intermediates and products, ESI-MS experiments were carried out by using a continuous-flow mixing set-up. A 1 mM solution of **[LTEACu(OAc)]**$^{+}$ and a 100 mM solution of H_2O_2/Et_3N were injected into coils that were cooled in a –85 °C bath. The solutions were

mixed in a Y-junction immersed in the cold bath and the mixed solution then entered the ESI-MS instrument through a short capillary. As the injection flow rate was varied, different stages of the reaction were observed. The solutions were initially prepared in methanol, but due to the proximity in mass of methanol to two oxygen atoms, the spectra were more easily interpreted when the experiments were carried out in absolute ethanol. The MS data (Figure 8 a-c) revealed a complex mixture of species; putative assignments are listed in Table 2. As the reaction time was increased from approximately 1.5 to 6.3 then to 16 min, peaks corresponding to oxidized products increased in intensity. Unfortunately, due to the technical difficulty of keeping the entire length of the capillary containing the mixed solutions at very low temperature, and given the residence times prior to reaching the MS ionization chamber, it is unlikely that the intermediate was observed in this experiment as it decays fast at temperatures above –40 °C.

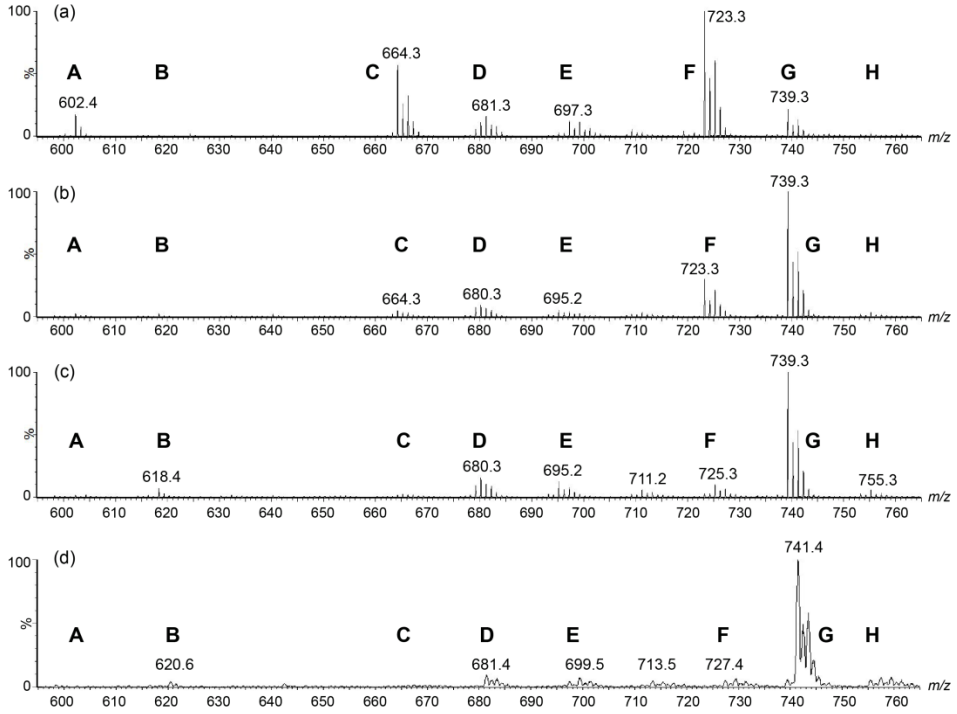

Figure 8. (a)-(c) ESI-MS of ethanol solutions of **[LTEACu(OAc)]**$^{+}$ and H_2O_2/Et_3N mixed by continuous-flow methods at –85°C prior to injection. The spectra were recorded after (a) 1.5, (b) 6.3, (c) 16 min of residence time after mixing. Assignments for groups A-H are given in Table 2. (d) ESI-MS of a **[LTEACu(OAc)]**$^{+}$ solution reacted with $H_2{}^{18}O_2$/Et_3N (5 equiv., –78 °C).

Table 2. Assignment of the main peaks in the low temperature continuous-flow MS experiments from Figure 8. The most relevant peaks are given in bold.

Position	*m/z* [a]	Assignment
A	**602**	**[LTEA]H$^+$ (reactant)**
B	**618**	**[LTEA+O]H$^+$**
C	**664**	**[LTEA+Cu]$^+$**
D	679	[(**LTEA**+O-H)+Cu]$^+$ (deprotonated hemiaminal)
	680	[(**LTEA**+O)+Cu]$^+$
	681	[**LTEA**+Cu+OH]$^+$
E	**695**	**[(LTEA+O-2H)+Cu+OH]$^+$** (double oxidation)
	697	**[LTEA+Cu+OOH]$^+$ or [(LTEA+O)+Cu+OH]$^+$**
	699	[**LTEA**+Cu+OH+OH$_2$]$^+$
F	**723**	**[LTEA+Cu+OAc]$^+$ (reactant)**
	725	[(**LTEA**+O-CH$_2$)+Cu+OAc]$^+$ (double oxidation)
G	**739**	**[(LTEA+O)+Cu+OAc]$^+$ (main product)**
H	755	[(**LTEA**+2O)+Cu+OAc]$^+$ (double oxidation)

[a] These *m/z* ratios correspond to the position of the peak using isotopes ^{1}H, ^{12}C, ^{14}N, ^{16}O and ^{63}Cu.

This ESI-MS experiment reveals the evolution of reactants and products upon reaction. Upon longer reaction times, the peaks corresponding to the starting material (F, C and traces of free ligand A) decreased. Conversely, peaks assigned to oxidized products containing one extra oxygen atom increased in intensity upon longer reaction times, especially **[LTEACu(OAc)+O]**$^+$ (G; *m/z* = 739.3). One signal at *m/z* = 697.3 (in the E group) could correspond to the Cu(II)-hydroperoxo species [**LTEACuOOH**]$^+$, but it could also be due to a product in which the ligand is oxygenated: **[(LTEA+O)CuOH]$^+$**, that is the Cu(II)-hydroxo complex of an oxygenated ligand (see below; for comparison, the Cu(II)-hydroxo complex of **LTEA** is found in D at *m/z* = 681.3, a peak that decreases with reaction time). As a note, a neutral [**LTEACu(OAc)(OOH)**] complex could be the prevalent form of the intermediate observed by stopped-flow UV/Vis spectroscopy; the fact that this species would be MS-silent could explain the relatively small [**LTEACuOOH**]$^+$ signal. Peaks assigned to over-oxidized compounds are also observed and increase in intensity upon longer reaction times, but remain in small quantities. In particular, a peak at *m/z* = 695.2 could correspond to **[(LTEA+O-2H)+Cu+OH]$^+$**, that is the Cu(II)-hydroxo complex of a ligand that was doubly oxidized to either an amide or an aldehyde/imine (see below). Overall, however, the major product is the **[LTEACu(OAc)+O]**$^+$ species and it is concluded that the reaction is selective for monooxygenation despite the large excess of oxidant.

Isotopic labeling using ^{18}O-enriched hydrogen peroxide (from a solution in ^{16}O-water) proved that the oxygen atom that is incorporated into the complex comes from the oxidant. When $H_2{}^{18}O_2$ was used (5 equivalents of $H_2{}^{18}O_2/Et_3N$ per **[LTEACu(OAc)]**$^+$), the MS data displayed a peak at 741.4, which corresponds to **[LTEACu(OAc)+^{18}O]**$^+$, with a signal at 739.3 not significantly more intense than the 10% expected from the 90% isotopic enrichment of the oxidant (Figure 8, d). Thus, the entirety of the oxygen incorporated into the complex after reaction originated from H_2O_2 and this oxygen did not exchange with water in the timescale of the experiments (less than one hour).

To analyze the ligand modifications resulting from the oxidation reaction, demetallation was carried out by treatment with ammonium hydroxide or Na_4EDTA. The residual organic matter was then analyzed by ESI-MS. The cryptand nature of ligand **LTEA** prevented much fragmentation and led to simple spectra with one major signal at *m*/*z* = 618.3 corresponding to [**LTEA**+O]$^+$ and some intact ligand at *m*/*z* = 602.3 (Figure 9, a). This experiment demonstrates the insertion of one oxygen atom into the ligand backbone and negligible amounts of double oxidation products, either as [**LTEA**+2O]$^+$, [**LTEA**+O-2H]$^+$ or [**LTEA**-4H]$^+$. As a control experiment, ligand **LTEA** was treated with H_2O_2/Et_3N under the same conditions but no significant oxidation of the ligand occurred. Thus, the presence of Cu(II) is essential to carry out the oxygenation reaction efficiently. In addition, when $H_2{}^{18}O_2$ was used, the oxygenated peak shifted to *m*/*z* = 620.4 for a [**LTEA**+^{18}O]$^+$ species (Figure 9, b), thereby confirming the incorporation of one oxygen atom from H_2O_2 into a non-exchangeable position of the ligand.

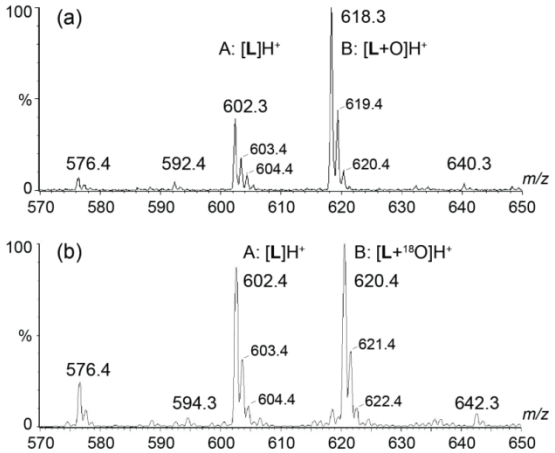

Figure 9. ESI-MS of the organic products of the oxidation reaction after demetallation, principally A = [**LTEA**]H$^+$ and B = [**LTEA**+O]H$^+$. The residual A signals arise because the reactions were stopped before completion. These signals decrease at long time-scales.

After demetallation, the solution contained several compounds (according to TLC, MS, and NMR spectroscopy) but we were unable to separate the compounds into their pure form for quantification purposes. This is likely the result of all products remaining as cryptands or macrocycles with structures close to that of the **LTEA** precursor. Our best purification efforts using flash chromatography led to two impure fractions. The oxidized solution reacted with the Fuchsin-aldehyde reagent; the resulting aldehyde could clearly be seen after the reaction. This aldehyde was identified in the first fraction by ^{1}H-NMR (well-defined peak at δ = 9.96 ppm in $CDCl_3$) and by solution IR spectroscopies (intense peak at 1708 cm^{-1}). The second fraction displayed a weak peak at 1667 cm^{-1} in the IR spectrum, which is tentatively assigned to an amide. As the benzylic positions in **LTEA** are the most sensitive ones to oxidation conditions, we propose that one of these positions is the target of the oxygen-atom transfer by the CuOOH intermediate. If oxygen-atom transfer had occurred to an *N*-Methyl group, demethylation would occur together with the release of formaldehyde in solution. This pathway was not observed to be a major contributor to the reactivity of the complex (Table 2). Furthermore, a recent study involving $[Cu(Me_6Tren)\text{-}(OOH)]^+$ showed no decay reactivity of the intermediate with the permethylated Tren ligand system.[153]

Based on the above MS and UV/Vis analyses, we propose the reaction pathway shown in Scheme 11, which is inspired by the known reactivity of many Cu-dioxygen intermediates[16] and Cu(II)-hydroperoxo species.[47,52] This reaction pathway only accounts for the formation of the major **[LTEACu(OAc)+O]**$^+$ species observed by ESI-MS. The first step is the formation of a Cu(II)-hydroperoxo species in an associative reaction between **[LTEACu(OAc)]**$^+$ and HOO^- generated in situ by deprotonation of H_2O_2.[57,160] This intermediate was observed by UV/Vis spectroscopy but its proper formulation, geometry and charge is yet unknown due to its relative instability. This intermediate then reacts with the benzylic position along an oxygen-atom transfer reaction akin to the current literature proposals for similar species,[47,60] thus producing a hemiaminal intermediate, which is deprotonated and bonded to Cu (*m*/*z* = 679 for [(**LTEA**+O-H)+Cu]$^+$) or protonated (*m*/*z* = 680 for [**(LTEA+O)+Cu**]$^+$ and *m*/*z* = 739 for [**(LTEA+O)+Cu+OAc**]$^+$). Under the protic conditions used, this hemiaminal intermediate can readily hydrolyze to a secondary amine and an aldehyde (*m*/*z* = 739 as well), a functional group whose presence was confirmed in the decomposed mixture by both NMR and IR spectroscopies. Finally, minor products resulting from over-oxidation could form through an intermolecular reaction of the hemiaminal with

H_2O_2,[47] intermolecular attack of HOO^- on an iminium intermediate (see below), or the complex of an already oxygenated ligand reentering the whole oxidation cycle.

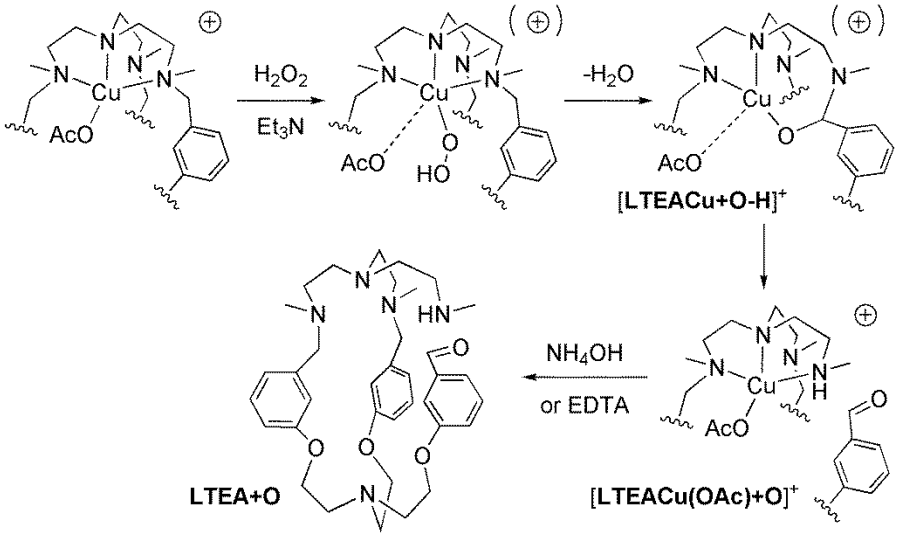

Scheme 11. Proposed reaction pathway for the inner-sphere oxidation reaction of **[LTEACu(OAc)]$^+$** with H_2O_2/Et_3N. For clarity, the cryptand backbone has been simplified. The Cu(II)-hydroperoxo complex (and other intermediates) may or may not be bonded to the acetate couterion, which would also influence the overall charge and their detection by ESI-MS.

The mechanism of the oxygen-atom transfer is still unknown but could proceed along two well-studied oxidative *N*-dealkylation pathways: a direct hydrogen-atom abstraction followed by rebound, or a single-electron transfer followed by further electron and proton transfers.[161] The hydrogen-atom abstraction mechanism entails hydrogen abstraction from the weak *N*-benzylic position by the electrophilic oxygen of the Cu(II)-hydroperoxo complex to generate a carbon radical in the α position of the amine. Rebound of the putative Cu(II)-oxyl species then produces the hemiaminal intermediate.[47] The single electron transfer mechanism, on the other hand, would generate an amine-based radical that can then lose a proton and an electron to form an iminium intermediate. Intramolecular nucleophilic attack of a coordinated oxo or hydroxo ion then leads to the same hemiaminal intermediate as above. Importantly, the hypothesis of an intermolecular attack of water onto the iminium intermediate has been refuted by the ^{18}O isotopic labeling experiments. Thus, as per recent literature on oxygen atom transfer reactions with Cu(II)-hydroperoxo species, the hydrogen-atom abstraction mechanism seems to be the favored pathway.[47,60]

More studies are needed to substantiate the proposed reaction pathway of Scheme 11. In particular, ^{18}O isotopic labeling would be useful for measuring the O-O stretch of the Cu(II)-hydroperoxo species by resonance Raman spectroscopy and to confirm its nature and involvement in the oxygenation reaction. Given the transient nature of this intermediate, however, excess $H_2{}^{18}O_2$ would be required for the intermediate to accumulate and be observed. Instead, we are currently trying to stabilize the intermediate by deuterating the oxidation-sensitive C-H bonds of the ligand (*i.e.*, the benzylic positions and *N*-Methyl substituents). This substitution would slow down the C-H activation step, which is thought to be rate-determining (kinetic isotope effect). Increasing the oxidative stability of the ligand shall therefore lead to a Cu(II)-hydroperoxo intermediate that can both be isolated at low-temperatures and reactive upon warming. This approach will facilitate the study of the electronic structure (by resonance Raman spectroscopy), the geometry (by EPR spectroscopy), and the reactivity of the intermediate.

2.4 Conclusion

The reaction between the Cu(II)-cryptand complex **[LTEACu(OAc)]**$^+$ and H_2O_2/NEt_3 leads to a single major oxygenated species upon oxygen-atom insertion into a weak C-H bond. Observation of a reactive intermediate in this reaction was achieved using pseudo-first-order conditions, very low temperatures and fast-mixing/recording stopped-flow techniques. The intermediate has the same UV/Vis spectroscopy and reactivity signatures as that of known Cu(II)-hydroperoxo species,[1,60] which strongly suggests that the reaction involves such a Cu(II)-hydroperoxo species borne by the cryptand. It is not yet known whether the hydroperoxo group is encapsulated by the cavity of the cryptand and thereby supported by second coordination sphere interactions. Whereas the crystal structure of the acetate complex suggests that *N*-Methylation prevents the cryptand from adopting a pseudo-C_3 symmetry once coordinated, the coordination geometry could change upon binding the smaller and more linear hydroperoxide anion. A correlation indeed exists between coordination geometry and anion size in cryptand complexes.[162] Further studies are in progress to render the ligand less sensitive to oxidation and stabilize the intermediate species to enable a more complete characterization.

2.5 Experimental

General: All materials were used as received. The synthesis of ligand $\mathbf{1^H}$ has been reported elsewhere.[118] NMR spectroscopic measurements were made at 22 °C in a 5 mm tube on a Varian Innova 300 or 500 MHz instrument and referenced to internal TMS. ESI-MS spectra were measured using direct injection

on a Micromass Q-TOF or a Micromass Quattro LC at Concordia's Centre for Biological Applications of Mass Spectrometry. The *m*/*z* data reported is based on ^{1}H, ^{12}C, ^{14}N, ^{16}O, ^{63}Cu. X-ray crystallography was performed on the molybdenum source of a Bruker APEX DUO (**LTEA**) or the copper rotating anode source of a Bruker Microstar **[[LTEACu(OAc)(MeOH)](SbF$_6$)]**. UV/Vis spectra were recorded on an Agilent 8453 spectrophotometer equipped with a Unisoku USP-203-A cryostat for temperatures down to –60 °C.

Ligand LTEA: 1^{H} (1.00 g, 1.8 mmol) was added to a solution of formaldehyde (740 µL, 10.6 mmol) and formic acid (400 µL, 10.6 mmol). The mixture was heated under reflux for 24 h. The solution cooled and was poured onto an aqueous solution of NaOH (30 mL, 2 M). The product was extracted with dichloromethane (3 × 20 mL) and the organic phase extracts were dried with anhydrous Na_2SO_4. The solvent was removed under reduced pressure, yielding a precipitate that was suspended in acetonitrile. Filtration, washing with acetonitrile and drying under vacuum yielded 0.82 g (76%) of a white powder. Single crystals amenable to X-ray diffraction analysis were grown by the slow diffusion of acetonitrile into a dichloromethane solution of **LTEA** at –30 °C (Table 1). ^{1}H-NMR (300 MHz, $CDCl_3$): δ = 2.15 (s, 9H, CH_3), 2.32 (t, 6H, J = 7, CH_2), 2.59 (t, 6H, J = 7, CH_2), 3.08 (t, 6H, J = 5, CH_2), 3.31(s, 6H, CH_2), 4.04 (t, 6H, J = 5, CH_2), 6.67 (m, 3H, Ar), 6.73 (m, 3H, Ar), 7.00 (s, 3H, Ar), 7.11 (m, 3H, Ar) ppm. ^{13}C-NMR (300 MHz, $CDCl_3$): δ 43.4 (CH_3), 52.5 (CH_2), 54.5 (CH_2), 57.4 (CH_2), 62.8 (CH_2), 68.9 (CH_2), 114.7 (Ar), 114.8 (Ar), 121.5 (Ar), 129.0 (Ar), 141.0 (Ar), 159.4 (Ar) ppm. MS (ESI, 1:1 CH_3OH:CH_2Cl_2): *m*/*z* = 602.41 $[M+H]^+$.

[LTEACu(OAc)(MeOH)]$^+$ solutions and [LTEACu(OAc)(MeOH)](SbF$_6$) crystals: A solution of copper(II) acetate (8.0 mg, 39 µmol) dissolved in 800 µL of methanol was added to a solution of **LTEA** (24 mg, 39 µmol) dissolved in dichloromethane (200 µL). The solution was used as is for further experiments (100% formation as evidenced by a single ESI-MS signal at *m*/*z* = 723.31). Single crystals were grown by the addition of $NaSbF_6$ (1 equiv.) dissolved in the minimum amount of methanol to a solution of the complex in methanol and allowing the solution to stand for 1 h (Table 1).

Bulk Oxidation Studies: A methanol solution (1 equiv.) of H_2O_2/Et_3N (1:1; the H_2O_2 was from a 30 wt.-% aqueous solution) was added to a methanol solution of **[LTEACu(OAc)(MeOH)]$^+$** (1.0 mm) at –78 °C turning the solution green. After 10 min, the solution was warmed to room temperature and analyzed by ESI-MS. Whether the reaction was performed under an air or nitrogen atmosphere did not change the kinetics, colors, and products.

Isotopic Labeling Experiments: A methanol solution (5 equiv.) of $H_2{}^{18}O_2/Et_3N$ (1:1; the $H_2{}^{18}O_2$ came from a 2.5 wt.-% solution in $H_2{}^{16}O$) was added to a methanol solution of **[LTEACu(OAc)]$^+$** (1.0 mm) at –78 °C and the resulting solution turned green. After 10 min, the solution was warmed to room temperature and analyzed by ESI-MS.

Analysis of Organics: After decomposition of the oxidized reaction mixture, excess NH_4OH or Na_4EDTA was added and the solution was filtered through an alumina column eluted with 20% MeOH in CH_2Cl_2. The filtrate was analyzed by ESI-MS. Our attempts to isolate pure oxygenated products from the mixture were unsuccessful.

Kinetic Measurements: Kinetic studies of the reaction of H_2O_2/NEt_3 with **[LTEACu(OAc)]$^+$** were recorded on a modified Hi Tech SF-3L low-temperature stopped-flow unit (Salisbury, UK) equipped with a J&M TIDAS 16-500 diode array spectrophotometer (J&M, Aalen, Germany).[158-159,163] Complex solutions before mixing were 1.0 mM and the concentration of the H_2O_2/NEt_3 mixture was 100 mM to ensure pseudo-first-order conditions and help the formation of the intermediate before it could decay. The reaction was studied at temperatures between +20 and –90 °C. Complete spectra were collected with the integrated J&M software Kinspec 2.30 and analyzed with a global analysis fitting routine using the program Specfit (Spectrum Software Associates, Chapel Hill, USA).

CCDC-808560 (for **LTEA**) and -795492 [for **LTEACu(OAc)(MeOH)](SbF$_6$)**] contain supplementary crystallographic data. These data can be obtained free of charge from The Cambridge Crystallographic Data Centre via www.ccdc.cam.ac.uk/data_request/cif.

2.6 Acknowledgments

This work was supported by grants from the Fonds de Recherche sur la Nature et les Technologies of Quebec (FQRNT) and the Natural Sciences and Engineering Research Council of Canada (NSERC). S. S. gratefully acknowledges financial support from the Deutsche Forschungsgemeinschaft (DFG) (SPP1118 and SCHI377/6-2). We are grateful to Francine Bélanger-Gariépy (Université de Montréal) for X-ray crystallography studies on **[LTEACu(OAc)](SbF$_6$)**, to Frank Schaper (Université de Montréal) for access to his Specfit software, and to Scott Bohle (McGill University) for recording the EPR spectra. M.S.A. acknowledges NSERC for CGS-M and PGS-D scholarships and a Michael Smith Foreign Study Supplements award.

Chapter 3: Supramolecular Control of Monooxygenase Reactivity in a Copper(II) Cryptate

L. Chaloner[a], A. Khomutovskaya[a], F. Thomas[b] and X. Ottenwaelder*[a]

[a] Department of Chemistry and Biochemistry, Concordia University, 7141 Sherbrooke Street West, Montreal, H4B 1R6, Canada.

[b] Équipe de Chimie Inorganique Redox, Département de Chimie Moléculaire, Université Joseph Fourier, 38041 Grenoble, Cedex 9, France.

3.1 Abstract

Herein, we report the detailed investigation of the formation and self-decomposition of Cu(II)-hydroperoxo intermediates under the influence of second-coordination-sphere features provided by a cryptand. In solution, an equilibrium between two copper complexes with square-planar and square-pyramidal geometry was identified by EPR. Upon addition of H_2O_2/Et_3N, two copper(II) hydroperoxo intermediates formed at different rates. Their decomposition via self-oxidation was probed by deuterating select positions on the cryptand. This led to a small kinetic isotope effect of 1.5. MS analysis of the demetallated organic products is consistent with a direct oxygen-atom transfer to a tertiary amine on the cryptand, forming an N-oxide, unlike other models of copper(II) mononuclear monooxygenase enzymes.

3.2 Introduction

In contrast to energy-consuming or hazardous industrial processes,[2-3,164] biological systems serve as an inspiration to develop synthetic oxidative transformations such as oxygen-atom transfers (OAT) and C–H bond hydroxylations.[9] Mechanistically, OATs are characterized by the direct transfer of an oxygen atom from a donor to an acceptor molecule while C–H bond hydroxylations generally entail a hydrogen-atom abstraction/transfer (HAT) followed by an oxygen or hydroxyl group transfer.[14-15] While a general synthetic procedure for OAT or C–H bond hydroxylation under mild, efficient and selective conditions remains elusive,[3] several enzymes can selectively perform this reaction using dioxygen (O_2) as the oxidant and forming water as a by-product.[7,164] For this reason, bio-inorganic chemists strive to understand and mimic biological systems to inspire synthetic oxidative transformations.[60,165] In this paper, we focus on copper (Cu) oxidative chemistry in relation to copper-dependent enzymes.

Development in this field can be achieved by understanding the nature and reactivity of Cu(II)-dioxygen intermediates in biological systems.[9] The Cu(II)-superoxo and Cu(II)-hydroperoxo are of

particular interest because they are involved in mononuclear monooxygenases such as peptidylglicine-α-hydroxylating monooxygenase (PHM), dopamine-β-monooxygenase (DβM) and tyramine-β-monooxygenase.[7,166] PHM catalyzes the C–H bond hydroxylation of a glycine-extended peptide to form peptidyl-α-hydroxyglycine, DβM catalyzes the hydroxylation of dopamine to form norepinephrine and TβM hydroxylates tyramine, forming octopamine.[17] These enzymes bear similar structures composed of two domains each containing a single Cu centre. In PHM, and by extension in the other analogous enzymes, dioxygen is activated at a mononuclear Cu(I) active site. The rate-determining step (RDS) is typically a HAT from the substrate, which is then followed by a fast transfer of the oxygen-atom. It is now widely accepted that a Cu(II)-superoxo intermediate is the hydrogen abstractor in enzymatic systems,[7,17] yet many synthetic complexes show the viability of the Cu(II)-hydroperoxo species as a HAT or OAT agent.[44-48,52,167]

The structure and reactivity of Cu/O_2 intermediates is dependent on the ligand system.[95,110] For example, TMG_3Tren is a ligand that uses steric and electronic effects to stabilize a Cu(II)-superoxo species at low temperatures (Chart S1, A).[19] The TMG_3Tren-Cu(II)-superoxo does not oxygenate the ligand upon thermal decomposition, yet TMG_3Tren-Cu(II)-hydroperoxo intermediates are able preform a C–H bond hydroxylation on the ligand.[44] A second important study shows that by using a well-tailored N_2O_2 ligand system (Chart S1, B), a thermally stable Cu(II)-hydroperoxo complex is formed and involved in the catalysis of benzylic C–H bond oxidation of toluene and *o*-xylene.[46] In this example, DFT shows that the Cu(II)-hydroperoxo intermediate is stabilized through hydrogen bonding of the Cu(II)-hydroperoxo hydrogen to a phenolate group of the ligand. This is in contrast with BPPACu(II)(OOH) (Chart S1, C), where the hydroperoxo group stabilized by hydrogen bonding of the proximal oxygen to the pivalamide group.[58] Taken together, these examples illustrate that the second coordination sphere of the metal centre can influence the reactivity of Cu/O_2 intermediates.

Cryptands can influence the geometry and reactivity of metals centres, imparting new behaviours on old coordinating moieties.[114-115,168-169] In previous work, we were able to synthesize and obtain a crystal structure of a novel Cu(II) cryptate, [**LTEA**Cu(OAc)(MeOH)]$^+$ (Scheme 12).[170] The geometry of the metal centre was found to be square-pyramidal, unlike typical Tren-based complexes that adopt trigonal-bipyramidal geometries.[126,153] When the Cu(II) cryptate was reacted with hydrogen peroxide (H_2O_2) in the presence of triethylamine (Et_3N), a Cu(II)-hydroperoxo intermediate was formed. We here present a

detailed analysis of its reactivity, which constitutes an extensive investigation into the influence of the second coordination sphere of a cryptand on the behaviour of a Cu(II)-hydroperoxo intermediate.

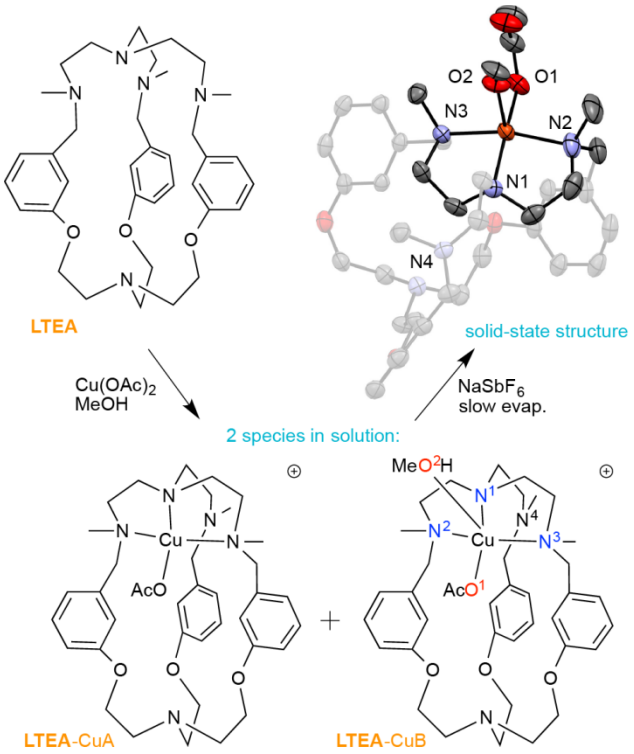

Scheme 12. Synthesis of [**LTEA**Cu(OAc)$(MeOH)_n]^+$ (n= 0 or 1) and its crystal structure (as a SbF_6^- salt) showcasing the geometry of the metal centre.[170] Crystal: ORTEP representation at 50% thermal ellipsoid probability. The hydrogen atoms and SbF_6^- counterion have been removed for clarity.

3.3 Results and Analysis

3.3.1 Synthesis and Characterization of the Copper(II) complexes

The reaction of **LTEA** with Cu(II) acetate leads to the formation of cryptand-Cu(II) complexes with different speciations in solution. Two Cu complexes, **LTEA**-CuA and **LTEA**-CuB, identified in frozen solution by EPR spectroscopy, were found in solutions I-IV (preparation of I-IV was described in the methods section). Solutions I and II were in methanol, a coordinating solvent, while solutions III and IV were in non-coordinating dichloromethane. A solvent effect was observed (below), but at parity of solvent no significant difference was observed regardless of having been prepared in-situ or by redissolving crystals of the pure complex (I vs. II; III vs. IV) (Figure 10 and Figure S1).

Table 3. EPR spectral parameters for solutions I-IV

Cond.	Complex	$g_{\perp}$ [1] ($A_{\perp}$ (G))[1]	$g_{\parallel}$ ($A_{\parallel}$ (G))	$g_{\parallel}$ / $A_{\parallel}$ [2] (cm)	A:B (%)
I: in situ / MeOH	**LTEA**-CuA	2.037 (22)	2.235 (189)	126	60
	LTEA-CuB	2.056 (37)	2.216 (181)	131	40
II: crystals / MeOH	**LTEA**-CuA	2.040 (17)	2.232 (188)	127	61
	LTEA-CuB	2.047 (41)	2.204 (183)	129	39
III: in situ / CH_2Cl_2	**LTEA**-CuA	2.059 (17)	2.244 (185)	130	89
	LTEA-CuB	2.059 (44)	2.209 (176)	134	11
IV: crystals / CH_2Cl_2	**LTEA**-CuA	2.052 (20)	2.238 (188)	127	83
	LTEA-CuB	2.054 (43)	2.204 (178)	132	17

[1] Significant overlap in this region creates an uncertainty in these values.
[2] A is in cm^{-1}

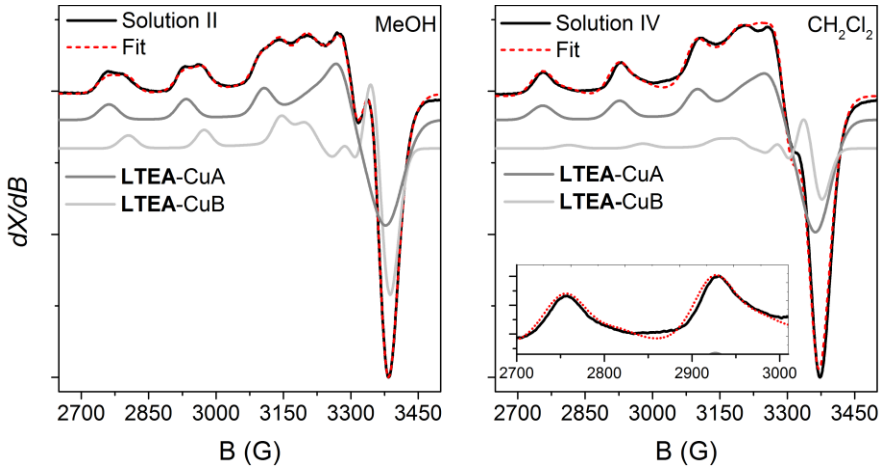

Figure 10. X-Band EPR spectra of solutions II and IV in black, Easyspin fit spectra in red and deconvolution of the fit spectra in grey.[135]

The EPR spectra of frozen solutions I-IV (Figure 10 and Figure S1) are consistent with a Cu(II) geometry similar to that in the crystal structure of [**LTEA**Cu(OAc)(MeOH)]$^{+}$.[170] The spin Hamiltonian parameters obtained from simulation are listed in Table 3.[135] The spectra were best fitted by considering a mixture of two mononuclear Cu(II) complexes, **LTEA**-CuA and **LTEA**-CuB, with $d(x^2\text{-}y^2)^1$ ground states ($g_{\parallel} > g_{\perp}$). Although the perpendicular regions were satisfactorily fitted using the parameters given in Table 3, we refrained from commenting on the values due to the significant overlap of the signals which results in large uncertainty. Addison et al. proposed that $g_{\parallel}/A_{\parallel}$ ratio reflects the metal ion geometry, with values

as low as 120 representing a square-planar geometry of the metal centre.[171] The $g_{\|}/A_{\|}$ ratio calculated for all the species (Table 3) fall within the range 124-130, *i.e.* close to 120. This indicates that the tetragonal distortions are very small in both species and that the metal ion geometry is not significantly different between them.

The distinguishing feature between **LTEA**-CuA and **LTEA**-CuB in solution was assigned to the presence or absence of a methanol molecule at the axial coordination site. Evidence for an equilibrium between the two complexes stems from the spectra of the crystals dissolved in coordinating versus non-coordinating solvent (Figure 10). The highest ratio of **LTEA**-CuB is observed in methanol suggesting that **LTEA**-CuB retains an axial methanol molecule (square-pyramidal geometry) in agreement with the crystal structure. Conversely, **LTEA**-CuA has a square-planar geometry formed by three nitrogens from **LTEA** and one acetate. Thus, in our formalism A represents $[(OAc)]^+$ and B represents $[(OAc)(MeOH)]^+$ (see Figure S2 for further analysis of coordinating anions).

3.3.2 Formation and Decomposition of the Copper(II)-Hydroperoxo Intermediate

As previously reported, the Cu(II)-hydroperoxo intermediate was formed from the reaction of the complex with a H_2O_2/Et_3N solution in methanol. A colour change from blue to green to yellow-green was observed as the reaction took place. This progression was followed at low temperatures with different spectroscopic and spectrometric techniques as described below.

3.3.2.1 EPR Analysis of the Intermediates

The EPR spectrum recorded after mixing solution I with 20 equiv. H_2O_2/Et_3N at -90°C for 1 min did not exhibit any signal attributable to the initial compound **LTEA**-CuA and **LTEA**-CuB, consistent with full consumption of the starting material (Figure 11). The EPR spectrum was composed of two signals typical for Cu(II) mononuclear complexes, indicating that again two species were present in solution, **LTEA**-CuC and **LTEA**-CuD (Figure 11 and Table 4). The spectra were fitted by using the Hamiltonian parameters in Table 4 for **LTEA**-CuC and **LTEA**-CuD. The $g_{\|}/A_{\|}$ ratios for **LTEA**-CuC and **LTEA**-CuD (148 and 136 cm respectively) are higher than for the starting complexes, demonstrating that the Cu(II) geometry evolved upon formation of the hydroperoxo intermediates. Complex **LTEA**-CuC displayed the highest tetragonal distortion. Both **LTEA**-CuC and **LTEA**-CuD have $g_{\|} > g_{\perp}$ with a $d(x^2-y^2)^1$ ground state. This is in contrast with Me_6TrenCuOOH (Chart S1, D) whose ligand donor set is similar, but the $g_{\perp} > g_{\|}$ ordering is instead

consistent with a trigonal-bipyramidal geometry.[153] Although the observed intermediates **LTEA**-CuC and **LTEA**-CuD have distorted geometries, neither has the TBP geometry expected from complete encapsulation of the intermediate.

The EPR spectrum of the decomposition products mainly consists of an axial copper(II) signal with $g_{\parallel} > g_{\perp}$. Attempts to fit the spectrum by considering a single species with a $d(x^2-y^2)^1$ ground state failed. The introduction of a second component with $g_{\perp} > g_{\parallel}$ ($d(z^2)^1$-like ground state) in ca. 16% improved the fit significantly (Table 4). The $g_{\perp}$ and $A_{\perp}$ values of this minor complex, **LTEA**-CuE, are similar to those reported by Karlin et al. for a trigonal-bipyramidal copper complex,[172] supporting a similar geometry of the copper(II) ion in **LTEA**-CuE. The major complex, **LTEA**-CuF, displays a $g_{\parallel}/A_{\parallel}$ ratio of 129 cm, which is very similar to that in the initial complexes **LTEA**-CuA and **LTEA**-CuB. This suggests that the ligand in **LTEA**-CuF retained a similar structure after reaction with H_2O_2.

Table 4. EPR spectral parameters for solution I + H_2O_2/Et_3N

Cond.	Complex	$g_{\perp}$ [1] ($A_{\perp}$ (G))[1]	$g_{\parallel}$ ($A_{\parallel}$ (G))	$A_{\parallel}$ (G)	$g_{\parallel}$ / $A_{\parallel}$ [2] (cm)	A:B (%)
I + H_2O_2/ Et_3N	**LTEA**-CuC	2.063 (31)	2.200 (158)	158	148	24
	LTEA-CuD	2.037 (32)	2.235 (174)	174	136	76
Decomposition	**LTEA**-CuE	2.178 (68)	2.017 (71)	71	306	16
	LTEA-CuF	2.055 (14)	2.251 (186)	186	129	84

[1] Significant overlap in this region creates an uncertainty in these values.
[2] A is in cm^{-1}

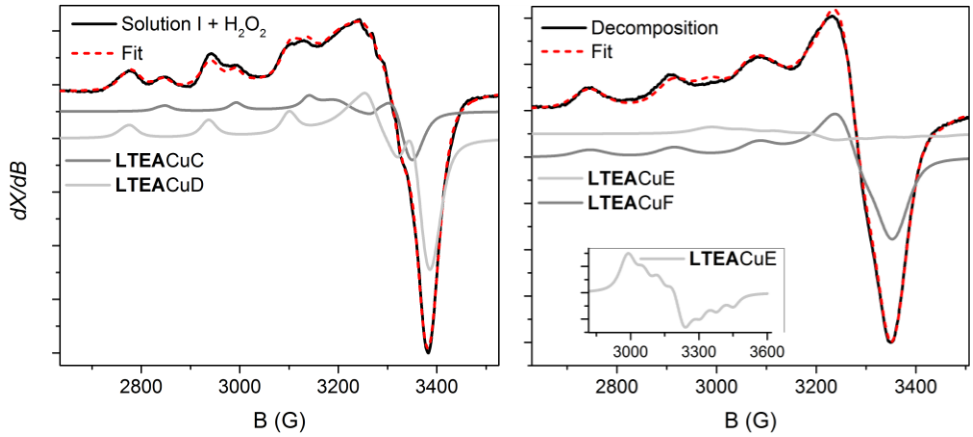

Figure 11. X-Band EPR spectra of Solution I + 50 equiv. H_2O_2/Et_3N and decomposition product

3.3.2.2 Kinetics of Formation of the Hydroperoxo Intermediates

Two Cu(II)-hydroperoxo intermediates were confirmed by low-temperature stopped-flow UV/Vis spectroscopy. A slower forming LMCT absorption band at 388 nm ($\varepsilon \approx 2000\ M^{-1}\ cm^{-1}$) was previously identified.[170] In addition to the slow-forming LMCT, a fast process with a λ_{max} of 375 nm was observed at -50°C (Figure 12). A spectral change in the visible region corresponding to the d-d transitions was only observed after the slow process, reflecting a greater change in geometry (Figure S3). We therefore assign the LMCT at 388 nm (slow process) to the complex with a greater tetragonal distortion, **LTEA**-CuC.

The rate constants of both the fast and slow processes were shown to be $[H_2O_2]$-dependent and obey saturation kinetics (Figure 12, A and B). The saturation behaviour, previously identified by Itoh and co-workers, arises from a rate-law involving the equilibrium $[H_2O_2] + [Et_3N] \rightleftharpoons [HOO{\cdot}Et_3NH]$ where $[HOO{\cdot}Et_3NH]$ reacts with the complex to form the hydroperoxo intermediate.[57] The equilibrium constant extracted from the fast and slow reactions using Itoh's model should be similar but we measured $K_1 = 133$ for the fast process and $K_2 = 14$ for the slower process. The difference in the equilibrium constants indicates that the fast and slow reactions cannot be fitted to the same reaction model and suggests two different mechanistic pathways. Despite our best attempts, the rate constants could not be extracted from the data presumably due to the additional [**LTEA**-CuA] + [MeOH] ⇌ [**LTEA**-CuB] equilibrium.

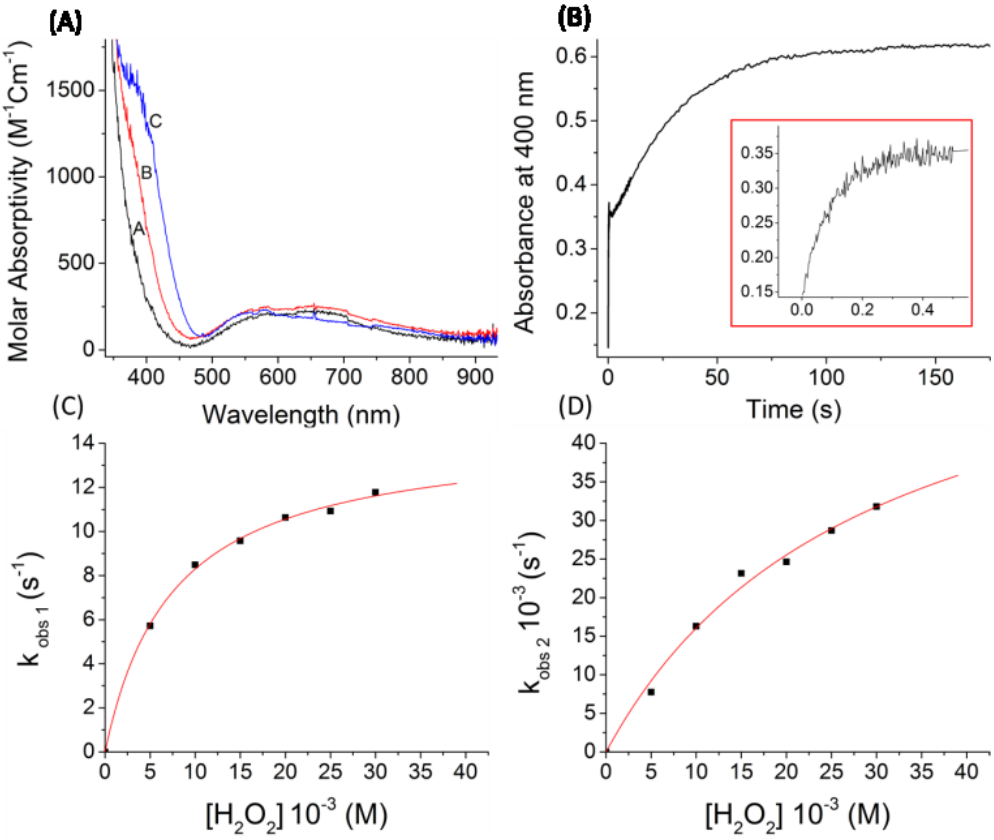

Figure 12. Top: Spectral data of the reaction of solution I (0.5 mM) and 10 equiv. Et_3N + 40 equiv. H_2O_2 at -50 °C in MeOH. (A) UV/Vis spectra at A: 2.5 ms B: 0.875 s and C: 174.87 s. (B) Time profile of absorbance at 400 nm. Inset: zoom from 0 to 0.55 s. (C) and (D): Observed pseudo first-order rate constants of the reaction of Solution I in the presence of 10 equiv. Et_3N + 10-60 equiv. H_2O_2 at -50 °C vs $[H_2O_2]$; (C) fast process and (D) slow process. The red trace indicates a fit to $k_{obs} = kK[H_2O_2][Et_3N] / 1 + K[Et_3N]$ where, $K_1 = 133$ and $k_1 = 2902\ s^{-1}$ for graph (C) and $K_2 = 14$ and $k_2 = 24$ for graph (D).

3.3.2.3 Kinetics of Decomposition of the Hydroperoxo Intermediate

The decomposition of the slow-forming intermediate was analysed with stopped-flow UV/Vis at 20°C by monitoring the decay of the absorption at 388 nm. Solution I, in the presence of 10 equiv. Et_3N in methanol, was mixed with 10-40 equiv. H_2O_2 and the resulting UV/Vis trace of the reaction was fitted to a first-order model. Statistics were used to determine if the rate of decomposition at 20°C was independent of $[H_2O_2]$.[173] Comparing the rates of reaction of **LTEA**, one-factor ANOVA showed that varying the concentration of H_2O_2 from 10 to 20 mM resulted in statistically similar means ($F_{2,12} = 0.072$,

p > 0.05) (see Note S1 for further details). The rate of decomposition was therefore considered to be independent of $[H_2O_2]$ (Figure 13).

To gain further insight into the decomposition of the hydroperoxo, a cryptand with 15 deuterium atoms was synthesized. The hydrogens replaced C–H bond that are the most sensitive to oxidation, namely the methyl groups and the benzylic positions (Scheme 13). ESI-MS analysis showed that 87% of the product had incorporated 15 deuterium atoms. A complex with **LTEA^{D}** was formed and examined under the same conditions as **LTEA**. No KIE was observed for the formation of the slower intermediate. From the decomposition profiles at several $[H_2O_2]$, a KIE was averaged to be 1.5 ± 0.1 (Figure 13, Table S1). This value is much lower than the one measured in DβH (k_H/k_D = 10.6).[174]

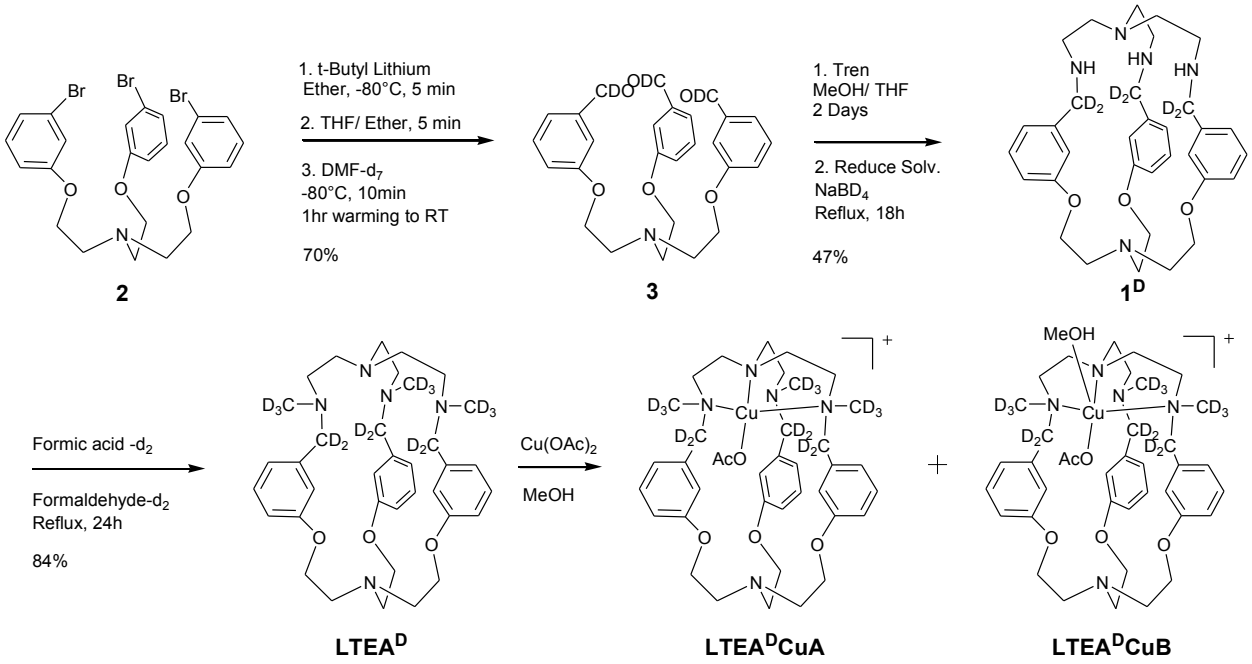

Scheme 13. Synthesis of the **LTEA^{D}** and its copper(II) acetate complexes **LTEA^{D}**CuA and **LTEA^{D}**CuB

Few KIEs have been reported for the decomposition of synthetic copper(II)-hydroperoxo intermediates. An oxidative N-dealkylation proceeded via a rate-limiting C–H abstraction (k_H/k_D = 2.3).[52] An aromatic C–H bond hydroxylation proceeded via an Cu(II)-alkylperoxo intermediate with a rate-limiting electrophilic aromatic substitution and an inverse KIE (k_H/k_D = 0.9).[48] In our case, the aliphatic C–H bonds are involved in the decomposition of the hydroperoxo intermediate, but the low magnitude of the KIE indicates a limited influence on the rate-determining step.

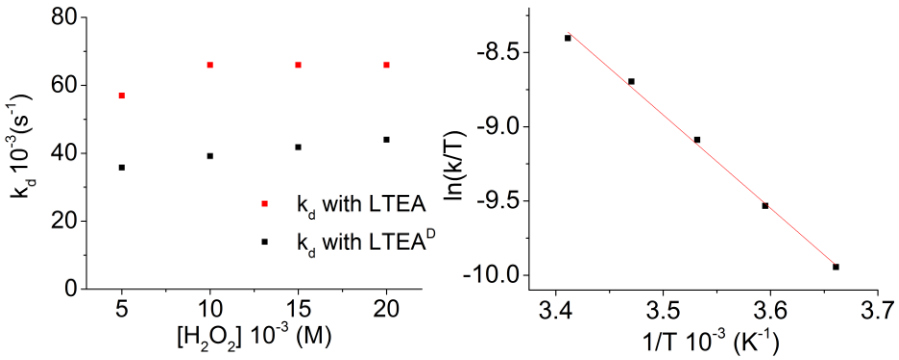

Figure 13. Left: Plot of the first order rate of decomposition of (black) [**LTEA**CuOOH]$^+$ and (red) [**LTEA**^{D}CuOOH]$^+$ versus $[H_2O_2]$ Average KIE was 1.5 ± 0.1 Right: Eyring plot for the first-order rate constants of decomposition measured at 0, 5, 10, 15 and 20 °C: 1.29 x 10^{-2}, 2.01 x 10^{-2}, 3.20 x 10^{-2}, 4.23 x 10^{-2}, 6.59 x 10^{-2} s^{-1}, respectively (standard deviation from fitting within 1.1 to 6.9 %).

Table 5. Activation parameters for intramolecular decomposition and natural decay pathways.

Intermediate	Decomposition Reaction	$\Delta H^{\ddagger}$ (kJ mol^{-1})	$\Delta S^{\ddagger}$ (J K^{-1} mol^{-1})	ref
Bis (μ-oxo), Peroxo[1]	Intramolecular N-dealkylation	52 to 63	–23 to –100	[16]
Bis (μ-oxo), Peroxo[1]	Intramolecular Benzylic hydroxylation	28 to 42	–62 to –155	[16]
CuOOH[2]	Natural decay	43	–119	[50]
CuOOR[3]	Intramolecular Aromatic Hydroxylation	24	–162	[48]
CuOOH[4]	Intramolecular Oxidation	51	–94	This work

[1]Several ligand systems used, [2]N,N-bis(2-pyridylmethyl)bis(2-pyridyl)methylamine), [3]N,N-di(2-pyridylmethyl)benzylamine, [4]**LTEA**

The rate of decomposition of the **LTEA**-based solution I was measured at different temperatures for an Eyring analysis (Figure 13). The activation parameters, $\Delta H^{\ddagger}$ = 51 kJ mol^{-1} and $\Delta S^{\ddagger}$ = –94 J K^{-1} mol^{-1}, are similar to those reported for the decomposition of Cu(II)-OOR (R = H or alkyl) and intramolecular C–H bond hydroxylation with bis(μ-oxo) and peroxo species (Table 5).[16,48,50] The negative sign of $\Delta S^{\ddagger}$ suggests that the transition state is constrained, consistent with an intramolecular decomposition pathway. The magnitude of the $\Delta S^{\ddagger}$ suggests significant structural changes during decomposition, consistent with EPR data showing a decrease in Cu geometric distortion in the decomposition products **LTEA**-CuE and **LTEA**-CuF compared with hydroperoxo intermediates **LTEA**-CuC and **LTEA**-CuD. Alternatively, a solvent molecule (MeOH) or anion may be associating to the complex upon decomposition. $\Delta S^{\ddagger}$ is, however, less

negative in comparison to the reported decomposition of Cu(II)–OOH/OOR species (Table 5).[16] This is consistent with a significant degree of preorganization of the cryptand-based system.

3.3.2.4 Analysis of the Oxidation Products

Intramolecular oxidation on a macrocycle or a cryptands offers a unique perspective on the reactivity of Cu/O_2 intermediates in that the products of the oxidation remain tethered to the scaffold. CSI-MS was used to monitor the oxidation in a similar manner to our previous ESI-MS procedure.[170] The softer CSI ionization technique and lower temperature resulted in cleaner spectra with fewer ions from side-reactions and/or fragments (Figure 14). The spectra (A to D) were dominated by the peaks for [**LTEA**CuOAc]$^+$ and [**LTEA**+O CuOAc]$^+$. In spectrum B, the peak at *m*/*z*= 697.3264 was found within 0.7 ppm of the exact mass of the formula $C_{36}H_{52}N_5O_5Cu$, which could represent either [**LTEA**CuOOH]$^+$ or [**LTEA**+O CuOH]$^+$, the latter being more likely given the time and temperature of mixing before injection. Over time, the signal for the monooxygenated complex (*m*/*z* = 739) increased in intensity (Figure 14, B to D). Minimal over-oxidation was observed.

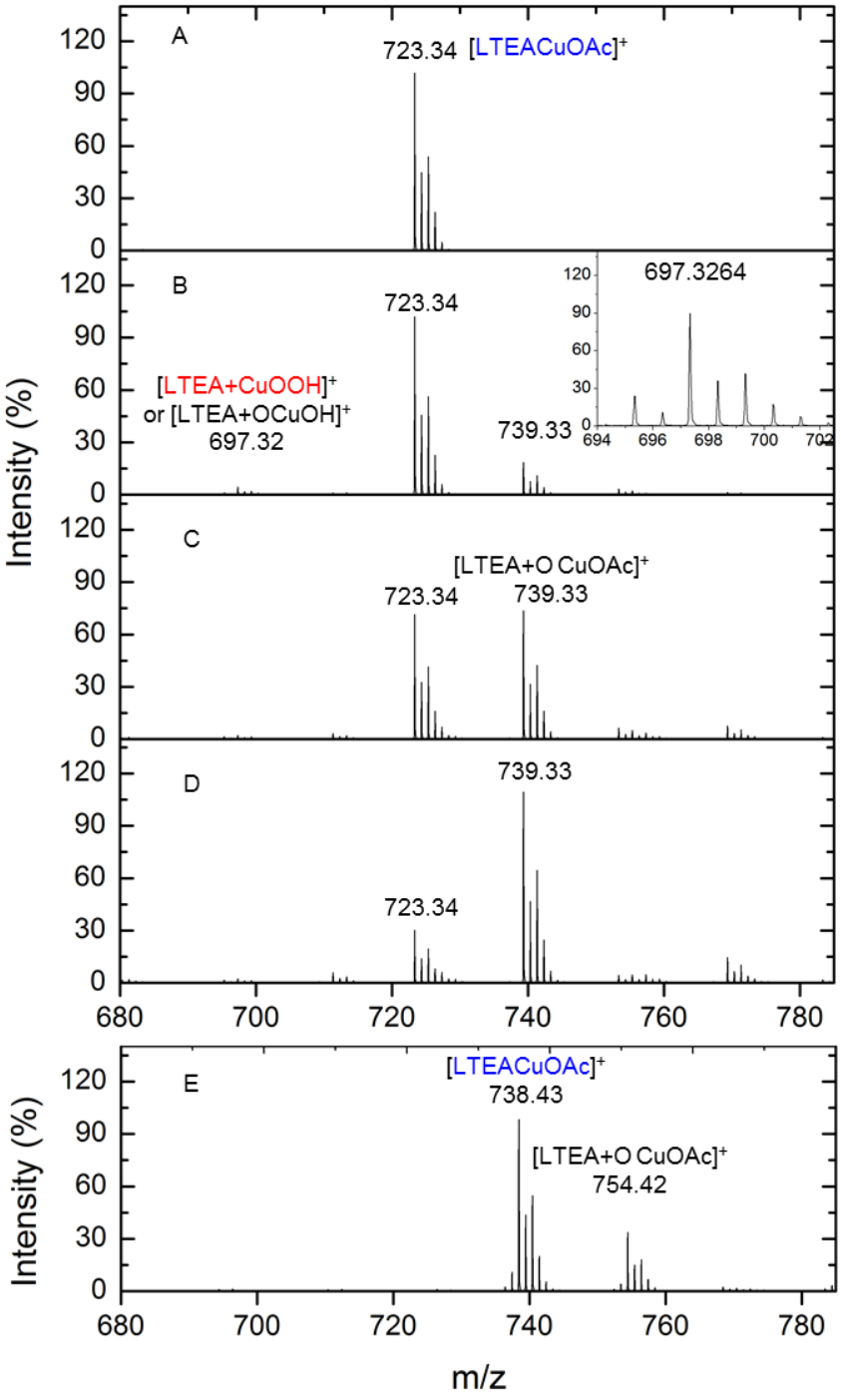

Figure 14. CSI-MS of solution I and 5 equiv. H_2O_2/Et_3N mixed with a continuous-flow method at RT. The spectra were recorded with **LTEA** at (A) 0 s, (B) 60 s with inset showing zoom of 697, (C) 270 s and (D) 540 s and with **LTEA^D** at (E) 270 s.

The CSI-MS experiment using deuterated ligand, **LTEA^{D}**, provided some of the most telling data in terms of reactivity (Figure 14, E). The *m/z* peaks seen in the reaction of both [**LTEA**CuOAc]$^{+}$ and [**LTEA^{D}**CuOAc]$^{+}$ differ by the number of deuterium atoms (15 units). This suggests that both complexes react in a similar fashion and that deuteration of the ligand has not affected the reaction pathway. Importantly, the major oxygenated product has conserved all of the deuterium atoms throughout the course of the reaction. This suggests that all C–D bonds remain intact during the major reaction pathway. This finding contradicts the previously proposed mechanism where the distal OH of the coordinated hydroperoxo unit abstracts a deuterium atom from the benzylic position of the ligand and leaves as a water molecule (Scheme S1). The final oxygenated product would thus have exchanged a deuterium for a hydrogen atom.[170] MS analysis of the organic matter after demetallation confirmed that all deuterium atoms were conserved in the oxygenated product (**LTEA**+O) (Figure 15).

The mass recovery, following demetallation, was analyzed using both EDTA and NH_4OH as demetallating agents and the products from both procedures were analyzed with ESI-MS and ^{1}H-NMR. Using NH_4OH to demetallate resulted in a mass recovery greater than 90 %. The organic products, identified by ESI-MS, were the starting ligand (**LTEA**), ligand with one additional oxygen atom (**LTEA**+O) and a very small amount of over oxidized product (**LTEA**+2O-2H) (Figure 15). The ^{1}H-NMR spectrum had only a small amount of an aldehyde signal indicating that the major product of the reaction, **LTEA**+O, was not an aldehyde as originally proposed (Scheme S1).[170] Alternatively, a solution of $EDTA_{(aq)}$ was used to wash the products with the organic matter extracted into dichloromethane. Surprisingly, this procedure resulted in less than five percent mass recovery, indicating that the bulk of the organic product remained in the water phase. The products recovered following EDTA demetallation were identified by ESI-MS as the starting ligand (**LTEA**) and the over-oxidized product (**LTEA**+2O-2H) (Figure S4, B). The ^{1}H-NMR spectrum of this solution contained a strong signal for an aldehydic proton, indicating that the over-oxidized product had the aldehyde function. In addition, the major change in the ^{1}H-NMR upon D/H substitution of the ligand was the disappearance of the aldehyde signal in the deuterated sample, indicating over-oxidation at the benzylic position.

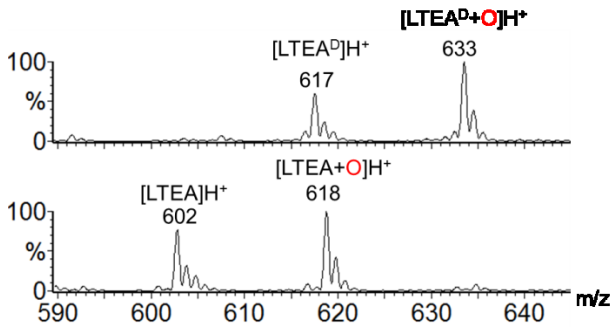

Figure 15. ESI-MS of the organic products after reaction with 5 equiv. H_2O_2/Et_3N and demetallation with NH_4OH. Top: **LTEA**^{D}, Bottom: **LTEA**.

3.4 Discussion

The analysis of EPR, stopped-flow UV/Vis and mass spectrometry, using both the deuterated and non-deuterated cryptand leads us to propose the formation of a mixture of two hydroperoxo intermediates that decompose via an oxygen-atom transfer reaction and not the hypothesized C–H bond abstraction pathway.

The mechanism for the formation of the hydroperoxo intermediates is complex and warrants speculation. It is likely that the two starting Cu(II) species (A and B) undergo separate fast and slow reactions, in parallel, to form the two hydroperoxo intermediates. This is supported by the fact that the EPR spectra of the intermediates show two new complexes in solution during acquisition, and both fast and slow rates of formation are dependent on [H_2O_2]. Although a sequential mechanism involving **LTEA**-CuC → **LTEA**-CuD cannot be ruled out, the evidence argues in favour of two parallel reactions.

Common intramolecular decomposition pathways for Cu(II)-hydroperoxo intermediates are N-dealkylation, benzylic hydroxylation and aromatic hydroxylation, all of which involve oxidation at a C–H bond.[44,47-48,51-52,167] While these reaction pathways are possible with the **LTEA**CuOOH species, the analysis (^{1}H-NMR, IR, MS) of the self-oxidation reaction suggests another pathway, namely through a nucleophilic attack of the uncoordinated tertiary amine (N4) of Tren on the hydroperoxo intermediates, causing cleavage of the OOH moiety and formation of an N-oxide (Scheme 14). The most compelling piece of evidence is the MS data that shows conservation of ligand structure and all deuterium atoms after the self-oxidation. If oxidation at a C–H bond had occurred, at least one deuterium atom would be replaced by a hydrogen atom upon work-up or demethylation would have been observed at *m*/*z* = 588.

This is illustrated in Scheme S1 via the formation a hemiaminal function (C), and rearrangement to an aldehyde and amine as the major products (D). The ^{1}H-NMR spectrum showed only a small amount of aldehyde present in the products, confirming that this was not the major reaction pathway. Through the process of elimination, ^{1}H-NMR and MS analysis leads us to propose an OAT from the hydroperoxo to the uncoordinated amine, where the most likely possibility for **LTEA**+O formula is an N-oxide. In this case, the small observed KIE can be explained as a secondary isotope effect and suggests that the OAT takes place near a C–H(D) bond.

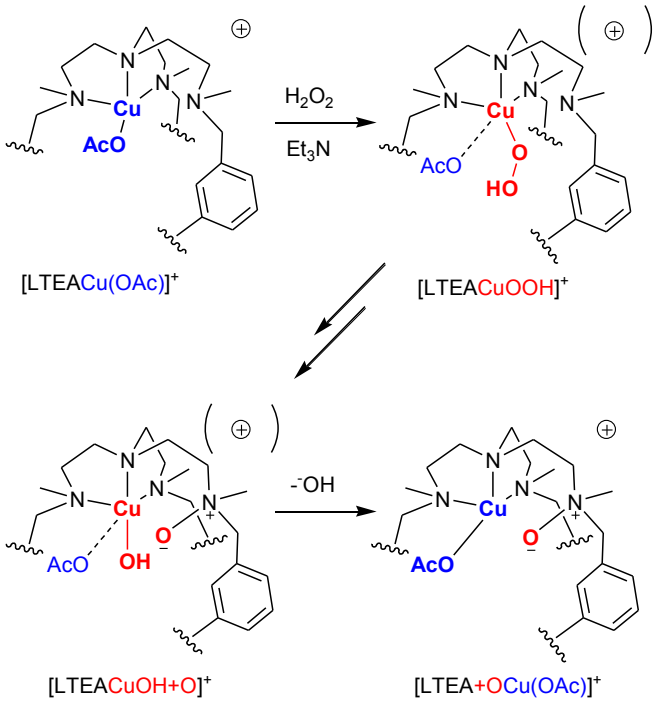

Scheme 14. Proposed mechanism for the decomposition of the hydroperoxo intermediate.

Although the formation of an N-oxide was an unexpected outcome, this type of reaction has been previously reported. Addition of H_2O_2 to tertiary amines in MeOH leads to the formation of N-oxides, but in low yields.[175] In our case, an outer-sphere oxidation of the aliphatic tertiary amine was ruled out with control experiments where 5 equivalents of H_2O_2/Et_3N added to **LTEA** in DCM/MeOH resulted in little to no oxidation of the ligand (< 5%). While OAT reactions from an N-oxide to a metal centre are typical,[176] the formation of metal complexes with aliphatic N-oxides, as seen with [**LTEA**+O CuOAc]$^{+}$, are quite rare.[81,175] Two examples of metal-promoted formation of an N-oxide on a ligand, one involving a Cu(I) complex reacting with dioxygen[177] and the other via the reaction of an Fe(III) complex with *t*BuOOH[81]

support the proposed mechanism of OAT from the hydroperoxo intermediate to the uncoordinated tertiary amine of the cryptand.

3.4.1.1 Second Coordination Sphere Effects

The supramolecular/rigid nature of the ligand has a pronounced effect on the reactivity of the Cu(II)-hydroperoxo species. *N*-Methylation imposes additional constraints in cryptands and prevent metal centres from adopting C_3 symmetry.[178] The geometries of **LTEA**-CuA and **LTEA**-CuB were identified as square-planar and square-pyramidal, respectively. In comparison, copper(II) complexes of Me_6Tren, a ligand with the same donor set but free from the restrictions of macrocycles, were trigonal-bipyramidal in solution state.[125-126,153] Masuda et al. proposed that the reactivity of a hydroperoxo intermediate is greatly influenced by the geometry of the metal centre; specifically that square-planar complexes have higher reactivity than trigonal-bipyramidal complexes.[45] With the Me_6Tren ligand, the Cu(II)-hydroperoxo undergoes neither intra- nor inter-molecular oxidations,[153] whereas Cu(II)-hydroperoxo complexes of the **LTEA** cryptand do show intramolecular reactivity. The difference can be explained in part by the rigidity of the cryptand enforcing the more reactive geometry.

LTEA has five tertiary amines available, yet the major product of the reaction is a singly oxygenated amine. There are several examples of copper complexes with ligands bearing tertiary amines that have been reacted with H_2O_2 in the presence of a base and have preferentially undergone C–H bond oxidation rather than formation of N-oxides.[44,47,52] The major difference between those ligands and the cryptand, **LTEA**, is the steric constraint that the cryptand enforces, likely positioning the tertiary amine for reactivity. The involvement of C–H bonds in the oxygen-atom transfer, observed as the small KIE, is a testament to the degree of control. By enforcing the geometry of the metal centre and positioning of the site of oxidation, the cryptand controls the reactivity of the hydroperoxo intermediate through second coordination sphere features.

3.5 Conclusions

The goal of the research was to explore the second coordination sphere effects of a coordinating cryptand on the reactivity of a hydroperoxo intermediate. In this context, the formation and decomposition of a hydroperoxo intermediate have been studied. Two copper complexes were identified in solution and when reacted with hydrogen peroxide formed two hydroperoxo

intermediates. The intermediates decomposed into one major copper complex. A deuterated cryptand was used to evaluate the decomposition pathway and help decipher the mechanism. It was found that upon decomposition and demetallation, there was no loss of deuterium atoms despite oxidation of the ligand. This evaluation led to an uncommon decomposition pathway for a Cu(II)-hydroperoxo intermediate, whereby an N-oxide was formed instead of C–H bond oxidation products. Mononuclear metallo-enzymes create protective pockets to specifically position the metal, oxidant and substrate to react cohesively. Although this level of control is currently out of reach in model systems, the present study shows that the semi-rigidity of cryptands can be used to control the reactivity of a mononuclear centre towards oxygen-atom transfer rather than hydrogen abstraction.

3.6 Experimental

Materials: All materials were used as received from Alfa Aesar and Sigma Aldrich. NMR spectroscopic measurements were made at 22 °C in a 5 mm tube on a Varian Innova 300 or 500 MHz instrument and referenced to internal tetramethylsilane. Electrospray ionization mass-spectrometry (ESI-MS) measurements were performed via direct injection on a Micromass Quattro LC or Micromass Q-TOF at Concordia's Centre for Biological Applications of Mass Spectrometry. Cryospray ionization MS (CSI-MS) data were acquired with a Bruker CSI Q-TOF at the Université de Montréal. The *m/z* data reported are based on ^{1}H, ^{12}C, ^{14}N, ^{16}O, and ^{63}Cu.

Synthesis of 2, Tris[2-(3-bromobenzene)-oxo]ethyl]amine: This synthesis was adapted from literature procedures.[118,179] To a solution of 3-bromophenol (1.52 g, 14.4 mmol) in 1-propanol (100 mL) was added crushed NaOH (0.6 g, 15 mmol). Solid tris(2-chloroethyl)amine (1 g, 4.8 mmol) was added to the solution. The reaction was heated at 110 °C for 4 h. After cooling, H_2O (50 mL) was added and the organic products were extracted with CH_2Cl_2 (3 x 30 mL). The combined extracts were concentrated under reduced pressure. The product was purified by flash chromatography with solid loading and a 40 g silica ReadiSep Gold column on an automated Combiflash (Teledyne Isco). The product was eluted with CH_2Cl_2 and the by-products were eluted with gradient from 0 to 100 % MeOH. The first fraction was collected and the solvent was removed under reduced pressure to afford 1.35 g (75 %) of a colourless oil. ^{1}H-NMR (500 MHz, $CDCl_3$): δ = 3.12 (t, 6H, J = 5, CH_2), 4.057 (t, 6H, J = 5, CH_2), 6.79 (m, 3H, Ar_2), 7.02 (m, 3H, Ar), 7.06 (m, 3H, Ar), 7.11 (m, 3H, Ar) ppm.

Synthesis of 3, Tris[2-(3-benzaldehyde-α-d_1)oxo]ethyl]amine: This reaction was carried out under inert conditions (nitrogen atmosphere, dry solvents). To a Schlenk flask containing distilled tetramethylethylenediamine (2.21 mL, 14.79 mmol) in diethyl ether (50 mL) was added **2** (1.345 g, 2.1 mmol). After cooling the solution to -78 °C, *t*BuLi (8.7 mL of a 1.7 M in pentane, 14.79 mmol) was cautiously added. The reaction was stirred for 10 minutes with a yellow precipitate forming. THF (15 mL) was added to the solution, which was stirred for an additional 5 min. DMF-d_7 (1.2 mL, 15.75 mmol) was then added and the reaction was allowed to warm to RT at which stage it was opened to the air. $NH_4Cl_{(sat)}$ (30 mL) was added and the organic products were extracted with CH_2Cl_2 (3 x 20 mL). The combined extracts were concentrated under reduced pressure. The product was purified with column chromatography using EtOAc/Hexane gradient elution from 20/80 to 50/50 on silica. The third fraction was collected and the solvent was removed under reduced pressure to afford 696 mg (71 %) of a colourless oil. ^{1}H-NMR (500 MHz, $CDCl_3$): δ = 3.2 (t, 6H, J = 6, CH_2), 4.15 (t, 6H, J = 6, CH_2), 7.12 (m, 3H, Ar_2), 7.35 (m, 3H, Ar), 7.42 (s, 3H, Ar), 7.45 (m, 3H, Ar) ppm.

Synthesis of 1^D: The following procedure was adapted from previously published work.[118] To a vigorously stirring solution of **3** (696 mg, 1.5 mmol) in 500 mL THF:MeOH (1:10) was added tris(2-aminoethyl)amine (220 µL, 1.5 mmol) in 50 mL methanol via syringe pump over 5 hours. The reaction was left to stir at 25 °C for 48 h. The solvent was reduced to 50 mL and $NaBD_4$ (313 mg, 7.5 mmol) was added slowly. The reaction was stirred at 25 °C for 30 min then refluxed for 48 h. The solvent was removed under reduced pressure. The resulting precipitate was washed with acetonitrile and dried under vacuum to give 400 mg (47 %) of a white powder. ^{1}H-NMR (500 MHz, $CDCl_3$): δ = 1.51 (s, 3H, NH), 2.58 (m, 12H, CH_2), 3.02 (t, 6H, J = 5, CH_2), 3.96 (t, 6H, J = 5, CH_2), 6.48 (s, 3H, Ar), 6.705 (m, 3H, Ar), 6.855 (m, 3H, Ar), 7.14 (m, 3H, Ar) ppm. ^{13}C-NMR (500 MHz, $CDCl_3$): δ 47.86 (CH_2), 55.78 (CH_2), 56.22 (CH_2), 67.77 (CH_2), 77.21 (CH_2), 112.85 (Ar), 114.36 (Ar), 120.48 (Ar), 128.98 (Ar), 142.09 (Ar), 159.42 (Ar). The signal-to-noise ratio was too low to see the ^{13}C signal of the CD_2 groups.

Synthesis of $LTEA^D$: Formic acid-d_2 (429 µL, 8.5 mmol) and formaldehyde-d_2 (1.336 mL, 8.5 mmol) were added to **3** (400 mg, 708 µmol). The solution was refluxed for 24 h, then cooled and poured onto chilled aqueous NaOH (30 mL, 2 M). The product was extracted with dichloromethane (3 x 20 mL) and the organic phase extracts were dried with anhydrous Na_2SO_4. The solvent was removed under reduced pressure, yielding a precipitate that was suspended in acetonitrile. Filtration, washing with acetonitrile and drying under vacuum afforded 370 mg (84 %) of a white crystalline powder. A suitable crystal for X-

ray crystallography was chosen and shows same unit cell as **LTEA**: *a* 13.2, *b* 13.5, *c* 18.5 [Å], α 90, β 90, γ 90 [°].[170] ^{1}H-NMR (500 MHz, $CDCl_3$): δ = 2.33 (t, 6H, J = 7, CH_2), 2.60 (t, 6H, J = 7, CH_2), 3.06 (t, 6H, J = 6, CH_2), 4.02 (t, 6H, J = 6, CH_2), 6.68 (m, 3H, Ar), 6.755 (m, 3H, Ar), 7.05 (s, 3H, Ar), 7.11 (m, 3H, Ar) ppm. ^{13}C-NMR (500 MHz, $CDCl_3$): δ 52.26 (CH_2), 54.12 (CH_2), 57.23 (CH_2), 68.75 (CH_2), 114.50 (Ar), 114.56 (Ar), 121.36 (Ar), 128.77 (Ar), 140.64 (Ar), 159.23 (Ar). The signal-to-noise ratio was too low to see the ^{13}C signal of the CD_2 and CD_3 groups. MS (ESI, 1:1 CH_3OH:CH_2Cl_2): *m/z* = 617 (87 % incorporation of 15 D), 616 (9 % incorporation of 14 D), 615 (3 % incorporation of 13 D) $[M+H]^+$.

Synthesis of LTEA and [LTEACu(OAc)(MeOH)](SbF$_6$): The syntheses of **LTEA** and [**LTEA**Cu(OAc)(MeOH)](SbF_6) were previously reported.[170] An alternative crystallization method is described here: to solution I (see below) was added 1 equiv. of solid $KSbF_6$ (9.20 mg, 50 µmol) or $NaSbF_6$. The solution was stirred for 20 min and then left to slowly evaporate over 48 h to give dark blue crystals. The crystals were washed with cold methanol and air-dried to give 37 mg of [**LTEA**Cu(OAc)(MeOH)](SbF_6), 73 % yield.

Synthesis of [LTEACu(OAc)](OAc) and [LTEACu(OAc)(MeOH)](OAc): Solution I: To **LTEA** (30 mg, 50 µmol) dissolved in 200 µL of dichloromethane was added $Cu(OAc)_2{\cdot}H_2O$ (10 mg, 50 µmol) dissolved in 800 µL of methanol. After 5 minutes of stirring, the solvent was removed under reduced pressure and 1 mL of methanol was added to dissolve the complex. The final volume of methanol was varied depending on the desired concentration.

Solution II: Crystals of [**LTEA**Cu(OAc)(MeOH)](SbF_6) (10 mg, 10 µmol) were added to methanol and stirred with reflux with for 0.5 h. The volume of methanol was varied depending on desired concentration.

Solution III: To **LTEA** (30 mg, 50 µmol) dissolved in 1 mL of dichloromethane was added $Cu(OAc)_2{\cdot}H_2O$ (10 mg, 50 µmol). The solution was stirred for 4 h and then used as is. The final volume of dichloromethane was varied depending on the desired concentration.

Solution IV: Crystals of [**LTEA**Cu(OAc)(MeOH)](SbF_6) (10 mg, 10 µmol) were added to dichloromethane and stirred for 10 min. The volume of dichloromethane was varied depending on desired concentration.

Synthesis of [LTEA^{D}Cu(OAc)](OAc), [LTEA^{D}Cu(OAc)(MeOH)](OAc) and [LTEA^{D}Cu(OAc)(MeOH)](SbF$_6$): To **LTEA^D** (31 mg, 50 µmol) dissolved in 200 µL of dichloromethane was added $Cu(OAc)_2{\cdot}H_2O$ (10 mg, 50

μmol) dissolved in 800 μL of methanol. The complex could be crystallized with 1 equivalent of $KSbF_6$ followed by slow evaporation.[170] The procedure for solution I-IV was used to prepare the sample. Formation was evidenced by a single ESI-MS signal: accurate mass = 738.4334, exact mass = 738.43569, mass accuracy = 3.1 ppm.

EPR Measurements: X-band EPR spectra were collected on a Bruker EMX Plus spectrometer controlled with Xenon software and equipped with a Bruker teslameter. A Bruker nitrogen-flow cryostat connected to a high-sensitivity resonant cavity was used for 100 K measurements. Samples of 400 μL of 0.5 mM solutions were frozen in liquid nitrogen. The spectra were fit with Easyspin Fitting software.[135]

Kinetic Measurements: Kinetic studies of the reaction of H_2O_2/Et_3N with solution I were recorded on a BioLogic low-temperature stopped-flow unit (Claix, France) equipped with a J&M TIDAS diode-array spectrophotometer (J&M, Aalen, Germany). Solutions after mixing were 0.5 mM with respect to Cu in 184 μL of methanol. All concentrations are reported as in-cell, after dilution. The concentration of H_2O_2 was varied from 5 to 30 mM with Et_3N held at 5 mM. The reaction was studied at temperatures between 20 and -50 °C. Spectra (330-1025 nm) were collected and analyzed with a global analysis fitting routine using the program Reactlab kinetics (Jplus Consulting, Palmyra, Australia).

Oxidation Reaction with H_2O_2/Et_3N: This procedure has been previously reported.[57,170]

Demetallation Studies: With NH_4OH: Solution I was reacted with 5 equiv. of H_2O_2/Et_3N and allowed to decompose (heat or time). NH_4OH (2 mL) was added and the solution was filtered over alumina in a Pasteur pipet. The alumina was rinsed with MeOH (10 mL) followed by CH_2Cl_2 (20 mL). The filtrate was washed with water (3 x 10 mL) and dried over Na_2SO_4. The solvent was removed under reduced pressure. Mass recovery: 31 mg, (103 w%) of **LTEA**, **LTEA**+O and **LTEA**+2O-2H, minor products.

With EDTA: Solution I was reacted with 5 equiv. of H_2O_2/Et_3N and allowed to decompose (heat or time). Solid Na_2EDTA (100 mg) was added and the solution was stirred for 5 min. The solution was then filtered over a pipet-full of alumina, which was rinsed with MeOH and CH_2Cl_2 as above. The filtrate was washed with water (3 x 10 mL) and dried over Na_2SO_4. Mass recovery: 28 mg, (93 w%) of **LTEA**, **LTEA**+O and **LTEA**+2O-2H, minor products.

Alternatively, after the reaction of solution I with 5 equiv. of H_2O_2/Et_3N, $Na_2EDTA_{(aq)}$ (30 mL, 0.1 M) was added and the solution was left to stir for 5 min. **LTEA** and the over-oxidized product were extracted

with 3 x 10 mL of CH_2Cl_2, dried over Na_2SO_4 and the solvent was removed under reduced pressure. Mass recovery: 1 mg (3 w%) of **LTEA** and **LTEA**+2O-2H and minor products.

3.7 Acknowledgements

This work has been supported by Fonds de Recherche du Québec - Nature et les Technologies (FRQNT) and the Natural Sciences and Engineering Research Council of Canada (NSERC). L.C. acknowledges Concordia University for the Mobility Award and FRQNT for the Bourse de Stage International: Centre in Green Chemistry and Catalysis. We would like to thank Dr. Garry Hanan (Université de Montréal) for access to the CSI-MS and Dr. Jingwei Luo (Universtiy of Victoria) for training on the CSI-MS. We are grateful to Dr. Andrey Moiseev and Dr. Scott Bohle (McGill University) for preliminary EPR measurements.

Chapter 4: Bio-Inspired Oxidation Chemistry of a Cu(II)-Fluoride Cryptate with C_3-Symmetry

L. Chaloner[a] and X. Ottenwaelder*[a]

[a] Department of Chemistry and Biochemistry, Concordia University, 7141 Sherbrooke Street West, Montreal, H4B 1R6, Canada.

4.1 Abstract

Three copper complexes with an *N*-methylated cryptand bearing a tris(2-aminoethylamine) moiety have been synthesized and compared. Two copper(II)-chloride complexes, [**LTEA**CuCl](SbF_6)(MeOH) and [**LTEA**$CuCl_2$](MeCN) were characterized in solution and solid state by UV/Vis and X-ray crystallography. Both had square-based geometries with C_1-symmetry with no encapsulation. A Cu(II)-fluoride complex, in which the ligand is protonated, [**LTEA**HCuF]$(BF_4)_2(MeCN)_{0.5}$, adopted C_3-symmetry with complete encapsulation as characterized by UV/Vis, EPR and X-ray crystallography. Reactivity of the complexes with H_2O_2/Et_3N was explored using UV/Vis and CSI-MS. Only the fluoride complex was found to form a Cu(II)-hydroperoxo intermediate.

4.2 Introduction

Biomimetic studies of Cu-F bonds are important because of the ability of fluoride ions to inhibit oxidative metallo-enzyme activity.[180] Tyrosinase, an ubiquitous oxygenase enzyme, is competitively inhibited by fluoride ions that coordinate to the dinuclear copper(II) active sites. The inhibition is regulated by physiological conditions (low pH) and conformational changes in the protein backbone.[17] Synthetically, cryptands are useful in studying highly reactive biomimetic intermediates because they have the ability to protect the metal centre through second coordination sphere features while simplifying the overall chemistry and reaction products.[110,170] We have applied this concept to the characterization of Cu-based oxidative reactions within coordinating cryptands. Herein, we provide the first study that explores the biomimetic relationship between Cu-F cryptates and the formation of Cu/O_2 intermediates.

Tren (tris-(2-aminoethyl)amine)-based coordinating cryptands are popular because of their high yielding syntheses when condensing with tris-aldehydes and because of their ability to form well-defined complexes with transition metals.[179,181-182] They have been used in applications such as ion

sequestering and sensing[114-115,183] and host-guest chemistry.[184] They are limited in the area of biomimetic oxidation chemistry because in the presence of metals, the secondary amines are easily oxidized to form imines complicating the reactions with several by-products.[111,185] *N*-Methylation is an easy solution to reduce side reactions under oxidative conditions but the additional steric constraint on the cryptand has been shown to prevent encapsulation of transition metals with anionic hosts,[123,178] with encapsulation defined here as coordination of the 5 donor atoms of Tren. Using cryptand, **LTEA** (Figure 16), we here present Cu(II)-halide cryptates and their reactivity with H_2O_2/Et_3N.

4.3 Results and Discussion

A protonated copper(II) fluoride complex is formed by mixing copper(II)-tetrafluoroborate with **LTEA** in acetonitrile followed by slow diffusion in ether. ESI-MS reveals that the complex has acquired a fluoride ion from the BF_4^- anion, a well-documented phenomenon.[186] The X-ray structure of [**LTEA**HCuF]$(BF_4)_2(MeCN)_{0.5}$ reveals that the copper centre is entirely encapsulated by the cryptand despite *N*-methylation of the Tren moiety (Figure 16). The overall C_3 symmetry of the complex is driven by intramolecular hydrogen bonding. A trifurcate hydrogen bond between the protonated amine and the electronegative oxygen atoms is observed at the base of the tris(ethanolamine) moiety (O···H = 2.17-2.38 Å, r_{vdW}: H, 1.20 O, 1.52 Å). The metal centre has trigonal-bipyramidal geometry with a fluoride ion in the axial positions (τ = 0.98).[187] The electronegative fluoride is stabilized by weak but significant hydrogen bonds with the aromatic rings of the ligand (H···F = 2.188-2.228 Å, r_{vdW}: H, 1.20 F, 1.47 Å). The three aromatic rings are all slightly rotated, creating C-H···F angles from 130 to 136° (Table S2). The Cu(II)-F bond is among the shortest ever reported at 1.824(1) Å, with the ten shortest bonds ranging from 1.821 to 1.878 Å.[188]

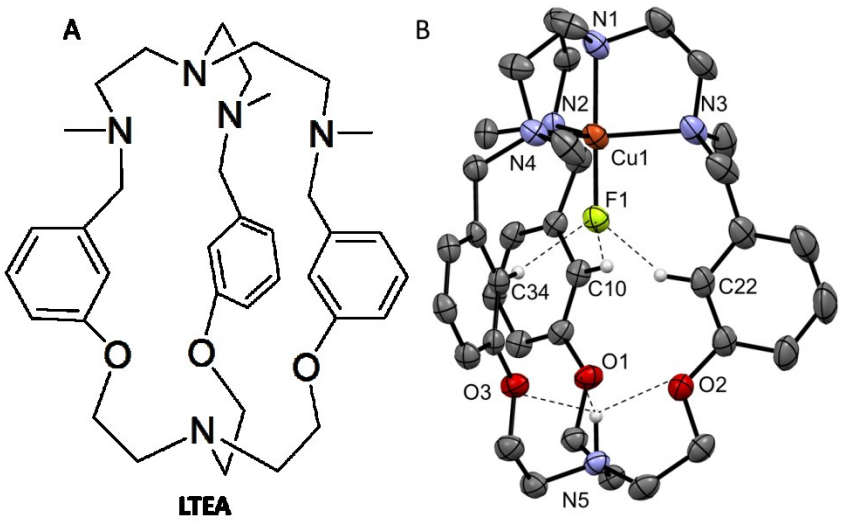

Figure 16. A) Cryptand **LTEA** B) ORTEP representation at 50% thermal ellipsoid probability of [**LTEA**HCuF]$(BF_4)_2(MeCN)_{0.5}$. Hydrogen atoms, non-coordinating anions and solvent molecules have been omitted for clarity except for H5N, H10, H22 and H34.

In parallel to the encapsulated Cu(II)-fluoride complex, we isolated two Cu(II)-chloride complexes, [**LTEA**CuCl](SbF_6)(MeOH) and [**LTEA**$CuCl_2$](MeCN), which, however, do not adopt an overall C_3 symmetry (Figure 17). The Cu(II) ion of [**LTEA**CuCl](SbF_6)(MeOH) has a distorted square-planar geometry (τ = 40%) and [**LTEA**$CuCl_2$](MeCN) has a square-pyramidal geometry (τ = 13%). In both complexes, three of the equatorial positions are occupied by amines from the Tren moiety (N1, N2 and N3) and the fourth equatorial position is occupied by a chloride ion (Cl1). The fourth nitrogen (N4) in the Tren moiety and is completely uncoordinated. [**LTEA**$CuCl_2$](MeCN) is distinguished by a second chloride ion (Cl2) in the axial position with the copper ion lying slightly above the N1, N2, N3, Cl1 plane, displaced towards Cl2. These *N*-Methylated cryptands are not encapsulating because of the steric influence of the methyl groups and the increased rigidity of the cryptand.[178] If the macrobicyclic tension of the cryptand is removed, the metal centre adopts a TBP geometry, as observed Suzuki and coworkers in the Cu(II)-chloride complex with tris(*N*-benzyl-*N*-methylaminoethyl)amine.[189] Alternatively, removing the methyl groups from the cryptand, as studied by Bharadwaj and Chand, allows for encapsulation of a Cu(II)-X metal centre (X = N_3^-, CN^-, SCN^-) in TBP geometry.[118,190] The two copper chloride structures in this work show that the steric influence from the cryptand and methyl groups prevent encapsulation of the metal-chloride centre and that [**LTEA**HCuF]$(BF_4)_2$ is a truly unique with its C_3 symmetry.

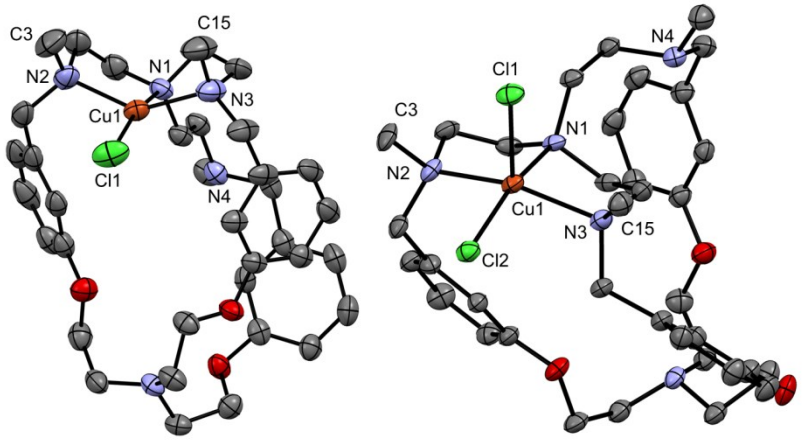

Figure 17. ORTEP representation at 50% thermal ellipsoid probability of [**LTEA**CuCl](SbF$_6$)(MeOH) (left) and [**LTEA**CuCl$_2$](MeCN) (right). Hydrogen atoms, non-coordinating anions and solvent molecules have been omitted for clarity.

Solution studies were carried out to confirm the conservation of the solid-state geometry in solution. The UV/Vis spectrum of [**LTEA**HCuF](BF$_4$)$_2$ in MeCN has d→d transitions at 690 nm (ε = 180 M^{-1} cm^{-1}) and 860 nm (ε = 168 M^{-1} cm^{-1}) that are traditionally associated with TBP complexes (Figure S6, (A)).[124-126] The EPR spectrum is best fitted to a mononuclear Cu(II) complex (S = 1/2) with a d(z^2)^1 ground state where $g_{\|}$ = 2.065, $A_{\|}$ = 68 G, $g_{\perp}$ = 2.221 and $A_{\perp}$ = 82 G. The ordering of $g_{\perp} > g_{\|}$ confirms the TBP geometry in solution. The UV/Vis spectra of the two chloride complexes show retention of a square-based geometry in solution, confirmed by the two characteristic transitions at 580 and 770 nm associated with square pyramidal or square-planar geometries (Figure S5).[124,127]

The geometry of [**LTEA**HCuF](BF$_4$)$_2$ is influenced by solvent and the protonation state of the cryptand. The geometry in MeCN is TBP but in methanolic solution the geometry changes with the appearance of a new transition with a maximum at 555 nm (ε = 100 M^{-1} cm^{-1}) (Figure S6, a). The complex in methanol shows a dependence on base (Et$_3$N) indicating that the cryptand is still protonated (Figure S6, b). This addition of base leads to a complex with a square-based geometry evidenced by absorption bands at 580 nm (ε = 135 M^{-1}cm^{-1}) and 672 (ε = 120 M^{-1} cm^{-1}).[124,127] The protonated cryptate can be regenerated by addition of an acid (Figure S6, C). Attempts to induce C_3 symmetry by adding acids to the chloride complexes failed and the reason is likely a combination of the increased ionic radius of the chloride ion and formation of weaker intramolecular hydrogen bonds. H···Cl bond distances are consistently 0.5 Å

longer then H···F bond distances.[191] To accommodate a chloride ion, the cryptand would have to severely expand the cavity in the equatorial direction and compress axially (increasing the CH···O bond length) and further rotate the aromatic rings (weaken the Cl···H hydrogen bond).

Bio-inspired oxidative studies were investigated by reacting the [**LTEA**$CuCl_2$] and [**LTEA**$HCuF](BF_4)_2$ complexes with H_2O_2/Et_3N at -30 °C and following with UV/Vis spectroscopy. No change was observed with [**LTEA**CuCl]Cl. When [**LTEA**$HCuF](BF_4)_2$ was reacted with H_2O_2/Et_3N, a colour change from turquoise to green was observed. A Cu(II)-hydroperoxo intermediate was identified, by the growth of a characteristic LMCT band at 388 nm (Figure 18).[56] The intermediate had the same UV/Vis spectrum as a previously characterize Cu(II)-hydroperoxo species starting from a Cu(II)-acetate complex with the **LTEA**.[170] This suggests that the two intermediates are the same, with a square-based geometry, despite different anions in the starting complexes (Chapter 3).

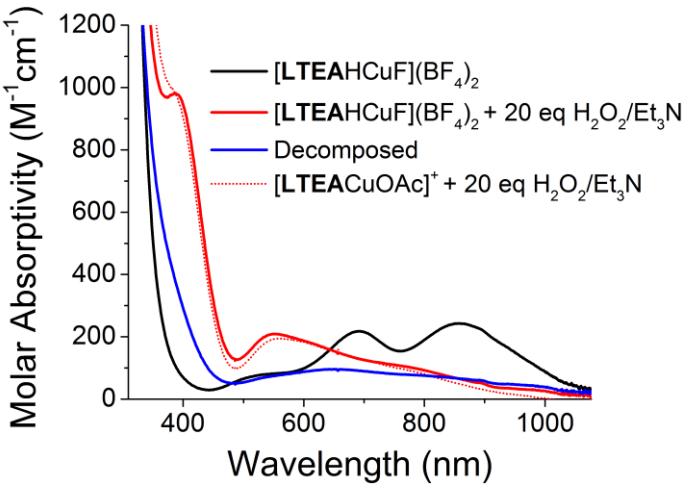

Figure 18. UV/Vis spectra of Black: 0.5 mM [**LTEA**$HCuF](BF_4)_2$ at -30°C Red: Addition of 20 eq H_2O_2/Et_3N, Blue: Decomposed after 35 min and Dotted Red: **LTEA**CuOAc + 20 eq H_2O_2/Et_3N at -30°C.[170]

The reaction of [**LTEA**$HCuF](BF_4)_2$ with 15 equiv. of H_2O_2/Et_3N was followed using a continuous-flow mixing setup directed into a CSI-MS. Before mixing, the spectrum consists mostly of [**LTEA**]H^+ (m/z = 602.40), [**LTEA**$CuF]^+$ (m/z = 683.32) and a small signal from [**LTEA**$Cu]^+$ m/z = 664.32 (Figure 19). The spectrum also contains a small amount of [**LTEA**$CuOAc]^+$ m/z = 723.33, an unavoidable contaminant. The MS after reacting with H_2O_2/Et_3N, shows the same m/z signals as the reaction starting solely from [**LTEA**$CuOAc]^+$ (with the exception of [**LTEA**$CuF]^+$ and [(**LTEA**+O) $CuF]^+$). The similarity in the two spectra further supports similar reaction pathways despite different starting complexes. The most intense signal

in the reaction of [**LTEA**CuOAc]$^+$ with H_2O_2/Et_3N is [(**LTEA**+O)CuOAc]$^+$ whereas the most intense signal from [**LTEA**HCuF]$(BF_4)_2$ with H_2O_2/Et_3N is *m/z* = 697, (identified as [(**LTEA**+O)CuOH]$^+$) and not [(**LTEA**+O)CuF]$^+$. This difference suggests a less favourable binding of the fluoride anion to the copper centre with (**LTEA+O**) compared with the acetate anion.

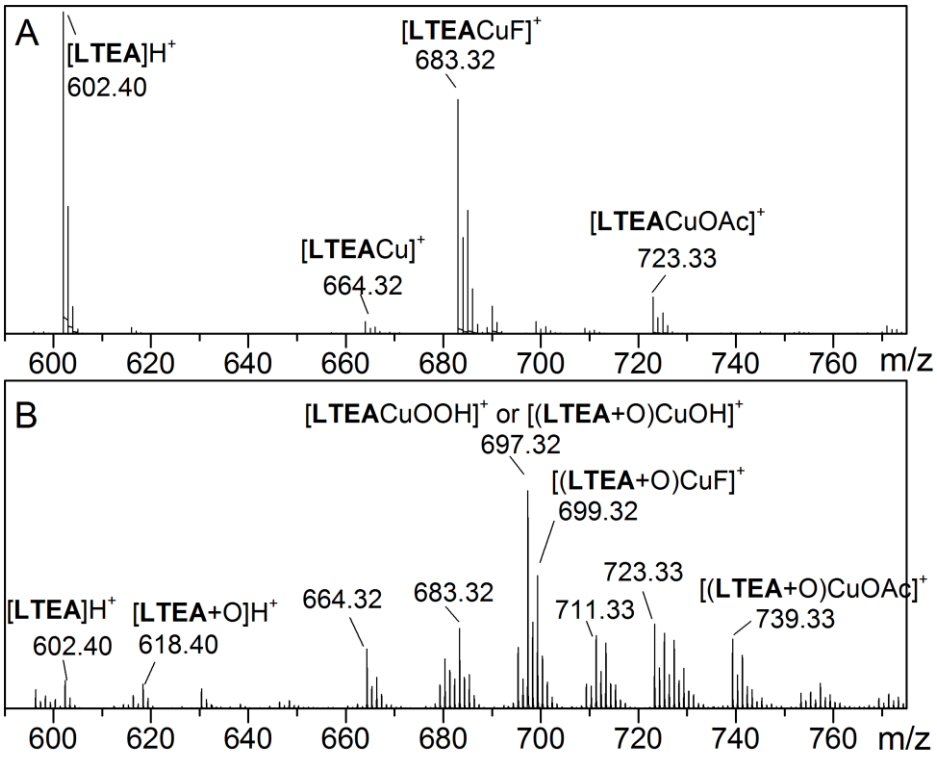

Figure 19. CSI-MS of [**LTEA**HCuF]$(BF_4)_2$ + 15 equiv. H_2O_2/Et_3N in methanol mixed with a continuous-flow methods at RT. The spectra were recorded A: before mixing and B: after mixing. Impurities from Cu(II)-acetate complexes are present.

The lack of reactivity of the chloride complex compared with the fluoride complex can be explained by the Cu-halide bond strength and hard/soft characteristics. The fluoride anion forms a weaker σ-bond with copper and has greater π-donation which has a more destabilizing effect due to the filled d orbitals of copper.[192] While the hard characteristic of the Cu(II) ion is unselective to halide ions the cryptand influences this property, creating a softer Cu(II) centre that more favourably binds chloride ions.[192]

Although mononuclear, the reactivity of [**LTEA**HCuF]$(BF_4)_2$ has similarities to the dinuclear biological system tyrosinase. Tyrosinase systems are inhibited by bridged halides at low pH but undergo reactions at high pH.[180] This behaviour is paralleled by the copper fluoride cryptate whereby addition of a base to

the protonated cryptand changes the environment of the metal centre. The geometry change triggered by the deprotonation of the cryptand is a behaviour that is reminiscent of a conformational change observed in many enzymes.[193] Under basic conditions the formation of a Cu(II)-hydroperoxo intermediate is possible. Current investigations are underway to determine if the pH change triggers release of the fluoride anion, as well as investigations into the reactivity of hydroperoxo intermediate.

4.4 Conclusion

In conclusion, Cu(II)-halide complexes were formed and characterized. C_3 symmetry was observed in the Cu(II)-fluoride cryptate, despite *N*-methylated, while C_1 symmetry was observed in the Cu(II)-chloride complexes. The difference in symmetry was attributed to the stronger intramolecular hydrogen bonding and smaller ionic radius with the fluoride anion. The Cu(II)-fluoride complex when reacted with basic hydrogen peroxide was capable of forming a bio-relevant Cu(II)-hydroperoxo intermediate. In comparison, a Cu(II)-chloride complex was unable to form the same intermediate and the difference in reactivity was rationalized by the different bond strengths and stability of Cu(II)-halide complexes.

4.5 Supporting Information

Experimental details and crystallographic data are available in Appendix 2.

4.6 Acknowledgement

This work has been supported by Fonds de Recherche du Quebec- Nature et les Technologies (FRQNT), the Natural Sciences and Engineering Research Council of Canada (NSERC) and Canadian Foundation for Innovation (CFI). We would like to thank Pr. Garry Hanan and Dr. Jingwei Luo for access to the CSI-MS at Université de Montréal. We are grateful to Pr. Fabrice Thomas (Université Joseph Fourier) for EPR measurements.

Chapter 5: High-yield Synthesis of Potentially Ditopic Coordinating Cryptands and their Metal Complexes

L. Chaloner[a] and X. Ottenwaelder*[a]

[a] Department of Chemistry and Biochemistry, Concordia University, 7141 Sherbrooke Street West, Montreal, Canada H4B 1R6

dx.doi.org/10.1016/j.tetlet.2013.04.074

5.1 Abstract

Cryptands containing a tetradentate tris(aminoethyl)amine moiety have been prepared in high-yield via copper-catalyzed alkyne-azide cycloaddition followed by a templated 3+3 condensation. Silver and zinc complexes of the cryptands are reported. Weak interactions between a chloride anion and the cryptand suggest possible ditopic coordination.

5.2 Introduction

Propelled by the importance of anions in environmental and biomedical processes,[194-195] anion recognition is now an important branch of supramolecular chemistry.[196-197] In order to efficiently and selectively bind anions, ligands incorporate functionalities such as hydrogen bond donors,[198-199] metal coordination sites,[114] π-systems,[200-202] or combinations thereof.[162,203-204] Furthermore, anion encapsulation is particularly selective with cryptands due to the geometric constraints imparted by their rigidity. Presented here are the high-yielding syntheses of novel cryptands with two different binding sites, one hard polyamine site and one soft tris(triazole) site. As described recently,[116-117,205-206] the polarized C-H bonds of the triazoles are conducive to bind anions and thus impart the cryptands with attributes to serve as a heteroditopic ligand for anion recognition.

5.3 Results and Discussion

The macrobicyclic scaffold was prepared in two steps from 3-(2-propyn-1-yloxy)benzaldehyde, **4**, and tris(2-azidoethyl)amine, **5** (**CAUTION**),[207] which syntheses were reported previously (Scheme 15).[208-209] The end caps of the cryptands were constructed successively, first by copper-catalysed azide-alkyne cycloaddition (CuAAC) to yield 93% of **6**, then by a [3+3] reversible condensation with tris(2-aminoethyl)amine (Tren) to yield triimine cryptand **7**. Though **7** can be isolated, a same-pot borohydride reduction was preferred as it yielded larger quantities of cryptand **LTTA**. The amine groups of **LTTA** can

be easily functionalized, as demonstrated by a methylation to yield cryptand **8**. The ^{1}H NMR of cryptands **7**, **LTTA,** and **8** in $CDCl_3$ indicate C_3 symmetry in solution. Complete assignment of ^{1}H chemical shifts, was realized via COSY and NOESY experiments (see Supplementary Information; Appendix 3).

The [3+3] condensation was implemented under both template and semi-dilute conditions. Templating with lanthanum(III) nitrate proved to be an efficient procedure, with a 72% yield for the one-pot, two-step **6**→**LTTA** sequence, compared with 30% under non-templated conditions. Different metal ions were tested as templating agents. Cobalt(II) chloride, zinc(II) chloride, and silver(I) nitrate were chosen as they form complexes with **LTTA** (see below), but lanthanum(III) nitrate was by far the best templating agent. With zinc and silver, yields of 30% were obtained, likely due to the difficulty in purifying **LTTA**. Cobalt(II) chloride had a negative effect on the reaction by inhibiting the formation of the cryptand completely. No complexes were observed between lanthanum nitrate and **6**, **7,** or **LTTA** by ESI-MS in 1:1 methanol/dichloromethane, consistent with a kinetic templating effect. The lanthanum ion likely coordinates to Tren, as previously reported,[210-211] and this complex is poised to react with trialdehyde **6**. Once the cryptand is formed, the oxophilic lanthanum(III) ion is easily removed during work-up with the oxygen-rich EDTA ligand. In contrast, removal of cobalt, zinc, and silver ions from the formed cryptand proved difficult as these ions form stable complexes in the nitrogen-rich environment of **LTTA**.

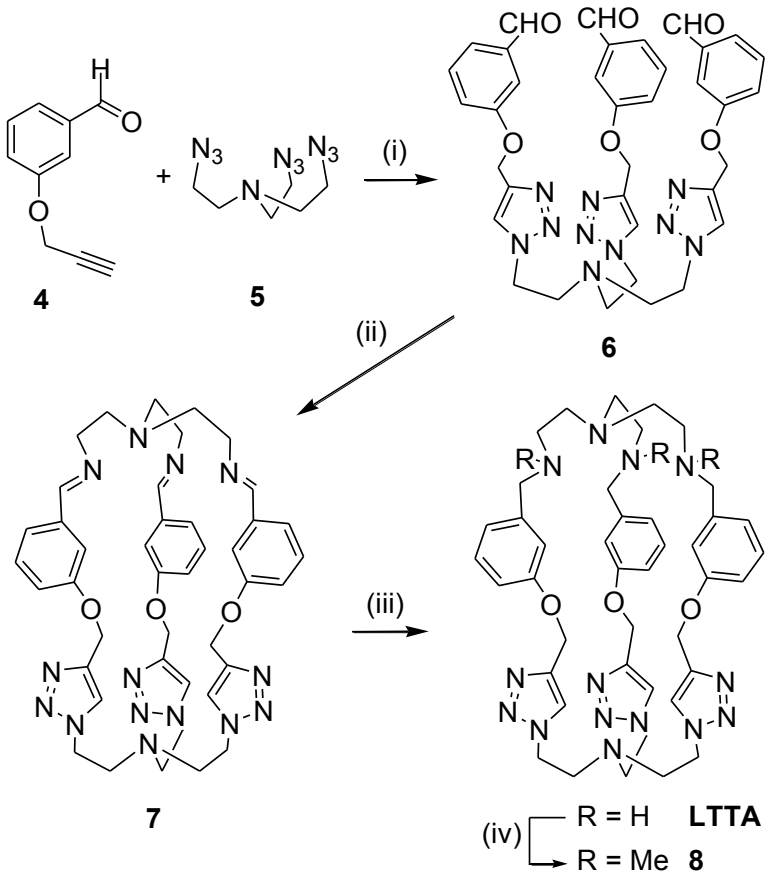

Scheme 15. Synthesis of cryptands **7**, **LTTA** and **8**. Conditions: (i) $CuSO_4$, NaAsc, *t*-BuOH:H_2O 1:1, 24h, 93%; (ii) Tren, $La(NO_3)_3$, MeOH:THF 10:1, 48h, 48%; (iii) $NaBH_4$, MeOH:THF 10:1, 3h, 72% over 2 steps; (iv) CH_2O, HCO_2H, 24h reflux, 80%.

X-Ray diffraction analysis of single crystals of **8**·Et_2O indicate that methylated cryptand **8** adopts an endo-endo conformation (Figure 20), as is customary with cryptands bearing Tren moieties.[118] The molecular structure of **8** has a C_1 symmetry due to the *anti* conformation of the N1-C31-C32-N10 linkage while the other two Tren nitrogens (N2 and N6) adopt a *syn* conformation in relation to N1 through their respective ethylene links. The only significant intramolecular contact within the cryptand is a C-H···π interaction between two triazole units (H28A···C12 = 2.684 and H28A···C13 = 2,792 Å, van der Waals radii: C, 1.70; H, 1.20 Å).

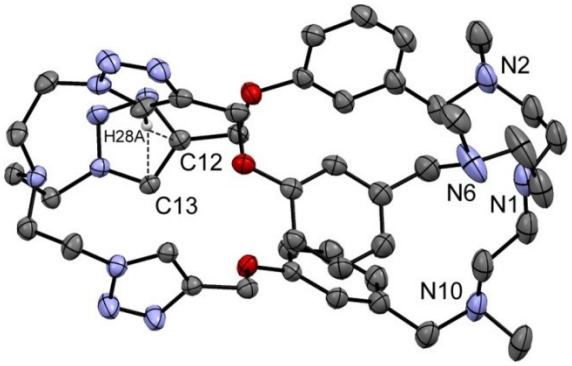

Figure 20. ORTEP representation at 50% thermal ellipsoid probability of **8**·Et_2O. The co-crystallized diethyl ether and hydrogen atoms (except H28A) were omitted for clarity.

The coordination ability of cryptands **LTTA** and **8** resides principally in the multi-chelating Tren moiety, as illustrated here with monomeric silver(I) and zinc(II) complexes of **LTTA**. Attempts to isolate dinuclear complexes involving coordination to the triazole moieties[212-213] have yet to be successful. Addition of silver(I) nitrate to a hot solution of **LTTA** in methanol led to a crystalline precipitate after cooling. The structure of this complex, [**LTTA**Ag](NO_3)·CH_3OH, was solved by X-ray diffraction (Figure 21). The inner-sphere complex, [**LTTA**Ag]$^+$, has a pseudo-C_3 symmetry. The Ag atom is coordinated to the Tren moiety, despite the potential to coordinate with the triazole groups, as shown in the literature.[214-216] Two of the triazoles are facing each other, and a weak C-H···π interaction exists between two triazole units, thus competing with coordination at this site. The Ag atom sits in a distorted trigonal-pyramidal environment composed of the nitrogen atoms of three Tren moiety, with the Ag sitting below the equatorial plane. The out-of-plane effect is commonly found in silver complexes with Tren.[217-224]

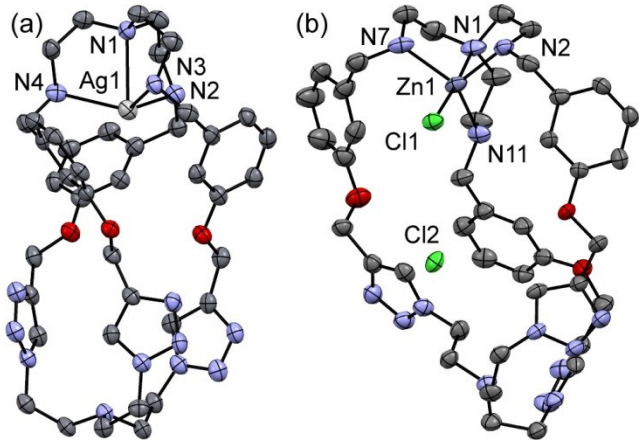

Figure 21. ORTEP representations at 50% thermal ellipsoid probability of: (a) the cationic part of [**LTTA**Ag](NO_3)·CH_3OH, and (b) [**LTTA**ZnCl](Cl). The hydrogen atoms were omitted for clarity. Selected bond lengths (Å) and angles (º) for [**LTTA**Ag](NO_3)·CH_3OH: Ag1-N1 = 2.506(5), Ag1-N2 = 2.398(5), Ag1-N3 = 2.385(4), Ag1-N4 = 2.370(5), N1-Ag1-N2 = 74.85(15), N1-Ag1-N3 = 74.99(15), N1-Ag1-N2 = 75.29(15); for [**LTTA**ZnCl](Cl): Zn1-N1 = 2.245(5), Zn1-N2 = 2.104(4), Zn1-N7 = 2.160(5), Zn1-N11 = 2.110(4), Zn1-Cl1 = 2.2861(14).

The ditopic nature of cryptand **LTTA** is revealed upon solid-state characterization of its zinc(II) chloride complex. A mononuclear complex of formula [**LTTA**ZnCl](Cl)·H_2O was obtained by mixing **LTTA** with zinc(II) chloride in hot methanol and letting the solution cool down. Formation of the complex was confirmed in solution with ESI-MS, the major peaks corresponding to the isotopic pattern of [**LTTA**ZnCl]$^+$. Single crystals amenable to X-ray diffraction analysis were grown by slow diffusion of diethyl ether into a methanol solution of the compound. The complex crystallizes as [**LTTA**ZnCl](Cl) in the chiral $P2_1$ space group (Figure 21).[225] The cryptand adopts an endo-endo conformation and has an overall C_1 symmetry. Akin to free ligand **8** and silver complex [**LTTA**Ag]$^+$, this structure reveals a weak C-H···π interaction between two triazole units (H40A on Figure 22). The Zn atom adopts a trigonal-bipyramidal coordination geometry within the Tren moiety with the chloride (Cl1) and central nitrogen (N1) atoms in the axial positions and the remaining nitrogens in the equatorial positions. The second chloride ion, Cl2, interacts with the hydrogens of two NH groups from the Tren moiety of a neighbouring molecule (Cl2···H2C^{i}-N2^{i} = 2.324, Cl2···H7B^{i}-N7^{i} = 2.356 Å; *i* = 1-*x*, 0.5+*y*, 1-*z;* vdW radii: H, 1.20; Cl, 1.75 Å) and is involved in four contacts with the cryptand itself (Figure 22). Two of these contacts are with H-C(triazole) groups (Cl2···H12A = 2.601, Cl2···H26A = 2.658 Å), likely the result of the triazole rings being electron-deficient.[117] The two other H···Cl2 contacts are with CH_2 groups, one adjacent to a triazole (Cl2···H13A = 2.728 Å) and the other adjacent to the tertiary nitrogen N6 (Cl2···H28A = 2.893 Å). This set of weak yet

multiple interactions is responsible for the cryptand to splay open to accommodate Cl2. This demonstrates a possible role of the triazole part of the cryptand to act as a secondary binding site and suggests that, with a proper substrate, cryptand **LTTA** will act as a ditopic ligand.

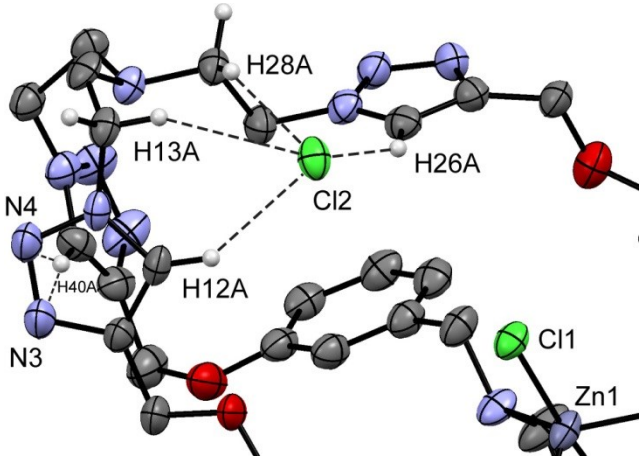

Figure 22. Zoom of the ORTEP representation (50% thermal ellipsoid probability) of [**LTTA**ZnCl](Cl). The hydrogen atoms were omitted for clarity except those of functions involved in weak contacts. Selected distances (Å): Cl2···H12A = 2.601, Cl2···H26A = 2.657, Cl2···H13A = 2.728, Cl2···H28A = 2.893, H40A···N3 = 2.614, H40A···N4 = 2.774.

To test this hypothesis, we carried out solution studies of chloride binding followed by ^{1}H-NMR. To a solution of [**LTTA**ZnCl](Cl)·H_2O in acetonitrile-d_3 was added increasing amounts of silver triflate (AgTfO) dissolved in acetonitrile-d_3 (0-2.5 equivalents per Zn). After addition of each aliquot, AgCl precipitated and the NMR spectral evolution was recorded (Figure 23 and Figure S21).[226] This experiment highlighted two types of protons that are the most susceptible to the abstraction of chloride ions: *C* (triazole C-H bond) and *H* (on the benzene ring). Addition of the first equivalent of AgTfO affects the triazole protons *C* more than any other, while benzene protons *H* are more sensitive to the second equivalent of AgTfO. Notwithstanding conformational reorganization, this behavior is consistent with a weak Cl···$H_{triazole}$ interaction that is disrupted first, while the second abstraction requires chloride decoordination from Zn^{2+}. In addition, the fact that protons *H* are sensitive to the chloride abstraction and not the other protons on the benzene ring suggests that protons *H* are oriented toward the inside of the cryptand where the chloride abstractions occur.

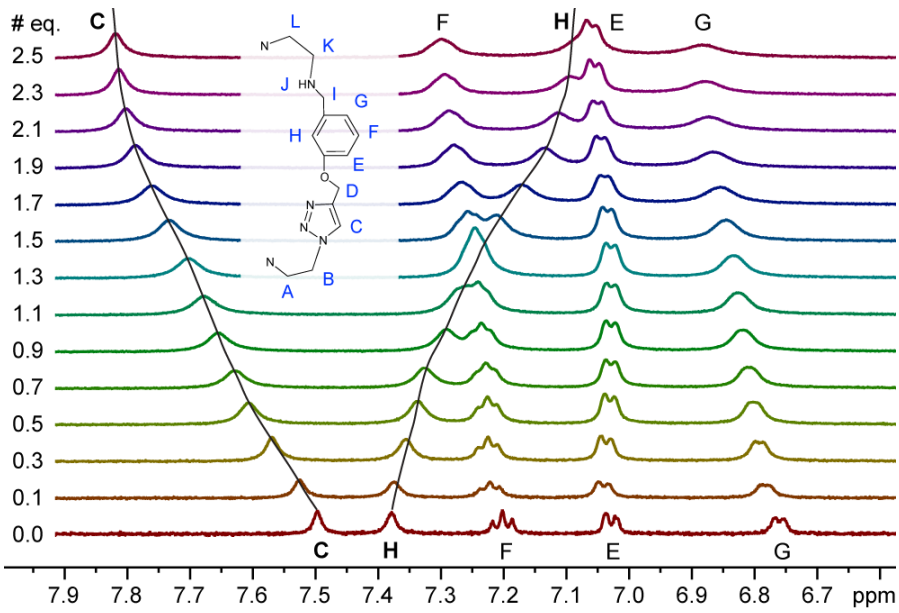

Figure 23. ^{1}H NMR titration of [**LTTA**ZnCl](Cl) with AgOTf in acetonitrile-d_3 at 60°C. Aliquots of a 125 mM solution of AgOTf were added to a 41.6 mM solution of [**LTTA**ZnCl](Cl).

5.4 Conclusion

In conclusion, we have synthesized novel cryptands in high yields by choosing reactions such as CuAAC and taking advantage of the templating capability of the lanthanum(III) ion. Cryptand **LTTA** has demonstrated its ability to coordinate transition metals such as silver, zinc and cobalt. Weak interactions in the zinc complex suggest that the cryptand can be used for ditopic binding through the coordinating Tren moiety (for a metal ion) and the triazole functions (for an anion or substrate). Current investigations into the binucleating and docking properties of the cryptands are underway.

5.5 Acknowledgments

This work was funded by these agencies: FQRNT (Québec), NSERC (Canada) and CFI (crystallography facility).

5.6 Supplementary Data

Supplementary data is available for all compounds including ^{1}H and ^{13}C NMR spectral assignments, elemental analyses and X-ray crystallography data. See Appendix 3.

Chapter 6: Formation and Reactivity of a Fe(III)-Hydroperoxo Supported by a Coordinating Cryptand

L. Chaloner[a], and X. Ottenwaelder*[a]

[a] Department of Chemistry and Biochemistry, Concordia University, 7141 Sherbrooke Street West, Montreal, H4B 1R6, Canada.

6.1 Abstract

An Fe(III)-hydroperoxo is a proposed intermediate in the aromatic C-H bond hydroxylation reaction executed by non-heme mononuclear iron enzymes. We here report the formation of an Fe(III)-hydroperoxo intermediate supported by a coordinating cryptand, **LTTA**. The reaction of [**LTTA**Fe](TfO)$_2$ with H_2O_2 led to the formation of Fe(III)-phenolate, confirmed by CSI-MS and UV/Vis. Low-temperature spectroscopy identified the formation of a Fe(III)-hydroperoxo intermediate before the formation the Fe(III)-phenolate. The Fe(III)-hydroperoxo is proposed to undergo heterolytic cleavage to form a high valent Fe(V)-oxo-hydroxo, a mechanism that is comparable to C-H bond activation in Rieske dioxygenases.

6.2 Introduction

Mononuclear heme and non-heme iron enzymes, such as Rieske dioxygenases and cytochrome P450s, facilitate one-step aromatic C-H bond hydroxylation reactions selectively and efficiently.[30,37-38,68] The enzymes are proposed to react through a common Fe(III)-hydroperoxo intermediate. In the established mechanism of cytochrome P450, the hydroperoxo intermediate undergoes protonation and heterolytic cleavage of the O-O bond to form compound I, a low spin Fe(IV)-oxo with a porphyrin-π-cation radical.[30] It is compound I that is responsible for abstracting the hydrogen atom from the substrate.[32] Upon hydrogen atom abstraction, an Fe(IV)-hydroxide is formed and a subsequent rebound mechanism is proposed to complete the C-H bond hydroxylation step.[227] The oxidative potency of cytochromes P450 relies on the porphyrin ring to delocalize the radical cation of compound I. In non-heme enzymes, where the coordination environment contains only redox-innocent ligands, the mechanism is much less understood. Notwithstanding, deciphering the different roles of the reaction intermediates in non-heme enzymes is fundamental to developing catalysts for the coveted one-step C-H bond hydroxylation.[3,228-229]

Synthetic models have been use to evaluate possible intermediates for aromatic C-H bond activation in non-heme iron enzymes. The Fe(III)-hydroperoxo intermediate is proposed to 1) attack the substrate directly 2) undergo heterolytic cleavage to form a high-valent Fe(V)-oxo-hydroxo or 3) undergo homolytic cleavage to form an Fe(IV)-oxo and a hydroxyl radical.[9,65] The Fe(III)-hydroperoxo intermediate has been generally classified as a poor oxidant, only being able to abstract weak C-H bonds.[75] With model systems, the majority of authors propose O-O bond cleavage before electrophilic attack on the aromatic ring.[79-85,88,91] The Fe(IV)-oxo has been identified as a viable intermediate for C-H bond activation.[79-80,86-87] However, the Fe(V)-oxo is targeted due to its greater oxidation potency and radical-free reaction pathway.

The understanding of Fe/O_2 chemistry has been driven forward with the use of macrocycles,[107,230] which entails increased stability to their complexes leading to easier characterization of the high-valent intermediates.[89-91] This has been proven with TMC (tetramethylcyclam) macrocycle, where several intermediates have been isolated and characterized.[78,101-105] Our research builds upon this concept by using cryptands (macrobicycles) to help stabilize complexes and to influence reactivity through second coordination sphere properties. The cryptands provide a protective pocket to help control nuclearity and prevent side reactions. Supramolecular cavitands have been used to study biomimetic Fe oxidation reactions, but they only provide a protective pocket and do not benefit from the cryptate effect.[110] While the use of cryptands for mimicking mononuclear Fe monooxygenase reactions is unexplored, a few examples in Cu/O_2 chemistry have been reported. In one specific example, a Tren-capped calix[6]arene cryptate was shown to protect the Cu centre from dimerization and disproportionation.[111] In another example a Tren-based cryptand was shown to influence and direct the reactivity of Cu(II)-hydroperoxo intermediate (Chapter 3). The potential benefits of the cryptate effect and protection of the active site has led us to investigate Fe/O_2 chemistry supported by a cryptand (**LTTA**) (Scheme 16).

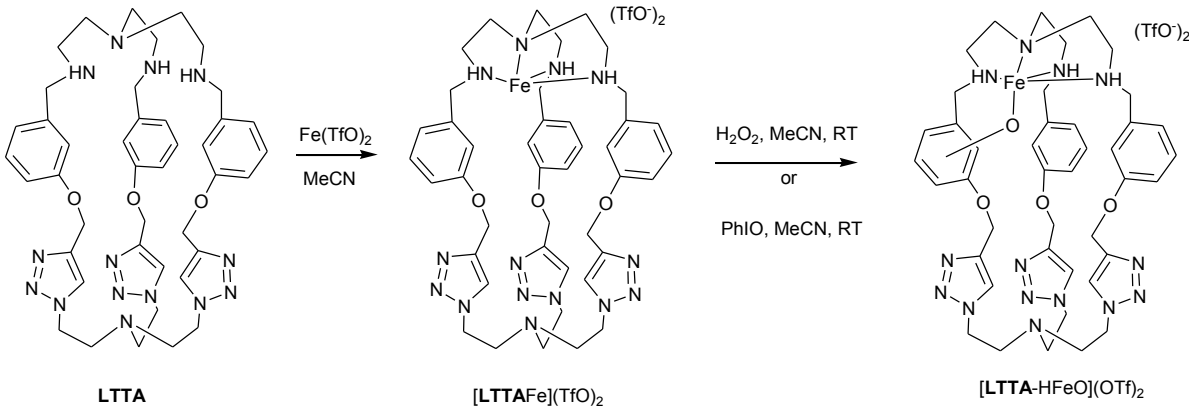

Scheme 16. Ligand **LTTA** and the synthesis of its Fe(II)-triflate complex and Fe(III)-phenolate from H_2O_2 or PhIO

6.3 Results and Analysis

6.3.1 Synthesis and Characterization of [LTTAFe](TfO)$_2$

The synthesis of **LTTA** was previously reported.[169] [**LTTA**Fe](TfO)$_2$ was synthesized in 97% yield by reacting iron(II)-triflate with a small excess of **LTTA** in MeCN and precipitating with ether (Scheme 16). The complex was stable as a powder under an inert atmosphere for an indefinite period of time and decomposed slowly in air to give a brown precipitate. The complex was characterized by ESI-MS and CHN analysis. The ESI-MS showed two fragment ions, *m/z* = 429 [**LTTA**Fe]$^{2+}$ and 1007 [**LTTA**FeTfO]$^{+}$, corresponding to the complex having lost one or two of the anions. The CHN analysis revealed that the [**LTTA**Fe](TfO)$_2$ sample also contained one of each: water, ether and MeCN. Despite many attempts, single crystals suitable for X-ray diffraction could not be made. The complex was EPR silent and the ^{1}H-NMR contained very broad signals resulting from a high-spin Fe(II) centre.

6.3.2 Formation of an Fe(III)-phenolate

The Fe(III)-phenolate, [**LTTA**-HFeO](TfO)$_2$, was formed using two different oxidants (Scheme 16). When [**LTTA**Fe](TfO)$_2$ was reacted with 2 to 100 equiv. of H_2O_2 at room temperature in MeCN, the solution immediately turned dark blue. The blue species was stable at low concentrations of oxidant (2 equiv.) for a short time (about 1/2 h) but decomposed quickly with higher concentrations. Attempts to isolate the blue product resulted in decomposition of the sample. This Fe(III)-phenolate species (see below) was alternatively formed from the reaction of [**LTTA**Fe](TfO)$_2$ with slight excess PhIO suspended in MeCN. The reaction with PhIO was qualitatively slower (several seconds before colour change) compared to the

reaction with H_2O_2 (immediate colour change). The product of the reaction with PhIO could be isolated by precipitation with ether. The blue powder remained stable for at least 24 hours under an inert atmosphere. Attempts to form crystals with the blue powder were, however, unsuccessful.

6.3.2.1 Mass Spectrometric Analysis

The reaction of [**LTTA**Fe](TfO)$_2$ with H_2O_2 or PhIO was characterized by direct-injection-ESI-MS. The Fe(III)-phenolate was identified by the *m*/*z* = 1022, i.e. 15 mass units higher than [**LTTA**FeTfO]$^+$ corresponding to the gain of one oxygen and loss of a hydrogen (Figure S22, A and B). The isotope pattern was consistent with the molecular formula of [**LTTA**-HFeOTfO]$^+$ and a +3 oxidation state of Fe. At 2 equiv. of oxidant the ESI-MS was dominated by the signal of [**LTTA**FeTfO]$^+$. The intensity of the signal of [**LTTA**-HFeOTfO]$^+$ increased with increasing concentration of H_2O_2 along with over-oxidation peaks (Figure S22, C). Using high concentrations of PhIO was not possible due its insolubility in MeCN.

Cold-spray ionization mass spectrometry (CSI-MS) was used to further evaluate the reaction of [**LTTA**Fe](TfO)$_2$ with H_2O_2. A continuous-flow set-up was used to mix the reactants at a Y-junction before introduction to the MS. One syringe was loaded with [**LTTA**Fe](TfO)$_2$ and pumped from inside the glovebox and the other was loaded with H_2O_2 and pumped from outside. The tubing was first filled with [**LTTA**Fe](TfO)$_2$ and addition of H_2O_2 was started after, which marked time zero. This allowed for observation of the reaction at gradually increasing mixing times.

With the gradual mixing of H_2O_2 with [**LTTA**Fe](TfO)$_2$, several spectral changes occurred. The most notable changes were the decrease in intensity of [**LTTA**Fe(TfO)]$^+$ at *m*/*z* = 1007.34 and the increase in intensity of oxidized products. Of the oxidized products, *m*/*z* = 1022.3235 [**LTTA**-HFeOTfO]$^+$ was the most dominant peak upon complete mixing (*m*/*z* = 1022.3235 is within 0.3 ppm of the exact mass of [**LTTA**-HFeOTfO]$^+$). The peaks at *m*/*z* = 888.34, 886.34, 1038.32 and 1036.32 are assigned [**LTTA**FeOO-2H]$^+$, [**LTTA**FeOO-4H]$^+$, [**LTTA**FeOO(TfO)-1H]$^+$ and [**LTTA**FeOO(TfO)-3H]$^+$, respectively and are likely from over-oxidation. The peak at *m*/*z* = 1103.37 and 981.41 correspond to decoordination of Fe centre. The peak at *m*/*z* = 1103.37 is assigned [**LTTA**(TfOH)$_2$]H$^+$ and 981.41 is assigned [**LTTA**-2H(TfO)(CH$_3$OH)]$^+$. The intensity of [**LTTA**(TfOH)$_2$]H$^+$ compared to the other ions indicates that coordination of the metal centre is inefficient under these conditions. When the experiment was repeated with an ESI-MS (H_2O_2 as the oxidant) the contribution from this peak was negligible (< 5% intensity). However, the ESI-MS with PhIO as the oxidant showed signals corresponding to decoordination of the iron centre (Figure S22).

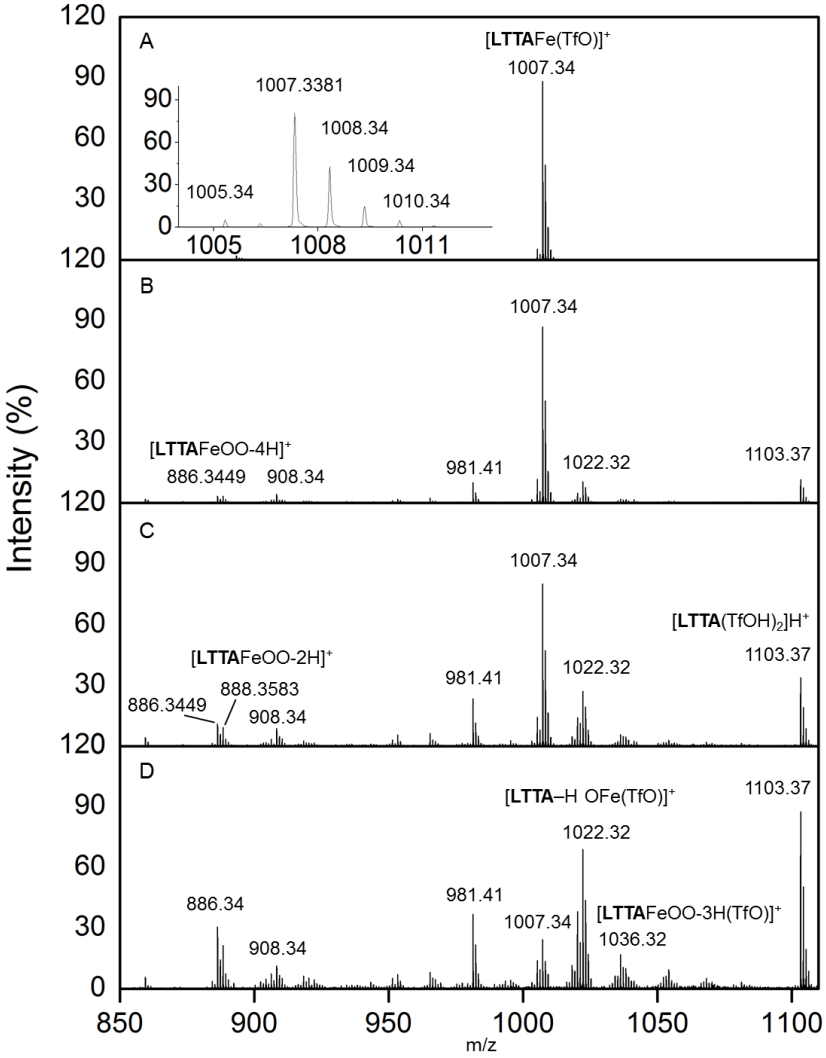

Figure 24. CSI-MS of 1mM [**LTTA**Fe](TfO)$_2$ in MeCN and 1 equiv. H_2O_2 in MeCN were mixed with a continuous-flow setup at RT. The spectra were recorded at (A) 30 s, inset shows isotope pattern of [**LTTA**Fe(TfO)]$^+$ (B) 78 s, (C) 96 s, (D) 108 s from the time of adding H_2O_2.

6.3.2.2 UV/Vis and EPR Spectroscopy

The reactions of [**LTTA**Fe](TfO)$_2$ with H_2O_2 (2 equiv.) or PhIO (ca. 4 equiv.) were monitored by UV/Vis at room temperature and both reactions showed very similar spectra to each other (Figure S23). Two LMCT bands, characteristic of Fe(III)-phenolate species, were observed (Table 6).[79,231] The charge-transfer bands at 350 nm are assigned to the phenolate p(π) → Fe(III) d(σ*) transition and the charge-transfer bands at 640 nm or 650 nm are assigned the phenolate p(π) → Fe(III) d(π*) transition.[79,231]

Table 6. UV/Vis absorption bands from 0.2 mM [**LTTA**Fe](TfO)$_2$ + oxidant in acetonitrile at RT.

Oxidant	λ_{max} (nm)	ε (M^{-1} cm^{-1})	λ_{max} (nm)	ε (M^{-1} cm^{-1})
H_2O_2	350	3100	640	1150
PhIO	350	2780	650	1000

The Fe(III)-phenolate species was further characterized by EPR. The reaction of [**LTTA**Fe](TfO)$_2$ with 1 equiv. of H_2O_2 at room temperature was mixed for 20 s under an inert atmosphere. The sample was removed from the inert atmosphere, loaded into an EPR tube and immediately frozen to minimize exposure to air. The sample had an intense blue colour indicating formation of the Fe(III)-phenolate with little to no decomposition. The EPR clearly shows that the product is a high-spin rhombic Fe(III) centre with g = 4.3 (Figure S25).

6.3.2.3 Kinetics

The reaction of [**LTTA**Fe](TfO)$_2$ with H_2O_2 in MeCN was monitored with stopped-flow UV/Vis spectroscopy. The data was fitted to a simple A → B → C model revealing the formation of an intermediate prior to the observation of the Fe(III)-phenolate (Scheme 17). The intermediate was postulated to be an Fe(III)-hydroperoxo and deconvolution of the spectral profile from the fitting revealed a band with an absorption maxima at 525 nm (ε = 1575 M^{-1} cm^{-1}), characteristic of the Fe(III)-hydroperoxo LMCT (Figure 25).[37] To directly observe the absorption band at 525 nm the experiment was repeated in propionitrile and -70 °C. Upon addition of H_2O_2, the complex turned purple as the band at 525 nm began to accumulate before decomposing into the Fe(III)-phenolate (Figure S24).

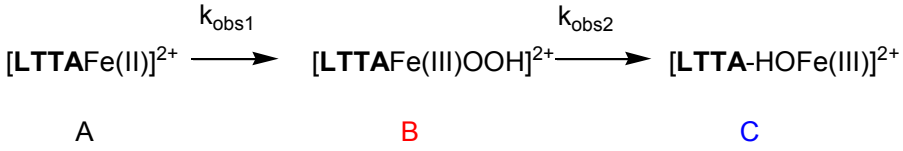

Scheme 17. Proposed reaction mechanism for the formation of the Fe(III)-phenolate.

The rate constant, k_{obs1}, for the formation of the Fe(III)-hydroperoxo was analysed at different concentrations and temperatures. k_{obs1} was found to be dependent on the concentration of [H_2O_2]. When [H_2O_2] was varied from 5 to 50 mM at -5 °C the plot of k_{obs1} vs [H_2O_2] was linear with an intercept near zero, consistent with $d[B]/dt = k_1[A][H_2O_2]$. A fractional reaction order (1.2) with respect to H_2O_2, deduced from the slope of the log plot (Figure 25), is consistent with a complex mechanism where H_2O_2

is required to both oxidize Fe(II) to Fe(III) and form the hydroperoxo intermediate.[37,71] The temperature of the reaction was varied from -30 to 20°C, and the activation parameters were extracted from the corresponding Eyring plot (Table 7). The activation parameters are consistent with an associative bimolecular reaction pathway leading to the formation of an Fe(III)-hydroperoxo.

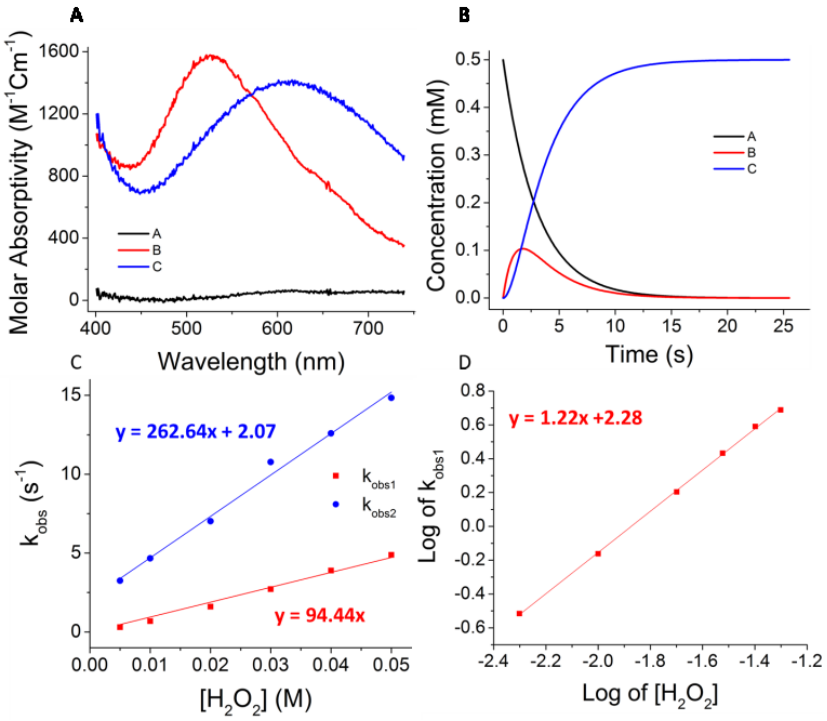

Figure 25. (A) UV/Vis profile from the pseudo-first order fit A⟶B⟶C for the reaction of 0.5 mM [**LTTA**Fe](TfO)$_2$ in MeCN with 30mM H_2O_2 at -30°C (B) Concentration profile with respect to time of A, B and C (C) Observed rate constants versus $[H_2O_2]$ from the reaction of 0.5 mM [**LTTA**Fe](TfO)$_2$ with H_2O_2 at -5°C. (D) Log plot of the observed k_{obs1} versus $[H_2O_2]$.

Table 7. Activation parameters for the reaction of [**LTTA**Fe(II)]$^{2+}$ with H_2O_2

Reaction	k	$\Delta H^{\ddagger}$ (kJ mol^{-1})	$\Delta S^{\ddagger}$ (J K^{-1} mol^{-1})
[**LTTA**Fe(II)]$^{2+}$ + $[H_2O_2]$ ⟶ [**LTTA**Fe(III)OOH]$^{2+}$	k_1	33	-84
[**LTTA**Fe(III)OOH]$^{2+}$ ⟶ [**LTTA**-HFeO]$^{2+}$	k_{2a}	53	-37
[**LTTA**Fe(III)OOH]$^{2+}$ + $[H_2O_2]$ ⟶ [**LTTA**-HFeO]$^{2+}$ or [**LTTA**Fe(III)OOH]$^{2+}$ + $[H_2O]$ ⟶ [**LTTA**-HFeO]$^{2+}$	k_{2b}	49	-12 or -19

The plot of k_{obs2} vs $[H_2O_2]$ is linear with a non-zero intercept, indicating the rate law $d[C]/dt = k_{2a}[B] + k_{2b}[B][H_2O_2 \text{ or } H_2O]$. This rate law is consistent with a mechanism where the Fe(III)-hydroperoxo decomposes to the Fe(III)-phenolate independently and through a H_2O_2- or H_2O-assisted mechanism. The rate constants, k_{2a} and k_{2b}, were extracted from the plot of k_{obs2} vs $[H_2O_2]$ or k_{obs2} vs $[H_2O_2]$, where k_{2a} is the y-intercept and k_{2b} is the slope. The plots were repeated at -5, -15 and -30 to obtain the activation parameters in Table 7. The negative entropy of activations, $\Delta S^{\ddagger}_{k2a}$ and $\Delta S^{\ddagger}_{k2b}$ indicate a mildly constrained transition state, consistent with an intramolecular reaction pathways. The rate-determining step is typically O-O bond cleavage and the less negative $\Delta S^{\ddagger}_{k2b}$ value compare to $\Delta S^{\ddagger}_{k2a}$ suggests that the H_2O_2- or H_2O-assisted mechanism involves pre-equilibrium binding of H_2O or H_2O_2 followed by cleavage of the hydroperoxo moiety with a concomitant dissociation of a molecule.

6.3.2.4 Analysis of Organics

Ligand oxidation was confirmed by demetallating the complexes with NH_4OH following the oxidation reaction with 2 equiv. of oxidant. The organic matter was analyzed by MS, NMR and IR. The ESI-MS showed that for both PhIO and H_2O_2 as the oxidants, the molecular ion peak was the starting ligand, [**LTTA**]H^+. The second major ion was the ligand with one oxygen atom inserted [**LTTA**+O]H^+ (Figure S26, B and C). The **LTTA**+O could be partially isolated from **LTTA** by extracting unreacted **LTTA** with MeCN (complete removal of the **LTTA** was not possible) (Figure S26, A). As a control experiment, **LTTA** was reacted with 2 equivalents of H_2O_2. Minimal oxidation was observed in the control experiment (< 4%) and no [**LTTA**+O]H^+ was observed (Figure S26, D).

The NMR and IR provide clues to the site of oxygenation. The aromatic region of the semi-purified oxygenated ligand had the most dramatic changes. Complete analysis of the product was, however, difficult (Figure S27). The aromatic peak (G) has either shifted or disappeared. Further evidence of aromatic hydroxylation came from the lack of proton shift corresponding to an aldehyde, eliminating the possibility of hydroxylation at the benzylic position. The IR of the semi-purified oxygenated ligand showed an increase in the O-H stretching region at about 3400 cm^{-1} (Figure S28). The IR together with the NMR provided some evidence that an Fe(III)-phenolate was being formed however neither spectra are entirely convincing.

6.3.3 Formation of the Fe(IV)-oxo

An Fe(IV)-oxo complex was synthesized by mixing [**LTTA**Fe](TfO)$_2$ in MeCN with PhIO dissolved in MeOH at -40 °C. The solution turned vibrant yellow and when analyzed by UV/Vis and absorption bands at 525 nm (ε = 125 M^{-1} cm^{-1}) and 770 nm (ε = 210 M^{-1} cm^{-1}) were observed (Figure 26). The band at 770 nm is characteristic of the ligand field transition of a Fe(IV)-oxo species.[43] Heating the reaction caused the intermediate to decompose with no observation of any other species. When a low-temperature reaction was repeated with PhIO crushed in MeCN, the transition at 770 nm did not appear. Furthermore the Fe(III)-phenolate was not observed at any point during the experiment, demonstrating the Fe(IV)-oxo is not responsible for the aromatic hydroxylation seen from the reaction of [**LTTA**Fe](TfO)$_2$ with H_2O_2.

6.3.3.1 Kinetics

The reaction of [**LTTA**Fe](TfO)$_2$ with PhIO was followed by stopped flow UV/Vis spectroscopy at -40°C. The formation of the absorption band corresponding the Fe(IV)-oxo (650 nm to 875 nm) was fit to a A → B model. The experiment was repeated from -35 to 0°C and the corresponding Eyring plot was generated. The activation parameters were extracted from the plot as $\Delta H^{\ddagger}$ = 25 kJ mol^{-1} and $\Delta S^{\ddagger}$ = -92 J K^{-1} mol^{-1}, indicating an associative mechanism for the formation of the Fe(IV)-oxo species.

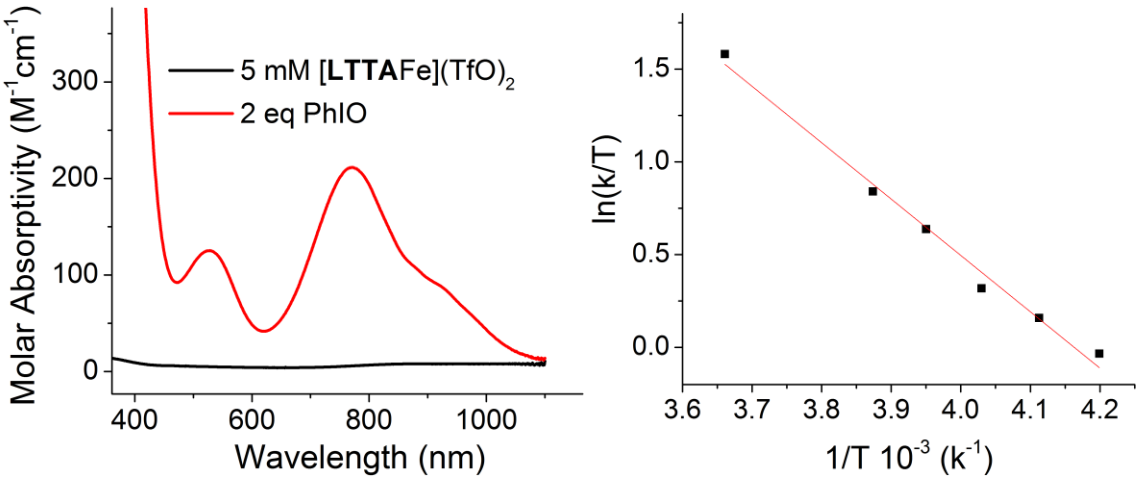

Figure 26. UV/Vis spectra of the reaction of 5 mM [**LTTA**Fe](TfO)$_2$ in MeCN with 2 equiv. PhIO in MeOH at -40°C. Eyring plot for the formation of Fe(IV)=O from 2 mM [**LTTA**Fe](TfO)$_2$ with 20mM PhIO in MeOH.

6.3.3.2 Analysis of Organics

Analysis of the ligand was achieved by demetallating the Fe(IV)-oxo with NH_4OH after decomposing the intermediate. ESI-MS of the demetallated solution revealed that only a small amount of oxygen-atom transfer to the ligand had occurred (< 10 % intensity) (Figure S29). The majority of the product was from the dehydrogenation of the ligand (**LTTA**-2H and **LTTA**-4H), evidenced by the loss of 2 and 4 mass units from the initial ligand at *m*/*z* = 803. These results are dramatically different from decomposition and demetallation of the Fe(III)-phenolate where the major product was C-H bond hydroxylation with little to no dehydrogenation observed.

6.3.4 Mechanism for the Formation of the Fe(III)-phenolate

The reaction of [**LTTA**Fe](TfO)$_2$ with H_2O_2 forms a Fe(III)-hydroperoxo intermediate that leads C-H activation and the formation of an Fe(III)-phenolate. A common query is whether the Fe(III)-hydroperoxo attacks the aromatic ring directly or first cleaves the O-O bond to form a high-valent intermediate. In our case, heterolytic cleavage of the Fe(III)-hydroperoxo to form a high-valent Fe(V)-oxo-hydroxo is proposed (Scheme 18). This mechanism is supported by the kinetic analysis of the formation of the Fe(III)-phenolate where the rate law is $d[C]/dt = k_{2a}[B] + k_{2b}[B][H_2O_2 \text{ or } H_2O]$. The dependence of the rate on [H_2O_2 or H_2O] indicates a pathway with water-assisted cleavage of the hydroperoxo moiety, a mechanism implicated in heterolytic cleavage mechanism via isotope-labelling and computational studies.[37,232] However, the direct attack by the hydroperoxo intermediate cannot be ruled out without further experiments. Finally, the decomposition of an independently formed Fe(IV)-oxo did not lead to a phenolate product, eliminating the possibility of a homolytic cleavage pathway.The Fe(III)-phenolate formed from PhIO may go through a similar Fe(V)-oxo intermediate or more likely involve a concerted, Fe-mediated, oxygen-atom transfer to the aromatic ring.

The arene hydroxylation likely occurs at a position *ortho* to the benzylic functional group on the aromatic ring because this would form a favourable 6-membered ring in the Fe(III)-phenolate product. The formation of an Fe(III)-phenolate at the *ortho* position has been previously established in the reaction of $[Fe(II)(bpmen)(MeCN)_2]^{2+}$, H_2O_2 and benzoic acid where the carboxylic group anchors the substrate to the complex.[233] Two *ortho* positions are available on **LTTA**, both of which are activated by the O-R group. Further studies are necessary to identify the site of oxidation as well as isotope labelling studies to confirm a water-assisted cleavage mechanism.

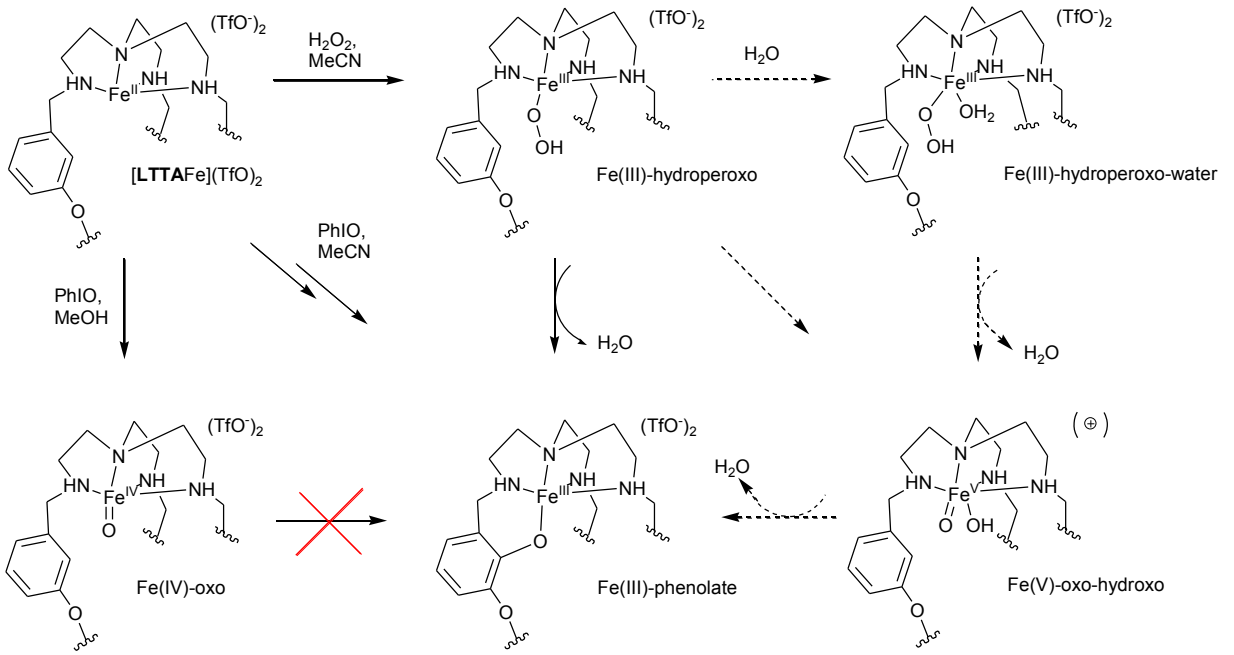

Scheme 18. Proposed mechanism for the formation of the Fe(III)-phenolate. The cryptand backbone has been removed for clarity. The hydroxylation is depicted at position H however position G is also likely.

6.4 Conclusion

In conclusion, the reaction of [**LTTA**Fe](TfO)$_2$ and H_2O_2 leads to an intramolecular aromatic hydroxylation reaction. An Fe(III)-hydroperoxo intermediate was observed with stopped-flow and low temperature UV/Vis spectroscopy. The hydroperoxo moiety is proposed to undergo heterolytic cleavage to form a Fe(V)-oxo-hydroxo, akin to Rieske dioxygenases. An Fe(IV)-oxo, independently formed, showed no signs of aromatic hydroxylation eliminating its participation in the mechanism. This study is unique in that it is the first attempt at studying model non-heme iron chemistry with a coordinating cryptand. The next step will be to further investigate the mechanism of C-H bond hydroxylation and look at the impact of the second coordination sphere of the cryptand on the reactivity of the Fe complex.

6.5 Experimental

Materials: All materials were used as received from Alfa Aesar and Sigma Aldrich except iron(II)-triflate which was synthesized from a previously reported procedure[234] and acetonitrile which was distilled over CaH_2 and stored over sieves under an inert atmosphere. NMR spectroscopic measurements were made at 22 °C in a 5 mm tube on a Varian Innova 300 or 500 MHz instrument and referenced to internal

tetramethylsilane. Electrospray ionization mass-spectrometry (ESI-MS) measurements were performed via direct injection on a Micromass Quattro LC at Concordia's Centre for Biological Applications of Mass Spectrometry. Cryospray ionization MS (CSI-MS) data were acquired with a Bruker CSI Q-TOF at the Université de Montréal. The *m*/*z* data reported are based on ^{1}H, ^{12}C, ^{14}N, ^{16}O, and ^{63}Cu. UV/Vis spectra were recorded on an Agilent 8453 spectrophotometer equipped with a Unisoku USP-203-A cryostat for temperatures down to –70 °C. Kinetic studies were recorded on a BioLogic low-temperature stopped-flow unit (Claix, France) equipped with a J&M TIDAS diode-array spectrophotometer (J&M, Aalen, Germany). X-band EPR spectra were collected on a Bruker EMX Plus spectrometer controlled with Xenon software and equipped with a Bruker teslameter. A Bruker nitrogen-flow cryostat connected to a high-sensitivity resonant cavity was used for 100 K measurements.

Synthesis of [LTTAFe](TfO)$_2$: [**LTTA**Fe](TfO)$_2$: Under an inert atmosphere, Iron(II) triflate (215 mg, 495 µmol) dissolved in 1 mL MeCN was added to **LTTA** (401 mg, 500 µmol) suspended in 1 mL of MeCN. The mixture was stirred for 10 minutes and the undissolved ligand was filtered off. The pale yellow filtrate was concentrated and layered with diethyl ether. The complex was isolated by collecting and drying the beige precipitate (578.5 mg, 97%). MS (ESI, MeCN): *m*/*z* = 429 [M^{2+}-TfO] and 1007 [M^{+} -TfO]. Accurate mass = 1007.3381, exact mass = 1007.33675, mass accuracy = 1.3 ppm Elemental analysis calcd (%) for $C_{50}H_{69}N_{15}O_{11}S_2F_6Fe$: C 46.55, H 5.39, N 16.29, S 4.97; C 46.18, H 5.36, N 16.31, S 5.03. NMR.

6.5.1 Formation of Fe(III)-phenolate

Synthesis: Under an inert atmosphere, 23 mg (20 µmol) of [**LTTA**Fe](TfO)$_2$ was dissolved in 5 mL of MeCN. To this solution was added 25µL of a H_2O_2 stock solution (80 mM in MeCN). The solution immediately turned dark blue. (Evidence of formation by CSI-MS: Accurate mass = 1022.3235, exact mass = 1022.3238, mass accuracy = 0.3 ppm).

Under an inert atmosphere, 23 mg (20 µmol) of [**LTTA**Fe](TfO)$_2$ was dissolved in 2 mL of MeCN. To this solution was added 17.6 mg (80 µmol) PhIO crushed in 1 mL MeCN. The solution turned dark blue after a few minutes. The solution was used for further experiments (evidence of formation was by an ESI-MS signal at *m*/*z* =1022, other signals were present as well). The product was isolated by removing the unreacted PhIO and layering the filtrate with ether. A blue powder precipitated out and was collected on a frit.

Characterization by UV-Vis: A 3 mL cuvette with 1 cm pathlength was equipped with a stir bar and sealed with a septum. The cuvette was degassed with nitrogen and filled with 2 mL of MeCN. To the cuvette was added 20 µL of a [**LTTA**Fe](TfO)$_2$ stock solution (20 mM in MeCN) followed by 20 µL of H_2O_2 stock solution (40 mM in MeCN). The reaction was observed over 10 minutes by UV/Vis to ensure complete formation of the [**LTTA**-HFeO](TfO)$_2$.

Under the inert atmosphere of a glove box, a 3 mL cuvette with 1 cm pathlength was filled with 2 mL of MeCN and equipped with a stir bar. The cuvette was sealed with a septum and removed from the glovebox. 100 µL of a [**LTTA**Fe](TfO)$_2$ stock solution (10 mM in MeCN) was added to the cuvette followed by 125 µL of a 80 mM stock solution of PhIO crushed in MeCN. The reaction was monitored with UV/Vis for 10 minutes.

Kinetic Studies with H_2O_2: A 1 mM solution of [**LTTA**Fe](TfO)$_2$ in MeCN was prepared under an inert atmosphere and added to varying concentrations of H_2O_2 between -30 to 20 °C (final concentration in Fe is 0.5 mM). Solutions after mixing were 0.5 mM with respect to Fe in 184 µL of MeCN. All concentrations are reported as in-cell, after dilution. The resulting spectra were analyzed with a global analysis fitting routine using the program Reactlab kinetics (Jplus Consulting, Palmyra, Australia). The experiments were repeated 5 times and the average rate constants were used.

CSI-MS Analysis with H_2O_2: To observe the reaction of [**LTTA**Fe](TfO)$_2$ with H_2O_2 at various times, two syringes, one filled with 0.2 mM of [**LTTA**Fe](TfO)$_2$ under inert atmosphere and the second filled with 1 equiv. H_2O_2 were injected into the CSI-MS through a Y-junction. The rate of injection was from 1 mL/hr per syringe.

EPR Analysis: To a 1 mM solutions of [**LTTA**Fe](TfO)$_2$ in MeCN was added to 2 mM of H_2O_2 in MeCN in a 1:1 ration at RT to make a 0.5 mM solution of the Fe(III)-phenolate. A sample of 400 µL of the 0.5 mM solution was frozen in liquid nitrogen and the spectrum was acquired.

Characterization of the Fe(III)-Hydroperoxo: A UV/Vis spectra of a 0.5 mM solution of [**LTTA**Fe](TfO)$_2$ in propionitrile was recorded at -70°C. Ten equiv. of H_2O_2 were added. The progression of the reaction was followed for 50 min.

Analysis of the Organics: After decomposition of the bulk solution, excess NH_4OH was added and the solution was filtered on an alumina column with a 1:1 MeCN/DCM mobile phase. The filtrate was

analyzed by ESI-MS. Alternatively, EDTA was added to the solution and extracted 3 times with dichloromethane. The extracts were dried over Na_2SO_4 and the solution was condensed.

Attempts to purify the oxygenate ligand were made by precipitating the **LTTA** with MeCN, collecting and condensing the filtrate containing the oxygenate ligand. This procedure was repeated several times. The condensed filtrate was then analyzed by ESI-MS, IR and NMR.

6.5.2 Formation of Fe(IV)-oxo

Characterization by UV/Vis: Under the inert atmosphere of a glove box, a 3 mL cuvette with 1cm path length was filled with 2 mL of MeCN and equipped with a stir bar. The cuvette was sealed with a septum, removed from the glovebox and cooled to -40 °C. To the cuvette was added 100 µL of a [**LTTA**Fe](TfO)$_2$ stock solution (40 mM in MeCN) followed by 100 µL of a 80 mM stock solution of PhIO dissolved in MeOH. The formation of the intermediate was followed by UV/Vis.

Kinetic Studies: A 4 mM solution of [**LTTA**Fe](TfO)$_2$ in MeCN was prepared under an inert atmosphere and added to 40 mM PhIO dissolved in MeOH at various temperatures. Solutions after mixing were 2 mM with respect to Fe in 184 µL of 1:1 MeCN/MeOH. The resulting spectra were analyzed with a global analysis fitting routine using the program Reactlab kinetics (Jplus Consulting, Palmyra, Australia). The experiments were repeated 5 times and the average rate constants were used.

Analysis of the Organics: After decomposition of the bulk solution, excess NH_4OH was added and the solution was filtered on an alumina column with a 1:1 MeCN/DCM mobile phase. The filtrate was analyzed by ESI-MS.

6.6 Supporting Information and Acknowledgements

Supplementary figures are available in Appendix 4.

This work has been supported by Fonds de Recherche du Québec - Nature et les Technologies (FRQNT) and the Natural Sciences and Engineering Research Council of Canada (NSERC). L.C. acknowledges Concordia University for the Mobility Award and FRQNT for the Bourse de Stage International- CCVC. We would like to that Dr. Fabrice Thomas for the EPR experiments and access to the stopped-flow UV/Vis. We would also like to thank Dr. Garry Hanan and Dr. Jingwei Luo (Université de Montréal) for access to the CSI-MS.

Chapter 7: Conclusion

7.1 Conclusion

This research has shown that coordinating cryptands can be used to study intramolecular oxygenation reactions that proceed through Cu(II)- and Fe(III)-hydroperoxo intermediates. Two cryptands **LTEA** and **LTTA** were used to achieve this bio-inspired oxidation chemistry.

With **LTEA**, the addition of *N*-methylation to the Tren moiety of the cryptand provided too much steric constraint to encapsulate Cu(II)-acetate centres (Chapter 2). The reaction was further complicated by the presence of two complexes in solution (Chapter 3). Nevertheless, the cryptate was able to support the formation of Cu(II)-hydroperoxo intermediates that led to an intramolecular oxidation. The cryptand was shown to influence the reaction pathway of the hydroperoxo intermediates through second coordination sphere features. While C-H bond oxidation did not take place, the reaction did proceed through an oxygen-atom transfer to form an N-oxide. Further insight could come from isolating the N-oxide to confirm the exact site of oxidation. However, preliminary experiments show that this is not a simple task.

The structure and reactivity of copper halide complexes of **LTEA** were investigated (Chapter 4). Hydrogen bonding from the cryptand to the coordinated anion, in conjunction with protonation led to complete encapsulation of the Cu(II)-fluoride centre. Conversely, the Cu(II)-chloride centres were unable to form sufficient hydrogen bonds to overcome the strain of encapsulation. A hydroperoxo intermediate was formed from the Cu(II)-fluoride complex and found to have the same UV/Vis profile as hydroperoxo species formed from the Cu(II)-acetate complex. The Cu(II)-chloride complex showed no reactivity. Further insight into the reactivity of the hydroperoxo intermediate starting from the fluoride complex can come from mechanistic studies using stopped-flow UV/Vis, and EPR spectroscopy studies to situate the reactivity in comparison to the Cu(II)-acetate complex. These studies would help determine how many Cu(II)-hydroperoxo intermediates are formed and help differentiate the reactivity of the two Cu(II)-acetate complexes.

The design and synthesis of **LTTA** resulted in a high-yielding ditopic cryptand (Chapter 5). **LTTA,** in comparison to **LTEA,** has a large cavity with triazole groups that can interact directly with an anion. An Fe(III)-hydroperoxo, supported by **LTTA,** was shown to hydroxylate aromatic C-H bonds on the ligand

(Chapter 6). Furthermore, **LTTA** was able to support the formation of a high-valent Fe(IV)-oxo intermediate. These are the first examples of Fe/O_2 intermediates with a cryptand. While this research is young, it shows great promise for future studies of the second coordination sphere impact on the oxidation chemistry. A great deal of insight will come from fully characterizing the intermediates with Mössbauer, MCD and EPR, as these techniques will provide local information about the geometry and spin state of the iron complexes. However, these techniques require specific solvents that form a glass-like frozen state. Preliminary results show that the reaction is complicated by the change in solvent system and that optimization of the solvent conditions will be needed. Finally, investigations into the exact site of oxidation will provide more clues to elucidate the mechanism of C-H bond oxidation. Again, isolation and purification prove challenging.

7.2 Future Work

The future direction of these projects can be divided into three categories:

1) Expanding the reactivity of [**LTTA**Fe(TfO)]$^+$ and [**LTEA**CuF]$^+$;
2) Investigating the reactivity of **LTEA** and **LTTA** with different metal centres;
3) Re-designing cryptands.

The Cu(II)-acetate chemistry with **LTEA** was complicated by the prescence of two complexes in solution. It could therefore be advantageous to pursue the oxidative studies starting from the Cu(II)-fluoride complex, which may be forming one Cu(II)-hydroperoxo intermediate. These simplified studies may provide greater insight into how the oxygen atom is transferred from the hydroperoxo to the ligand. In the case of the oxidative iron chemistry with **LTTA**, further investigation into the mechanism of the aromatic C-H bond hydroxylation is necessary. This will include mechanistic probes such as isotope labelling studies, using radical scavengers and synthesizing a deuterated **LTTA** for kinetics and identification of a 1,2-hydride shift. Finally, an Fe(IV)-oxo complex was formed and preliminary results show intermolecular oxygen-atom transfer to phosphines. Further investigation is warranted to gain a greater insight into the mechanism of OAT of an Fe(IV)-oxo species.

The second research stream would be aimed at investigating different M/O_2 intermediates supported by the cryptands. From the perspective of comparing the reactivity of one metal centre supported by two different cryptands, it would be interesting to look at iron complexes with **LTEA** and copper

complexes with **LTTA.** To compare copper complexes, methylated **LTTA** (**8**) would be used and conditions to form a hydroperoxo intermediate would be optimized. Alternatively, non-methylated **LTEA** ($\mathbf{1}^{H}$) would be used to investigate the formation of Fe(III)-hydroperoxo intermediate. The comparison of the reactivity between the two cryptands would provide insight into which functional groups/geometry/electronic structures are necessary to induce selectivity between oxygen-atom transfers or C-H bond hydroxylations.

Finally, this project has provided insight into how coordinating cryptands can interact with anions. Thus, redesigning cryptands to enhance the second coordination sphere interactions would be useful. The findings from the copper fluoride versus chloride research suggest that expanding **LTEA** and incorporating stronger hydrogen bond donor groups could yield a cryptand that fully encapsulates a reactive intermediate. Molecular modelling would be valuable in selecting target ligands. With **LTTA,** methylation of the secondary amines would potentially reduce the number of side reaction and simplify mechanistic studies. The synthesis LTTA with *ortho* and *para* phenylene groups could potentially provide insight into the location of C-H bond hydroxylation.

As these studies expand, a picture will emerge on how to control the reactivity of M/O_2 intermediates, which will lead to new elements of design for enhancing the selectivity of O_2- and H_2O_2-based oxidations of substituents. In addition, this understanding of the second coordination sphere will help develop intermolecular reactions with substrates that would bind to the cryptand prior to being oxidized.

Chapter 8: References

1. Itoh, S., Mononuclear copper active-oxygen complexes. *Curr. Opin. Chem. Biol.* **2006,** *10* (2), 115-122.

2. Arakawa, H.; Aresta, M.; Armor, J. N.; Barteau, M. A.; Beckman, E. J.; Bell, A. T.; Bercaw, J. E.; Creutz, C.; Dinjus, E.; Dixon, D. A.; Domen, K.; DuBois, D. L.; Eckert, J.; Fujita, E.; Gibson, D. H.; Goddard, W. A.; Goodman, D. W.; Keller, J.; Kubas, G. J.; Kung, H. H.; Lyons, J. E.; Manzer, L. E.; Marks, T. J.; Morokuma, K.; Nicholas, K. M.; Periana, R.; Que, L.; Rostrup-Nielson, J.; Sachtler, W. M. H.; Schmidt, L. D.; Sen, A.; Somorjai, G. A.; Stair, P. C.; Stults, B. R.; Tumas, W., Catalysis Research of Relevance to Carbon Management: Progress, Challenges, and Opportunities. *Chem. Rev.* **2001,** *101* (4), 953-996.

3. Wencel-Delord, J.; Droge, T.; Liu, F.; Glorius, F., Towards mild metal-catalyzed C-H bond activation. *Chem. Soc. Rev.* **2011,** *40* (9), 4740-4761.

4. Pérez, P. J., *Alkane C-H Activation by Single-Site Metal Catalysis*. Springer Netherlands: 2012.

5. Gormisky, P. E.; White, M. C., Catalyst-Controlled Aliphatic C–H Oxidations with a Predictive Model for Site-Selectivity. *J. Am. Chem. Soc.* **2013,** *135* (38), 14052-14055.

6. Conde, A.; Vilella, L.; Balcells, D.; Díaz-Requejo, M. M.; Lledós, A.; Pérez, P. J., Introducing Copper as Catalyst for Oxidative Alkane Dehydrogenation. *J. Am. Chem. Soc.* **2013,** *135* (10), 3887-3896.

7. Solomon, E. I.; Heppner, D. E.; Johnston, E. M.; Ginsbach, J. W.; Cirera, J.; Qayyum, M.; Kieber-Emmons, M. T.; Kjaergaard, C. H.; Hadt, R. G.; Tian, L., Copper Active Sites in Biology. *Chem. Rev.* **2014,** *114* (7), 3659-3853.

8. Que, L.; Ho, R. Y. N., Dioxygen Activation by Enzymes with Mononuclear Non-Heme Iron Active Sites. *Chem. Rev.* **1996,** *96* (7), 2607-2624.

9. Que, L.; Tolman, W. B., Biologically inspired oxidation catalysis. *Nature* **2008,** *455* (7211), 333-340.

10. Decker, A.; Solomon, E. I., Dioxygen activation by copper, heme and non-heme iron enzymes: comparison of electronic structures and reactivities. *Curr. Opin. Chem. Biol.* **2005,** *9* (2), 152-163.

11. Lu, T.; Zhuang, X.; Li, Y.; Chen, S., C−C Bond Cleavage of Acetonitrile by a Dinuclear Copper(II) Cryptate. *J. Am. Chem. Soc.* **2004,** *126* (15), 4760-4761.

12. Mirica, L. M.; Ottenwaelder, X.; Stack, T. D. P., Structure and Spectroscopy of Copper−Dioxygen Complexes. *Chem. Rev.* **2004,** *104* (2), 1013-1046.

13. Costas, M.; Mehn, M. P.; Jensen, M. P.; Que, L., Dioxygen Activation at Mononuclear Nonheme Iron Active Sites: Enzymes, Models, and Intermediates. *Chem. Rev.* **2004,** *104* (2), 939-986.

14. Holm, R. H., Metal-centered oxygen atom transfer reactions. *Chem. Rev.* **1987,** *87* (6), 1401-1449.

15. Mayer, J. M., Understanding Hydrogen Atom Transfer: From Bond Strengths to Marcus Theory. *Acc. Chem. Res.* **2011,** *44* (1), 36-46.

16. Lewis, E. A.; Tolman, W. B., Reactivity of Dioxygen−Copper Systems. *Chem. Rev.* **2004,** *104* (2), 1047-1076.

17. Osborne, R. L.; Klinman, J. P., Insights into the Proposed Copper–Oxygen Intermediates that Regulate the Mechanism of Reactions Catalyzed by Dopamine β-Monooxygenase, Peptidylglycine α-Hydroxylating Monooxygenase, and Tyramine β-Monooxygenase. In *Copper-Oxygen Chemistry*, John Wiley & Sons, Inc.: 2011; pp 1-22.

18. Tian, G.; Berry, J. A.; Klinman, J. P., Oxygen-18 kinetic isotope effects in the dopamine .beta.-monooxygenase reaction: Evidence for a new chemical mechanism in non-heme, metallomonooxygenase. *Biochemistry* **1994,** *33* (1), 226-234.

19. Würtele, C.; Gaoutchenova, E.; Harms, K.; Holthausen, M. C.; Sundermeyer, J.; Schindler, S., Crystallographic Characterization of a Synthetic 1:1 End-On Copper Dioxygen Adduct Complex. *Angew. Chem. Int. Ed.* **2006,** *45* (23), 3867-3869.

20. Prigge, S. T.; Mains, R. E.; Eipper, B. A.; Amzel, L. M., New insights into copper monooxygenases and peptide amidation: structure, mechanism and function. *Cell. Mol. Life Sci.* **2000,** *57* (8), 1236-1259.

21. Solomon, E. I.; Ginsbach, J. W.; Heppner, D. E.; Kieber-Emmons, M. T.; Kjaergaard, C. H.; Smeets, P. J.; Tian, L.; Woertink, J. S., Copper dioxygen (bio)inorganic chemistry. *Faraday Discuss.* **2011,** *148* (0), 11-39.

22. Prigge, S. T.; Kolhekar, A. S.; Eipper, B. A.; Mains, R. E.; Amzel, L. M., Amidation of Bioactive Peptides: The Structure of Peptidylglycine α-Hydroxylating Monooxygenase. *Science* **1997,** *278* (5341), 1300-1305.

23. Ali, A. M. H.; Lee, J. M.; Yoshida, M.; Sakashita, K.; Torii, J.; Kusakabe, T.; Hirashima, A., Expression and characterization of a recombinant Drosophila tyramine-β-hydroxylase in silkworm infected with recombinant baculovirus. *J. Asia Pac. Entomol.* **2012,** *15* (4), 567-572.

24. Prigge, S. T.; Eipper, B. A.; Mains, R. E.; Amzel, L. M., Dioxygen Binds End-On to Mononuclear Copper in a Precatalytic Enzyme Complex. *Science* **2004,** *304* (5672), 864-867.

25. Klinman, J. P.; Humphries, H.; Voet, J. G., Deduction of kinetic mechanism in multisubstrate enzyme reactions from tritium isotope effects. Application to dopamine beta-hydroxylase. *J. Biol. Chem.* **1980,** *255* (24), 11648-11651.

26. Chen, P.; Solomon, E. I., Oxygen Activation by the Noncoupled Binuclear Copper Site in Peptidylglycine α-Hydroxylating Monooxygenase. Reaction Mechanism and Role of the Noncoupled Nature of the Active Site. *J. Am. Chem. Soc.* **2004,** *126* (15), 4991-5000.

27. Miller, S. M.; Klinman, J. P., Secondary isotope effects and structure-reactivity correlations in the dopamine .beta.-monooxygenase reaction: evidence for a chemical mechanism. *Biochemistry* **1985,** *24* (9), 2114-2127.

28. Humphreys, K. J.; Mirica, L. M.; Wang, Y.; Klinman, J. P., Galactose Oxidase as a Model for Reactivity at a Copper Superoxide Center. *J. Am. Chem. Soc.* **2009,** *131* (13), 4657-4663.

29. Francisco, W. A.; Wille, G.; Smith, A. J.; Merkler, D. J.; Klinman, J. P., Investigation of the Pathway for Inter-Copper Electron Transfer in Peptidylglycine α-Amidating Monooxygenase. *J. Am. Chem. Soc.* **2004,** *126* (41), 13168-13169.

30. Denisov, I. G.; Makris, T. M.; Sligar, S. G.; Schlichting, I., Structure and Chemistry of Cytochrome P450. *Chem. Rev.* **2005,** *105* (6), 2253-2278.

31. Ortiz de Montellano, P. R., Hydrocarbon Hydroxylation by Cytochrome P450 Enzymes. *Chem. Rev.* **2009,** *110* (2), 932-948.

32. Rittle, J.; Green, M. T., Cytochrome P450 Compound I: Capture, Characterization, and C-H Bond Activation Kinetics. *Science* **2010,** *330* (6006), 933-937.

33. Burger, R., Nature of Activated Bleomycin. In *Metal-Oxo and Metal-Peroxo Species in Catalytic Oxidations*, Meunier, B., Ed. Springer Berlin Heidelberg: 2000; Vol. 97, pp 287-303.

34. Solomon, E. I.; Wong, S. D.; Liu, L. V.; Decker, A.; Chow, M. S., Peroxo and oxo intermediates in mononuclear nonheme iron enzymes and related active sites. *Curr. Opin. Chem. Biol.* **2009,** *13* (1), 99-113.

35. Chow, M. S.; Liu, L. V.; Solomon, E. I., Further insights into the mechanism of the reaction of activated bleomycin with DNA. *Proc. Natl. Acad. Sci. U. S. A.* **2008,** *105* (36), 13241-13245.

36. Hegg, E. L.; Jr, L. Q., The 2-His-1-Carboxylate Facial Triad — An Emerging Structural Motif in Mononuclear Non-Heme Iron(II) Enzymes. *Eur. J. Biochem.* **1997,** *250* (3), 625-629.

37. Bruijnincx, P. C. A.; van Koten, G.; Klein Gebbink, R. J. M., Mononuclear non-heme iron enzymes with the 2-His-1-carboxylate facial triad: recent developments in enzymology and modeling studies. *Chem. Soc. Rev.* **2008,** *37* (12), 2716-2744.

38. Ferraro, D. J.; Gakhar, L.; Ramaswamy, S., Rieske business: Structure–function of Rieske non-heme oxygenases. *Biochem. Biophys. Res. Commun.* **2005,** *338* (1), 175-190.

39. Karlsson, A.; Parales, J. V.; Parales, R. E.; Gibson, D. T.; Eklund, H.; Ramaswamy, S., Crystal Structure of Naphthalene Dioxygenase: Side-on Binding of Dioxygen to Iron. *Science* **2003,** *299* (5609), 1039-1042.

40. Ashikawa, Y.; Fujimoto, Z.; Usami, Y.; Inoue, K.; Noguchi, H.; Yamane, H.; Nojiri, H., Structural insight into the substrate- and dioxygen-binding manner in the catalytic cycle of rieske nonheme iron oxygenase system, carbazole 1,9a-dioxygenase. *BMC Struct. Biol.* **2012,** *12* (1), 15.

41. Neibergall, M. B.; Stubna, A.; Mekmouche, Y.; Münck, E.; Lipscomb, J. D., Hydrogen Peroxide Dependent cis-Dihydroxylation of Benzoate by Fully Oxidized Benzoate 1,2-Dioxygenase†. *Biochemistry* **2007,** *46* (27), 8004-8016.

42. Purpero, V.; Moran, G., The diverse and pervasive chemistries of the α-keto acid dependent enzymes. *J. Biol. Inorg. Chem.* **2007,** *12* (5), 587-601.

43. Kryatov, S. V.; Rybak-Akimova, E. V.; Schindler, S., Kinetics and Mechanisms of Formation and Reactivity of Non-heme Iron Oxygen Intermediates. *Chem. Rev.* **2005,** *105* (6), 2175-2226.

44. Maiti, D.; Lee, D.-H.; Gaoutchenova, K.; Würtele, C.; Holthausen, M. C.; Narducci Sarjeant, A. A.; Sundermeyer, J.; Schindler, S.; Karlin, K. D., Reactions of a Copper(II) Superoxo Complex Lead to C-H and O-H Substrate Oxygenation: Modeling Copper-Monooxygenase C-H Hydroxylation. *Angew. Chem. Int. Ed.* **2008,** *47* (1), 82-85.

45. Fujii, T.; Naito, A.; Yamaguchi, S.; Wada, A.; Funahashi, Y.; Jitsukawa, K.; Nagatomo, S.; Kitagawa, T.; Masuda, H., Construction of a square-planar hydroperoxo-copper(ii) complex inducing a higher catalytic reactivity. *Chem. Commun.* **2003,** (21), 2700-2701.

46. Biswas, S.; Dutta, A.; Debnath, M.; Dolai, M.; Das, K. K.; Ali, M., A novel thermally stable hydroperoxo-copper(ii) complex in a Cu(N2O2) chromophore of a potential N4O2 donor Schiff base ligand: synthesis, structure and catalytic studies. *Dalton Trans.* **2013,** *42* (36), 13210-13219.

47. Maiti, D.; Narducci Sarjeant, A. A.; Karlin, K. D., Copper−Hydroperoxo-Mediated N-Debenzylation Chemistry Mimicking Aspects of Copper Monooxygenases. *Inorg. Chem.* **2008,** *47* (19), 8736-8747.

48. Kunishita, A.; Scanlon, J. D.; Ishimaru, H.; Honda, K.; Ogura, T.; Suzuki, M.; Cramer, C. J.; Itoh, S., Reactions of Copper(II)-H2O2 Adducts Supported by Tridentate Bis(2-pyridylmethyl)amine Ligands: Sensitivity to Solvent and Variations in Ligand Substitution. *Inorg. Chem.* **2008,** *47* (18), 8222-8232.

49. Yamaguchi, S.; Nagatomo, S.; Kitagawa, T.; Funahashi, Y.; Ozawa, T.; Jitsukawa, K.; Masuda, H., Copper Hydroperoxo Species Activated by Hydrogen-Bonding Interaction with Its Distal Oxygen. *Inorg. Chem.* **2003,** *42* (22), 6968-6970.

50. Kamachi, T.; Lee, Y.-M.; Nishimi, T.; Cho, J.; Yoshizawa, K.; Nam, W., Combined Experimental and Theoretical Approach To Understand the Reactivity of a Mononuclear Cu(II)−Hydroperoxo Complex in Oxygenation Reactions†. *J. Phys. Chem. A* **2008,** *112* (50), 13102-13108.

51. Maiti, D.; Lucas, H. R.; Sarjeant, A. A. N.; Karlin, K. D., Aryl Hydroxylation from a Mononuclear Copper-Hydroperoxo Species. *J. Am. Chem. Soc.* **2007,** *129* (22), 6998-6999.

52. Maiti, D.; Narducci Sarjeant, A. A.; Karlin, K. D., Copper(II)−Hydroperoxo Complex Induced Oxidative N-Dealkylation Chemistry. *J. Am. Chem. Soc.* **2007,** *129* (21), 6720-6721.

53. Rolff, M.; Tuczek, F., How Do Copper Enzymes Hydroxylate Aliphatic Substrates? Recent Insights from the Chemistry of Model Systems. *Angew. Chem. Int. Ed.* **2008,** *47* (13), 2344-2347.

54. Maiti, D.; Fry, H. C.; Woertink, J. S.; Vance, M. A.; Solomon, E. I.; Karlin, K. D., A 1:1 Copper−Dioxygen Adduct is an End-on Bound Superoxo Copper(II) Complex which Undergoes Oxygenation Reactions with Phenols. *J. Am. Chem. Soc.* **2006,** *129* (2), 264-265.

55. Kim, S.; Lee, J. Y.; Cowley, R. E.; Ginsbach, J. W.; Siegler, M. A.; Solomon, E. I.; Karlin, K. D., A N3S(thioether)-Ligated CuII-Superoxo with Enhanced Reactivity. *J. Am. Chem. Soc.* **2015,** *137* (8), 2796-2799.

56. Itoh, S., Chemical Reactivity of Copper Active-Oxygen Complexes. In *Copper-Oxygen Chemistry*, John Wiley & Sons, Inc.: 2011; pp 225-282.

57. Osako, T.; Nagatomo, S.; Kitagawa, T.; Cramer, C.; Itoh, S., Kinetics and DFT studies on the reaction of copper(II) complexes and H2O2. *J. Biol. Inorg. Chem.* **2005,** *10* (5), 581-590.

58. Wada, A.; Harata, M.; Hasegawa, K.; Jitsukawa, K.; Masuda, H.; Mukai, M.; Kitagawa, T.; Einaga, H., Structural and Spectroscopic Characterization of a Mononuclear Hydroperoxo–Copper(II) Complex with Tripodal Pyridylamine Ligands. *Angew. Chem. Int. Ed.* **1998,** *37* (6), 798-799.

59. Kim, S.; Saracini, C.; Siegler, M. A.; Drichko, N.; Karlin, K. D., Coordination Chemistry and Reactivity of a Cupric Hydroperoxide Species Featuring a Proximal H-Bonding Substituent. *Inorg. Chem.* **2012,** *51* (23), 12603-12605.

60. Yamaguchi, S.; Masuda, H., Basic approach to development of environment-friendly oxidation catalyst materials. Mononuclear hydroperoxo copper(II) complexes. *Sci. Technol. Adv. Mater.* **2005,** *6* (1), 34-47.

61. Yamaguchi, S.; Kumagai, A.; Nagatomo, S.; Kitagawa, T.; Funahashi, Y.; Ozawa, T.; Jitsukawa, K.; Masuda, H., Synthesis, Characterization, and Thermal Stability of New Mononuclear Hydrogenperoxocopper(II) Complexes with N3O-Type Tripodal Ligands Bearing Hydrogen-Bonding Interaction Sites. *Bull. Chem. Soc. Jpn.* **2005,** *78* (1), 116-124.

62. Cheruzel, L. E.; Cecil, M. R.; Edison, S. E.; Mashuta, M. S.; Baldwin, M. J.; Buchanan, R. M., Structural and Spectroscopic Characterization of Copper(II) Complexes of a New Bisamide Functionalized Imidazole Tripod and Evidence for the Formation of a Mononuclear End-On Cu−OOH Species. *Inorg. Chem.* **2006,** *45* (8), 3191-3202.

63. Kodera, M.; Kita, T.; Miura, I.; Nakayama, N.; Kawata, T.; Kano, K.; Hirota, S., Hydroperoxo−Copper(II) Complex Stabilized by N3S-Type Ligand Having a Phenyl Thioether. *J. Am. Chem. Soc.* **2001,** *123* (31), 7715-7716.

64. Park, G. Y.; Lee, J. Y.; Himes, R. A.; Thomas, G. S.; Blackburn, N. J.; Karlin, K. D., Copper–Peptide Complex Structure and Reactivity When Found in Conserved His-Xaa-His Sequences. *J. Am. Chem. Soc.* **2014,** *136* (36), 12532-12535.

65. Ray, K.; Pfaff, F. F.; Wang, B.; Nam, W., Status of Reactive Non-Heme Metal–Oxygen Intermediates in Chemical and Enzymatic Reactions. *J. Am. Chem. Soc.* **2014,** *136* (40), 13942-13958.

66. Hohenberger, J.; Ray, K.; Meyer, K., The biology and chemistry of high-valent iron-oxo and iron-nitrido complexes. *Nat Commun* **2012,** *3*, 720.

67. Buongiorno, D.; Straganz, G. D., Structure and function of atypically coordinated enzymatic mononuclear non-heme-Fe(II) centers. *Coord. Chem. Rev.* **2013,** *257* (2), 541-563.

68. Bryliakov, K. P.; Talsi, E. P., Active sites and mechanisms of bioinspired oxidation with H2O2, catalyzed by non-heme Fe and related Mn complexes. *Coord. Chem. Rev.* **2014,** *276* (0), 73-96.

69. Nam, W.; Lee, Y.-M.; Fukuzumi, S., Tuning Reactivity and Mechanism in Oxidation Reactions by Mononuclear Nonheme Iron(IV)-Oxo Complexes. *Acc. Chem. Res.* **2014,** *47* (4), 1146-1154.

70. Solomon, E. I.; Light, K. M.; Liu, L. V.; Srnec, M.; Wong, S. D., Geometric and Electronic Structure Contributions to Function in Non-heme Iron Enzymes. *Acc. Chem. Res.* **2013,** *46* (11), 2725-2739.

71. Roelfes, G.; Lubben, M.; Chen, K.; Ho, R. Y. N.; Meetsma, A.; Genseberger, S.; Hermant, R. M.; Hage, R.; Mandal, S. K.; Young, V. G.; Zang, Y.; Kooijman, H.; Spek, A. L.; Que, L.; Feringa, B. L., Iron Chemistry of a Pentadentate Ligand That Generates a Metastable FeIII−OOH Intermediate. *Inorg. Chem.* **1999,** *38* (8), 1929-1936.

72. Guajardo, R. J.; Hudson, S. E.; Brown, S. J.; Mascharak, P. K., [Fe(PMA)]n+ (n = 1,2): good models of iron-bleomycins and examples of mononuclear non-heme iron complexes with significant oxygen-activation capabilities. *J. Am. Chem. Soc.* **1993,** *115* (18), 7971-7977.

73. Wada, A.; Ogo, S.; Nagatomo, S.; Kitagawa, T.; Watanabe, Y.; Jitsukawa, K.; Masuda, H., Reactivity of Hydroperoxide Bound to a Mononuclear Non-Heme Iron Site. *Inorg. Chem.* **2002,** *41* (4), 616-618.

74. Martinho, M.; Dorlet, P.; Rivière, E.; Thibon, A.; Ribal, C.; Banse, F.; Girerd, J.-J., Preparation and Characterization of a Microcrystalline Non-Heme FeIII(OOH) Complex Powder: EPR Reinvestigation of FeIII(OOH) Complexes—Improvement of the Perturbation Equations for the g Tensor of Low-Spin FeIII. *Chem. Eur. J.* **2008,** *14* (10), 3182-3188.

75. Park, M. J.; Lee, J.; Suh, Y.; Kim, J.; Nam, W., Reactivities of Mononuclear Non-Heme Iron Intermediates Including Evidence that Iron(III)−Hydroperoxo Species Is a Sluggish Oxidant. *J. Am. Chem. Soc.* **2006,** *128* (8), 2630-2634.

76. Kim, Y. M.; Cho, K.-B.; Cho, J.; Wang, B.; Li, C.; Shaik, S.; Nam, W., A Mononuclear Non-Heme High-Spin Iron(III)–Hydroperoxo Complex as an Active Oxidant in Sulfoxidation Reactions. *J. Am. Chem. Soc.* **2013,** *135* (24), 8838-8841.

77. Liu, L. V.; Hong, S.; Cho, J.; Nam, W.; Solomon, E. I., Comparison of High-Spin and Low-Spin Nonheme FeIII–OOH Complexes in O–O Bond Homolysis and H-Atom Abstraction Reactivities. *J. Am. Chem. Soc.* **2013,** *135* (8), 3286-3299.

78. Cho, J.; Jeon, S.; Wilson, S. A.; Liu, L. V.; Kang, E. A.; Braymer, J. J.; Lim, M. H.; Hedman, B.; Hodgson, K. O.; Valentine, J. S.; Solomon, E. I.; Nam, W., Structure and reactivity of a mononuclear non-haem iron(III)–peroxo complex. *Nature* **2011,** *478* (7370), 502-505.

79. Jensen, M. P.; Lange, S. J.; Mehn, M. P.; Que, E. L.; Que, L., Biomimetic Aryl Hydroxylation Derived from Alkyl Hydroperoxide at a Nonheme Iron Center. Evidence for an FeIVO Oxidant. *J. Am. Chem. Soc.* **2003,** *125* (8), 2113-2128.

80. Lange, S. J.; Miyake, H.; Que, L., Evidence for a Nonheme Fe(IV)O Species in the Intramolecular Hydroxylation of a Phenyl Moiety. *J. Am. Chem. Soc.* **1999,** *121* (26), 6330-6331.

81. Nielsen, A.; Larsen, F. B.; Bond, A. D.; McKenzie, C. J., Regiospecific Ligand Oxygenation in Iron Complexes of a Carboxylate-Containing Ligand Mediated by a Proposed FeV–Oxo Species. *Angew. Chem. Int. Ed.* **2006,** *118* (10), 1632-1636.

82. Thibon, A.; Jollet, V.; Ribal, C.; Sénéchal-David, K.; Billon, L.; Sorokin, A. B.; Banse, F., Hydroxylation of Aromatics with the Help of a Non-Haem FeOOH: A Mechanistic Study under Single-Turnover and Catalytic Conditions. *Chem. Eur. J.* **2012,** *18* (9), 2715-2724.

83. Mekmouche, Y.; Ménage, S.; Toia-Duboc, C.; Fontecave, M.; Galey, J.-B.; Lebrun, C.; Pécaut, J., H2O2-Dependent Fe-Catalyzed Oxidations: Control of the Active Species. *Angew. Chem. Int. Ed.* **2001,** *40* (5), 949-952.

84. Mekmouche, Y.; Ménage, S.; Pécaut, J.; Lebrun, C.; Reilly, L.; Schuenemann, V.; Trautwein, A.; Fontecave, M., Mechanistic Tuning of Hydrocarbon Oxidations with H2O2, Catalyzed by Hexacoordinate Ferrous Complexes. *Eur. J. Inorg. Chem.* **2004,** *2004* (15), 3163-3171.

85. Makhlynets, O. V.; Rybak-Akimova, E. V., Aromatic Hydroxylation at a Non-Heme Iron Center: Observed Intermediates and Insights into the Nature of the Active Species. *Chem. Eur. J.* **2010,** *16* (47), 13995-14006.

86. Mehn, M. P.; Fujisawa, K.; Hegg, E. L.; Que, L., Oxygen Activation by Nonheme Iron(II) Complexes: α-Keto Carboxylate versus Carboxylate. *J. Am. Chem. Soc.* **2003,** *125* (26), 7828-7842.

87. Bigi, J. P.; Harman, W. H.; Lassalle-Kaiser, B.; Robles, D. M.; Stich, T. A.; Yano, J.; Britt, R. D.; Chang, C. J., A High-Spin Iron(IV)–Oxo Complex Supported by a Trigonal Nonheme Pyrrolide Platform. *J. Am. Chem. Soc.* **2012,** *134* (3), 1536-1542.

88. Taktak, S.; Flook, M.; Foxman, B. M.; Que, J. L.; Rybak-Akimova, E. V., ortho-Hydroxylation of benzoic acids with hydrogen peroxide at a non-heme iron center. *Chem. Commun.* **2005,** (42), 5301-5303.

89. de Oliveira, F. T.; Chanda, A.; Banerjee, D.; Shan, X.; Mondal, S.; Que, L.; Bominaar, E. L.; Münck, E.; Collins, T. J., Chemical and Spectroscopic Evidence for an FeV-Oxo Complex. *Science* **2007,** *315* (5813), 835-838.

90. Kundu, S.; Thompson, J. V. K.; Ryabov, A. D.; Collins, T. J., On the Reactivity of Mononuclear Iron(V)oxo Complexes. *J. Am. Chem. Soc.* **2011,** *133* (46), 18546-18549.

91. Prat, I.; Mathieson, J. S.; Güell, M.; Ribas, X.; Luis, J. M.; Cronin, L.; Costas, M., Observation of Fe(V)=O using variable-temperature mass spectrometry and its enzyme-like C–H and C=C oxidation reactions. *Nature Chem.* **2011,** *3* (10), 788-793.

92. Shook, R. L.; Borovik, A. S., Role of the Secondary Coordination Sphere in Metal-Mediated Dioxygen Activation. *Inorg. Chem.* **2010,** *49* (8), 3646-3660.

93. England, J.; Guo, Y.; Farquhar, E. R.; Young Jr, V. G.; Münck, E.; Que Jr, L., The Crystal Structure of a High-Spin Oxoiron(IV) Complex and Characterization of Its Self-Decay Pathway. *J. Am. Chem. Soc.* **2010,** *132* (25), 8635-8644.

94. England, J.; Martinho, M.; Farquhar, E. R.; Frisch, J. R.; Bominaar, E. L.; Münck, E.; Que, L., A Synthetic High-Spin Oxoiron(IV) Complex: Generation, Spectroscopic Characterization, and Reactivity. *Angew. Chem. Int. Ed.* **2009,** *48* (20), 3622-3626.

95. Zhao, M.; Wang, H.-B.; Ji, L.-N.; Mao, Z.-W., Insights into metalloenzyme microenvironments: biomimetic metal complexes with a functional second coordination sphere. *Chem. Soc. Rev.* **2013,** *42* (21), 8360-8375.

96. Lacy, D. C.; Gupta, R.; Stone, K. L.; Greaves, J.; Ziller, J. W.; Hendrich, M. P.; Borovik, A. S., Formation, Structure, and EPR Detection of a High Spin FeIV—Oxo Species Derived from Either an FeIII—Oxo or FeIII—OH Complex. *J. Am. Chem. Soc.* **2010,** *132* (35), 12188-12190.

97. MacBeth, C. E.; Golombek, A. P.; Young, V. G.; Yang, C.; Kuczera, K.; Hendrich, M. P.; Borovik, A. S., O2 Activation by Nonheme Iron Complexes: A Monomeric Fe(III)-Oxo Complex Derived From O2. *Science* **2000,** *289* (5481), 938-941.

98. Widger, L. R.; Davies, C. G.; Yang, T.; Siegler, M. A.; Troeppner, O.; Jameson, G. N. L.; Ivanović-Burmazović, I.; Goldberg, D. P., Dramatically Accelerated Selective Oxygen-Atom Transfer by a Nonheme Iron(IV)-Oxo Complex: Tuning of the First and Second Coordination Spheres. *J. Am. Chem. Soc.* **2014,** *136* (7), 2699-2702.

99. Constable, E. C., *Coordination Chemistry of Macrocyclic Compounds*. Oxford University Press: 1999.

100. Bowman-James, K., Macrocyclic Ligands. In *Encyclopedia of Inorganic and Bioinorganic Chemistry*, John Wiley & Sons, Ltd: 2011.

101. Hong, S.; So, H.; Yoon, H.; Cho, K.-B.; Lee, Y.-M.; Fukuzumi, S.; Nam, W., Reactivity comparison of high-valent iron(iv)-oxo complexes bearing N-tetramethylated cyclam ligands with different ring size. *Dalton Trans.* **2013,** *42* (22), 7842-7845.

102. Cho, J.; Sarangi, R.; Nam, W., Mononuclear Metal–O2 Complexes Bearing Macrocyclic N-Tetramethylated Cyclam Ligands. *Acc. Chem. Res.* **2012,** *45* (8), 1321-1330.

103. Sastri, C. V.; Lee, J.; Oh, K.; Lee, Y. J.; Lee, J.; Jackson, T. A.; Ray, K.; Hirao, H.; Shin, W.; Halfen, J. A.; Kim, J.; Que, L.; Shaik, S.; Nam, W., Axial ligand tuning of a nonheme iron(IV)–oxo unit for hydrogen atom abstraction. *Proc. Natl. Acad. Sci. U. S. A.* **2007,** *104* (49), 19181-19186.

104. Jackson, T. A.; Rohde, J.-U.; Seo, M. S.; Sastri, C. V.; DeHont, R.; Stubna, A.; Ohta, T.; Kitagawa, T.; Münck, E.; Nam, W.; Que, L., Axial Ligand Effects on the Geometric and Electronic Structures of Nonheme Oxoiron(IV) Complexes. *J. Am. Chem. Soc.* **2008,** *130* (37), 12394-12407.

105. Decker, A.; Rohde, J.-U.; Klinker, E. J.; Wong, S. D.; Que, L.; Solomon, E. I., Spectroscopic and Quantum Chemical Studies on Low-Spin FeIVO Complexes: Fe−O Bonding and Its Contributions to Reactivity. *J. Am. Chem. Soc.* **2007,** *129* (51), 15983-15996.

106. Annaraj, J.; Suh, Y.; Seo, M. S.; Kim, S. O.; Nam, W., Mononuclear nonheme ferric-peroxo complex in aldehyde deformylation. *Chem. Commun.* **2005,** (36), 4529-4531.

107. de Visser, S. P.; Rohde, J.-U.; Lee, Y.-M.; Cho, J.; Nam, W., Intrinsic properties and reactivities of mononuclear nonheme iron–oxygen complexes bearing the tetramethylcyclam ligand. *Coord. Chem. Rev.* **2013,** *257* (0), 381-393.

108. Ariga, K.; Kunitake, T., *Supramolecular Chemistry - Fundamentals and Applications: Advanced Textbook*. Springer Berlin Heidelberg: 2006.

109. Dietrich, B.; Lehn, J. M.; Sauvage, J. P., Les Cryptates. *Tetrahedron Lett.* **1969,** *10* (34), 2889-2892.

110. Rebilly, J.-N.; Colasson, B.; Bistri, O.; Over, D.; Reinaud, O., Biomimetic cavity-based metal complexes. *Chem. Soc. Rev.* **2015,** *44* (2), 467-489.

111. Izzet, G.; Zeitouny, J.; Akdas-Killig, H.; Frapart, Y.; Ménage, S. p.; Douziech, B. n. d.; Jabin, I.; Le Mest, Y.; Reinaud, O., Dioxygen Activation at a Mononuclear Cu(I) Center Embedded in the Calix[6]arene-Tren Core. *J. Am. Chem. Soc.* **2008,** *130* (29), 9514-9523.

112. Thiabaud, G.; Guillemot, G.; Schmitz-Afonso, I.; Colasson, B.; Reinaud, O., Solid-State Chemistry at an Isolated Copper(I) Center with O2. *Angew. Chem. Int. Ed.* **2009,** *48* (40), 7383-7386.

113. Kharisov, B. I.; Elizondo Martínez, P.; Jiménez-Pérez, V. M.; Kharissova, O. V.; Nájera Martínez, B.; Pérez, N., Recent advances on ditopic ligands. *J. Coord. Chem.* **2009,** *63* (1), 1-25.

114. Fabbrizzi, L.; Poggi, A., Anion recognition by coordinative interactions: metal-amine complexes as receptors. *Chem. Soc. Rev.* **2013,** *42* (4), 1681-1699.

115. Kang, S. O.; Llinares, J. M.; Day, V. W.; Bowman-James, K., Cryptand-like anion receptors. *Chem. Soc. Rev.* **2010,** *39* (10), 3980-4003.

116. McDonald, K. P.; Hua, Y.; Lee, S.; Flood, A. H., Shape persistence delivers lock-and-key chloride binding in triazolophanes. *Chem. Commun.* **2012,** *48* (42), 5065-5075.

117. Hua, Y.; Flood, A. H., Click chemistry generates privileged CH hydrogen-bonding triazoles: the latest addition to anion supramolecular chemistry. *Chem. Soc. Rev.* **2010,** *39* (4), 1262-1271.

118. Chand, D. K.; Bharadwaj, P. K., Synthesis of a Heteroditopic Cryptand Capable of Imposing a Distorted Coordination Geometry onto Cu(II): Crystal Structures of the Cryptand (L), [Cu(L)(CN)](picrate), and [Cu(L)(NCS)](picrate) and Spectroscopic Studies of the Cu(II) Complexes. *Inorg. Chem.* **1996,** *35* (11), 3380-3387.

119. Dietrich, B.; Viout, P.; Lehn, J. M., *Macrocyclic chemistry: aspects of organic and inorganic supramolecular chemistry*. VCH: 1993.

120. Busch, D., First Considerations: Principles, Classification, and History. In *Templates in Chemistry II*, Schalley, C.; Vögtle, F.; Dötz, K., Eds. Springer Berlin Heidelberg: 2005; Vol. 249, pp 1-65.

121. Miessler, G. L.; Tarr, D. A., *Inorganic Chemistry*. 3rd ed.; Pearson Prentice Hall: Upper Saddle River, 2004.

122. Anthony Deeney, F.; J. Harding, C.; G. Morgan, G.; McKee, V.; Nelson, J.; J. Teat, S.; Clegg, W., Response to steric constraint in azacryptate and related complexes of iron-(II) and -(III) *. *J. Chem. Soc., Dalton Trans.* **1998,** (11), 1837-1844.

123. Meyerstein, D., Are M–N bonds indeed inherently weaker when N is a tertiary rather than a primary or secondary nitrogen atom? *Coord. Chem. Rev.* **1999,** *185–186* (0), 141-147.

124. Duggan, M.; Ray, N.; Hathaway, B.; Tomlinson, G.; Brint, P.; Pelin, K., Crystal structure and electronic properties of ammine[tris(2-aminoethyl)amine]copper(II) diperchlorate and potassium penta-amminecopper(II) tris(hexafluorophosphate). *J. Chem. Soc., Dalton Trans.* **1980,** (8), 1342-1348.

125. Barbucci, R.; Mastroianni, A.; Campbell, M. J. M., The effect of N-Alkylation on the properties of five-coordinate copper(II) complexes of tetra-amine ligands. *Inorg. Chim. Acta* **1978,** *27* (0), 109-114.

126. Thaler, F.; Hubbard, C. D.; Heinemann, F. W.; van Eldik, R.; Schindler, S.; Fábián, I.; Dittler-Klingemann, A. M.; Hahn, F. E.; Orvig, C., Structural, Spectroscopic, Thermodynamic and Kinetic Properties of Copper(II) Complexes with Tripodal Tetraamines. *Inorg. Chem.* **1998,** *37* (16), 4022-4029.

127. McLachlan, G. A.; Fallon, G. D.; Martin, R. L.; Spiccia, L., Synthesis, Structure and Properties of Five-Coordinate Copper(II) Complexes of Pentadentate Ligands with Pyridyl Pendant Arms. *Inorg. Chem.* **1995,** *34* (1), 254-261.

128. Shearer, J.; Scarrow, R. C.; Kovacs, J. A., Synthetic Models for the Cysteinate-Ligated Non-Heme Iron Enzyme Superoxide Reductase: Observation and Structural Characterization by XAS of an FeIII−OOH Intermediate. *J. Am. Chem. Soc.* **2002,** *124* (39), 11709-11717.

129. Simaan, A. J.; Döpner, S.; Banse, F.; Bourcier, S.; Bouchoux, G.; Boussac, A.; Hildebrandt, P.; Girerd, J.-J., FeIII-Hydroperoxo and Peroxo Complexes with Aminopyridyl Ligands and the Resonance Raman Spectroscopic Identification of the Fe−O and O−O Stretching Modes. *Eur. J. Inorg. Chem.* **2000,** *2000* (7), 1627-1633.

130. Nam, E.; Alokolaro, P. E.; Swartz, R. D.; Gleaves, M. C.; Pikul, J.; Kovacs, J. A., Investigation of the Mechanism of Formation of a Thiolate-Ligated Fe(III)-OOH. *Inorg. Chem.* **2011,** *50* (5), 1592-1602.

131. Mayilmurugan, R.; Visvaganesan, K.; Suresh, E.; Palaniandavar, M., Iron(III) Complexes of Tripodal Monophenolate Ligands as Models for Non-Heme Catechol Dioxygenase Enzymes: Correlation of Dioxygenase Activity with Ligand Stereoelectronic Properties. *Inorg. Chem.* **2009,** *48* (18), 8771-8783.

132. Solomon, E. I.; Brunold, T. C.; Davis, M. I.; Kemsley, J. N.; Lee, S.-K.; Lehnert, N.; Neese, F.; Skulan, A. J.; Yang, Y.-S.; Zhou, J., Geometric and Electronic Structure/Function Correlations in Non-Heme Iron Enzymes. *Chem. Rev.* **1999,** *100* (1), 235-350.

133. Lund, A.; Shimada, S.; Shiotani, M., *Principles and Applications of ESR Spectroscopy*. Springer: 2011.

134. Cammack, R.; Cooper, C. E., [12] Electron paramagnetic resonance spectroscopy of iron complexes and iron-containing proteins. In *Methods Enzymol.*, James F. Riordan, B. L. V., Ed. Academic Press: 1993; Vol. Volume 227, pp 353-384.

135. Stoll, S.; Schweiger, A., EasySpin, a comprehensive software package for spectral simulation and analysis in EPR. *J. Magn. Reson.* **2006,** *178* (1), 42-55.

136. Yamaguchi, K., Cold-spray ionization mass spectrometry: principle and applications. *J. Mass Spectrom.* **2003,** *38* (5), 473-490.

137. Meunier, B., *Biomimetic Oxidations Catalyzed by Transition Metal Complexes*. Imperial College Press: 2000.

138. Solomon, E. I.; Sundaram, U. M.; Machonkin, T. E., Multicopper Oxidases and Oxygenases. *Chem. Rev.* **1996,** *96* (7), 2563-2606.

139. Bauman, A. T.; Yukl, E. T.; Alkevich, K.; McCormack, A. L.; Blackburn, N. J., The Hydrogen Peroxide Reactivity of Peptidylglycine Monooxygenase Supports a Cu(II)-Superoxo Catalytic Intermediate. *J. Biol. Chem.* **2006,** *281* (7), 4190-4198.

140. Klinman, J. P., The Copper-Enzyme Family of Dopamine β-Monooxygenase and Peptidylglycine α-Hydroxylating Monooxygenase: Resolving the Chemical Pathway for Substrate Hydroxylation. *J. Biol. Chem.* **2006,** *281* (6), 3013-3016.

141. Himes, R. A.; Karlin, K. D., Copper-dioxygen complex mediated C-H bond oxygenation: relevance for particulate methane monooxygenase (pMMO). *Curr. Opin. Chem. Biol.* **2009,** *13* (1), 119-131.

142. Chen, P.; Solomon, E. I., O2 activation by binuclear Cu sites: Noncoupled versus exchange coupled reaction mechanisms. *Proc. Natl. Acad. Sci. U. S. A.* **2004,** *101* (36), 13105-13110.

143. Crespo, A.; Martí, M. A.; Roitberg, A. E.; Amzel, L. M.; Estrin, D. A., The Catalytic Mechanism of Peptidylglycine α-Hydroxylating Monooxygenase Investigated by Computer Simulation. *J. Am. Chem. Soc.* **2006,** *128* (39), 12817-12828.

144. Kamachi, T.; Kihara, N.; Shiota, Y.; Yoshizawa, K., Computational Exploration of the Catalytic Mechanism of Dopamine β-Monooxygenase: Modeling of Its Mononuclear Copper Active Sites. *Inorg. Chem.* **2005,** *44* (12), 4226-4236.

145. Cramer, C. J.; Tolman, W. B., Mononuclear Cu–O2 Complexes: Geometries, Spectroscopic Properties, Electronic Structures, and Reactivity. *Acc. Chem. Res.* **2007,** *40* (7), 601-608.

146. Donoghue, P. J.; Gupta, A. K.; Boyce, D. W.; Cramer, C. J.; Tolman, W. B., An Anionic, Tetragonal Copper(II) Superoxide Complex. *J. Am. Chem. Soc.* **2010,** *132* (45), 15869-15871.

147. Kunishita, A.; Kubo, M.; Sugimoto, H.; Ogura, T.; Sato, K.; Takui, T.; Itoh, S., Mononuclear Copper(II)−Superoxo Complexes that Mimic the Structure and Reactivity of the Active Centers of PHM and DβM. *J. Am. Chem. Soc.* **2009,** *131* (8), 2788-2789.

148. Woertink, J. S.; Tian, L.; Maiti, D.; Lucas, H. R.; Himes, R. A.; Karlin, K. D.; Neese, F.; Würtele, C.; Holthausen, M. C.; Bill, E.; Sundermeyer, J.; Schindler, S.; Solomon, E. I., Spectroscopic and Computational Studies of an End-on Bound Superoxo-Cu(II) Complex: Geometric and Electronic Factors That Determine the Ground State. *Inorg. Chem.* **2010,** *49* (20), 9450-9459.

149. Gupta, A. K.; Tolman, W. B., Copper/α-Ketocarboxylate Chemistry With Supporting Peralkylated Diamines: Reactivity of Copper(I) Complexes and Dicopper−Oxygen Intermediates. *Inorg. Chem.* **2010,** *49* (7), 3531-3539.

150. Kunishita, A.; Kubo, M.; Ishimaru, H.; Ogura, T.; Sugimoto, H.; Itoh, S., H2O2-Reactivity of Copper(II) Complexes Supported by Tris[(pyridin-2-yl)methyl]amine Ligands with 6-Phenyl Substituents. *Inorg. Chem.* **2008,** *47* (24), 12032-12039.

151. Ohta, T.; Tachiyama, T.; Yoshizawa, K.; Yamabe, T.; Uchida, T.; Kitagawa, T., Synthesis, Structure, and H2O2-Dependent Catalytic Functions of Disulfide-Bridged Dicopper(I) and Related Thioether−Copper(I) and Thioether−Copper(II) Complexes. *Inorg. Chem.* **2000,** *39* (19), 4358-4369.

152. Yamaguchi, S.; Wada, A.; Nagatomo, S.; Kitagawa, T.; Jitsukawa, K.; Masuda, H., Thermal Stability of Mononuclear Hydroperoxocopper(II) Species. Effects of Hydrogen Bonding and Hydrophobic Field. *Chem. Lett.* **2004,** *33* (12), 1556-1557.

153. Choi, Y. J.; Cho, K.-B.; Kubo, M.; Ogura, T.; Karlin, K. D.; Cho, J.; Nam, W., Spectroscopic and computational characterization of CuII-OOR (R = H or cumyl) complexes bearing a Me6-tren ligand. *Dalton Trans.* **2011,** *40* (10), 2234-2241.

154. Schindler, S., Reactivity of Copper(I) Complexes Towards Dioxygen. *Eur. J. Inorg. Chem.* **2000,** *2000* (11), 2311-2326.

155. Würtele, C.; Sander, O.; Lutz, V.; Waitz, T.; Tuczek, F.; Schindler, S., Aliphatic C−H Bond Oxidation of Toluene Using Copper Peroxo Complexes That Are Stable at Room Temperature. *J. Am. Chem. Soc.* **2009,** *131* (22), 7544-7545.

156. Cole, A. P.; Mahadevan, V.; Mirica, L. M.; Ottenwaelder, X.; Stack, T. D. P., Bis(μ-oxo)dicopper(III) Complexes of a Homologous Series of Simple Peralkylated 1,2-Diamines: Steric Modulation of Structure, Stability, and Reactivity. *Inorg. Chem.* **2005,** *44* (21), 7345-7364.

157. de la Lande, A.; Parisel, O.; Gérard, H.; Moliner, V.; Reinaud, O., Theoretical Exploration of the Oxidative Properties of a [(trenMe1)CuO2]+ Adduct Relevant to Copper Monooxygenase Enzymes: Insights into Competitive Dehydrogenation versus Hydroxylation Reaction Pathways. *Chem. Eur. J.* **2008,** *14* (21), 6465-6473.

158. Weitzer, M.; Schatz, M.; Hampel, F.; Heinemann, F. W.; Schindler, S., Low temperature stopped-flow studies in inorganic chemistry. *J. Chem. Soc., Dalton Trans.* **2002,** (5), 686-694.

159. Weitzer, M.; Schindler, S.; Brehm, G.; Schneider, S.; Hörmann, E.; Jung, B.; Kaderli, S.; Zuberbühler, A. D., Reversible Binding of Dioxygen by the Copper(I) Complex with Tris(2-dimethylaminoethyl)amine (Me6tren) Ligand. *Inorg. Chem.* **2003,** *42* (6), 1800-1806.

160. Osako, T.; Nagatomo, S.; Tachi, Y.; Kitagawa, T.; Itoh, S., Low-Temperature Stopped-Flow Studies on the Reactions of Copper(II) Complexes and H2O2: The First Detection of a Mononuclear Copper(II)–Peroxo Intermediate. *Angew. Chem. Int. Ed.* **2002,** *41* (22), 4325-4328.

161. Chiavarino, B.; Cipollini, R.; Crestoni, M. E.; Fornarini, S.; Lanucara, F.; Lapi, A., Probing the Compound I-like Reactivity of a Bare High-Valent Oxo Iron Porphyrin Complex: The Oxidation of Tertiary Amines. *J. Am. Chem. Soc.* **2008,** *130* (10), 3208-3217.

162. Mateus, P.; Delgado, R.; Brandão, P.; Félix, V., Recognition of Oxalate by a Copper(II) Polyaza Macrobicyclic Complex. *Chem. Eur. J.* **2011,** *17* (25), 7020-7031.

163. Westerheide, L.; Müller, F. K.; Than, R.; Krebs, B.; Dietrich, J.; Schindler, S., Syntheses and Structural Characterization of Dinuclear and Tetranuclear Iron(III) Complexes with Dinucleating Ligands and Their Reactions with Hydrogen Peroxide‡. *Inorg. Chem.* **2001,** *40* (8), 1951-1961.

164. Roduner, E.; Kaim, W.; Sarkar, B.; Urlacher, V. B.; Pleiss, J.; Gläser, R.; Einicke, W.-D.; Sprenger, G. A.; Beifuß, U.; Klemm, E.; Liebner, C.; Hieronymus, H.; Hsu, S.-F.; Plietker, B.; Laschat, S., Selective Catalytic Oxidation of C□H Bonds with Molecular Oxygen. *ChemCatChem* **2013,** *5* (1), 82-112.

165. Makita, Y.; Sugimoto, K.; Furuyoshi, K.; Ikeda, K.; Fujiwara, S.-i.; Shin-ike, T.; Ogawa, A., A Zinc(II)-Included Hemicryptophane: Facile Synthesis, Characterization, and Catalytic Activity. *Inorg. Chem.* **2010,** *49* (16), 7220-7222.

166. Klinman, J. P., Mechanisms Whereby Mononuclear Copper Proteins Functionalize Organic Substrates. *Chem. Rev.* **1996,** *96* (7), 2541-2562.

167. Mizuno, M.; Honda, K.; Cho, J.; Furutachi, H.; Tosha, T.; Matsumoto, T.; Fujinami, S.; Kitagawa, T.; Suzuki, M., A Mononuclear Alkylperoxocopper(II) Complex as a Reaction Intermediate in the Oxidation of the Methyl Group of the Supporting Ligand. *Angew. Chem. Int. Ed.* **2006,** *45* (41), 6911-6914.

168. Rebilly, J.-N.; Reinaud, O., Supramolecular Copper Dioxygen Chemistry. In *Copper-Oxygen Chemistry*, John Wiley & Sons, Inc.: 2011; pp 321-360.

169. Chaloner, L.; Ottenwaelder, X., High-yield synthesis of potentially ditopic coordinating cryptands and their metal complexes. *Tetrahedron Lett.* **2013,** *54* (26), 3363-3365.

170. Chaloner, L.; Askari, M. S.; Kutteh, A.; Schindler, S.; Ottenwaelder, X., Formation and Reactivity of a Biomimetic Hydroperoxocopper(II) Cryptate. *Eur. J. Inorg. Chem.* **2011,** *2011* (27), 4204-4211.

171. Yokoi, H.; Addison, A. W., Spectroscopic and redox properties of pseudotetrahedral copper(II) complexes. Their relation to copper proteins. *Inorg. Chem.* **1977,** *16* (6), 1341-1349.

172. Lee, Y.; Park, G. Y.; Lucas, H. R.; Vajda, P. L.; Kamaraj, K.; Vance, M. A.; Milligan, A. E.; Woertink, J. S.; Siegler, M. A.; Narducci Sarjeant, A. A.; Zakharov, L. N.; Rheingold, A. L.; Solomon, E. I.; Karlin, K. D., Copper(I)/O2 Chemistry with Imidazole Containing Tripodal Tetradentate Ligands Leading to μ-1,2-Peroxo−Dicopper(II) Species. *Inorg. Chem.* **2009,** *48* (23), 11297-11309.

173. Harris, D. C., *Quantitative Chemical Analysis*. Sixth Edition edition ed.; W. H. Freeman: 2002.

174. Miller, S. M.; Klinman, J. P., Magnitude of intrinsic isotope effects in the dopamine .beta.-monooxygenase reaction. *Biochemistry* **1983,** *22* (13), 3091-3096.

175. Bellus, D.; Chemler, S. R.; Enders, D.; Geffken, D.; Köllner, A.; Maison, W.; O'Neil, I.; Rademacher, P.; Schaumann, E., *Science of Synthesis: Houben-Weyl Methods of Molecular Transformations Vol. 40b: Amine N-Oxides, Haloamines, Hydroxylamines and Sulfur Analogues, and Hydrazines*. Thieme: 2014.

176. Hong, S.; Gupta, A. K.; Tolman, W. B., Intermediates in Reactions of Copper(I) Complexes with N-Oxides: From the Formation of Stable Adducts to Oxo Transfer. *Inorg. Chem.* **2009,** *48* (14), 6323-6325.

177. Zhang, C. X.; Liang, H.-C.; Kim, E.-i.; Gan, Q.-F.; Tyeklar, Z.; Lam, K.-C.; Rheingold, A. L.; Kaderli, S.; Zuberbuhler, A. D.; Karlin, K. D., Dioxygen mediated oxo-transfer to an amine and oxidative -dealkylation chemistry with a dinuclear copper complex. *Chem. Commun.* **2001,** (7), 631-632.

178. Derossi, S.; Farrell, D. T.; Harding, C. J.; McKee, V.; Nelson, J., N-methylation of macrobicycles reduces encapsulation ability. *Dalton Trans.* **2007,** (18), 1762-1772.

179. Ziach, K.; Ceborska, M.; Jurczak, J., Toward dynamic combinatorial libraries of cryptands. *Tetrahedron Lett.* **2011,** *52* (34), 4452-4455.

180. Tepper, A. W. J. W.; Bubacco, L.; Canters, G. W., Structural Basis and Mechanism of the Inhibition of the Type-3 Copper Protein Tyrosinase from Streptomyces antibioticusby Halide Ions. *J. Biol. Chem.* **2002,** *277* (34), 30436-30444.

181. Sarkar, B.; Mukhopadhyay, P.; Bharadwaj, P. K., Laterally non-symmetric aza-cryptands: synthesis, catalysis and derivatization to new receptors. *Coord. Chem. Rev.* **2003,** *236* (1–2), 1-13.

182. Alibrandi, G.; Amendola, V.; Bergamaschi, G.; Fabbrizzi, L.; Licchelli, M., Bistren cryptands and cryptates: versatile receptors for anion inclusion and recognition in water. *Org. Biomol. Chem.* **2015,** *13* (12), 3510-3524.

183. Amendola, V.; Fabbrizzi, L.; Mangano, C.; Pallavicini, P.; Poggi, A.; Taglietti, A., Anion recognition by dimetallic cryptates. *Coord. Chem. Rev.* **2001,** *219–221* (0), 821-837.

184. Gloe, K., *Macrocyclic Chemistry: Current Trends and Future Perspectives*. Springer: 2005.

185. Largeron, M., Protocols for the Catalytic Oxidation of Primary Amines to Imines. *Eur. J. Org. Chem.* **2013,** *2013* (24), 5225-5235.

186. Cresswell, A. J.; Davies, S. G.; Roberts, P. M.; Thomson, J. E., Beyond the Balz–Schiemann Reaction: The Utility of Tetrafluoroborates and Boron Trifluoride as Nucleophilic Fluoride Sources. *Chem. Rev.* **2014,** *115* (2), 566-611.

187. Addison, A. W.; Rao, T. N.; Reedijk, J.; van Rijn, J.; Verschoor, G. C., Synthesis, structure, and spectroscopic properties of copper(II) compounds containing nitrogen-sulphur donor ligands; the crystal and molecular structure of aqua[1,7-bis(N-methylbenzimidazol-2[prime or minute]-yl)-2,6-dithiaheptane]copper(II) perchlorate. *J. Chem. Soc., Dalton Trans.* **1984,** (7), 1349-1356.

188. Cambridge Structural database, CSD (version 5.35, June 2015)

189. Komiyama, K.; Furutachi, H.; Nagatomo, S.; Hashimoto, A.; Hayashi, H.; Fujinami, S.; Suzuki, M.; Kitagawa, T., Dioxygen Reactivity of Copper(I) Complexes with Tetradentate Tripodal Ligands Having Aliphatic Nitrogen Donors: Synthesis, Structures, and Properties of Peroxo and Superoxo Complexes. *Bull. Chem. Soc. Jpn.* **2004,** *77* (1), 59-72.

190. Chand, D. K.; Bharadwaj, P. K., Heteroditopic Cryptands of Tunable Cavity Size: Imposition of Distorted Geometry onto Copper(II) and Nickel(II) and Molecular Recognition of Water Molecules. *Inorg. Chem.* **1998,** *37* (20), 5050-5055.

191. Desiraju, G. R.; Steiner, T., *The Weak Hydrogen Bond: In Structural Chemistry and Biology*. Oxford University Press: 1999.

192. Fagnou, K.; Lautens, M., Halide Effects in Transition Metal Catalysis. *Angew. Chem. Int. Ed.* **2002,** *41* (1), 26-47.

193. Berg, J. M.; Tymoczko, J. L.; Stryer, L., *Biochemistry, Fifth Edition: International Version*. W. H. Freeman: 2002.

194. Mateus, P.; Lima, L. M. P.; Delgado, R., Di- and trinuclear copper(II) complexes of polyaza macrocycles and cryptands as anion receptors. *Polyhedron* **2013,** *52* (0), 25-42.

195. Bianchi, A.; Bowman-James, K.; García-España, E., Aspects of Anion Coordination from Historical Perspectives. In *Anion Coordination Chemistry*, Wiley-VCH Verlag GmbH & Co. KGaA: 2011; pp 1-73.

196. Gale, P. A.; Gunnlaugsson, T., Supramolecular chemistry of anionic species themed issue. *Chem. Soc. Rev.* **2010,** *39* (10), 3595-3596.

197. Wenzel, M.; Hiscock, J. R.; Gale, P. A., Anion receptor chemistry: highlights from 2010. *Chem. Soc. Rev.* **2012,** *41* (1), 480-520.

198. Pramanik, A.; Powell, D. R.; Wong, B. M.; Hossain, M. A., Spectroscopic, Structural, and Theoretical Studies of Halide Complexes with a Urea-Based Tripodal Receptor. *Inorg. Chem.* **2012,** *51* (7), 4274-4284.

199. Lopez, N.; Graham, D. J.; McGuire, R.; Alliger, G. E.; Shao-Horn, Y.; Cummins, C. C.; Nocera, D. G., Reversible Reduction of Oxygen to Peroxide Facilitated by Molecular Recognition. *Science* **2012,** *335* (6067), 450-453.

200. Brooker, S.; White, N. G.; Bauza, A.; Deya, P. M.; Frontera, A., Understanding the Forces That Govern Packing: A Density Functional Theory and Structural Investigation of Anion-π-Anion and Nonclassical C-H···Anion Interactions. *Inorg. Chem.* **2012,** *51* (19), 10334-10340.

201. Bauza, A.; Quinonero, D.; Deya, P. M.; Frontera, A., Tuning of the anion-π interaction. *Theor. Chem. Acc.* **2012,** *131*, 1-11.

202. Berryman, O. B.; Johnson, D. W., Experimental evidence for interactions between anions and electron-deficient aromatic rings. *Chem. Commun.* **2009,** (22), 3143-3153.

203. Mercer, D. J.; Loeb, S. J., Metal-based anion receptors: An application of second-sphere coordination. *Chem. Soc. Rev.* **2010,** *39*, 3612-3620.

204. Perez, J.; Riera, L., Stable metal-organic complexes as anion hosts. *Chem. Soc. Rev.* **2008,** *37* (12), 2658-2667.

205. Juwarker, H.; Lenhardt, J. M.; Pham, D. M.; Craig, S. L., 1,2,3-Triazole CH···Cl− Contacts Guide Anion Binding and Concomitant Folding in 1,4-Diaryl Triazole Oligomers. *Angew. Chem. Int. Ed.* **2008,** *47* (20), 3740-3743.

206. Juwarker, H.; Lenhardt, J. M.; Castillo, J. C.; Zhao, E.; Krishnamurthy, S.; Jamiolkowski, R. M.; Kim, K.-H.; Craig, S. L., Anion Binding of Short, Flexible Aryl Triazole Oligomers. *J. Org. Chem.* **2009,** *74* (23), 8924-8934.

207. Tris(2-azidoethyl)amine is explosive and should be treated with caution.

208. Banert, K.; Wutke, J.; Rüffer, T.; Lang, H., Reactions of Unsaturated Azides; Part 22: The Alkyne Azide Click Chemistry as a Synthetic Tool for the Generation of Cage-Like Triazole Compounds. *Synthesis* **2008,** *2008* (16), 2603-2609.

209. Hans, R. H.; Guantai, E. M.; Lategan, C.; Smith, P. J.; Wan, B.; Franzblau, S. G.; Gut, J.; Rosenthal, P. J.; Chibale, K., Synthesis, antimalarial and antitubercular activity of acetylenic chalcones. *Bioorg. Med. Chem. Lett.* **2010,** *20* (3), 942-944.

210. Forsberg, J. H.; Kubik, T. M.; Moeller, T.; Gucwa, K., Syntheses and properties of .beta.,.beta.',.beta.''-triaminotriethylamine chelates of the tripositive lanthanide ions. *Inorg. Chem.* **1971,** *10* (12), 2656-2660.

211. Johnson, M. F.; Forsberg, J. H., Synthesis and spectroscopic studies of .beta.,.beta.',.beta.''-triaminotriethylamine chelates of the trivalent lanthanide perchlorates. *Inorg. Chem.* **1976,** *15* (3), 734-737.

212. Struthers, H.; Mindt, T. L.; Schibli, R., Metal chelating systems synthesized using the copper(i) catalyzed azide-alkyne cycloaddition. *Dalton Trans.* **2010,** *39* (3), 675-696.

213. Crowley, J.; McMorran, D., "Click-Triazole" Coordination Chemistry: Exploiting 1,4-Disubstituted-1,2,3-Triazoles as Ligands. In *Click Triazoles*, Košmrlj, J., Ed. Springer Berlin Heidelberg: 2012; Vol. 28, pp 31-83.

214. Crowley, J. D.; Bandeen, P. H., A multicomponent CuAAC "click" approach to a library of hybrid polydentate 2-pyridyl-1,2,3-triazole ligands: new building blocks for the generation of metallosupramolecular architectures. *Dalton Trans.* **2010,** *39* (2), 612-623.

215. Gower, M. L.; Crowley, J. D., Self-assembly of silver(i) metallomacrocycles using unsupported 1,4-substituted-1,2,3-triazole "click" ligands. *Dalton Trans.* **2010,** *39* (9), 2371-2378.

216. Fleischel, O.; Wu, N.; Petitjean, A., Click-triazole: coordination of 2-(1,2,3-triazol-4-yl)-pyridine to cations of traditional tetrahedral geometry (Cu(i), Ag(i)). *Chem. Commun.* **2010,** *46* (44), 8454-8456.

217. de Mendoza, J.; Mesa, E.; Rodríguez-Ubis, J.-C.; Vázquez, P.; Vögtle, F.; Windscheif, P.-M.; Rissanen, K.; Lehn, J.-M.; Lilienbaum, D.; Ziessel, R., A New Macrobicyclic Tris-bipyridine Ligand and Its Cu 2I and Ag 3I Complexes. *Angew. Chem. Int. Ed.* **1991,** *30* (10), 1331-1333.

218. Wenzel, M.; Wichmann, K.; Gloe, K.; Gloe, K.; Buschmann, H.-J.; Otho, K.; Schroder, M.; Blake, A. J.; Wilson, C.; Mills, A. M.; Lindoy, L. F.; Plieger, P. G., Interaction of tripodal Schiff-base ligands with silver(i): structural and solution studies. *CrystEngComm* **2010,** *12* (12), 4176-4183.

219. Ray, D.; Bharadwaj, P. K., Alteration in the Binding Property of a Laterally Nonsymmetric Aza Cryptand toward CuII, AgI, and TlI Ions upon Derivatization with a Cyanomethyl Group. *Eur. J. Inorg. Chem.* **2006,** (9), 1771-1776.

220. Adams, H.; Elsegood, M. R. J.; Fenton, D. E.; Heath, S. L.; Ryan, S. J., Synthesis and structure of a disilver(I) complex of a thiophene-linked Schiff base azacryptand. *Inorg. Chem.* **1999,** *2* (4), 139-142.

221. Drew, M. G. B.; Harding, C. J.; Howarth, O. W.; Lu, Q.; Marrs, D. J.; Morgan, G. G.; McKee, V.; Nelson, J., Thiophene-linked azacryptand sites for dicopper and disilver; thiophene sulfur as an inert spacer? *Dalton Trans.* **1996,** (14), 3021-3030.

222. W. Howarth, O.; G. Morgan, G.; McKee, V.; Nelson, J., Conformational choice in disilver cryptates; an 1H NMR and structural study. *Dalton Trans.* **1999,** (12), 2097-2102.

223. Abidi, R.; Arnaud-Neu, F.; Drew, M. G. B.; Lahely, S.; Marrs, D.; Nelson, J.; Schwing-Weill, M.-J., Hexa Schiff-base cryptands: solution thermodynamic and X-ray crystallographic studies of main group, transition and heavy metal ion complexes. *J. Chem. Soc., Perkin Trans. 2* **1996,** (12), 2747-2755.

224. Ma, Z.; Cao, R., An N8O6 cryptand: the host for Ag+guests and H2O molecules. *J. Mol. Struct.* **2005,** *738* (1–3), 137-142.

225. The cobalt(II) chloride complex of LTTA is isostructural to the zinc(II) chloride complex.

226. ESI-MS measurements carried out after titration indicated zinc complexes exclusively: there was no evidence of Ag(I) coordinating to the triazole moeities nor substituting with the Zn(II) ion.

227. Groves, J. T., Key elements of the chemistry of cytochrome P-450: The oxygen rebound mechanism. *J. Chem. Educ.* **1985,** *62* (11), 928.

228. Bauer, I.; Knölker, H.-J., Iron Catalysis in Organic Synthesis. *Chem. Rev.* **2015,** *115* (9), 3170-3387.

229. Sun, C.-L.; Li, B.-J.; Shi, Z.-J., Direct C−H Transformation via Iron Catalysis. *Chem. Rev.* **2010,** *111* (3), 1293-1314.

230. Ye, W.; Staples, R. J.; Rybak-Akimova, E. V., Oxygen atom transfer mediated by an iron(IV)/iron(II) macrocyclic complex containing pyridine and tertiary amine donors. *J. Inorg. Biochem.* **2012,** *115*, 1-12.

231. Ainscough, E. W.; Brodie, A. M.; Plowman, J. E.; Brown, K. L.; Addison, A. W.; Gainsford, A. R., Small molecule analogs for the specific iron-binding site of lactoferrin: a single-crystal x-ray structure of bis(methanol)bis[2-(5-methylpyrazol-3-yl)phenolato]iron(III) nitrate-methanol and spectroscopic studies on iron(III) phenolate complexes. *Inorg. Chem.* **1980,** *19* (12), 3655-3663.

232. Bassan, A.; Blomberg, M. R. A.; Siegbahn, P. E. M.; Que, L., Two Faces of a Biomimetic Non-Heme HO-FeV=O Oxidant: Olefin Epoxidation versus cis-Dihydroxylation. *Angew. Chem. Int. Ed.* **2005,** *44* (19), 2939-2941.

233. Makhlynets, O. V.; Das, P.; Taktak, S.; Flook, M.; Mas-Ballesté, R.; Rybak-Akimova, E. V.; Que, L., Iron-Promoted ortho- and/or ipso-Hydroxylation of Benzoic Acids with H_2O_2. *Chem. Eur. J.* **2009,** *15* (47), 13171-13180.

234. Hagen, K. S., Iron(II) Triflate Salts as Convenient Substitutes for Perchlorate Salts: Crystal Structures of $[Fe(H_2O)_6](CF_3SO_3)_2$ and $Fe(MeCN)_4(CF_3SO_3)_2$. *Inorg. Chem.* **2000,** *39* (25), 5867-5869.

235. Sheldrick, G., A short history of SHELX. *Acta Crystallogr., Sect. A: Found. Crystallogr.* **2008,** *64* (1), 112-122.

Appendix 1: Supplement Information for Chapter 3

Supramolecular Control of Monooxygenase Reactivity in a Copper(II) Cryptate

Supporting Figures and Notes

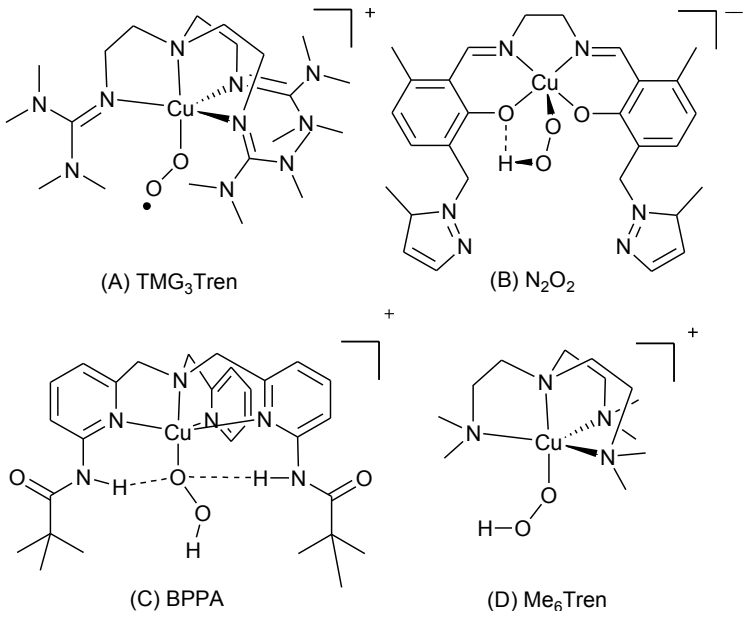

Chart S1. Well-characterized end-on mononuclear Cu/O_2 intermediates: TMG_3Tren-Cu(II)-superoxo,[19,44] N_2O_2-Cu(II)-hydroperoxo,[46] BPPA-Cu(II)-hydroperoxo [58], Me_6Tren-Cu(II)-Hydroperoxo.[153]

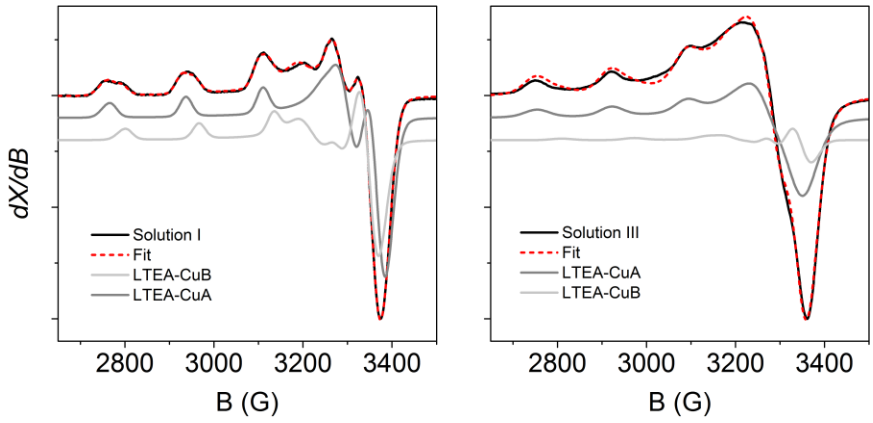

Figure S1. X-Band EPR spectra of solutions I and III in black, Easyspin fit spectra in red and deconvolution of the fitted spectra in gray.

It was unclear if **LTEA-**CuA had a vacant binding site or if an acetate ion was coordinating in place of the solvent. To distinguish between the two options excess sodium acetate was added to solution II. If $[\boldsymbol{LTEA}CuB]^+ \rightleftharpoons [\boldsymbol{LTEA}CuA]^+ + MeOH$ was the governing process then excess acetate would not affect the equilibrium. If $[\boldsymbol{LTEA}CuB]^+ + AcO^- \rightleftharpoons [\boldsymbol{LTEA}Cu(OAc)_2] + MeOH$ was the governing process then excess acetate would drive the reaction to the right and the EPR spectrum would be dominated by one copper complex. From Figure S2, it was clear that NaOAc did not significantly affect the **LTEA-**CuA to **LTEA-**CuB ratio and therefore **LTEA-**CuA was assigned a square-planar geometry in solution.

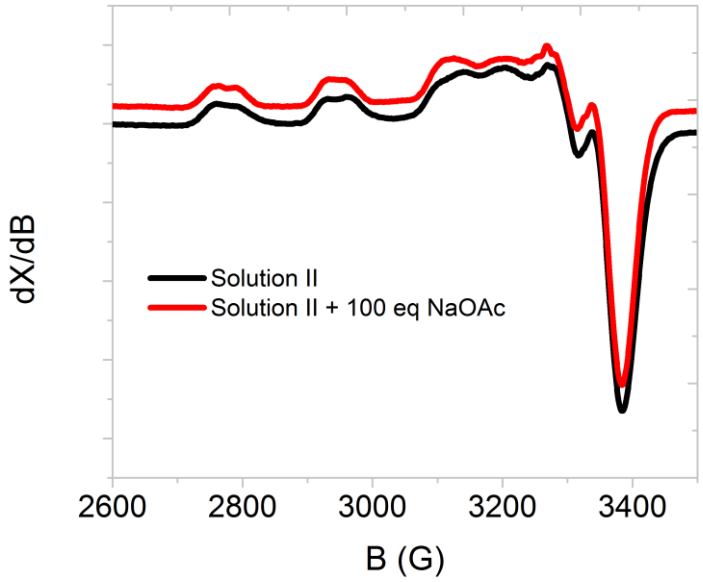

Figure S2. X-Band EPR spectra. Black: solution II. Red: Solution II + 100 equivalents of NaOAc.

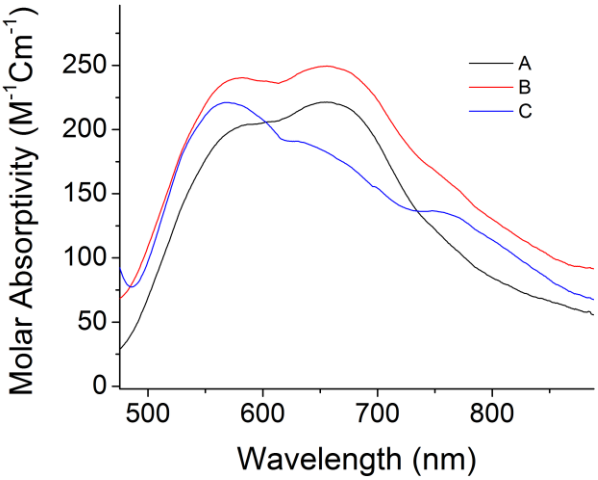

Figure S3. UV/Vis spectra at -50 °C in MeOH of Solution I (0.5 mM) and 10 equiv. Et_3N + 40 equiv. H_2O_2. Zoom of the d-d transitions. Spectra have been smoothed. (A) 2.5 ms (B) 0.875 s and (C) 174.87 s.

Table S1. Table of the average rate of decomposition of [**LTEA**CuOOH]$^+$ and [**LTEA**^{D}CuOOHOAc]$^+$, the sample size (N) and the calculated KIE.

$[H_2O_2]$ (M)	N	k_d C-H (s^{-1})	N	k_d C-D (s^{-1})	KIE
0.005	5	$5.7 \pm 0.1 \times 10^{-02}$	5	$3.58 \pm 0.06 \times 10^{-02}$	1.60 ± 0.05
0.01	5	$6.6 \pm 0.2 \times 10^{-02}$	5	$4.0 \pm 0.2 \times 10^{-02}$	1.66 ± 0.05
0.015	5	$6.6 \pm 0.2 \times 10^{-02}$	5	$4.3 \pm 0.3 \times 10^{-02}$	1.52 ± 0.06
0.02	5	$6.6 \pm 0.1 \times 10^{-02}$	5	$4.7 \pm 0.5 \times 10^{-02}$	1.41 ± 0.05
				Average KIE	1.5 ± 0.1

Note S1

In the case of both **LTEA** and **LTEA**^{D}, if the dataset with 5 mM H_2O_2 is accounted for in the ANOVA test, the means are found to be statistically different. If the 5 mM dataset is considered to be an outlier, the means are found to be statistically similar. For the simplicity of the analysis, the means are considered statistically similar and 5 mM is considered an outlier. However, it should be noted that the decomposition may have a small dependence on H_2O_2 when using 10 equivalents versus 20 or greater. Further stopped flow experiments would be needed to test this hypothesis, but are not necessary for the general conclusions made in this publication.

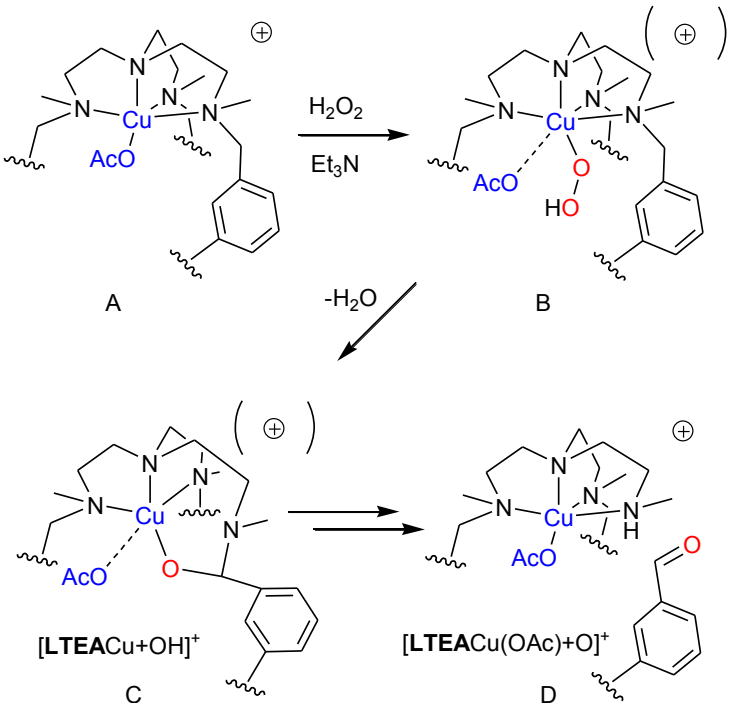

Scheme S1. Previously proposed mechanism of the inner-sphere oxidation reaction of solution I with H_2O_2/Et_3N.

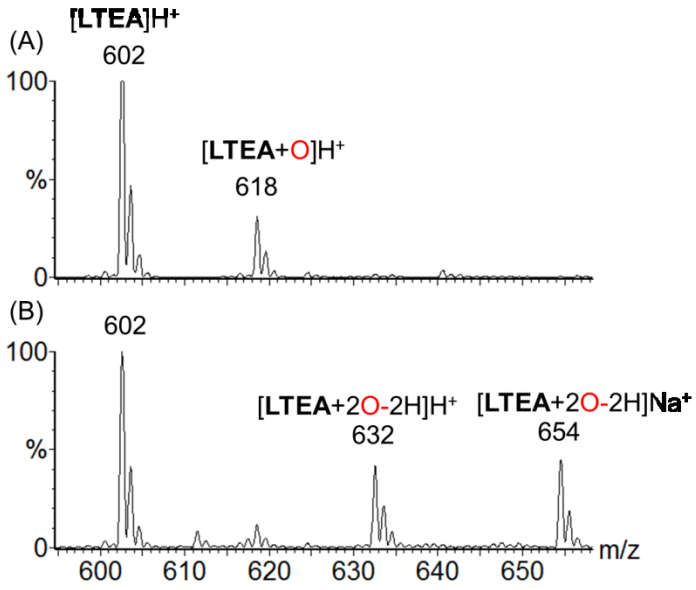

Figure S4. ESI-MS of the organic products after the reaction with 2 equiv. H_2O_2/Et_3N and demetallation with (A) NH_4OH and (B) washing with $EDTA_{(aq)}$

Appendix 2: Supplement Information for Chapter 4

Bio-Inspired Oxidation Chemistry of a Cu(II)-Fluoride Cryptate with C_3-Symmetry

X-Ray Crystallography

X-ray crystallographic analysis was performed using the Cu-Kα microfocus source of a Bruker APEX-DUO diffractometer. The frames were integrated with the Bruker SAINT software package using a narrow-frame algorithm. Data were corrected for absorption effects using the multi-scan method (SADABS). The structures were solved by direct methods and refined using the Bruker APEX2 software Package (SHELXL instructions).[235] All non-hydrogen atoms were refined with anisotropic thermal parameters. Hydrogen atoms were generated in idealized positions, riding on the carrier atoms, with isotropic thermal parameters.

Table S2. Hydrogen bond lengths and angles for [**LTEA**H^+CuF]$(BF_4)_2(MeCN)_{0.5}$

D-H···A	D-H (Å)	H···A (Å)	D···A (Å)	∢D-H···A (°)
C10-H10··· F1	0.950	2.194	2.904(3)	130.7
C22-H22··· F1	0.950	2.228	2.944(3)	131.5
C34-H34··· F1	0.949	2.188	2.951(3)	136.6
N5-H5N··· O1	1.04(2)	2.38(2)	2.820(3)	104(2)
N5-H5N··· O2	1.04(2)	2.21(2)	2.730(3)	109(2)
N5-H5N··· O3	1.04(2)	2.17(2)	2.734(3)	112(2)

Table S3. Summary of Crystallographic Data

		[**LTEA**CuCl](SbF$_6$)(MeOH)	[**LTEA**CuCl$_2$](MeCN)	[**LTEA**H^+CuF]$(BF_4)_2(MeCN)_{0.5}$
Formula		$C_{37}H_{55}Cl_1CuF_6N_5O_4Sb$	$C_{38}H_{54}Cl_2CuN_6O_3$	$C_{37}H_{53.5}B_2CuF_9N_{5.5}O_3$
M_w(g/mol); F(000)		968.60; 1980	777.31; 1644	879.51; 1832
T(K); wavelength		150; 1.54178	150; 1.54178	150; 1.54178
Crystal System		Monoclinic	Monoclinic	Monoclinic
Space Group		P 2_1/c	P 2_1/n	P 2_1/n
Unit Cell:	a (Å)	21.6285(7)	12.0729(11)	16.6170(5)
	b (Å)	12.1322(4)	11.5223(15)	12.5970(3)
	c (Å)	16.8581(6)	28.087(3)	20.2250(6)
	α (˚)	90	90	90
	β (˚)	111.381(2)	98.314(4)	90.935
	γ (˚)	90	90	90
V (Å^3)		4119.1(2)	3866.1(7)	4233.2(2)

Z; $d_{calcd.}$ (g/cm^3)	4; 1.562	4; 1.335	4; 1.380
Θ range (˚); completeness	2.19- 68.57; 0.979	3.18– 70.80; 0.985	3.14- 59.557; 0.991
Collected reflections; R_σ	57632; 0.0338	50926; 0.0892	53624; 0.0285
Unique reflections; R_{int}	7438; 0.0554	7330; 0.1503	6152; 0.0619
μ (mm^{-1}); Abs. Corr	7.054; Multi-Scan	2.416; Multi-Scan	1.442; Multi-Scan
R1(F); wR(F^2) [I> 2σ(*I*)]	0.0647; 0.1719	0.0561; 0.1140	0.0370; 0.0836
R1(F); wR(F^2) (all data)	0.0724; 0.1798	0.1021; 0.1397	0.0529; 0.911
GoF (F^2)	1.063	1.048	1.038
Residual electron density (e^-/Å^3)	0.927	0.535	0.374

Supporting Figures

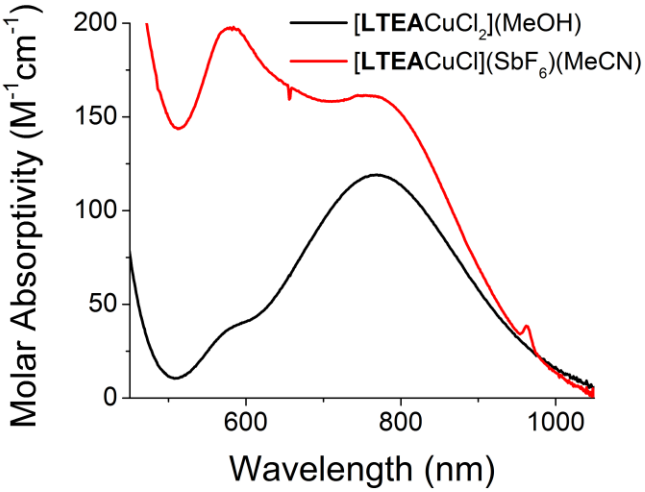

Figure S5. UV/Vis spectra Red: 0.5 mM [**LTEA**$CuCl_2$](MeOH) dissolved in CH_2Cl_2 and Black: 0.5 mM [**LTEA**CuCl](SbF_6)(MeCN) dissolved in CH_2Cl_2.

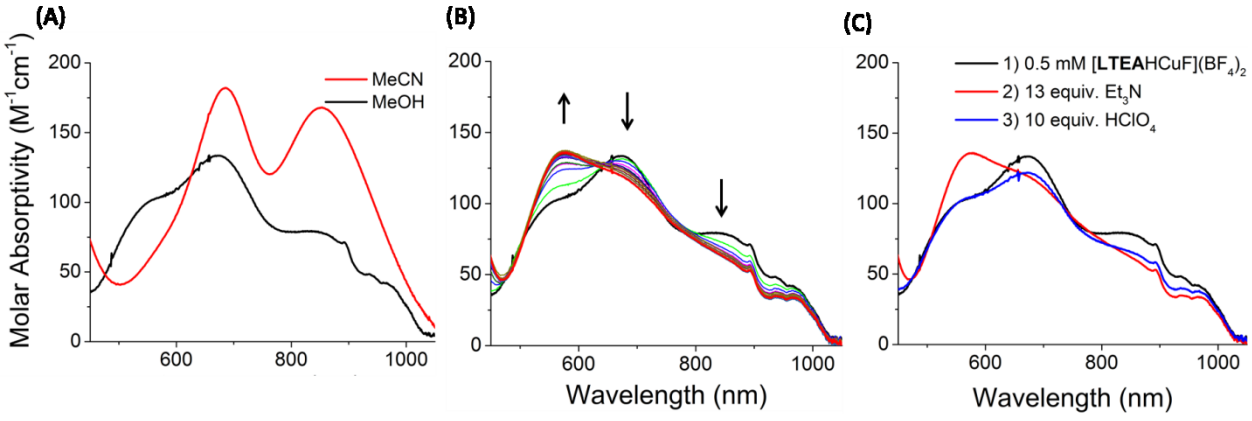

Figure S6. UV/Vis spectra (A) 0.5 mM [**LTEA**HCuF]$(BF_4)_2$ in MeCN and MeOH (B) Serial additions of 1 equiv. of Et_3N (Total = 10 equiv.) to 0.5 mM [**LTEA**HCuF]$(BF_4)_2$ in MeOH. The black arrows show the trend in spectral changes after addition of the base. (C) 1) [**LTEA**HCuF]$(BF_4)_2$ in MeOH followed by sequential addition of 2) Et_3N and 3) $HClO_4$

Experimental Section

General: All materials were used as received. The synthesis of **LTEA** was reported elsewhere.[170] ESI-MS spectra were measured using direct injection on Micromass Quattro LC at Concordia's Centre for Biological Applications of Mass Spectrometry. The CSI-MS was recorded on a Bruker Micro-TOF II equipped with a cold spray adapted at University of Montreal. The *m*/*z* data reported is based on ^{1}H, ^{12}C, ^{14}N, ^{16}O, ^{19}F, ^{35}Cl, ^{63}Cu. X-Ray crystallography was performed on the copper source of a Bruker APEX DUO. UV-Vis spectra were recorded on an Agilent 8453 spectrophotometer equipped with a Unisoku USP-203-A cryostat for temperatures down to –30°C. X-band EPR spectra were collected on a Bruker EMX Plus spectrometer controlled with Xenon software and equipped with a Bruker teslameter. A Bruker nitrogen-flow cryostat connected to a high-sensitivity resonant cavity was used for 100 K measurements. The EPR spectra were fit with Easyspin Fitting software.[135]

Synthesis

[LTEACuCl](SbF_6)(MeOH): To **LTEA** (10 mg, 20 µmol) suspended in 1 mL of methanol was added copper(II) chloride (3.4 mg, 20 µmol) dissolved in 1 mL of methanol. The mixture was stirred for 10 minutes and a dark green color formed. The solution was used as is or alternatively single crystals were grown by adding $NaSbF_6$ (5.2 mg, 20 µmol) to the solution and evaporating the solvent overnight. The dark turquoise/ green crystals were collected in 58 % yield (11 mg, 11 µmol) (Table S3). ESI-MS in MeOH: signal at *m*/*z* = 699.

[LTEACuCl_2](MeCN): To **LTEA** (12 mg, 20 µmol) suspended in 1 mL of acetonitrile was added copper(II) chloride (3.4 mg, 20 µmol) dissolved in 1 mL of acetonitrile. The mixture was stirred for 10 minutes. The solvent was left to evaporate slowly overnight resulting in pale green crystals in 77 % yield (12.2 mg, 15 µmol)(Table S3). ESI-MS in MeCN: signal at *m*/*z* = 699.

[LTEAHCuF]$(BF_4)_2$ and [LTEAHCuF]$(MeCN)_{0.5}(BF_4)_2$: To **LTEA** (15 mg, 25 µmol) suspended in 1 mL of acetonitrile was added copper(II) tetrafluoroborate (8.61 mg, 25 µmol) dissolved in 1 mL acetonitrile. The mixture was stirred for 10 minutes and a dark green solution evolved. The complex was isolated by precipitating with ether to afford 11.5 mg (50 %) of a turquoise powder. Single crystals suitable for x-ray

diffraction were grown with slow diffusion ether into a solution of the complex in MeCN at RT (Table S3). MS of the solution (ESI, MeCN): *m*/*z* = 683.

Reactivity: To a 1 cm UV cell equipped with a stir bar, 1.8 mL of MeOH and cooled to -30°C was added 100 µL of 10 mM stock solution of [**LTEA**H^+CuF]$(BF_4)_2$ in MeCN or [**LTEA**CuCl](Cl) in MeOH. To the solutions was added 100 µL of a 200 mM stock solution of H_2O_2/Et_3N in MeOH.

A continuous flow set-up was used to mix a 10mM solution of [**LTEA**H^+CuF]$(BF_4)_2$ in MeOH with 15 equivalents H_2O_2/Et_3N in MeOH. The final concentration was 3.33 mM in Cu.

Appendix 3: Supplement Information for Chapter 5

High-yield Synthesis of Potentially Ditopic Coordinating Cryptands and their Metal Complexes

Experimental Section

General procedures: Chemicals and solvents were used as received from commercial sources. The synthesis of 2-azido-*N*,*N*-bis(2-azidoethyl)ethanamine, **4**,[208] and 3-(2-propyn-1-yloxy)benzaldehyde, **5**,[209] were reported previously and the procedure at the end of the appendix. NMR measurements were performed at 22°C (unless otherwise stated) in a 5 mm tube on a Varian Innova 500 MHz instrument and referenced to internal TMS. Elemental analyses were carried out by the Laboratoire d'Analyse Élémentaire of the Université de Montréal. ESI-MS spectra were measured using direct injection on a Micromass Quattro LC at Concordia's Centre for Biological Applications of Mass Spectrometry. The *m*/*z* data reported is based on ^{1}H, ^{12}C, ^{14}N, ^{16}O, ^{64}Zn and ^{107}Ag. X-Ray crystallography was performed on the Cu microfocus source of a Bruker APEX DUO instrument at 110 K. Further crystallographic details are provided below.

6: To a stirring solution of copper(II) sulfate pentahydrate (40 mg, 0.16 mmol), 2-azido-*N*,*N*-bis(2-azidoethyl)ethanamine[208] (1.49 g, 6.66 mmol) and 3-(2-propyn-1-yloxy)benzaldehyde[209] (3.2 g, 20 mmol) in 200 mL of 1:1 *t*-butanol/H_2O was added sodium ascorbate (31.7 mg, 0.16 mmol). The mixture was stirred at room temperature for 24 h. Then, 100 mL of dichloromethane were added and the solution was further stirred for 24 h. To the mixture was added 100 mL of 1 M NaOH and 50 mL of 0.2 M EDTA. The product was extracted with 3 x 50 mL of dichloromethane and the organic phase extracts were dried over anhydrous Na_2SO_4. The solvent was removed under reduced pressure and drying under vacuum, yielding 4.40 g (94%) of a yellow oil. ^{1}H-NMR (500 MHz, $CDCl_3$): δ = 3.16 (t, 6H, J = 6, *A*), 4.15 (t, 6H, J = 6, *B*), 5.11 (s, 6H, *D*), 7.13 (d, 3H, J = 8, *G*), 7.27 (s, 3H, *H*), 7.32 (s, 3H, *C*), 7.33 (t, 3H, J = 8, *F*), 7.41 (d, 3H, J = 8, *E*), 9.82 (s, 3H, *I*) ppm. . ^{13}C-NMR (500 MHz, $CDCl_3$): δ 48.84 (CH_2), 54.52 (CH_2), 61.89 (CH_2), 113.19 (Ar), 121.74 (Ar), 123.92 (Ar), 124.79 (Ar), 130.24 (Ar), 137.81

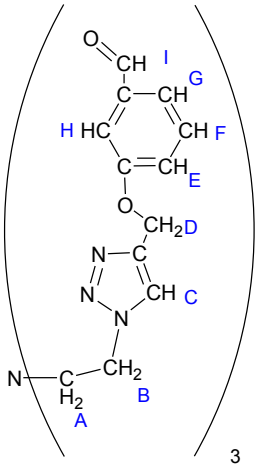

3

(Ar), 142.87 (Ar), 158.82 (Ar), 191.71 (CHO). Elemental analysis calcd (%) for $C_{36}H_{36}N_{10}O_6$: C 61.35, H 5.15, N 19.88; found C 60.83, H 5.18, N 19.80.

7: To a stirring solution of **6** (4.40 g, 6.2 mmol) and lanthanum nitrate hexahydrate (2.68 g, 6.2 mmol) in 600 mL of methanol/tetrahydrofuran (10:1) was added dropwise tris(2-aminoethyl)amine (0.933 mL, 6.2 mmol) in 100 mL of methanol. The mixture was stirred at room temperature for 48 hours and was then used for the next step directly (synthesis of **LTTA**). Tris(imine) **7** can, however, be isolated via the following procedure: after evaporating the solvent under reduced pressure, dichloromethane was added and the mixture was stirred for 5 min. The precipitate was filtered off and the solvent was removed under reduced pressure. Addition of acetonitrile to the residue yielded **7**·CH_3OH as a white precipitate (2.36 g, 48%). ^{1}H-NMR (500 MHz, $CDCl_3$): δ = 2.90 (t, 6H, J = 4, *L*), 3.23 (s, 6H, *A*), 3.53 (s, 6H, *K*), 4.02 (s, 6H, *B*), 4.74 (s, 6H, *D*), 5.64 (s, 3H, *I*), 6.84 (s, 3H, *H*), 7.00 (d, 3H, J = 8, *G*), 7.41 (t, 3H, J = 8, *F*), 7.56 (s, 3H, *C*), 7.85 (d, 3H, J = 8, *E*) ppm. ^{13}C-NMR (500 MHz, $CDCl_3$): δ 49.28 (CH_2), 55.86 (CH_2), 57.51 (CH_2), 60.10 (CH_2), 61.21 (CH_2), 113.63 (Ar), 119.23 (Ar), 119.89 (Ar), 126.25 (Ar), 129.94 (Ar), 138.91 (Ar), 142.08 (Ar), 158.40 (Ar), 160.56 (CH). Elemental analysis calcd (%) for $C_{43}H_{52}N_{14}O_4$: C 62.30, H 6.32, N 23.66; found C 62.51, H 6.18, N 23.68.

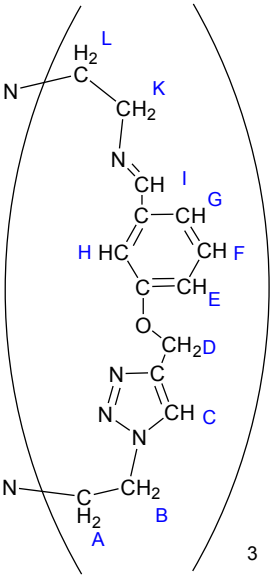

3

LTTA: Tris(imine) **7** was reduced in situ by adding $NaBH_4$ (0.844 g, 22.3 mmol) to the above stirring solution refluxed for 3 h. After removing the solvent under reduced pressure, 100 mL of 1 M NaOH and EDTA (2.00 g, 6.8 mmol) were added. The product was extracted with 3 x 50 mL of dichloromethane and the organic phase extracts were dried over anhydrous Na_2SO_4. The solvent was removed under reduced pressure, yielding a precipitate that was suspended in acetonitrile. Filtration, washing with acetonitrile and drying under vacuum yielded **LTTA** as a white powder (3.57 g, 72% over two steps). ^{1}H-NMR (500 MHz, $CDCl_3$): δ = 1.52 (s, 3H, *J*), 2.67 (s, 6H, *K*), 2.67 (s, 6H, *L*), 3.20 (m, 6H, *A*), 3.49 (s, 6H, *I*), 3.99(m, 6H, *B*), 4.89 (s, 6H, *D*), 6.30 (s, 3H, *H*), 6.82 (d, 3H, J = 8, *G*), 6.91 (s, 3H, *C*), 7.08 (d, 3H, J = 8, *E*), 7.22 (t, 3H, J = 8, *F*) ppm. ^{13}C-NMR (500

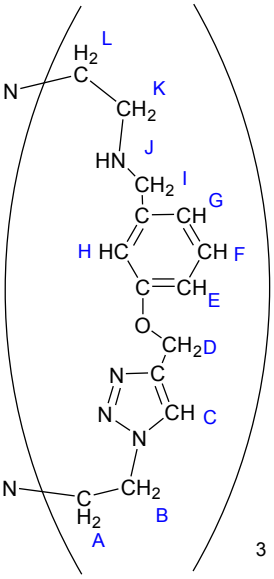

3

MHz, $CDCl_3$): δ 48.19 (CH_2), 49.34 (CH_2), 53.86 (CH_2), 55.87 (CH_2), 56.15 (CH_2), 61.26 (CH_2), 112.18 (Ar), 114.61 (Ar), 120.99 (Ar), 125.83 (Ar), 129.83 (Ar), 142.90 (Ar), 142.91 (Ar), 158.33 (Ar). Elemental analysis calcd (%) for $C_{42}H_{54}N_{14}O_3$: C 62.82, H 6.78, N 24.42; found C 62.36, H 6.93, N 24.22.

8: To a solution of formaldehyde (762 µL, 7.5 mmol) and formic acid (206 µL, 7.5 mmol) was added **LTTA** (1.00 g, 1.25 mmol). The mixture was heated under reflux for 24 h. The solution was allowed to cool to room temperature and was poured onto 30 mL of 2 M NaOH. The product was extracted with 3 × 20 mL of dichloromethane and the organic phase extracts were dried over anhydrous Na_2SO_4. The solvent was removed under reduced pressure, yielding a precipitate that was suspended in diethyl ether. Filtration, washing with cold diethyl ether and drying under vacuum yielded **8**·C_2H_5O as a beige powder (0.846 g, 80%). Single crystals amenable to X-ray diffraction analysis were grown by slow recrystallization of **8**·C_2H_5O in diethyl ether at 2°C (Table S4). ^{1}H-NMR (500 MHz, $CDCl_3$): δ = 2.16 (s, 9H, *J*), 2.36 (t, 6H, J = 6, *K*), 2.54 (t, 6H, J = 6, *L*), 3.21 (m, 6H, *A*), 3.33 (s, 6H, *I*), 4.03 (m, 6H, *B*), 4.95 (s, 6H, *D*), 6.55 (s, 3H, *C*), 6.78 (d, 3H, J = 8, *G*), 6.89 (s, 3H, *H*), 6.99 (d, 3H, J = 7, *E*), 7.18 (t, 3H, J = 7, *F*) ppm. ^{13}C-NMR (500 MHz, $CDCl_3$): δ 43.7 (CH_3), 49.1 (CH_2), 54.2 (CH_2), 54.6 (CH_2), 55.2 (CH_2), 61.4 (CH_2), 62.5 (CH_2), 113.9 (Ar), 114.0 (Ar), 121.4 (Ar), 125.6 (Ar), 129.130 (Ar), 141.9 (Ar), 143.3 (Ar), 158.3 (Ar). Elemental analysis calcd (%) for $C_{49}H_{70}N_{14}O_4$: C 64.03, H 7.68, N 21.33; found C 63.64, H 7.60, N 21.74.

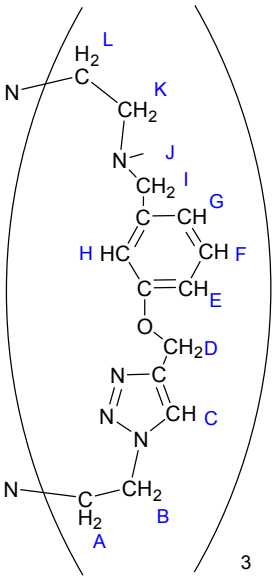

[LTTAAg]$^+$ solutions and [LTTAAg](NO$_3$)·CH$_3$OH crystals: To **LTTA** (23.5 mg, 29 µmol) dissolved in 500 µL of refluxing methanol was added silver(I) nitrate (4.97 mg, 29 µmol) dissolved in 500 µL methanol. The mixture was refluxed for 20 min then filtered. The filtrate was layered with ether and the complex was isolated by collecting and drying the precipitate (21.3 mg, 76%). ^{1}H-NMR (500 MHz, CD_3CN): δ = 2.35 (s, 6H, *L*), 2.58 (s, 6H, *K*), 3.00 (t, 6H, J = 5, *A*), 3.36 (s, 6H, *I*), 4.12 (t, 6H, J = 5, *B*), 5.12 (s, 6H, *D*), 6.83 (d, 3H, J = 7, *G*), 7.03 (d, 3H, J = 7, *E*), 7.12 (s, 3H, *H*), 7.27 (t, 3H, J = 7, *F*), 7.30 (s, 3H, *C*) ppm. Elemental analysis calcd (%) for $C_{43}H_{58}N_{15}O_7Ag$: C 51.39, H 5.82, N 20.91; found C 51.78, H 5.78, N 20.90.

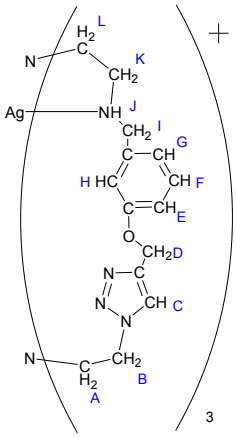

Single crystals of [**LTTA**Ag](NO_3)·CH_3OH were obtained by slow diffusion of diethyl ether in a methanol solution of the compound (Table S4).

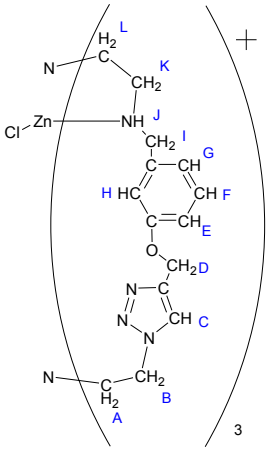

[LTTAZn(Cl)]Cl·H_2O powder and [LTTAZn(Cl)]Cl single-crystals: To **LTTA** (20 mg, 24.9 µmol) dissolved in 500 µL of refluxing methanol was added zinc(II) chloride (3.38 mg, 24.9 µmol) dissolved in 500 µL of methanol. The mixture was refluxed for 5 min then filtered. The filtrate was layered with ether and the complex was isolated by collecting and drying the precipitate (17 mg, 73%). ^{1}H-NMR (500 MHz, CD_3OD): δ = 2.60 (t, 6H, J = 6, *L*), 2.65 (s, 6H, *K*), 2.91 (t, 6H, J = 6, *A*), 4.05 (s, 6H, *I*), 4.10 (t, 6H, J = 6, *B*), 5.31 (s, 6H, *D*), 6.82 (d, 3H, J = 8, *G*), 7.08 (d, 3H, J = 8, *E*), 7.21 (t, 3H, J = 8, *F*), 7.48 (s, 3H, *C*), 7.48 (s, 3H, *H*) ppm. MS (ESI, CH_3OH): *m/z* = 901.18 [M^+ -Cl [Elemental analysis calcd (%) for $C_{42}H_{56}N_{14}O_4Cl_2Zn$: C 52.69, H 5.90, N 20.48; found C 52.46, H 5.86, N 20.28. Single crystals of [**LTTA**Zn(Cl)]Cl were obtained by slow diffusion of diethyl ether in a methanol solution of the compound (Table S4).

Titration of [5ZnCl](Cl) with Ag(OTf): [5Zn(Cl)]Cl·H_2O: (23. 4 mg, 24.5 mmol) was dissolved in 0.6 mL of acetonitrile-d_3 to make a 41.66 mM solution. Aliquots of a 125 mM solution of AgOTf (19.3 mg, 75.1 mmol) in 0.6 mL acetonitrile-d_3 were added to the [**LTTA**ZnCl](Cl) solution. The titration was followed by ^{1}H NMR at 60°C.

X-ray crystallography

X-ray crystallographic analysis was performed using the Cu-Kα microfocus source of a Bruker APEX-DUO diffractometer. The frames were integrated with the Bruker SAINT software package using a narrow-frame algorithm. Data were corrected for absorption effects using the multi-scan method (SADABS). The structures were solved by direct methods and refined using the Bruker APEX2 software Package (SHELXL instructions).[235] All non-hydrogen atoms were refined with anisotropic thermal parameters. Hydrogen atoms were generated in idealized positions, riding on the carrier atoms, with isotropic thermal parameters.

Table S4. Crystallographic data for 6·Et_2O, [5Ag](NO_3)·CH_3OH and [5ZnCl](Cl).

	8·Et_2O	[**LTTA**Ag](NO_3)·CH_3OH	[**LTTA**ZnCl](Cl)
CCDC number	906881	906882	906883
Empirical formula	$C_{49}H_{70}N_{14}O_4$	$C_{43}H_{58}AgN_{15}O_7$	$C_{42}H_{54}Cl_2N_{14}O_3Zn$
Moiety formula	$C_{45}H_{60}N_{14}O_3$, $C_4H_{10}O$	$C_{42}H_{54}AgN_{14}O_3$, NO_3, CH_4O	$C_{42}H_{54}ClN_{14}O_3Zn$, Cl
Formula weight (g/mol)	919.19	1004.91	939.26
Temperature (K)	110(2)	110(2)	110(2) K
Wavelength (Å)	1.54178	1.54178	1.54178 Å
Crystal system	Monoclinic	Monoclinic	Monoclinic
Space group	$P2_1/c$	$P2_1/c$	$P2_1$
a (Å)	19.7552(3)	19.8027(7)	9.4145(2)
b (Å)	9.51120(10)	13.6102(3)	15.4263(3)
c (Å)	27.2949(4)	16.7725(4)	16.3950(3)
α (°)	90	90	90.00
β (°)	91.9600(10)	99.010(2)	103.216(2)
γ (°)	90	90	90.00
Volume ($Å^3$)	5125.59(12)	4464.7(2)	2318.00(8)
Z	4	4	2
Density [calculated]	1.191	1.495	1.346
Absorption coefficient	0.631	4.195	2.236
F(000)	1976	2096	984
Crystal size (mm)	0.07 × 0.18 × 0.20	0.07 × 0.09 × 0.16	0.07 × 0.18 × 0.30
Index ranges	h = −23→23 k = −11→11 l = −32→32	h = −22→22 k = −15→15 l = −18→18	h = −10→11 k = −18→18 l = −19→19
Reflections collected	71792	55703	34171
Independent reflections	9343	6419	8422
Reflections with I > 2σ(I)	7067	4470	5857
Parameters	643	597	559
Goodness of fit	1.022	1.016	1.016
Final R indices [I > 2σ(I)]	R_1 = 5.01% wR_2 = 12.86%	R_1 = 5.13% wR_2 = 12.07%	R_1 = 5.79% wR_2 = 12.24%
R indices [all data]	R_1 = 6.99% wR_2 = 14.30%	R_1 = 8.61% wR_2 = 14.08%	R_1 = 9.71% wR_2 = 14.28%
Largest diff. peak/hole (e $Å^{-3}$)	0.394 / -0.459	0.996 / -0.922	0.476 / -0581

Nuclear magnetic resonance data

Figure S7. **6** ^{1}H NMR, $CDCl_3$

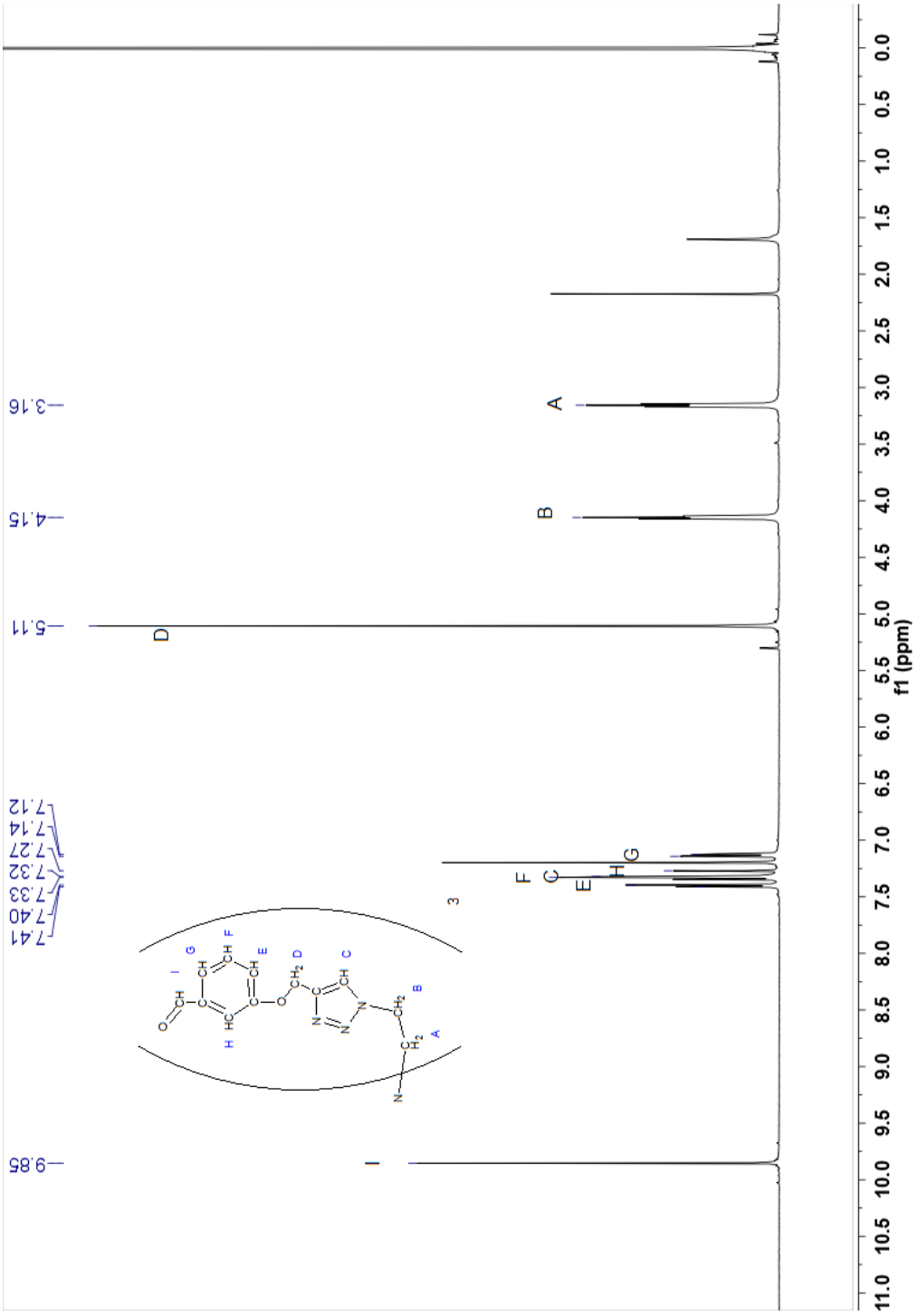

Figure S8. **6** ^{13}C NMR, $CDCl_3$

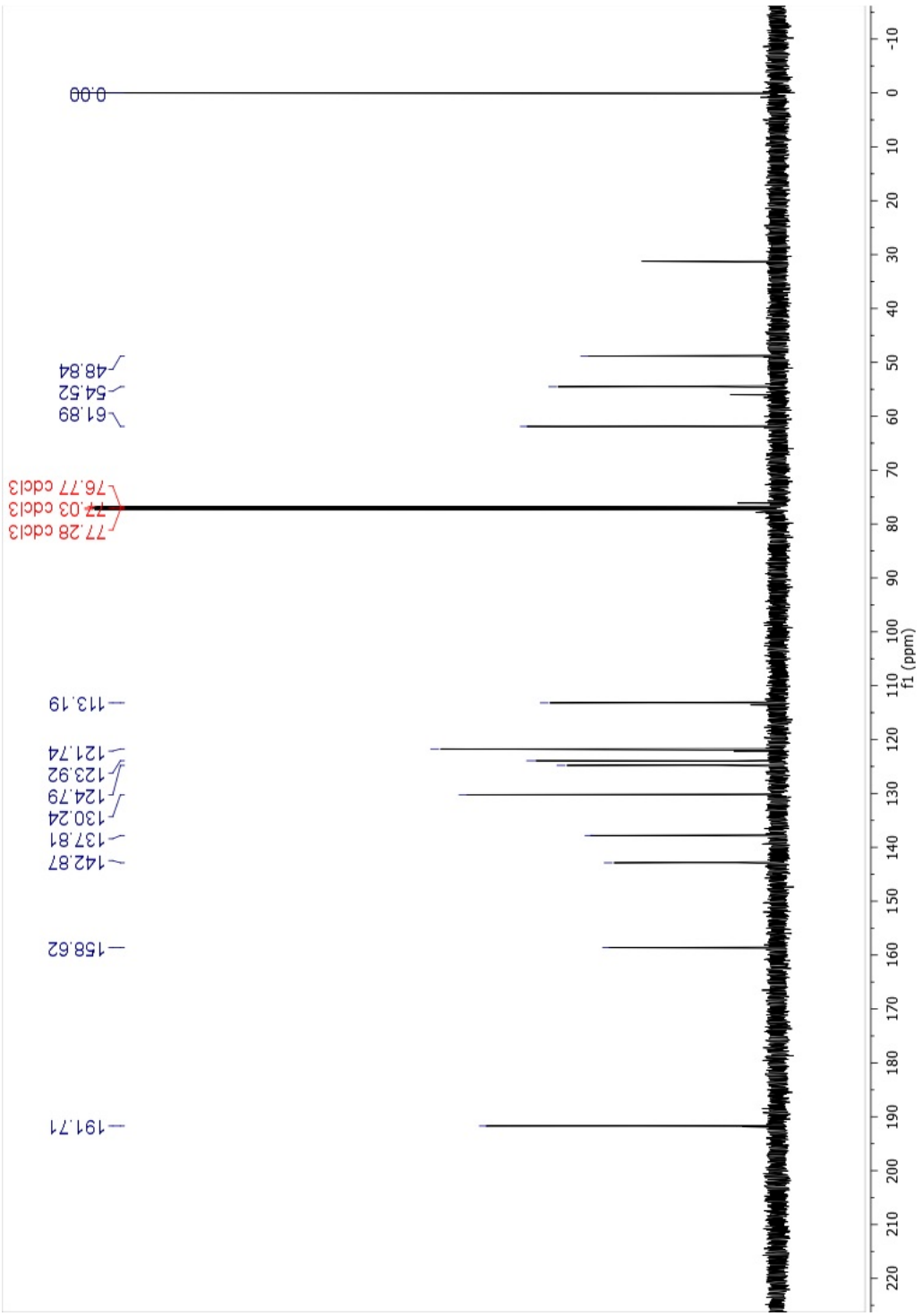

Figure S9. **7** ^{1}H NMR, $CDCl_3$

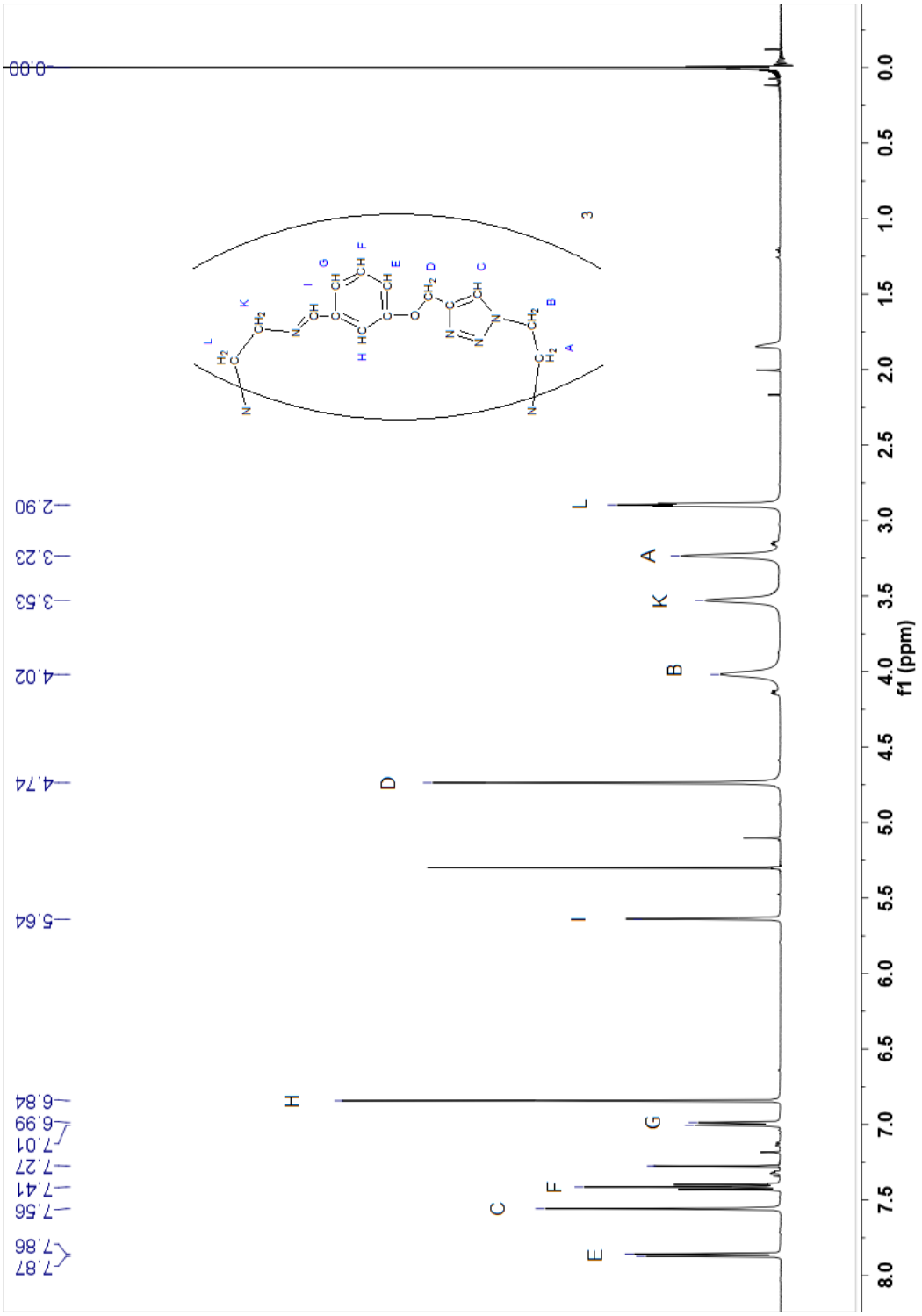

Figure S10. **7** ^{13}C NMR, $CDCl_3$

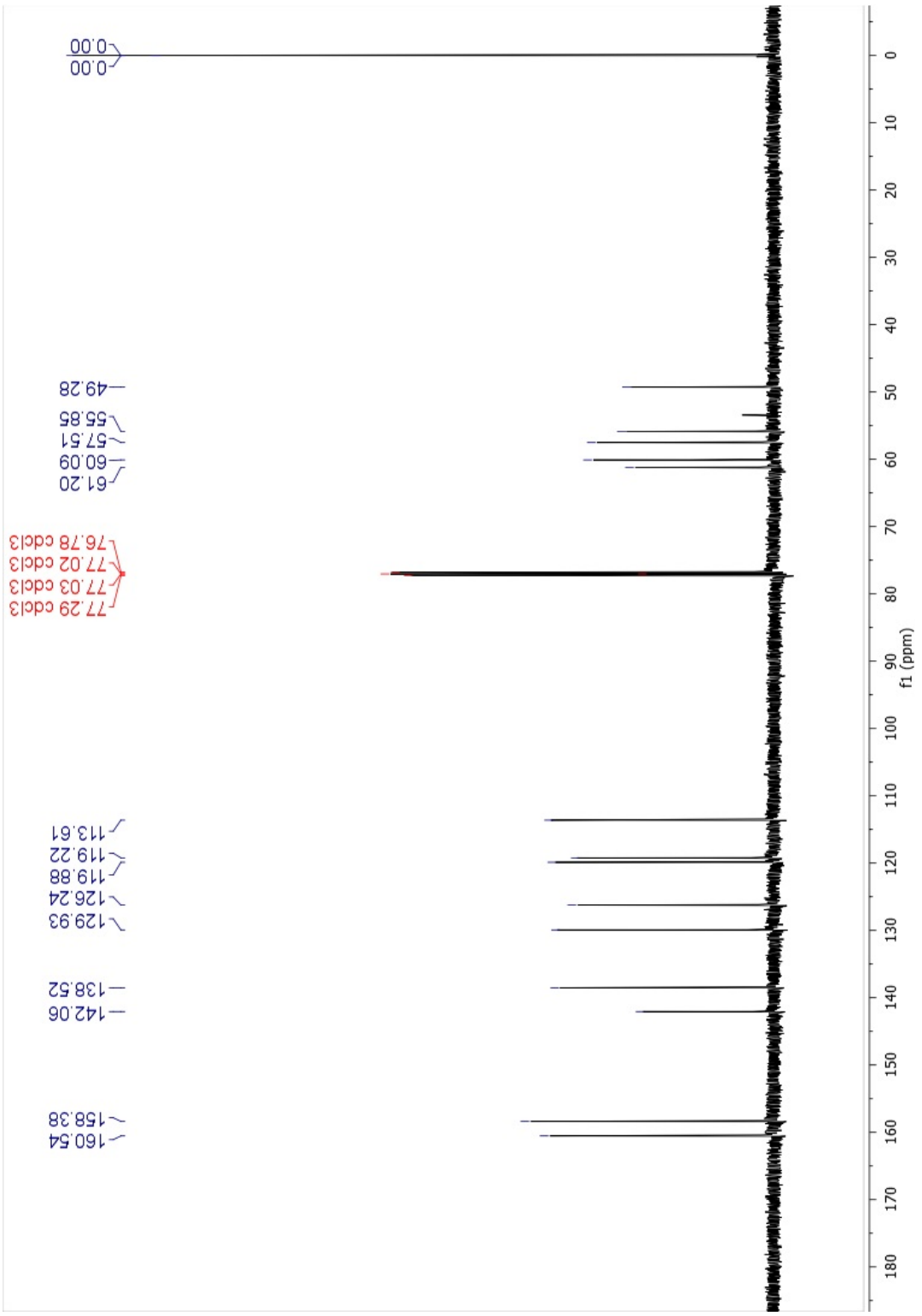

Figure S11. **LTTA** ^{1}H NMR, $CDCl_3$

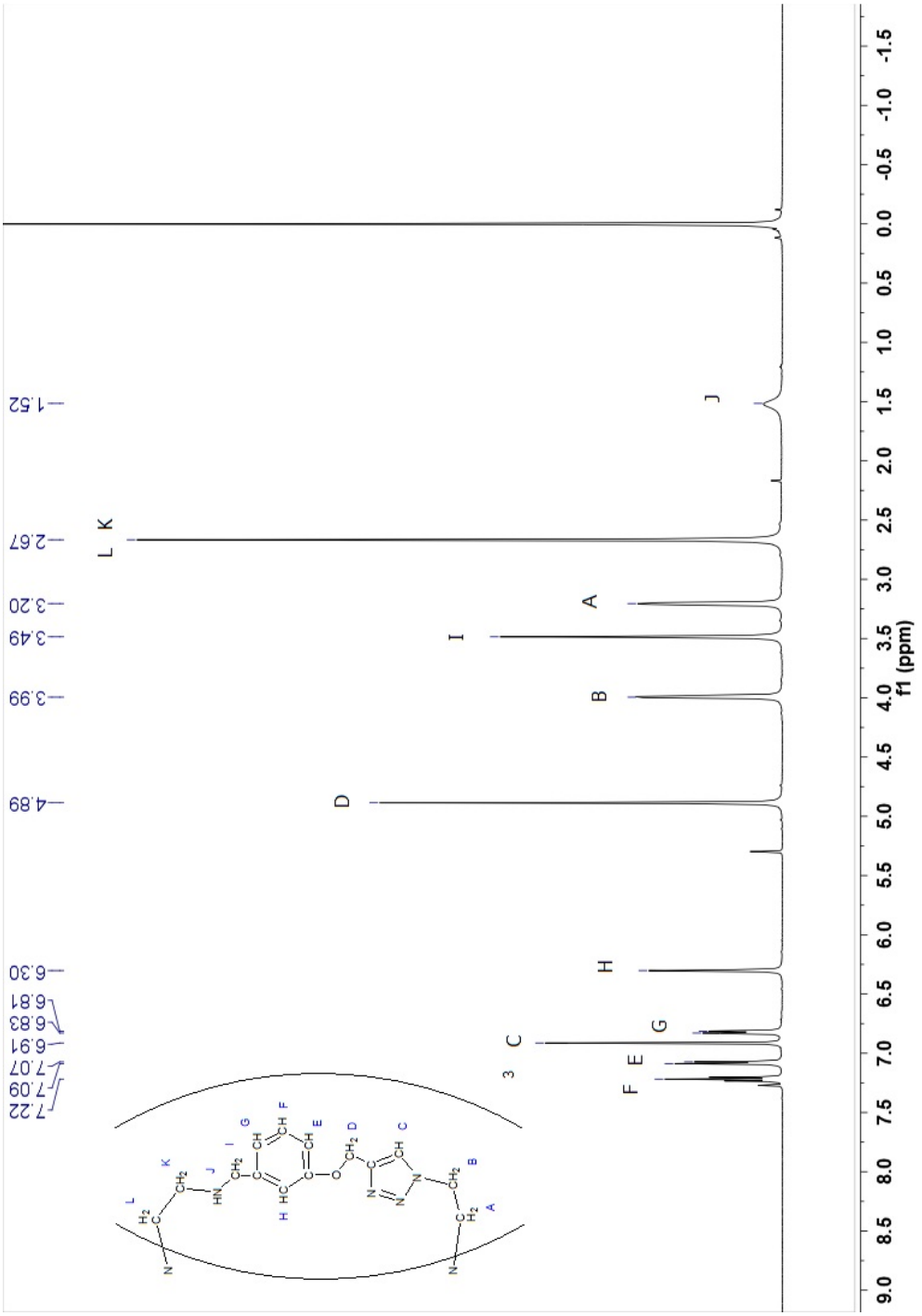

Figure S12. **LTTA** ^{13}C NMR, $CDCl_3$

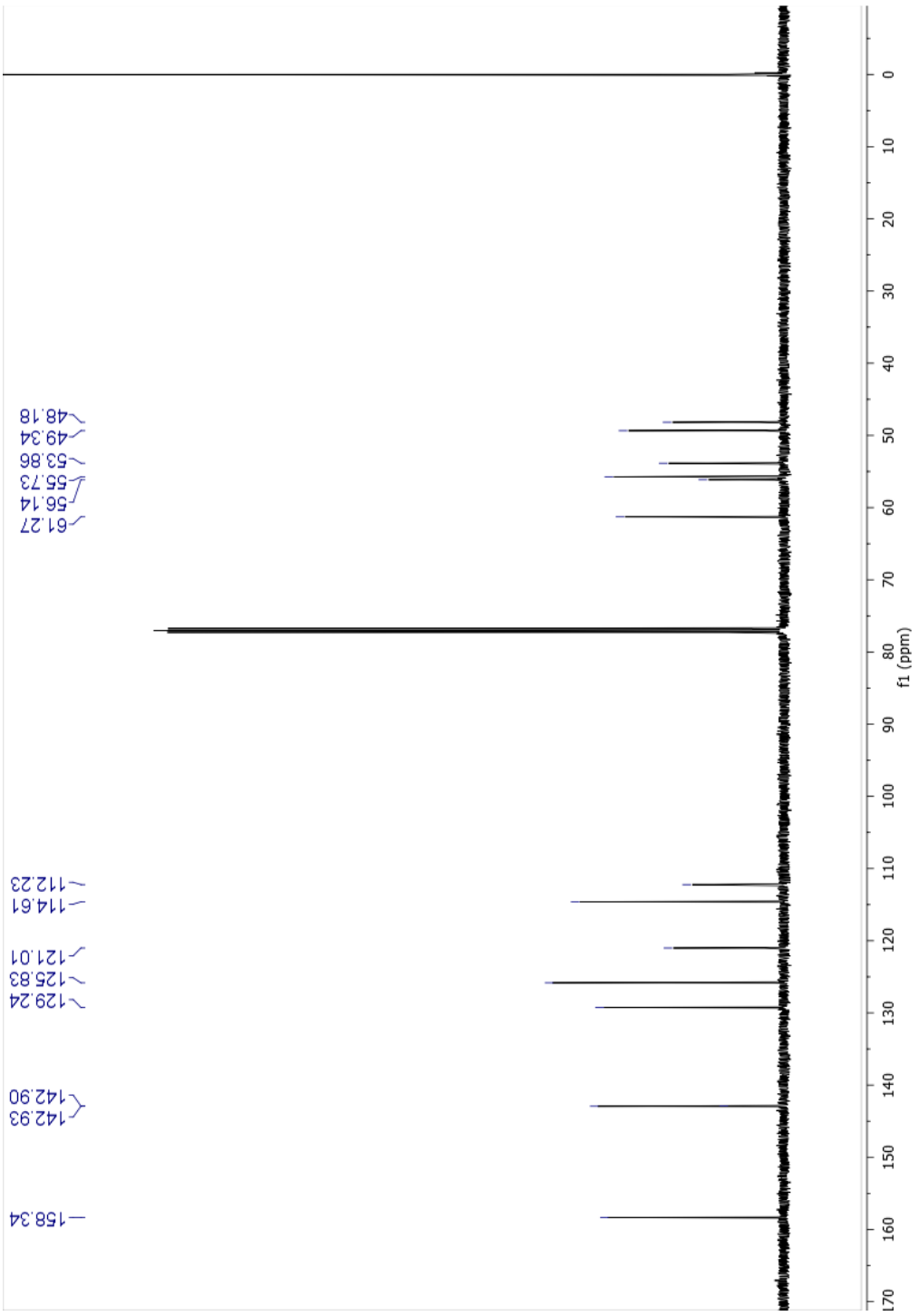

Figure S13. **LTTA** NEOSY, $CDCl_3$

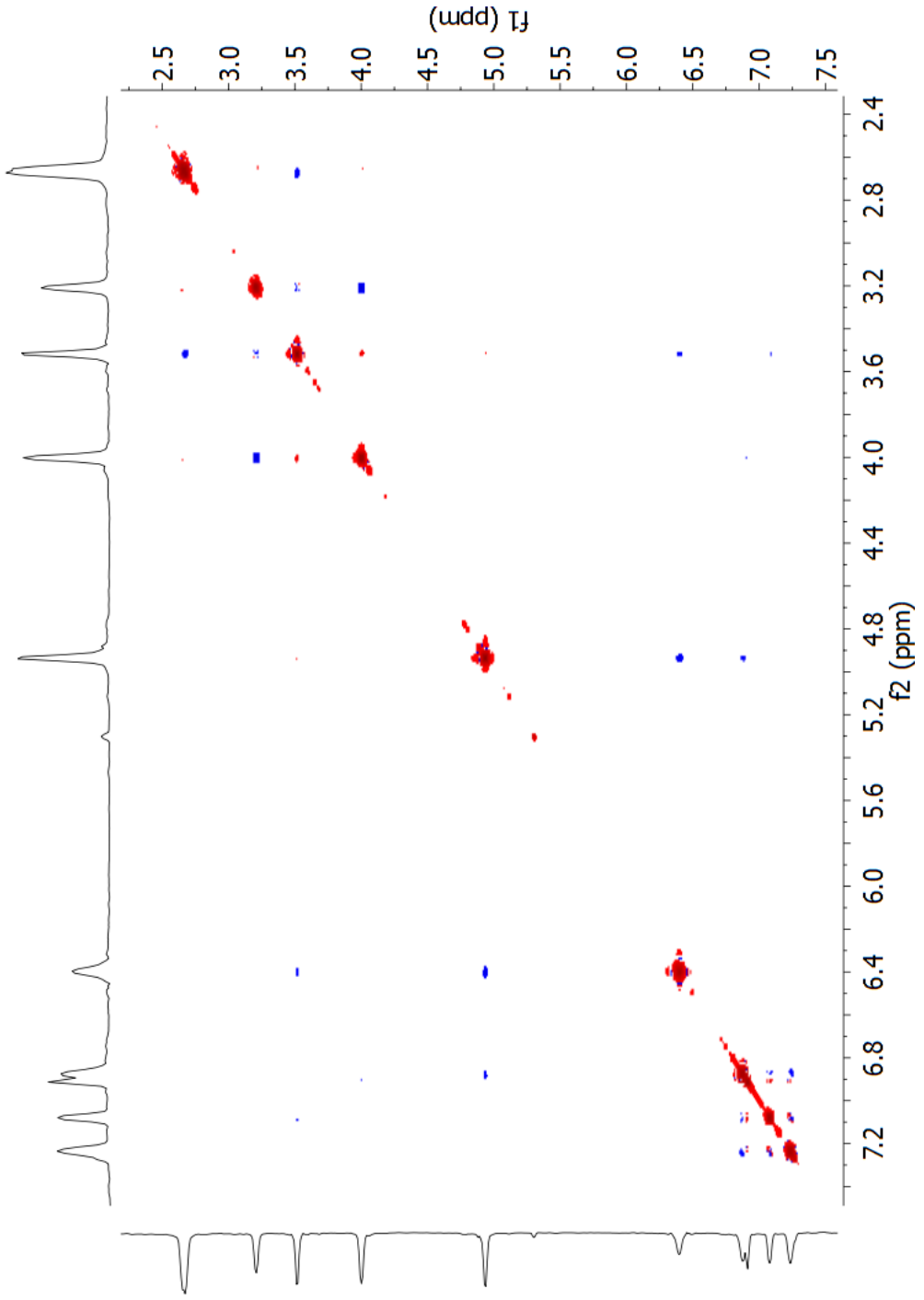

Figure S14. **LTTA** COSY, $CDCl_3$

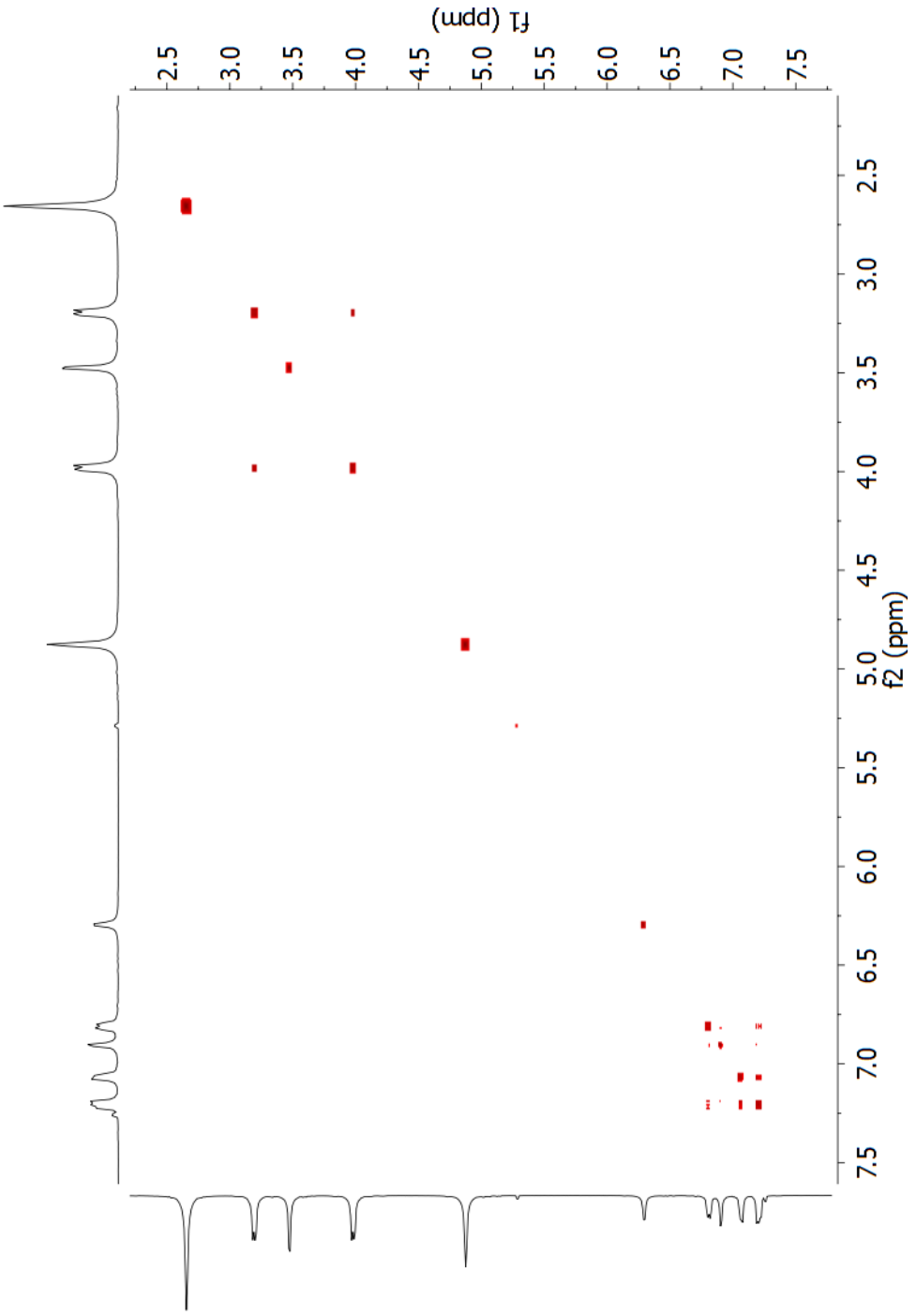

Figure S15. **8** ^{1}H NMR, $CDCl_3$

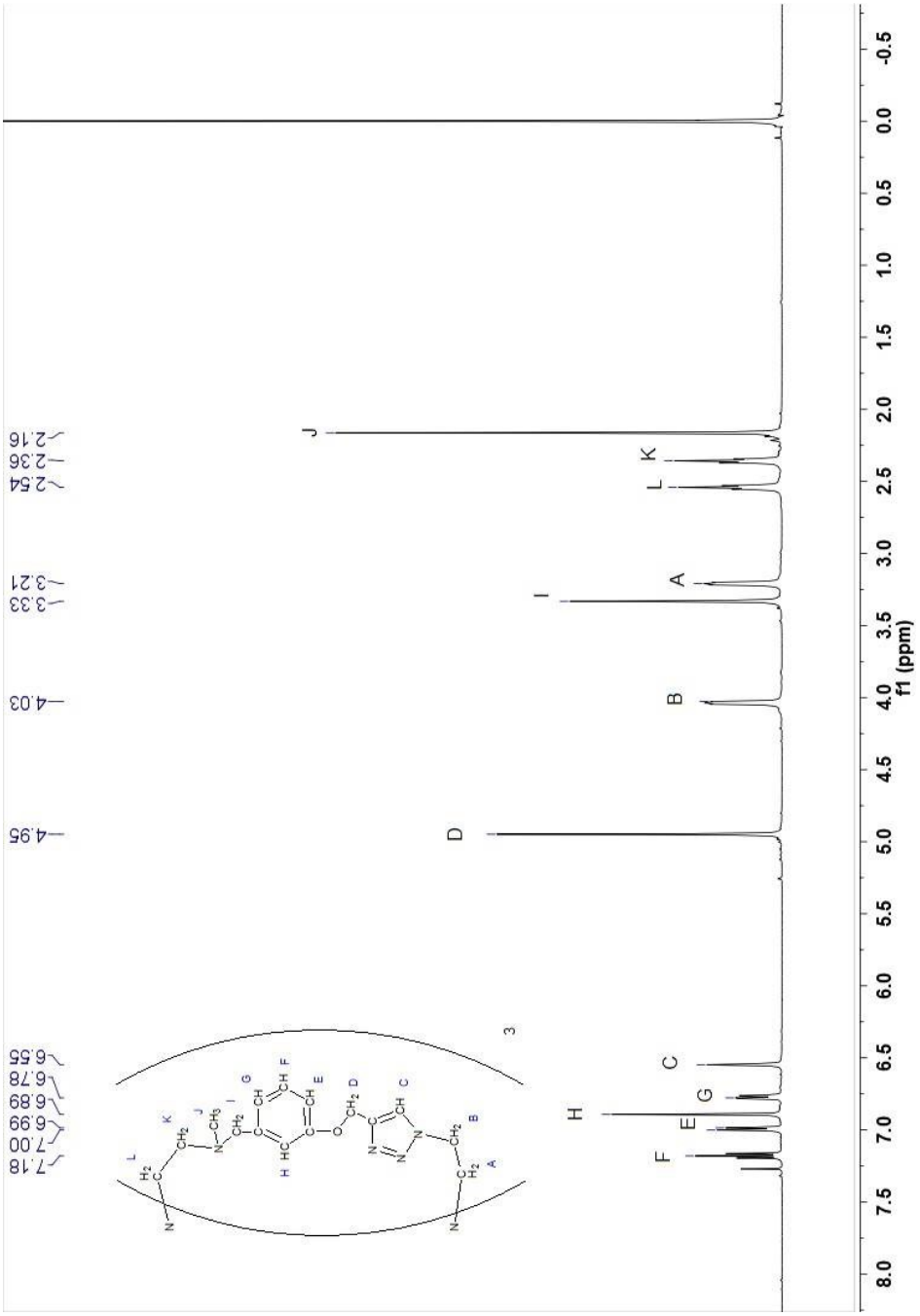

Figure S16. **8** ^{13}C NMR, $CDCl_3$

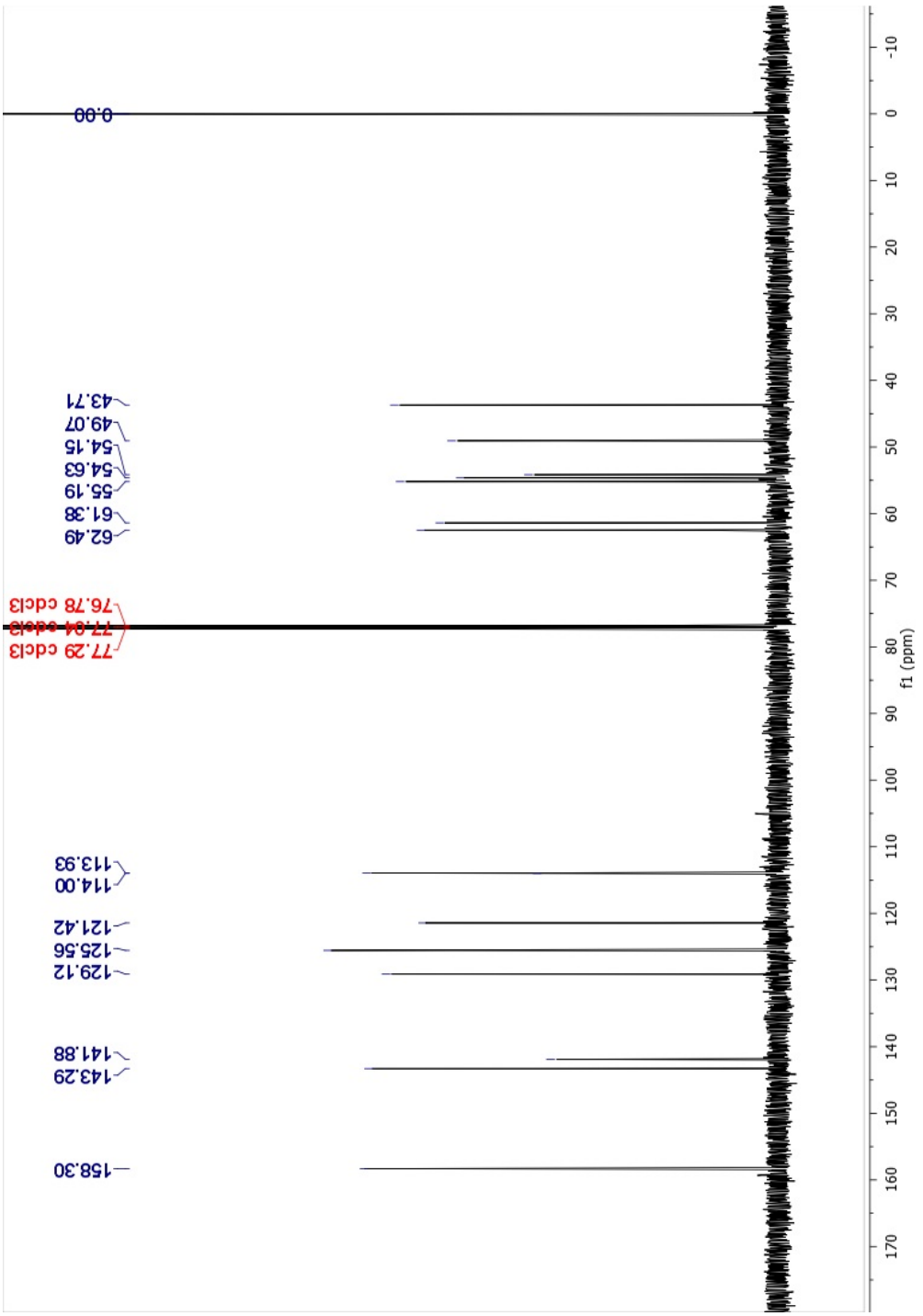

Figure S17. [**LTTA**Ag]NO_3 ^{1}H NMR, CD_3CN

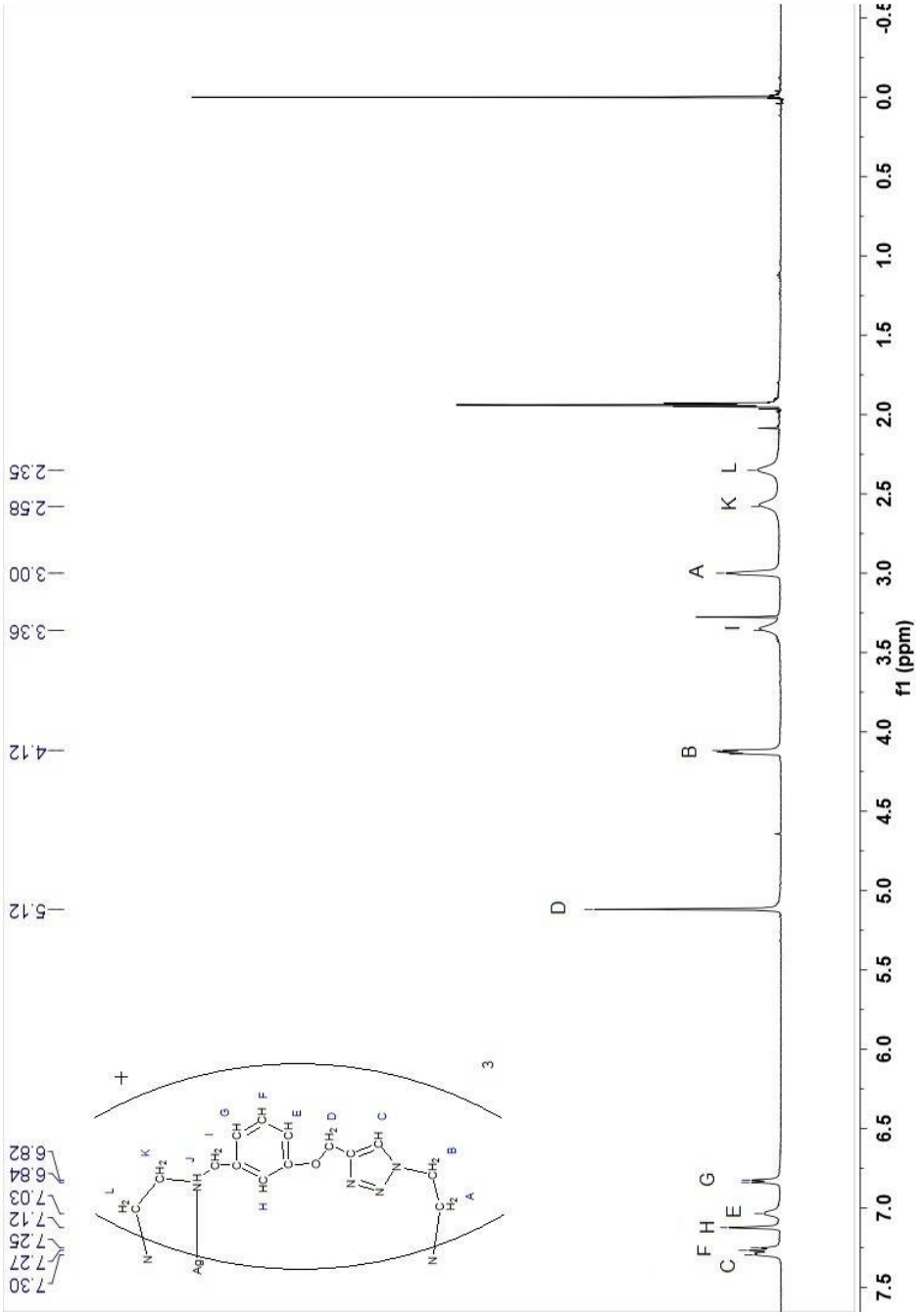

Figure S18. [**LTTA**Zn(Cl)]Cl ^{1}H NMR, CD_3OD, 60°C

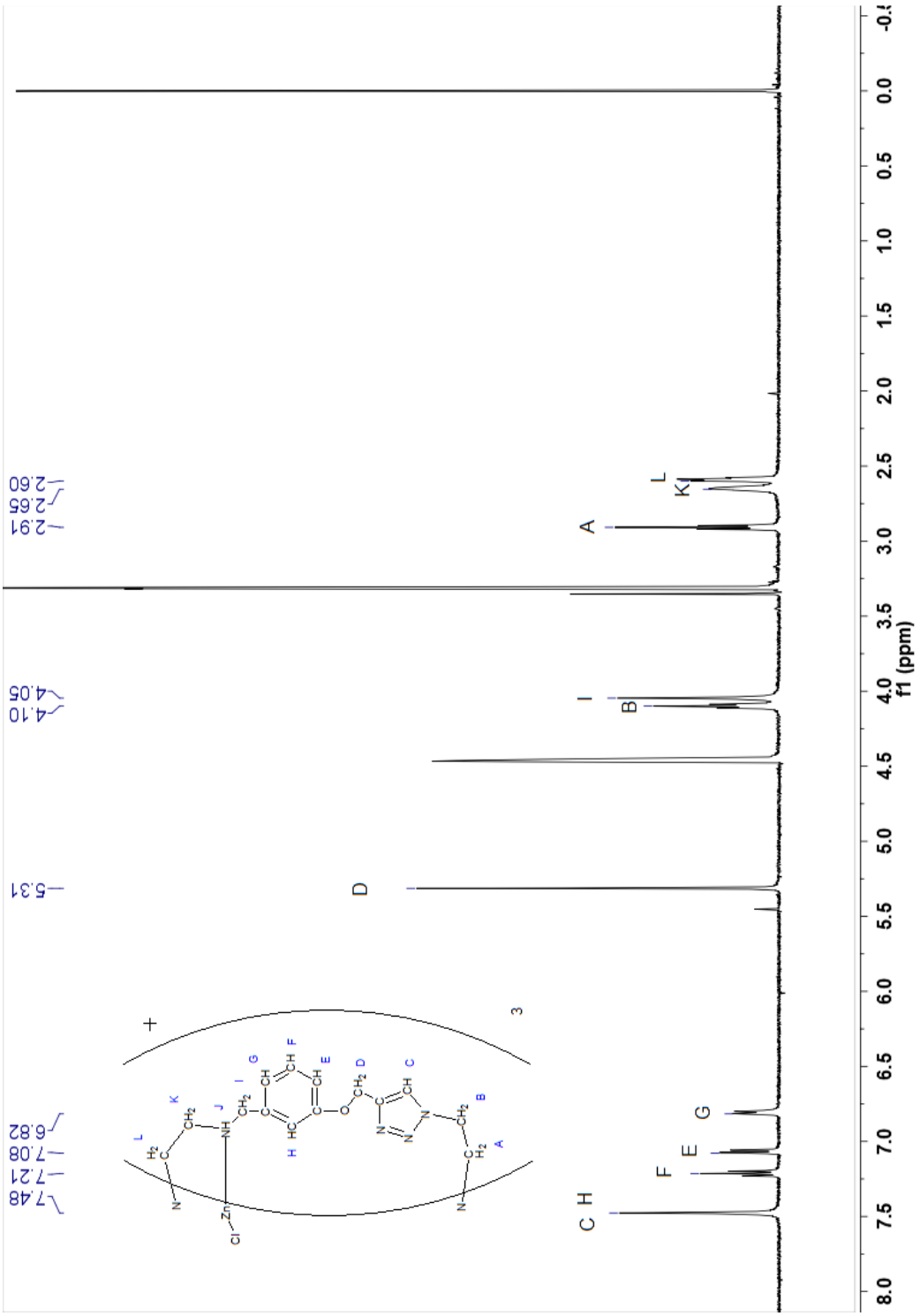

Figure S19. [**LTTA**Zn(Cl)]Cl ^{1}H NMR, ACN, 60°C

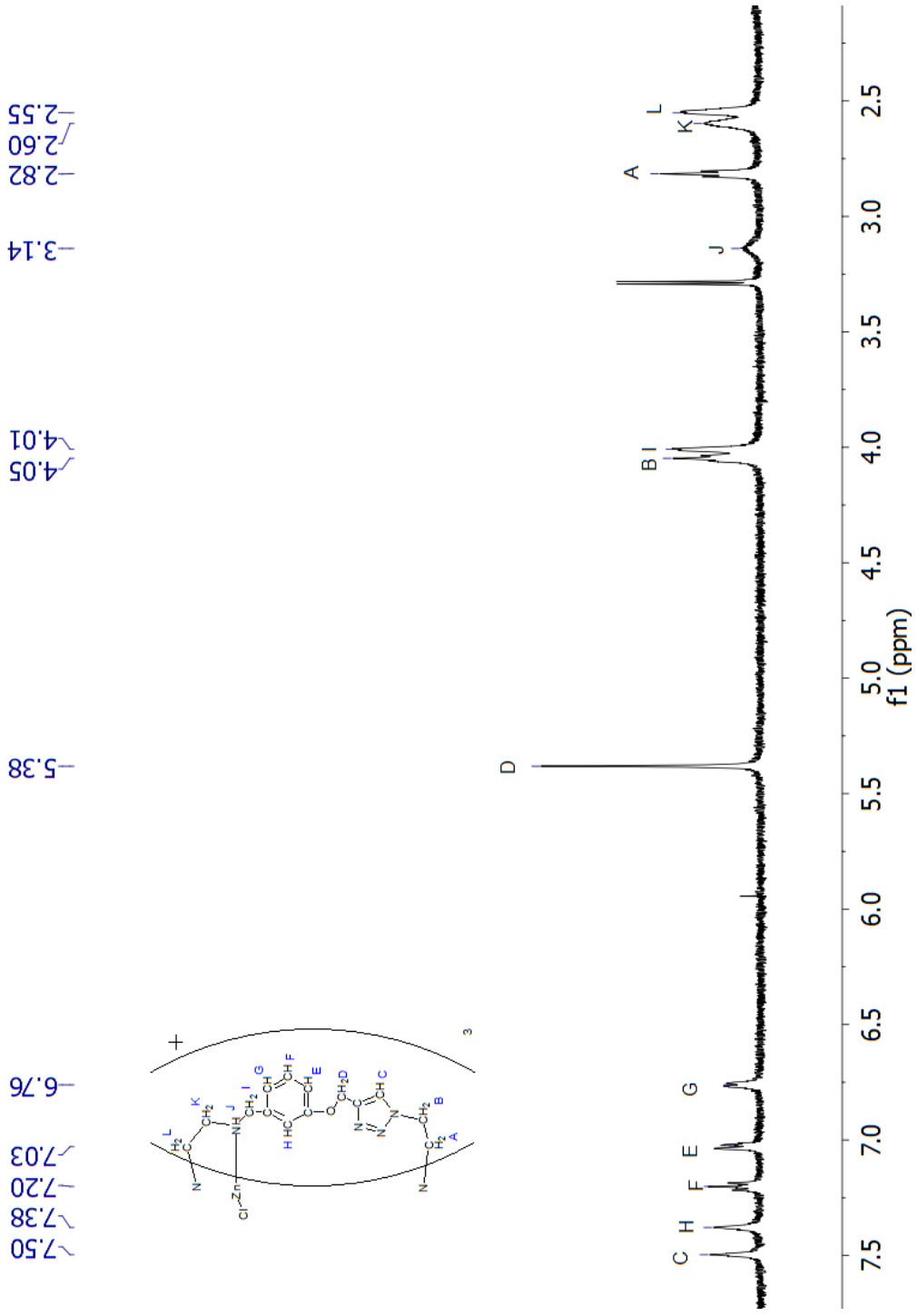

Figure S20. [**LTTA**Zn(Cl)]Cl COSY, ACN, 60˚C

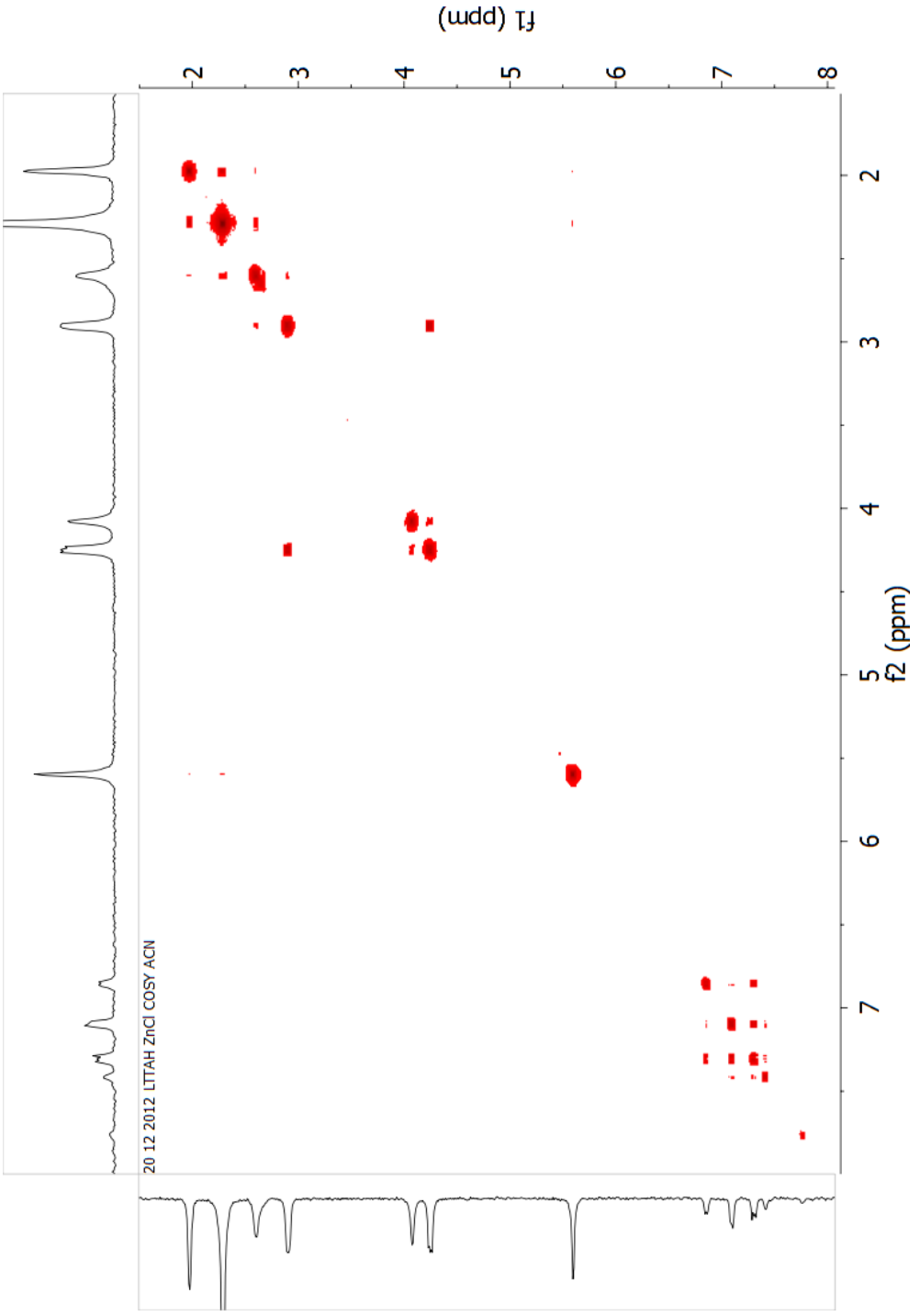

Figure S21. ^{1}HNMR titration of [**LTTA**Zn(Cl)]Cl with AgOTf, ACN, 60°C

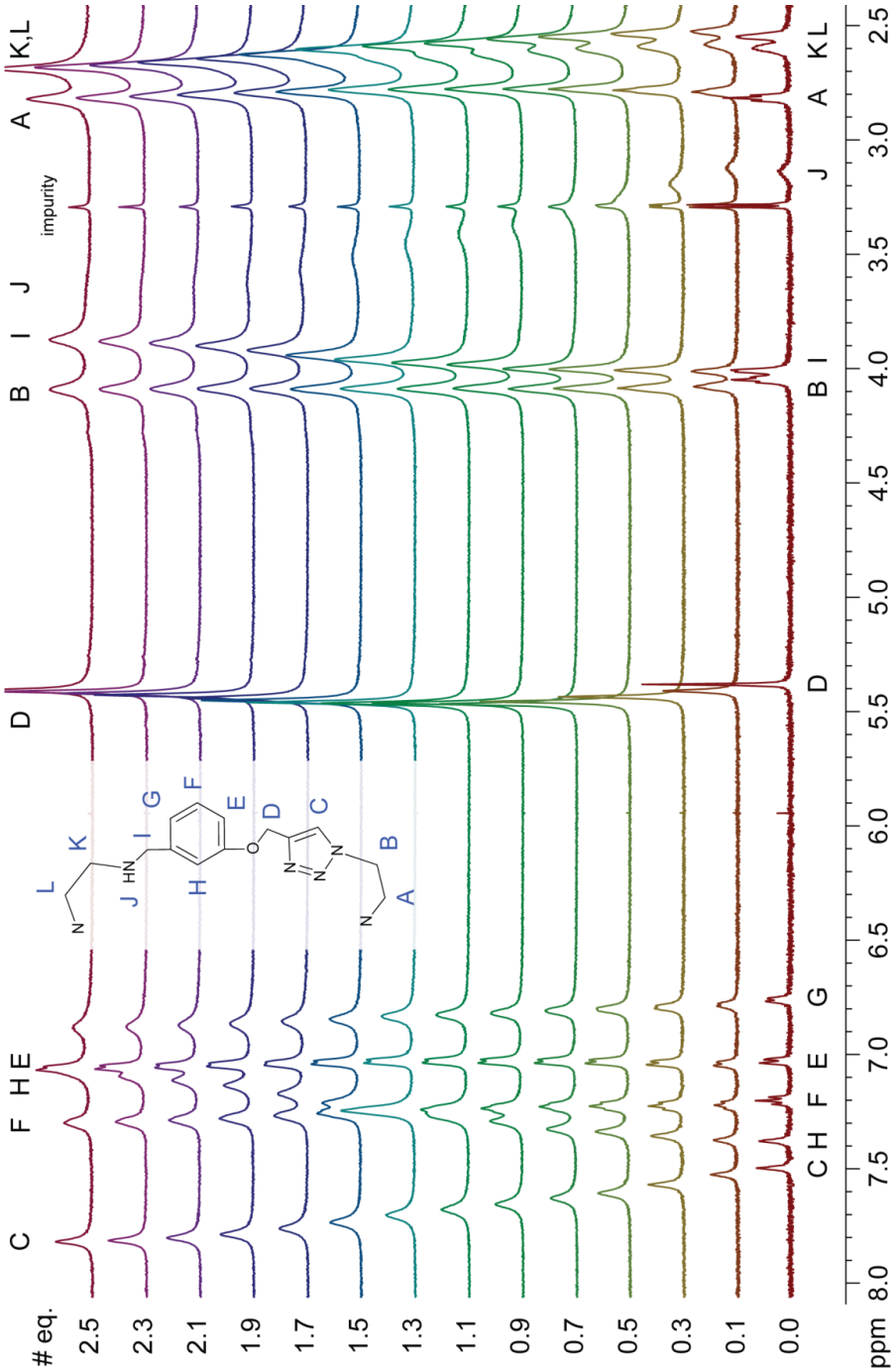

4: To a stirring solution of tris(2-chloroethyl)amine (5g, 24.4 mmol) in 50 mL water was added NaN_3 (7.94g, 122 mmol). The reaction was stirred at 80 °C for 18 h. To to the solution was added NaOH (50 mL of 1M solution) followed by product extraction with 3 x 30 mL of dichloromethane. The solvent was removed under reduced pressure for weighing (4.4 g, 80%) and returned to solution immediately to reduce the risk of explosion.

5: To a stirring solution of propargyl bromide (2.4 mL, 21 mmol) in 5 mL of dimethylformamide was added 3-hydroxybenzaldehyde (2.4 g, 20 mmol) and K_2CO_3 (3.4 g, 24 mmol). The reaction was stirred at room temperature for 24 h. Cold water (50 mL) was added to the solution and the product was extracted with 3 x 20 mL of ethyl acetate. The solvent was removed under reduced pressure and drying under vacuum, yielding a colourless oil, 3.2 g (99%).

Appendix 4: Supplement Information for Chapter 6

Formation and Reactivity of a Fe(III)-Hydroperoxo Supported by a Coordinating Cryptand

Supporting Figures

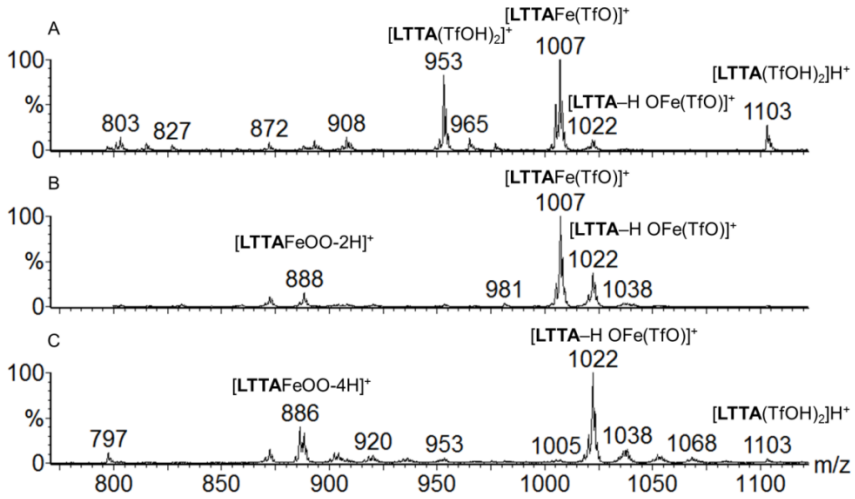

Figure S22. ESI-MS of (A) [**LTTA**Fe](TfO)$_2$ + 2 equiv. PhIO (B) [**LTTA**Fe](TfO)$_2$ + 2 equiv. H_2O_2 (C) [**LTTA**Fe](TfO)$_2$ + 100 equiv. H_2O_2

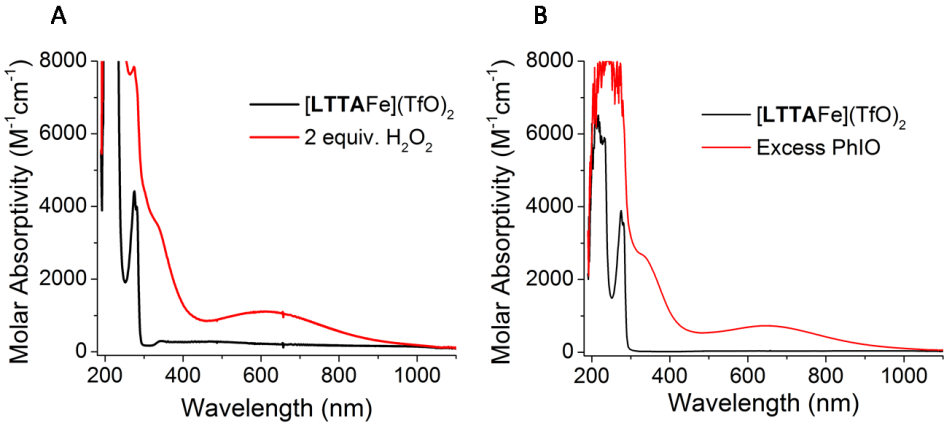

Figure S23. (A) Black: UV/Vis spectrum of 0.2 mM [**LTTA**Fe](TfO)$_2$ in acetonitrile at 20°C. Red: Reaction of [**LTTA**Fe](TfO)$_2$ with H_2O_2 (B) Black UV/Vis spectrum of 0.5 mM [**LTTA**Fe](TfO)$_2$ in acetonitrile at 20°C. Red UV/Vis spectrum of following the addition of excess PhIO (~ 4 equiv.).

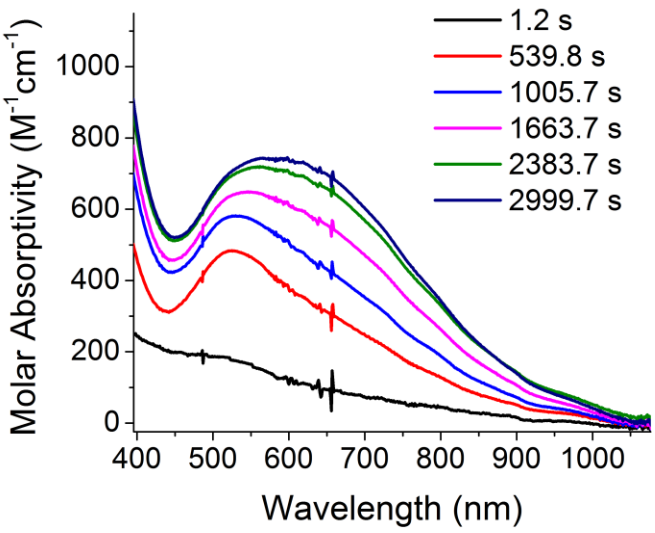

Figure S24. UV/Vis Spectral change from the reaction of 0.5 mM [**LTTA**Fe](TfO)$_2$ with 10 equiv. H_2O_2 in propionitrile at -70°C.

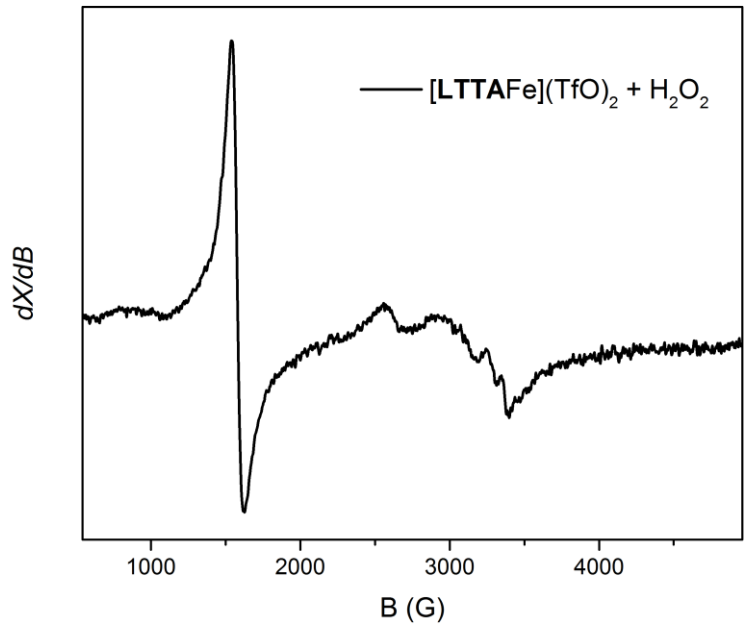

Figure S25. EPR Spectrum obtained from the reaction of 1mM [**LTTA**Fe](TfO)$_2$ with 2mM H_2O_2 in MeCN. The final concentration with respect to Fe was 0.5 mM.

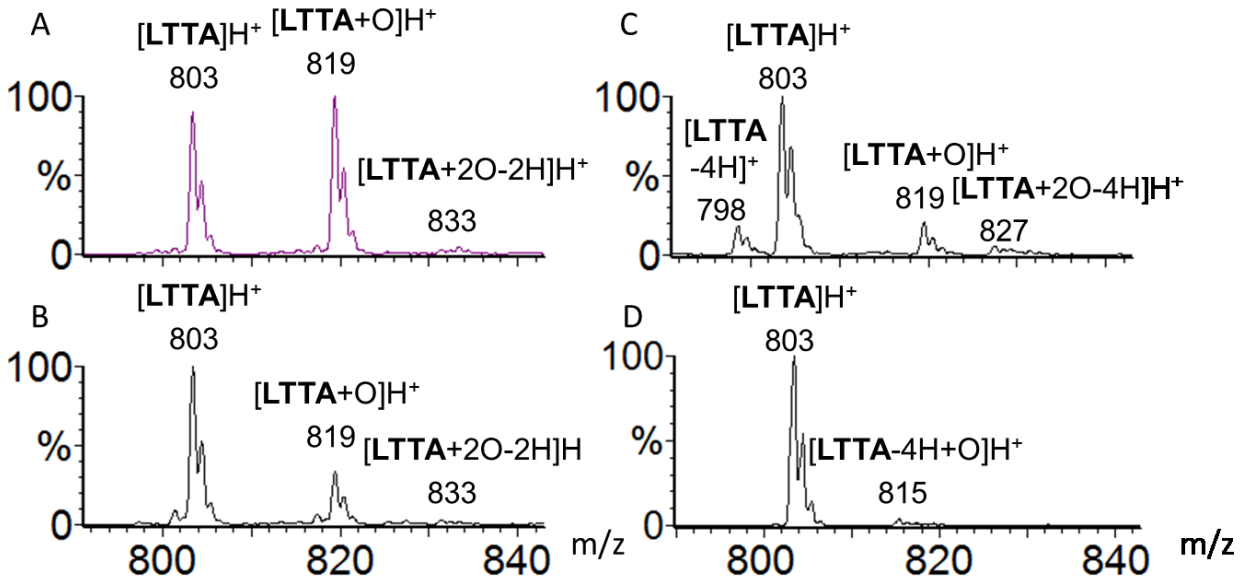

Figure S26. ESI-MS of the organic products of the oxidation (A) [**LTTA**Fe](TfO)$_2$ with 2 equiv. PhIO after purifications steps (B) [**LTTA**Fe](TfO)$_2$ with 2 equiv. PhIO (C) [**LTTA**Fe](TfO)$_2$ with 2 equiv. H_2O_2 (D) **LTTA** with 2 equivalents H_2O_2 (control)

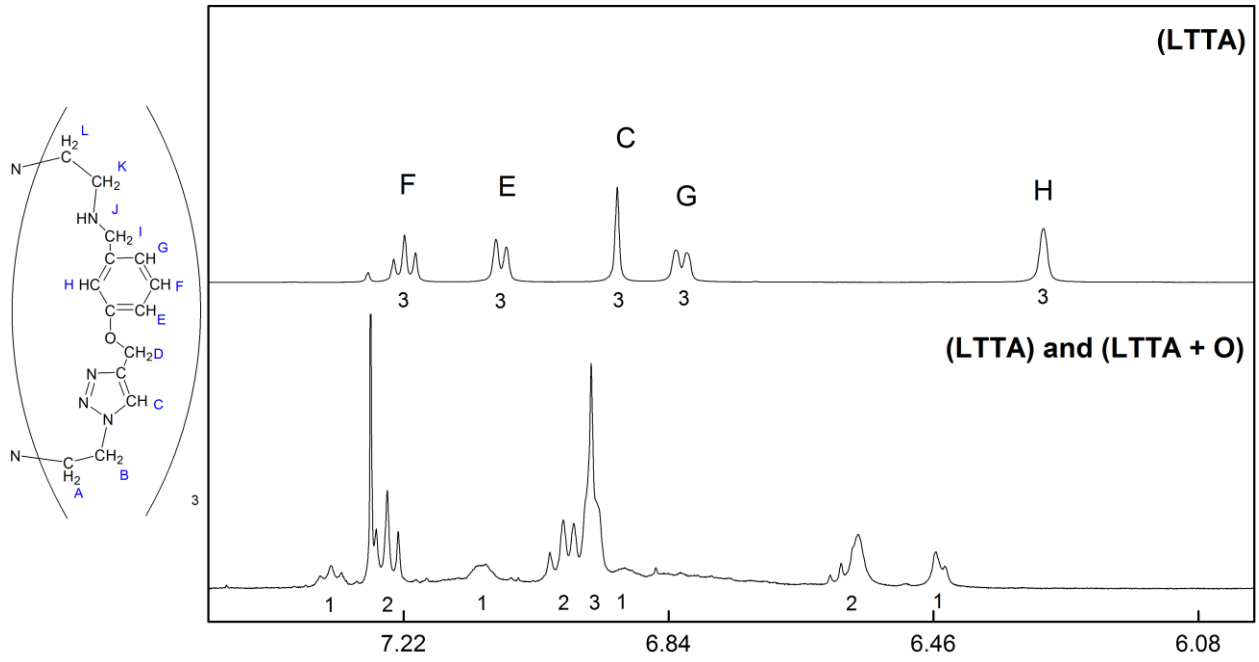

Figure S27. Comparison of the aromatic region of the NMRs Top: **LTTA** Bottom: **LTTA** after oxidation, demetallation and purification. The values below the peaks indicate the relative intergration.

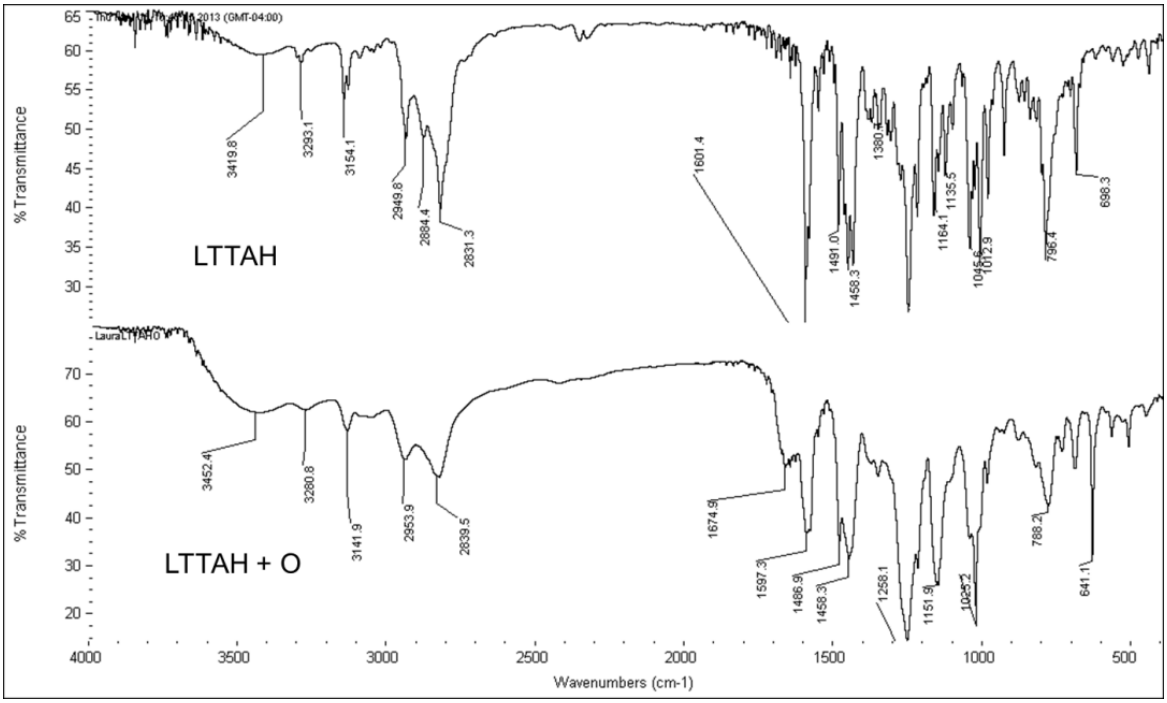

Figure S28. Comparison of IR spectra Top: **LTTA** Bottom: **LTTA** after reaction with oxidation, demetallation and purification.

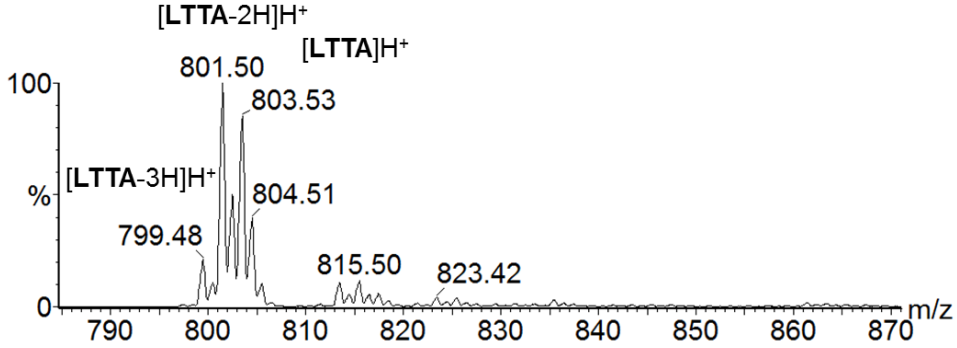

Figure S29. Mass Spectra of the demetallation of the Fe(IV) oxo after decomposition.